Institute of Fundamental Technological Research
Polish Academy of Sciences

DOCTORAL DISSERTATION

Karol M. Golasiński

Analysis of thermomechanical couplings in Gum Metal under selected loadings

Advisor Elżbieta A. Pieczyska, Ph.D., Dr. Habil., Eng.
Department of Experimental Mechanics
Division of Applied Thermomechanics

Warsaw 2019

Oświadczenie autora rozprawy

Oświadczam, że niniejsza rozprawa została napisana przeze mnie samodzielnie.

data podpis autora rozprawy

Oświadczenie promotora rozprawy

Niniejsza rozprawa jest gotowa do oceny przez recenzentów.

data podpis promotora rozprawy

The research presented in this dissertation has been realized to a certain extent with the support of the National Science Centre (NCN), Poland under Grants 2014/13/B/ST8/04280, 2016/23/N/ST8/03688 and 2017/27/B/ST8/03074.

I would like to greatly acknowledge my advisor Elżbieta A. Pieczyska, Ph.D., Dr. Habil., Eng. for introducing me to the fascinating research field of superelastic materials, her constant support and involvement in preparation of this dissertation.

Acknowledgements

Selected research tasks were realized in collaboration with specialized scientific centers and laboratories due to the lack of access to certain equipment. The cooperation with the following colleagues and institutions is greatly acknowledged.

Research task	Scientific coordinator	Institution
Characterization of Gum Metal by means of optical microscopy, scanning electron microscopy and X-rays diffraction	Dr. Maciej Zubko, Dr. Grzegorz Dercz, M.Sc. Paweł Świec	University of Silesia, Department of Structural Studies
Differential scanning calorimetry and determination of specific heat	Dr. Arkadiusz Gradys	Institute of Fundamental Technological Research Polish Academy of Sciences, Laboratory of Polymers and Biomaterials
Determination of elastic constants by ultrasonic measurements	Dr. Sławomir Mackiewicz	Institute of Fundamental Technological Research Polish Academy of Sciences, Division of Non-Destructive Testing

I am very thankful to Prof. Shigeru Kuramoto from Ibaraki University, Dr. Tadahiko Furuta from Toyota Central Research and Development Labs and Prof. Naohisa Takesue from Fukuoka University for providing Gum Metal samples and their scientific support.

I am grateful to Prof. Shuichi Miyazaki and Prof. Hee Young Kim from University of Tsukuba, Prof. Zenji Horita from Kyushu University, Prof. Hisaaki Tobushi, Prof. Ryosuke Matsui, Dr. Kohei Takeda from the AICHI Institute of Technology as well as Prof. Tadashige Ikeda from Chubu University for the opportunity to discuss the research results during my research program in Japan in 2018.

My scientific and technical knowledge was enriched during two one-month internships at Friedrich-Alexander-Universität Erlangen-Nürnberg under supervisor of Prof. Aldo Boccaccini financed by The European Virtual Institute on Knowledge-based Multifunctional Materials (KMM-VIN) and at Fraunhofer Institute for Manufacturing Technology and Advanced Materials, Dresden under guidance of Dr. Alexander Kirchner supported by German Academic Exchange Service (DAAD).

I would like to acknowledge Dr. Michał Maj for conducting measurements with use of infrared thermography and digital image correlation, and Leszek Urbański for his help in design and realization of mechanical tests of Gum Metal.

Abstract

Gum Metal is a trademark of Toyota Central Research and Development Laboratories, Incorporated coined in 2003, which stands for a group of β titanium alloys that exhibit multiple "super" properties and drastic changes in physical properties after plastic working at room temperature. These alloys simultaneously offer low Young's modulus, large range of nonlinear recoverable deformation, no mechanical hysteresis, super strength, super coldworkability and Invar and Elinvar properties. This set of outstanding properties is caused by unconventional deformation mechanisms activated in Gum Metal under mechanical or thermal loads.

The objective of this dissertation is to investigate the unconventional deformation mechanisms of Gum Metal by analyzing the thermomechanical couplings in the alloy under selected loadings. To this end, mechanical and thermal responses of three types of Gum Metal obtained using full-field techniques of digital image correlation and infrared thermography under selected loadings were analyzed. Tension tests were conducted on two sets of flat specimens fabricated and machined at the Toyota Central Research and Development Laboratory and delivered to the IPPT PAN. Compression tests were performed using samples machined from a Gum Metal rod, which was delivered to IPPT PAN by Fukuoka University. The samples of Gum Metal were subjected to structural and thermal analysis by optical and scanning electron microscopy, X-ray diffraction, ultrasonic testing or differential scanning calorimetry.

This dissertation presents experimental results of a comprehensive research program focused on the effects of thermomechanical couplings in Gum Metal under tension and compression. The nonlinear, mechanically recoverable deformation range of Gum Metal was determined by performing cyclic tension with a small strain step. The analysis of the thermal responses of Gum Metal in subsequent tensile cycles demonstrated that the specimen temperature during loading reaches minimum at significantly lower strain than the recoverable strain limit. It means that the activity of stress-induced unconventional deformation mechanisms was found to be exothermic during the loading. During unloading it was found to be endothermic. So it was demonstrated that the mechanically recoverable deformation of Gum Metal is also recoverable from the thermodynamic viewpoint. This observation was also used in the estimation of energy balance of Gum Metal in subsequent loading-unloading cycles. Furthermore, it was shown that Gum Metal is sensitive to the strain rate applied during its loading and deformation. It was manifested in mechanical and thermal responses of the alloy subjected to monotonic tension at selected strain rates. In particular, the analysis of the evolutions of deformation and temperature fields captured at selected stages of Gum Metal tension was important for understanding the strain rate sensitivity of the alloy exhibited particularly in the plastic regime of deformation.

Experimental investigation of mechanical anisotropy in Gum Metal was also realized. The elastic anisotropy of Gum Metal was evaluated by ultrasonic testing. The results demonstrated a significant difference between the Young's moduli determined in the cold-swaging and perpendicular directions. The mechanical anisotropy of Gum Metal under compression was analyzed with a special focus on its plastic behavior. Significant difference between mechanical characteristics and dissimilar characters of the deformation fields obtained for Gum Metal samples with two orientations during the compression was observed. The effect of cyclic compressive loading of Gum Metal conducted along its swaging direction was discussed by analyzing thermomechanical couplings. Hardening phenomena of the alloy in subsequent loading cycles was revealed. Clearly pronounced yield point were observed. A thermal response of Gum metal under compressive loading served to determine critical stages and transition points of its unique mechanical behavior.

Streszczenie

Gum Metal jest znakiem towarowym Centralnych Laboratoriów Badawczo-Rozwojowych Toyoty (Toyota Central Research and Development Laboratories, TCRDL) zgłoszonym w 2003 i oznacza grupę stopów na bazie tytanu β, które cechuje wiele unikatowych właściwości oraz znaczna zmiana charakterystyk po zastosowaniu obróbki plastycznej w temperaturze pokojowej. Stop Gum Metal wyróżnia niski moduł Younga, duży zakres nieliniowego i mechanicznie odwracalnego odkształcenia, brak histerezy mechanicznej, wysoka wytrzymałość, doskonałe parametry tłoczne oraz charakterystyki termiczne podobne do Inwaru i Elinwaru. Ten zestaw wyjątkowych właściwości wynika z aktywności niekonwencjonalnych mechanizmów odkształcenia stopów Gum Metal w procesach obciążeń mechanicznych lub termicznych.

Celem pracy było zbadanie niekonwencjonalnych mechanizmów odkształcenia stopów Gum Metal poprzez analizę sprzężeń termomechanicznych w tych stopach przy wybranych obciążeniach. Zaprezentowane wyniki obejmują analizę mechanicznych i temperaturowych charakterystyk trzech typów stopu Gum Metal przy wybranych obciążeniach, które zostały wyznaczone z zastosowaniem technik polowych tj. korelacji obrazów cyfrowych oraz termografii w podczerwieni. Próby rozciągania zostały zrealizowane na dwóch seriach próbek wytworzonych w TCRDL i przekazanych do IPPT PAN. Próby ściskania zostały przeprowadzone na próbkach przygotowanych z pręta stopu Gum Metal, który został dostarczony do IPPT PAN z Uniwersytetu Fukuoka. Próbki stopu Gum Metal zostały poddane charakteryzacji mikrostrukturalnej i termicznej tj.: mikroskopii optycznej i skaningowej, dyfraktometrii rentgenowskiej, pomiarów ultradźwiękowych oraz skaningowej kalorymetrii różnicowej.

Niniejsza praca przedstawia wyniki kompleksowych badań eksperymentalnych, których program był skupiony na analizie efektów sprzężeń termomechanicznych w stopach Gum Metal w procesach rozciągania i ściskania. Zakres nieliniowego, mechanicznie odwracalnego odkształcenia został wyznaczony w procesie cyklicznego ściskania stopu z niewielkim krokiem odkształcenia. Analiza zmian temperatury stopu Gum Metal w kolejnych cyklach obciążenie-odciążenie wykazała, że spadek temperatury podczas obciążenia następuje przy niższych wartościach odkształcenia niż zakres mechanicznie odwracalnej deformacji. Tym samych udowodniono, że indukowana obciążeniem aktywność niekonwencjonalnych mechanizmów odkształcenia stopu Gum Metal jest egzotermiczna podczas obciążania. Natomiast podczas odciążania jej charakterystyka jest endotermiczna. Pokazano zatem, że mechanicznie odwracalne odkształcenie stopu Gum Metal jest również odwracalne z termodynamicznego punktu widzenia. Ta obserwacja była zastosowana przy analizie oszacowanego bilansu energetycznego stopu Gum Metal w kolejnych cyklach obciążenie-odciążenie. Ponadto stwierdzono, że stop Gum Metal jest wrażliwy na prędkość odkształcenia w procesie monotonicznego rozciągania co jest widoczne w odpowiedziach mechanicznych oraz temperaturowych stopu. Analiza ewolucji pól odkształcenia i temperatury na poszczególnych etapach rozciągania Gum Metalu pozwoliła na wytłumaczenie wpływu prędkości odkształcenia na jego charakterystyki szczególnie w zakresie plastyczności.

W pracy zbadano również anizotropię mechaniczną stopu Gum Metal. Anizotropia sprężysta była zmierzona za pomocą badań ultradźwiękowych. Wyniki wskazały na znaczną różnicę w modułach sprężystości wyznaczonych w dwóch kierunkach: prostopadłych i równoległym do osi ciągnienia pręta stopu. Anizotropia plastyczna stopu Gum Metal została przeanalizowana w procesie ściskania próbek z dwiema orientacjami. Otrzymano znacząca różnicę w charakterystykach mechanicznych oraz odmienny charakter pól odkształcenia próbek stopu Gum Metal w procesie ściskania. Przeanalizowano też wpływ cyklicznego ściskania w kierunku osi ciągnienia stopu Gum Metal w kontekście sprzężeń termomechanicznych. Zaobserwowano zjawisko umacniania się stopu w kolejnych cyklach obciążenie-odciążenie i wyraźnie zarysowane granice plastyczności. Pokazano, że odpowiedź temperaturowa stopu Gum Metal w procesie cyklicznego ściskania może służyć do wyznaczenia poszczególnych etapów odkształcenia stopu.

Contents

List of symbols

G	the shear modulus
E	the Young's modulus
τ	the ideal strength for shear, which is needed for plastic shear along <111> on {011}, {112}, or {123} planes for body-centered cubic crystal
G_{111}	the shear modulus along <111> on {011}, {112}, or {123} planes for body-centered cubic crystal
c_{11}, c_{12}, c_{44}	elastic constants for body-centered cubic crystal
K	the spring constant
d	the wire diameter
D	the coil diameter
α	the coefficient of linear thermal expansion
T	the absolute temperature of the specimen
$\Delta\sigma_{ik}$	the stress tensor
Δl	the change in specimen length
l_0	the initial gauge length
F	the instantaneous force
S_0	the initial cross-section
σ	true stress
ε	true strain
$\Delta\varepsilon$	true strain step
ΔT	the average temperature change
ΔT_{Lmin}	the maximum temperature drop during loading
ΔT_{trans}	the temperature change at mechanically recoverable deformation limit
ΔT_{max}	the maximal temperature change
$\Delta T_{max} - \Delta T_{trans}$	the temperature change during plastic deformation
ΔT_{Umin}	the temperature drop accompanying the unloading process
ΔT_{fin}	the final temperature change after unloading

$\Delta T_{CALCmin}$	the calculated theoretical value of the temperature drop
W_{ext}	the entire work needed to deform the alloy since the beginning of loading
W_{rec}	the work used for recoverable deformation
W_{el}	the part of work used for elastic deformation
W_{pt}	the part of work used for superelastic-like and mechanically recoverable deformation caused by phase transformation of nanodomains
E_{th}	the energy associated with thermoelastic effect
Q_{pt}	the energy of the stress-induced activity of nanodomains
E_s	the energy stored in the alloy
W_d	the entire heat dissipated in the process of deformation
W_{ind}	the heat loss related to heat conductivity
W_{conv}	the heat loss related to convection
W_{rad}	the heat loss related to radiation
$Z = \frac{E_s}{W_{ir}}$	the ratio of the stored energy to the plastic work
H	the displacement gradient tensor
L	the velocity gradient
v	the velocity field
u	the displacement vector
u_x, u_y	the displacement components
ε_{xx}, ε_{yy}	the Hecky strain components
D_{yy}	the deformation rate tensor component
c_p	the specific heat at constant stress

List of abbreviations

IRFS	infrared Fourier-transform spectrometer
EDS	electron dispersive spectroscopy
EBSD	electron backscatter diffraction
SEM	scanning electron microscope
KMM-VIN	The European Virtual Institute on Knowledge-based Multifunctional Materials
DAAD	German Academic Exchange Service
bcc	body-centered cubic
hcp	hexagonal close packed
SMA	Shape Memory Alloy
SME	Shape Memory Effect
SE	superelasticity
TiNi; nitinol	titanium-nickel
XRD	X-ray powder diffraction
TEM	transmission electron microscopy
HRTEM	high resolution transmission electron microscopy
GL	gauge length
UTS	ultimate tensile strength
DB	deformation band
DIC	digital image correlation
IR	infrared
IRT	infrared thermography
VE	virtual extensometer
PLC	Portevin–Le Chatelier
thermogram	temperature distribution

Chapter 1

1. Background, literature review and motivation

1.1. Titanium and its conventional alloys

A new element was first discovered in 1791 by a famous British mineralogist William Gregor. In 1795, Martin Klaproth, a German chemist, independently isolated an oxide of the new element, which he later named titanium after the story of the Greek mythological children of Uranos and Gaia, the Titans. The Titans, who were hated by their father, were held in captivity in the earth's crust, similar to the hard to extract ore. It took more than 100 years to isolate the metal. Titanium was used only in the laboratory until 1932 when William Justin Kroll proved that it can be produced by reducing titanium tetrachloride ($TiCl_4$) with calcium. Eight years later he refined this process with magnesium and even sodium in what became known as the Kroll process. Although research continues into more efficient and cheaper processes, the Kroll process is still used for commercial production. The titanium first alloys, were developed in the late 1940s in the United States. Today a large number of titanium alloys have paved the way for light metals to vastly expand into many industrial applications. More detailed history of advancements in the industry of titanium is given in [Leyens C. et al. 2003, 2013 and Lutjering G. et at. 2007].

Titanium and its alloys provide high specific strength (material's strength/density ratio) and excellent corrosion resistance when compared to other metals. Comparison of density for selected metals with titanium is shown in Fig. 1.1 (a), while specific strength for different classes of materials including Ti alloys is presented in Fig. 1.1 (b). This advantage explains early success of Ti alloys in aerospace and the chemical industries. Other markets such as architecture, chemical processing, medicine, power generation, marine and offshore, sports and leisure, as well as transportation are seeing increased application of titanium. However, one should remember that Ti alloys are relatively expensive and are used for demanding applications.

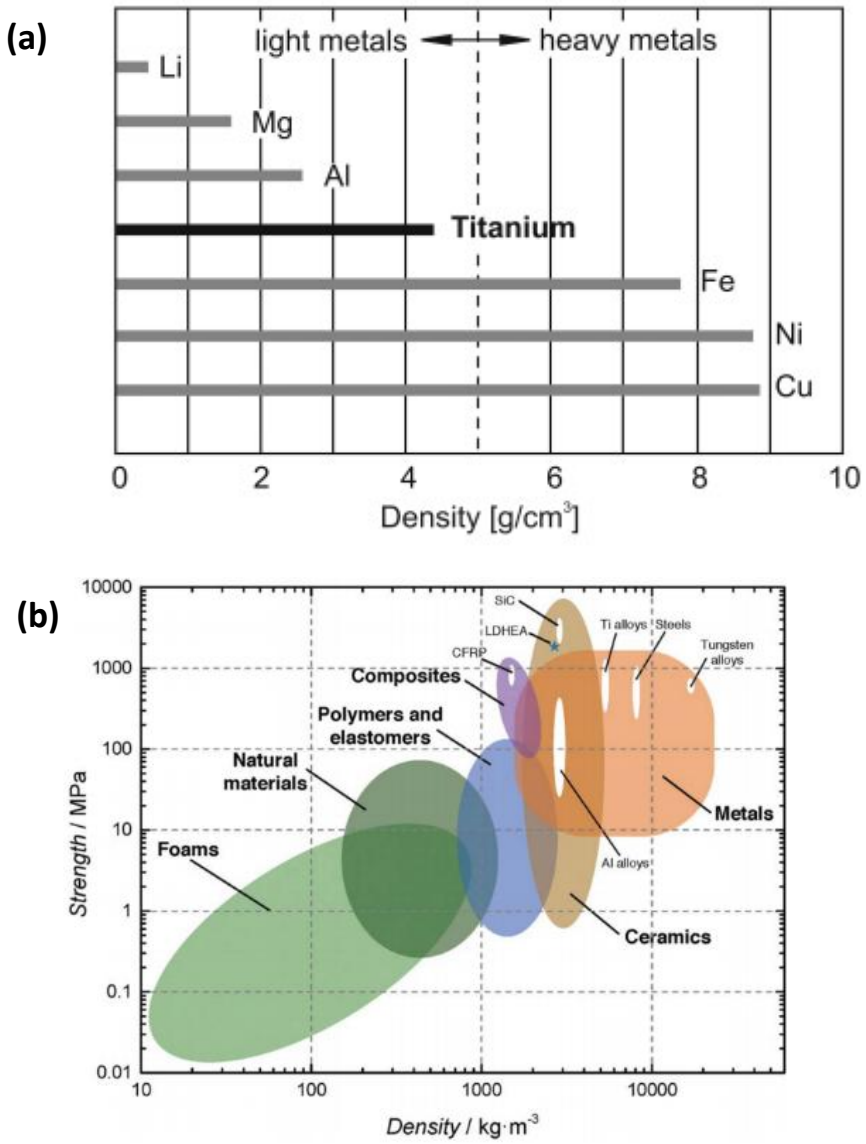

Fig. 1.1 (a) Density of selected metals in comparison to titanium [Leyens C. et al. 2003,]; (b) strength/density ration for different classes of materials including various alloys [Ashby M.F. 2016].

Pure titanium crystallizes at low temperatures in a hexagonal close packed structure, called α titanium. At high temperatures, however, the body-centered cubic structure is stable and is referred to as β titanium. The β-transus temperature for pure titanium is 882±2°C. The atomic unit cells of the hexagonal close packed (hcp) α titanium and the body-centered cubic (bcc) β titanium are schematically shown in Fig. 1.2 with their most densely packed planes and directions highlighted.

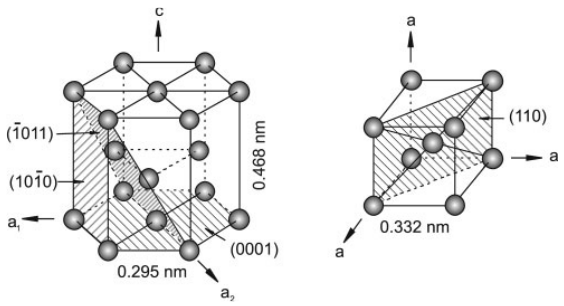

Fig. 1.2 Crystal structure of hcp α and bcc β phase [Leyens C. et al. 2003].

Titanium and its alloys derive many of their properties from the metal's allotropic modifications at 1155 K from the low temperature hcp α phase to the high temperature, bcc β phase. Depending on their influence on the β-transus temperature, the alloying elements of titanium are classified as neutral, α-stabilizers, or β-stabilizers. The influence of selected alloying elements on phase diagrams of Ti alloys is schematically shown in Fig. 1.3. As a consequence depending on the amount of certain stabilizing elements, titanium alloys are classified as α, α + β and β alloys, with further subdivision into near-α and metastable β alloys.

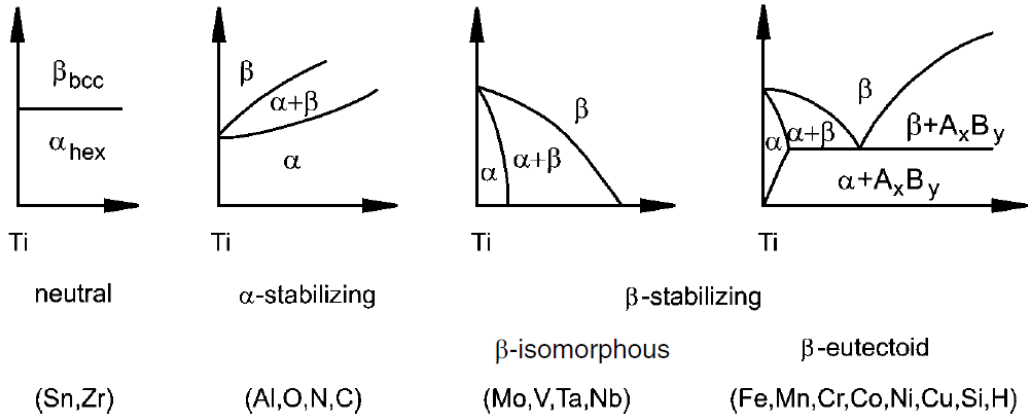

Fig. 1.3 Schematic phase diagrams of Ti alloys showing the influence of certain alloying elements [Leyens C. et al. 2003].

The ability to manipulate the effect of alloying on the stability and physical and mechanical behavior of these two phases both individually and in a variety of microstructural permutations and combinations is critical for functional performance of Ti alloys. Properties of α, α + β and β Ti alloys are compared in Table 1.1.

Table 1.1 Properties of α, α + β and β Ti alloys [Leyens C. et al. 2003].

	α	α+β	β
Density	+	+	–
Strength	–	+	++
Ductility	–/+	+	+/–
Fracture toughness	+	–/+	+/–
Creep strength	+	+/–	–
Corrosion behavior	++	+	+/–
Oxidation behavior	++	+/–	–
Weldability	+	+/–	–
Cold formability	– –	–	–/+

++ excellent
+ good
-/+ moderate
- poor
-- very poor

Single-phase α-Ti alloys are extensively used in applications that are not particularly demanding in terms of strength but focus more on the attractive corrosion resistance of titanium. Alternatively, two-phase α + β alloys offer a range of combinations of strength, toughness and high temperature properties that make them attractive in wide ranging aerospace and other products demanding high specific properties to temperatures of 873 K. Moreover on one hand, the metallurgy of β-Ti alloys enables the development of compositions and processing routes that can satisfy diverse requirements of very high strength with adequate toughness and fatigue resistance required for instance in airframe applications. Characteristics of selected Ti alloys from each phase group namely α, near-α, α + β and metastable β Ti alloys are given in Table 1.2.

Table 1.2 Characteristics of selected Ti alloys.

Alloy	Phase content	Chemical composition [wt. %]	Year of development	Density [g/cm^3]	Young's modulus [GPa]	Yield strength [MPa]	Tensile strength [MPa]	Elongation [%]
cp-Ti (Grade 1)	α	cp-Ti: 0.2Fe, 0.18O	1791 (discovery of Ti)	4.51	100-120	480–655	>550	15
TIMETAL 685	Near-α	Ti-6Al-5Zr-0.5Mo-0.25Si	1969	4.45	120	850–910	990–1020	6–11
Ti6Al4V ELI (Grade 23)	α + β	Ti-6Al-4V	1954	4.42	110-140	800–1100	900–1200	13–16
Beta C	Metastable β	Ti-3Al-8V-6Cr-4Mo-4Zr	1969	4.81	86-115	800-1200	900-1300	50-90

On the other hand, Ti alloys paved their way towards implant applications such as total hip replacement thanks to their biocompatibility and good fatigue performance. However, Young's modulus of conventional Ti alloys, which is even over six times higher than a Young's modulus of cortical bone, poses a significant drawback [Gordin et. al 2014]. The mismatch in elastic properties between the implant and the bone can lead to so-called stress-shield effect, which results in a gradual loss of the bone density and fracture at the bone/implant interphase [Kuroda D. et al. 1998, Niinomi M. 1998, Niinomi M. et al. 2012, 2015]. Thus recently, the development of Ti-based materials with low Young's modulus for biomedical applications has been of particular interest in many research centers.

1.2. Ti-based superelastic and shape memory alloys

Shape memory alloys (SMAs) are functional materials with fascinating properties including shape memory effect (SME) and superelasticity (SE), which are not possessed by ordinary metals. Schematic stress vs. strain curves of alloys with SME and SE are shown in Fig. 1.4 (a, b). An alloy with SME being previously deformed can recover its original shape by heating (Fig. 1.4(a)); while an alloy with SE is characterized by a large recoverable strain obtained via mechanical hysteresis loop (Fig. 1.4(b)).

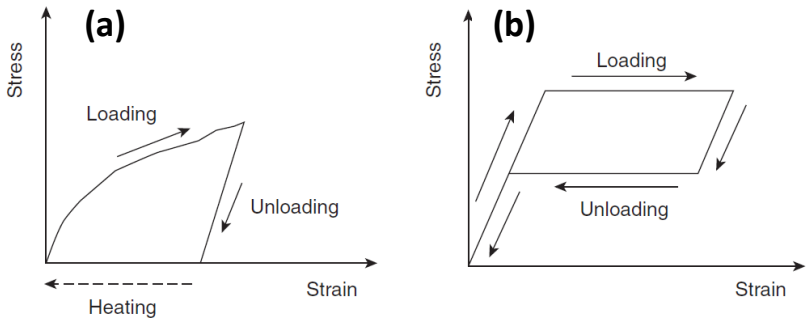

Fig. 1.4 Schematic stress vs. strain curves of materials with (a) shape memory effect; (b) superelasticity [Yamauchi K. et al. 2011].

Thanks to their unique properties, SMAs are widely used in a range of appliances, from coffee maker, thermostats, glasses frames, coupling for piping, Intelligent Reinforced Concrete, vibration dampers, dental braces, stent grafts etc. In particular, titanium-nickel (TiNi; nitinol) SMA, which was first reported in 1963 [Buehler W. J. et al. 1963], has gone through a long way of optimization towards successful applications in a wide spectrum of technological areas

[Miyazaki S. et al. 1981a, 1981b, 1982, 1983, 1984, 1986, 1989a, 1989b, 1989c, Takei F. et al. 1983, Kudoh Y. et al. 1985, Kim J.I. 2004, 2005a, 2005b, Miyazaki S. 2017].

The underlying mechanism of SME and SE is associated with the stress- or temperature-induced crystallographically reversible martensitic transformation which appears in SMAs. The parent phase of the Ti–Ni has a CsCl-type B2 superlattice, while the martensite phase is three-dimensionally close packed (monoclinic or B19') as shown in Fig. 1.5.

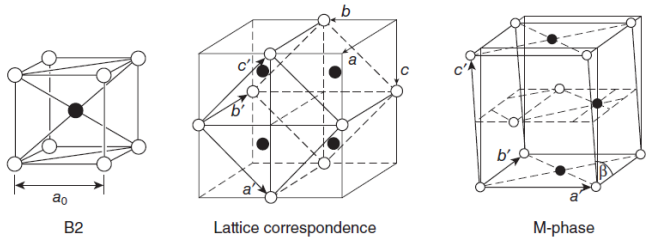

Fig. 1.5 Crystal structures of the parent (B2) and martensite (B19') phases and the lattice correspondence between the two phases [Yamauchi K. et al. 2011].

Use of Ti-Ni SMAs is present in the medical sector for appliances such as stents, guide and orthodontic wires as well as filtration devices. However, it has been pointed out that pure Ni is a toxic element and causes Ni hypersensitivity [Kuroda D. et al. 1998, Niinomi M., 1998]. Although the Ti–Ni alloys are considered to be safe in the human body based on experience and scientific consideration, in order to solve the psychological problem of the risk of Ni hypersensitivity, Ni-free Ti-based shape memory and superelastic alloys among them Ti-Nb-based systems have been recently developed [Kim H.Y. et al. 2016].

Stress-strain curves of Ti – x Nb (20<x<28 at. %) alloys are shown in Fig. 1.6. As a consequence of the Nb content optimization shape memory effect is observed in Ti-20Nb, Ti-21Nb, Ti-22Nb, Ti-23Nb, Ti-24Nb and Ti-25Nb, superelasticity was achieved in Ti-26Nb and Ti-27Nb, whereas Ti-28Nb does not exhibit any peculiar effect.

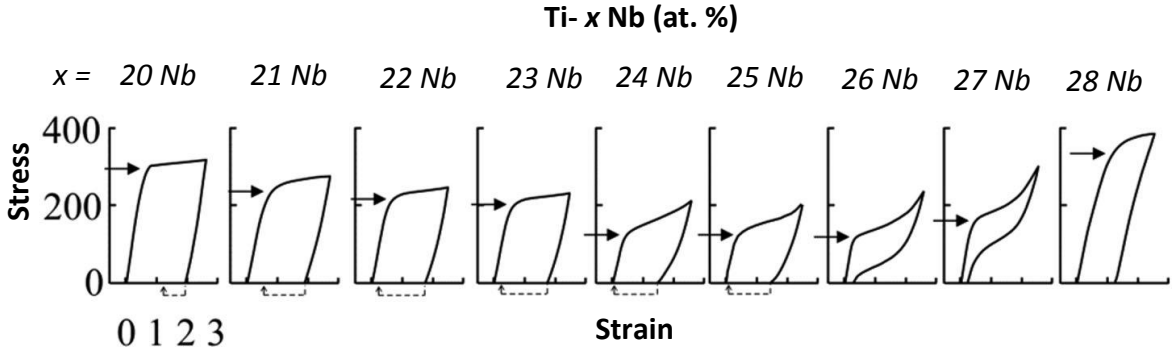

Fig. 1.6 Stress-strain curves of Ti – x Nb (20<x<28 at. %) alloys [Kim H.Y. et al. 2016].

The shape memory effect and superelasticity observed in Ti-Nb alloys is associated with the stress-induced martensitic transformation from β to α" and its reverse transformation. Lattice correspondence between the parent β and martensite α" phases is shown in Fig. 1.7.

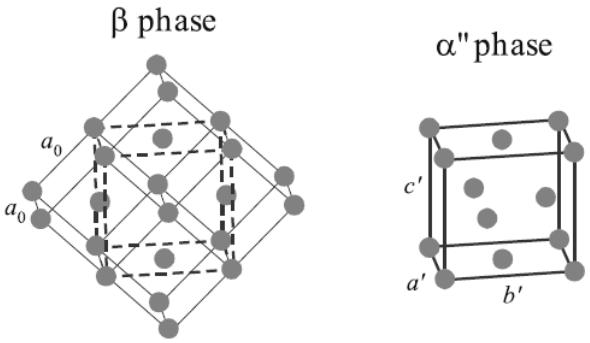

Fig. 1.7 Lattice correspondence between the parent β and martensite α" phases [Kim H.Y. et al. 2016].

1.3. Gum Metal – Ti-based Ni-free superalloy

1.3.1. General information about Gum Metal

High Young's modulus of titanium and its conventional alloys as well as cytotoxicity of Ni in Ti-Ni were dominant reasons for development of a new class of Ni-free Ti-based alloys with low Young's modulus and high strength named Gum Metal. Gum Metal is a trademark of Toyota Central Research and Development Laboratories, Incorporated coined in 2003 and stands for a group of alloys that exhibit multiple "super" properties and drastic changes in physical properties after plastic working at room temperature [Saito T. et al. 2003]. These alloys simultaneously offer low Young's modulus, large range of recoverable deformation, no mechanical hysteresis, super strength, super coldworkability and Invar and Elinvar properties. Comparison of tensile strength vs. Young's modulus of selected alloys and Gum Metal is shown in Fig. 1.8(a), while stress vs. strain curves of Gum Metal, superleastic Ti-Ni and steel are presented in Fig. 1.8(b).

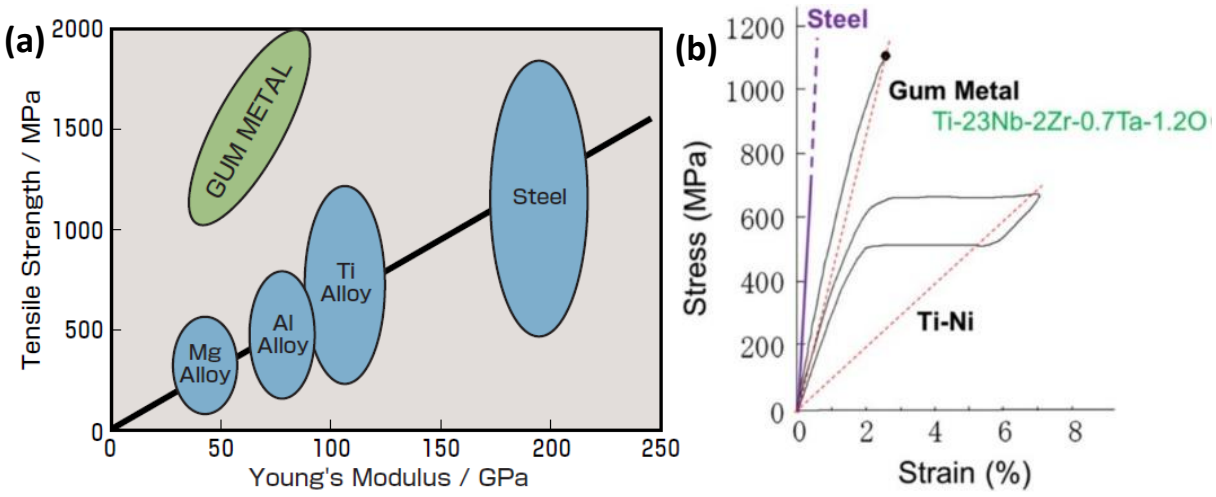

Fig. 1.8 (a) Comparison of tensile strength vs. Young's modulus of selected alloys and Gum Metal [Nishino K. 2003]; (b) stress vs. strain curves of Gum Metal, superelastic Ti-Ni and steel [Miyazaki S. 2017].

1.3.2. Design of Ti-based alloys with low Young's modulus

The design of Gum Metal included ab-initio calculations for determination of possible compositions resulting in low Young's modulus in Ti-based binary alloys [Ikehata H. et al. 2004]. The elastic constants of selected systems including $Ti_{1-x}X_x$ (*X*=V, Nb, Ta, Mo, and W) for *x*=0.0, 0.25, 0.5, 0.75, and 1.0 were investigated experimentally and were calculated by the ultrasoft pseudopotential method within the generalized gradient approximation to density functional theory. The Young's moduli of the polycrystals for these Ti binary alloys were calculated from the calculated elastic constants of the single crystal by using the Voigt-Reuss-Hill averaging scheme. Theoretical (solid line) and experimental (dots) values of Young's modulus vs. content of alloying element X for binary systems Ti-X (where, X is V, Nb, Ta, Mo, or W) are shown in Fig. 1.9(a). The results showed that the Young's moduli of the Ti-*X* binary alloys have the minimum values in the vicinity of *x*=0.25. This value corresponds to the metastable β Ti alloys where the hcp lattice becomes unstable with respect to the bcc crystal structure, as one can notice in the phase diagram of Ti alloys shown in Fig. 1.9(b).

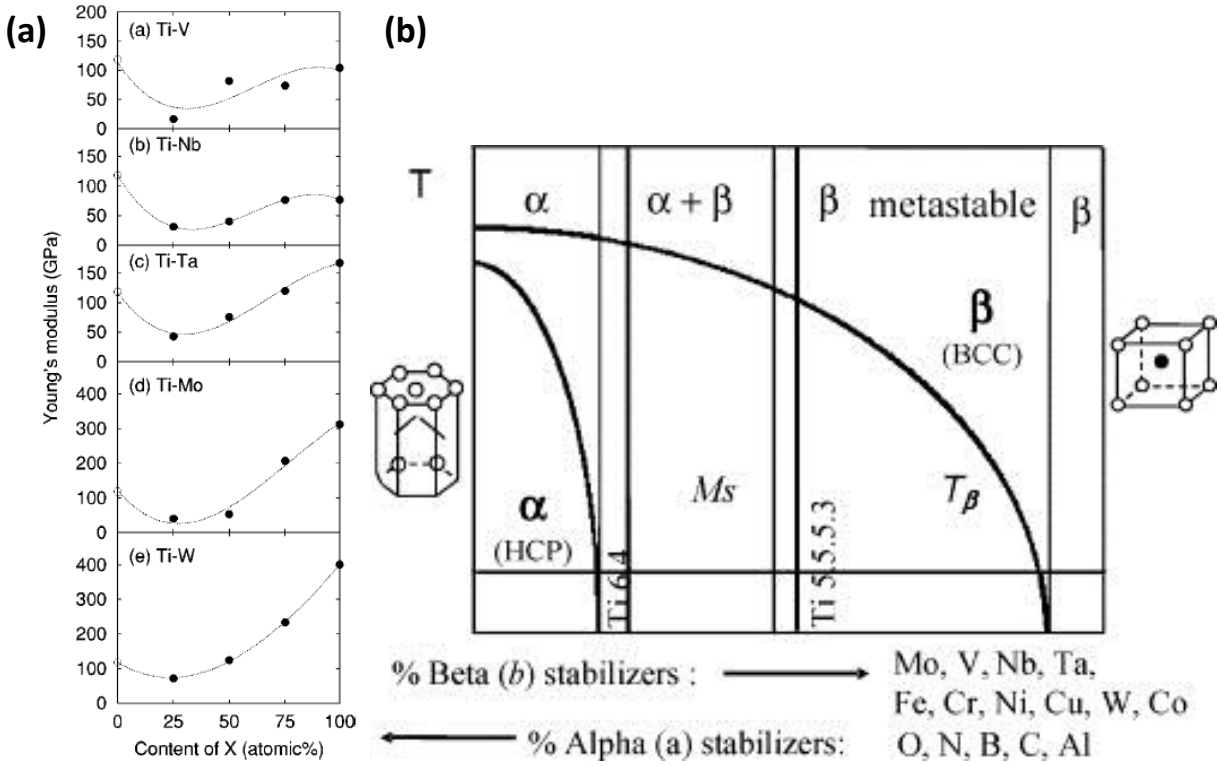

Fig. 1.9. (a) Theoretical (solid line) and experimental (dots) values of Young's modulus vs. content of alloying element X for binary sytems Ti-X (where, X is V, Nb, Ta, Mo, or W) [Ikehata H. et al. 2004]; (b) Phase diagram of Ti alloys depending of the content of specific alloying elements [Arrazola P.J. et al. 2009].

From the calculation results of elastic constants (c_{11}, c_{12}, c_{44}) for various bcc binary systems, it was found that the difference $c_{11}-c_{12}$ becomes nearly zero with the valence electron number of around 4.20–4.24 [Ikehata H. et al. 2004]. The very low value of $c_{11}-c_{12}$ also represents the low stability of the bcc structure in these alloys, which are classified as metastable β-Ti alloys. It was pointed that controlling the valence electron number at around 4.20–4.24 is important to realize a low Young's modulus material in the Ti binary alloys having bcc structure.

1.3.3. Composition and outstanding properties of Gum Metal

The composition of the developed alloy is fundamentally expressed as Ti–24 at% (Ta + Nb + V)–(Zr, Hf)–O. Various alloy compositions are available, such as Ti–23Nb–0.7Ta–2Zr–O alloy and Ti–12Ta–9Nb–3V–6Zr–O alloy (at. %). Gum Metal requires substantial cold working usually around 90% in area reduction and the presence of a certain amount of oxygen (0.7 to 3.0 at. %) to achieve unique characteristics.

In most of publications concerning investigation of the alloy, Gum Metal with an optimized composition near Ti–23Nb–0.7Ta–2Zr–1.2 O (at. %) processed by cold working with 90% in area reduction is of main interest [Saito T. et al. 2003, Furuta T. et al. 2005, Kuramoto S. et al. 2006, Yano T. et al. 2009, Morris Jr. J.W. et al. 2010]. Tensile stress vs. strain, Young's modulus vs. temperature and linear thermal expansion vs. temperature curves of Gum Metal before and after cold working are shown in Figs. 1.10(a), (b) and (c), respectively. The process of cold working induces large range of nonlinear recoverable deformation (so-called nonlinear elasticity in Fig. 1.10(a)) with high strength of the alloy as well Elinvar and Invar behaviors in the temperature range between 100K and 500K of Gum Metal, shown in Fig. 1.10(b) and Fig. 1.10(c), respectively [Saito T. et al. 2003].

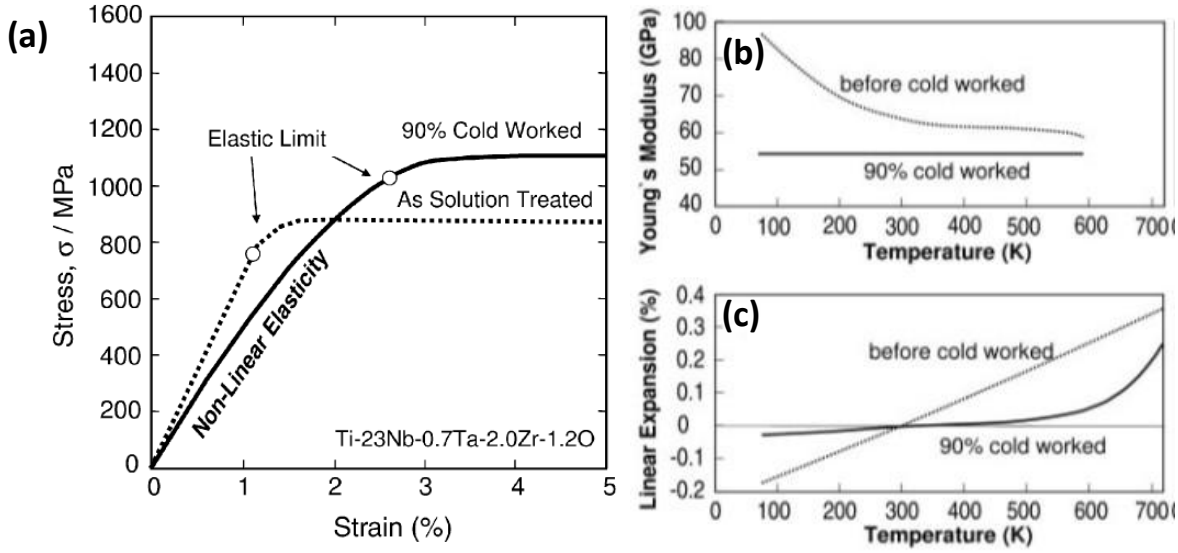

Fig. 1.10 (a) Tensile stress vs. strain [Kuramoto S. et al. 2006]; (b) Young's modulus vs. temperature [Saito T. et al. 2003] and (c) linear thermal expansion vs. temperature curves of Gum Metal before and after cold working [Saito T. et al. 2003].

Various techniques applied for material characterization were used to elucidate changes in microstructure and phase content induced to the alloy by the process of cold working were described in literature.

Optical microstructure of Gum Metal before cold working is composed with the equiaxed beta grains as presented in Fig. 1.11(a). After cold working changes into "marble-like" microstructure were observed as shown in Fig. 1.11(b). Local nanodisturbances (bending) in the crystal lattice of the cold-worked alloy were imaged by a high-magnification TEM as

illustrated in Fig. 1.11(c). The distribution of discrete 2 to 3 nm order strain contours is found to correspond to disturbances in the crystal lattice. In addition to exhibiting this nanoscale bending, the crystal lattice was found to bow at a radius of about 500 nm and at a scale of several tens of micrometers.

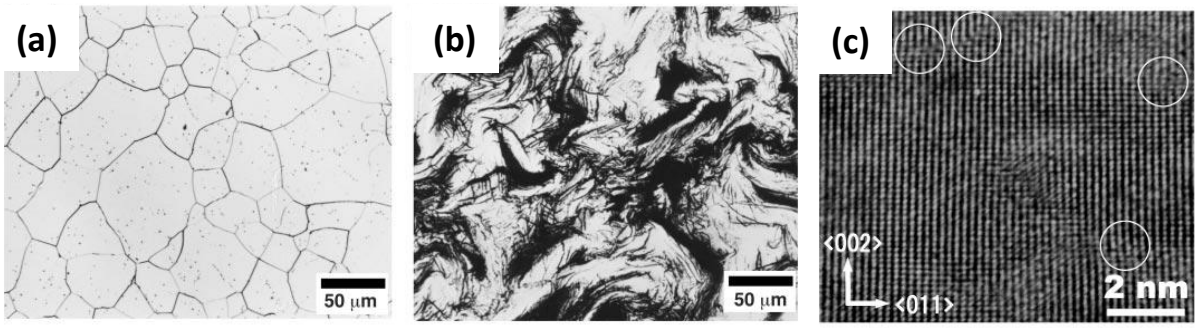

Fig 1.11 Comparison of optical microstructure of Ti-23Nb-0.7Ta-2Zr-1.2O (at. %) alloy: (a) before cold working and (b) cold-worked by 90% reduction in area; (c) a high-magnification TEM image of the cold-worked specimen. Local disturbances in the crystal lattice are indicated within open circles [Saito T. et al. 2003].

However, TEM observations at different magnifications and orientations revealed virtually no dislocations, as presented in Figs. 1.12 (a) and (b).

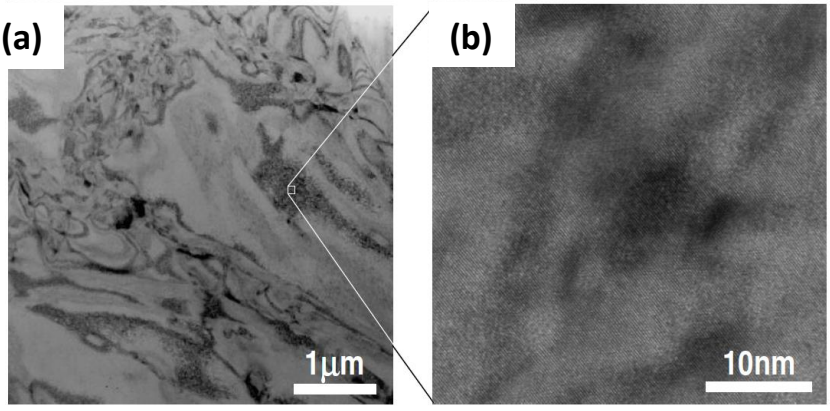

Fig. 1.12. TEM images of 90 % cold-worked Ti-23Nb-0.7Ta-2Zr-1.2O alloy indicating no presence of dislocation after a large amount of plastic deformation [Saito T. et al. 2003].

Results of texture analysis of Gum Metal performed by EBSD are shown in Fig. 1.13(a) and (b) [Morris Jr. J.W. et al. 2010]. Almost all the crystals in the severely worked sample have <1 1 0> axes parallel to the swaging (normal) axis. However, the grain orientations in the plane

that contains the swaging axis are more nearly random, and the grains themselves are severely distorted; the crystal planes are bent and puckered around the <1 1 0> swaging axis.

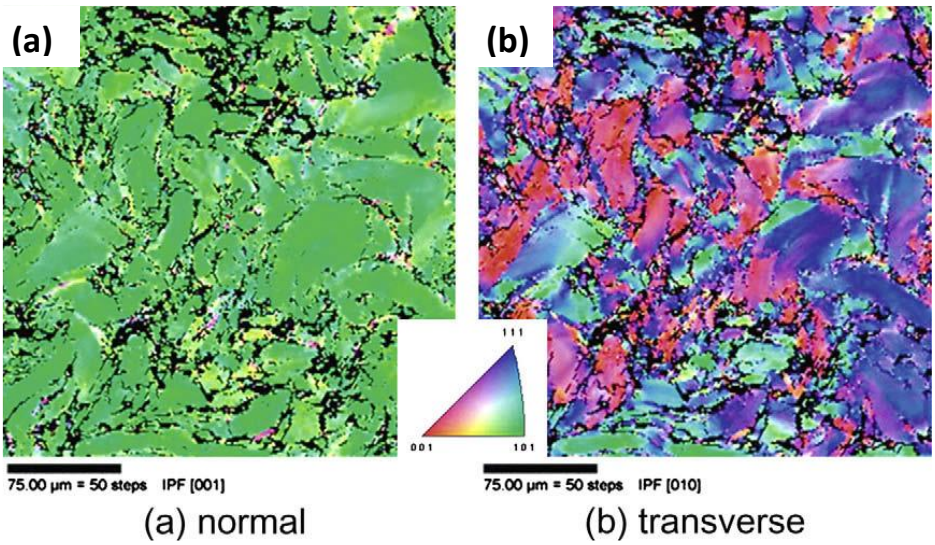

Fig. 1.13 EBSD maps of grain orientations in an 85% cold-swaged specimen of Gum Metal: (a) normal direction <1 1 0> parallels the axis and (b) transverse direction, planes randomly oriented and severely distorted through rotation about <1 1 0> [Morris Jr. J.W. et al. 2010].

Phase content of the alloy before and after cold working was analyzed by X-ray powder diffraction (XRD) [Furuta T. et al. 2005]. Both XRD profiles, shown in Fig. 1.14, do not show the presence of any peaks other than the β (bcc) phase. It is also inferred from the XRD profile after cold working that the preferred orientation of (011) is formed by crystallographic rotation as the plastic working proceeds.

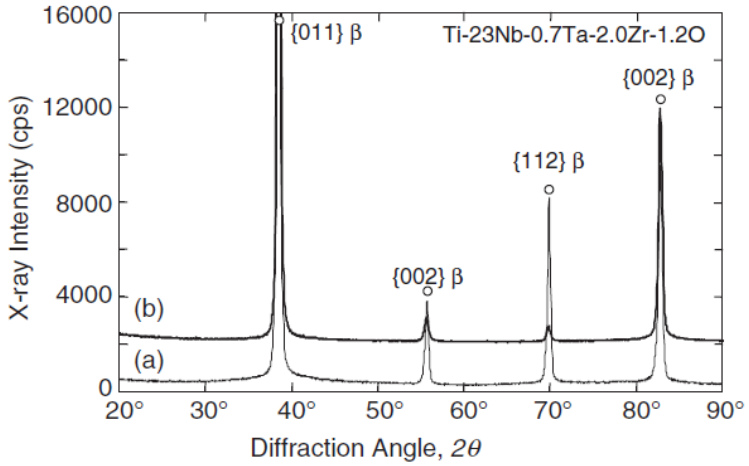

Fig. 1.14 XRD profiles of Gum Metal after (a) solution treatment at 1173K and (b) cold working by 90% [Furuta T. et al. 2005].

Results of more detailed observations of the phase content in Gum Metal were realized using energy-filtered transmission electron microscopy (TEM) as shown in Fig. 1.15 [Yano T. et al. 2009].

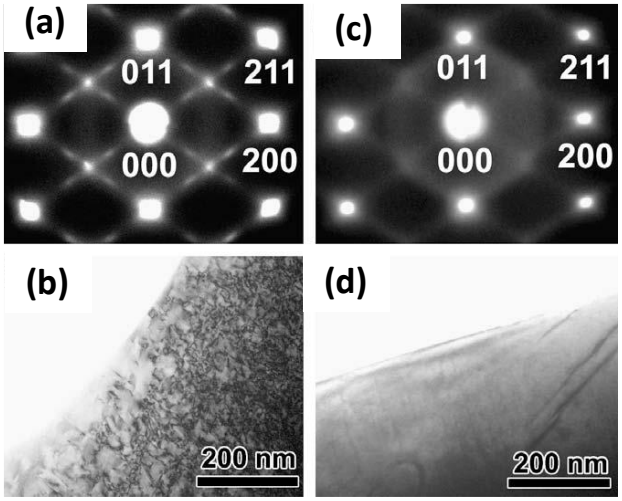

Fig. 1.15 (a) Electron diffraction pattern and (b) bright-field image of the Gum Metal specimen. (c) Electron diffraction pattern and (d) bright-field image of the as-annealed alloy specimen [Yano T. et al. 2009].

Besides the primary β phase, nanosized secondary phases i.e. orthorhombic α" phase as well as hexagonal ω precipitates were found in the cold worked alloy as shown in Fig. 1.15 (a, b). The secondary phases were hardly observed in the alloy before cold working as presented in Fig. 1.15 (c, d). The crystal structures of the parent β, orthorhombic α" and hexagonal ω phases are shown in Fig. 1.16.

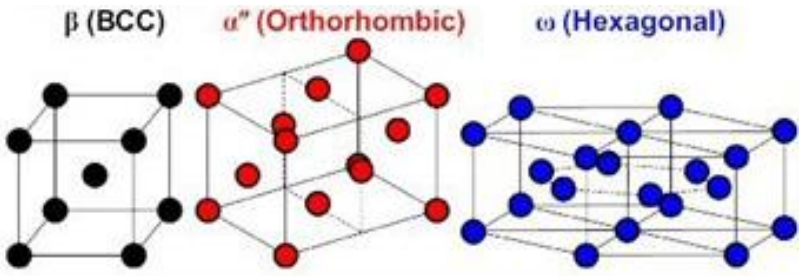

Fig. 1.16 Crystal structures of the parent β, orthorhombic α" and hexagonal ω phases [Zhang J. et al. 2017].

In general, the ω-phase can occur under ambient pressure in a metastable manner in alloys in which the β - phase is stabilized with respect to the martensitic β → α" transformation. Gum Metal is also this case. Depending on the formation process, ω-phases can be isothermal or athermal.

The isothermal β → ω transformation is a product of thermally activated β–phase decomposition and is accompanied by solute rejection by diffusional processes from the β to the ω–phase and is thus partially replacive in nature.

The athermal β → ω transformation, which appears in Gum Metal, is displacive, diffusionless and of the first-order and the ω–phase so obtained has a composition very close to that of the β–phase. It has also been indicated that this phase can be obtained either by rapidly quenching from the β–phase field (athermal ω). The athermal β → ω transformation cannot be suppressed even by extremely rapid quenching and is completely and continuously reversible with negligible hysteresis [Banerjee S. et al. 2007].

1.3.4. Origin of non-linear recoverable deformation in Gum Metal

Origin of the relatively large range non-linear recoverable deformation in Gum Metal has been a puzzling phenomenon since the development of the alloy. As previously mentioned, the composition of Gum Metal has been carefully designed. In particular Ti/Nb ratio was of great importance. The effect of Nb content in Ti–xNb–0.7Ta–2Zr–1.2O (at %, x=21, 23, 25) alloys on their recoverable tensile deformation was studied in [Furuta T. et al. 2005]. As presented in Fig. 1.17, the stress–strain curve of Ti–21Nb–0.7Ta–2Zr–1.2O indicates superelastic deformation, while Ti–25Nb–0.7Ta–2Zr–1.2O is characterized by a linear elastic stress–strain relationship similar to conventional β titanium alloys. However, the intermediate value x=23 of Nb content results in Gum Metal's (Ti–23Nb–0.7Ta–2Zr–1.2O, at. %) nonlinear recoverable deformation.

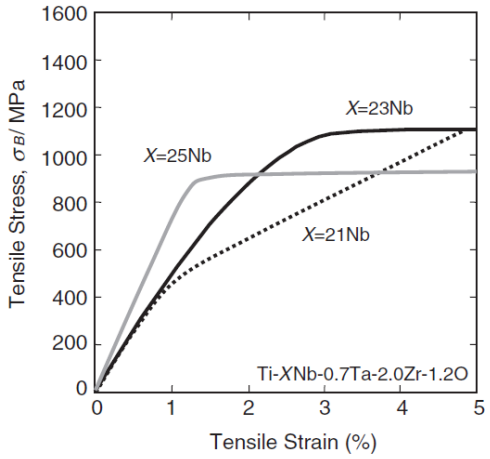

Fig. 1.17 Effect of Nb content in Ti–xNb–0.7Ta–2Zr–1.2O (at. %, x=21, 23, 25) alloys on tensile stress vs. strain curves [Furuta T. et al. 2005].

During tensile loading of the alloys, in-situ XRD measurements were performed. A reflection peak of stress-induced martensite is observed in Ti–21Nb–0.7Ta–2Zr–1.2O before tensile loading, as presented in Fig. 1.18(a). Along with increasing strain reflection becomes weaker while the reflection becomes stronger. In the higher Nb containing alloy, the {011} peak shifts monotonically with increasing tensile strain up to 1.2%, and then the peak shift stops, as seen in Fig. 1.18 (b) and (c).

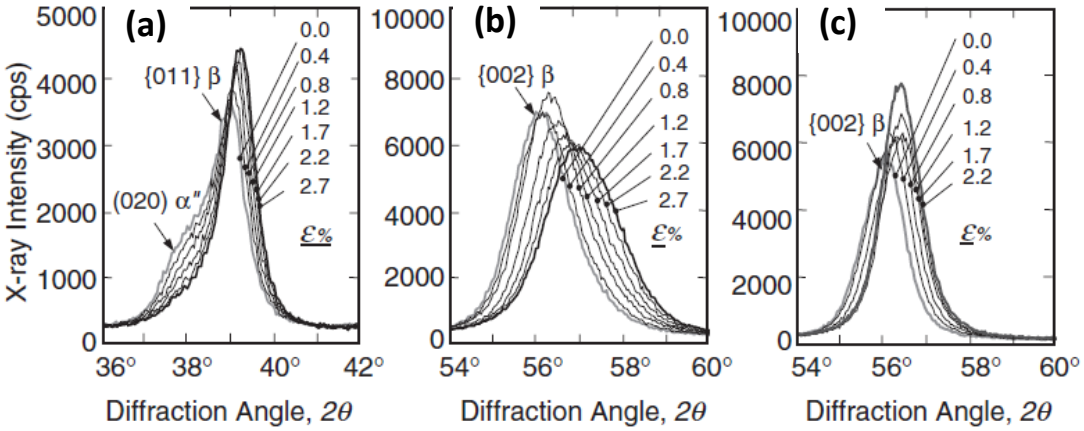

Fig. 1.18 The change in the lattice plane spacing estimated from the peak shift values of (002) β and (112) β as a function of the tensile strain in (a) Ti–21Nb–0.7Ta–2Zr–1.2O; (b) Ti–23Nb–0.7Ta– 2Zr–1.2O alloy and (c) Ti–25Nb–0.7Ta–2Zr–1.2O alloy [Furuta T. et al. 2005].

Changes in the lattice plane spacing estimated from the peak shift values of (002) β and (112) β as a function of the tensile strain in Ti–23Nb–0.7Ta–2Zr–1.2O alloy and Ti–25Nb–0.7Ta–2Zr–1.2O alloy are shown in Figs. 1.19 (a) and (b).

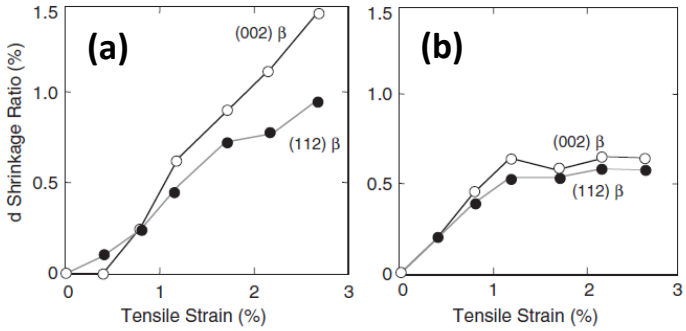

Fig. 1.19 Changes in the lattice plane spacing estimated from the peak shift values of (002) β and (112) β as a function of the tensile strain in (a) Ti–23Nb–0.7Ta–2Zr–1.2O alloy and (b) Ti–25Nb–0.7Ta–2Zr–1.2O alloy [Furuta T. et al. 2005].

The most comprehensive explanation of the underlying mechanism of the nonlinear recoverable deformation in Gum Metal comes from the careful TEM characterization of the alloy realized in S. Miyazaki & H.Y. Kim Laboratory at the University of Tsukuba. The findings underline the crucial combination of oxygen content and cold working effect.

In oxygen-added alloys after cold working, a lattice distortion for the α" martensitic transformation is formed, as shown in Fig. 1.20. The O locates at the center of the octahedron, and hence the lattice of the parent β phase is distorted to generate strain energy. In order to reduce the strain energy around the oxygen atom, the shuffling is effective. This indicates that oxygen assists the martensitic transformation, because the shuffling is necessary to form the martensite structure. However, the perfect lattice distortion to form the martensite is suppressed by the surrounding oxygen-induced strain fields [Miyazaki S. 2017]**.**

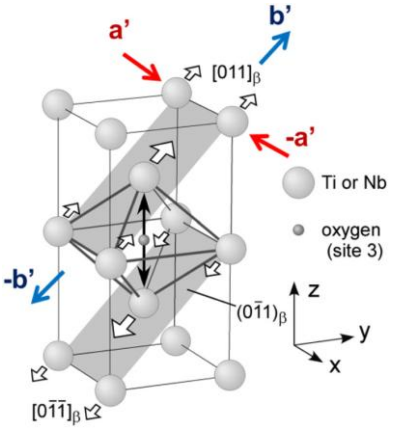

Fig. 1.20. Lattice distortion (nanodomain) for the α" martensitic transformation around the oxygen atom [Miyazaki S. 2017].

This local lattice distortion around O is named nanodomain which is an intermediate phase between the β phase and the α”martensite. Thus, there are six nanodomain variants similarly to the martensite variants as listed in Table 1.3.

Table 1.3 Relationship between the shuffling modes and corresponding variant number in the β-α” martensitic transformation [Miyazaki S. 2017].

Corresponding variant no.	Shuffling modes	Lattice correspondence		
		$[1\,0\,0]_{\alpha''}$	$[0\,1\,0]_{\alpha''}$	$[0\,0\,1]_{\alpha''}$
V1	$(0\,\bar{1}\,1)[0\,1\,1]_{\beta}$	$[1\,0\,0]_{\beta}$	$[0\,1\,1]_{\beta}$	$[0\,\bar{1}\,1]_{\beta}$
V2	$(0\,1\,1)[0\,\bar{1}\,1]_{\beta}$	$[\bar{1}\,0\,0]_{\beta}$	$[0\,\bar{1}\,1]_{\beta}$	$[0\,1\,1]_{\beta}$
V3	$(1\,0\,\bar{1})[1\,0\,1]_{\beta}$	$[0\,1\,0]_{\beta}$	$[1\,0\,1]_{\beta}$	$[1\,0\,\bar{1}]_{\beta}$
V4	$(1\,0\,1)[1\,0\,\bar{1}]_{\beta}$	$[0\,\bar{1}\,0]_{\beta}$	$[1\,0\,\bar{1}]_{\beta}$	$[1\,0\,1]_{\beta}$
V5	$(\bar{1}\,1\,0)[1\,1\,0]_{\beta}$	$[0\,0\,1]_{\beta}$	$[1\,1\,0]_{\beta}$	$[\bar{1}\,1\,0]_{\beta}$
V6	$(1\,1\,0)[\bar{1}\,1\,0]_{\beta}$	$[0\,0\,\bar{1}]_{\beta}$	$[\bar{1}\,1\,0]_{\beta}$	$[1\,1\,0]_{\beta}$

The nonlinear recoverable deformation of Gum Metal was explained based on behavior simpler Ti–Nb–O alloys. Stress vs. strain curves for Ti-Nb, Ti–Nb–0.3O, Ti–Nb–0.5O and Ti–Nb–1O (at. %) are shown in Fig. 1.21(a). In this alloy system, the non-linear elasticity and the low Young’s modulus can be achieved by adding 1% O. Without adding oxygen, this alloy shows typical superelasticity induced by the martensitic transformation upon loading and its reverse transformation upon unloading as shown by the stress–strain curve of Ti–26Nb, as compared in XRD patterns obtained upon loading of Ti-Nb and Ti-Nb-1O alloys presented in Fig. 1.21(b).

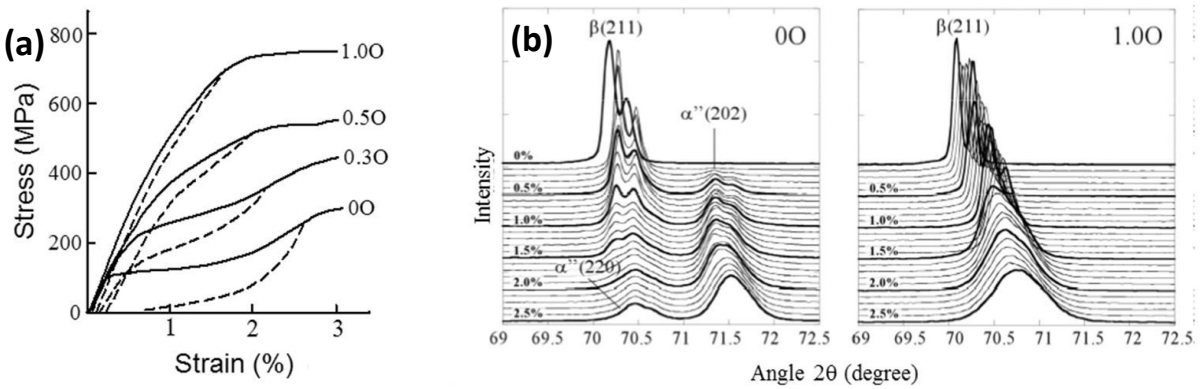

Fig. 1.21 (a) Stress vs. strain curves for Ti-Nb, Ti–Nb–0.3O, Ti–Nb–0.5O and Ti–Nb–1O (at. %); (b) XRD profiles of Ti-Nb and Ti–Nb–1O (at. %) under loading up to 2.5% of strain [Miyazaki S. 2017].

The Ti–26Nb binary alloy reveals typical first-order martensitic transformation, because a XRD peak of the α" martensite appears at a different position apart from the parent β phase position once the transformation occurs upon loading, representing the characteristics of the first-order transformation.

However, in the case of 1% oxygen added specimen, such a first-order martensitic transformation does not occur. The β phase peak shifts continuously to the higher angle position during the nonlinear elastic deformation upon loading. This suggests that the non-linear elastic deformation appears due to the second-order phase transformation. Nanosized modulated region (nanodomain), shown in Fig. 1.22 and pointed by arrows, acted as obstacles for the long-ranged martensitic transformation in the Ti–26Nb–1.0 O alloy.

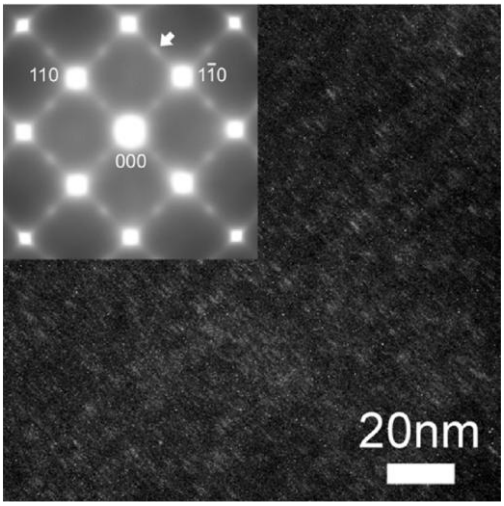

Fig. 1.22 A dark field image of the modulated region (nanodomain) in Ti–26Nb-1O (at. %) alloy [Tahara M. et al. 2013].

The non-linear elastic strain of the Ti–26Nb–1.0 O (at. %) alloy was generated by the continuous increase in lattice distortion strain of the favorable nanodomain variant during tensile deformation.

The nanodomain morphology in Gum Metal was carefully observed via TEM. The results were in good agreement with previous those of Ti–26Nb-1O (at. %) and it was shown that the favorable variants V5 and V6 of the nanodomains were developed in the process of cold working of Gum Metal as presented in Fig. 1.23.

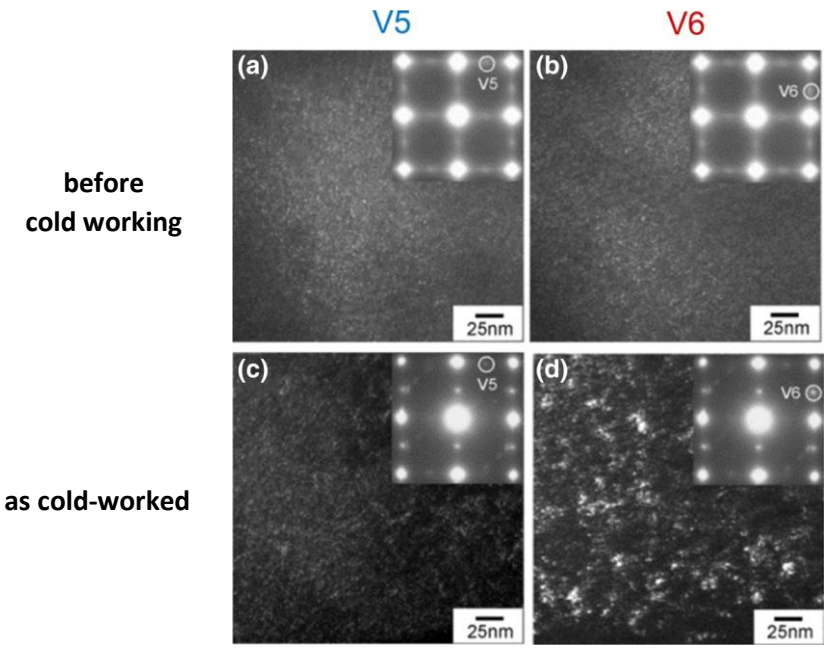

Fig. 1.23 Dark field images of (a, b) annealed and (c, d) as-rolled specimens, revealing two types of nano-domain variants V5 and V6 [Miyazaki S., 2017].

The activity of the nanodomains upon change of temperature was also studied in [Kim H.Y. et al. 2013 and Wei L.S. et al 2015]. It was realized via observation of diffraction pattern and dark-field micrographs for shuffling modes V5 and V6 imaged at room temperature (Fig. 1.24) and at 90 K (Fig. 1.25).

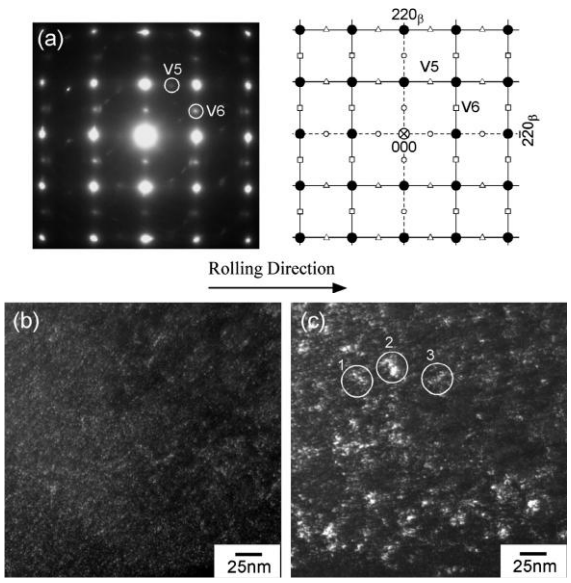

Fig. 1.24 (a) A selected-area diffraction pattern and dark-field micrographs for shuffling modes (b) V5 and (c) V6 in the as-rolled specimen at room temperature [Kim H.Y. et al. 2013].

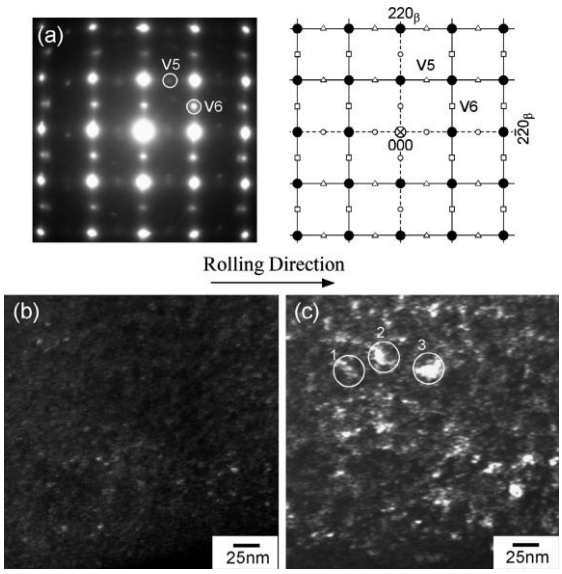

Fig. 1.25 (a) A selected-area diffraction pattern and dark-field micrographs for shuffling modes (b) V5 and (c) V6 in the as-rolled specimen at 90 K [Kim H.Y. et al. 2013].

A significant expanding activity of shuffling mode V6 explains Invar and Elinvar-like thermal behaviors of Gum Metal.

1.3.5. Peculiarities in the plastic behavior of Gum Metal

The ideal shear strength of bcc metal can be expressed by Eq. 1.1. As previously explained, the calculations for design of Gum Metal cause that ($c_{11} - c_{12}$) approaches zero when e/a = 4.24, so the ideal shear strength of the alloy is expected to reach a very small value.

$$\tau = 0.11 G_{111} = 0.11 \times \frac{3c_{44}(c_{11} - c_{12})}{c_{11} - c_{12} + 4c_{44}} \qquad \text{(Eq 1.1)}$$

where

τ is ideal strength for shear, which is needed for plastic shear along <111> on {011}, {112}, or {123} planes;
G_{111} is shear modulus along <111> on {011}, {112}, or {123} planes;
c_{11}, c_{12}, c_{44} are elastic constants for bcc crystal.

A comparison of proof strength vs. shear modulus for Gum Metal and conventional alloys with respect to its ideal strength is shown in Fig. 1.26(a). Ideal strength, tensile strength and ultimate tensile strength (UTS) of selected metals and Gum Metal are contrasted in Fig. 1.26(b).

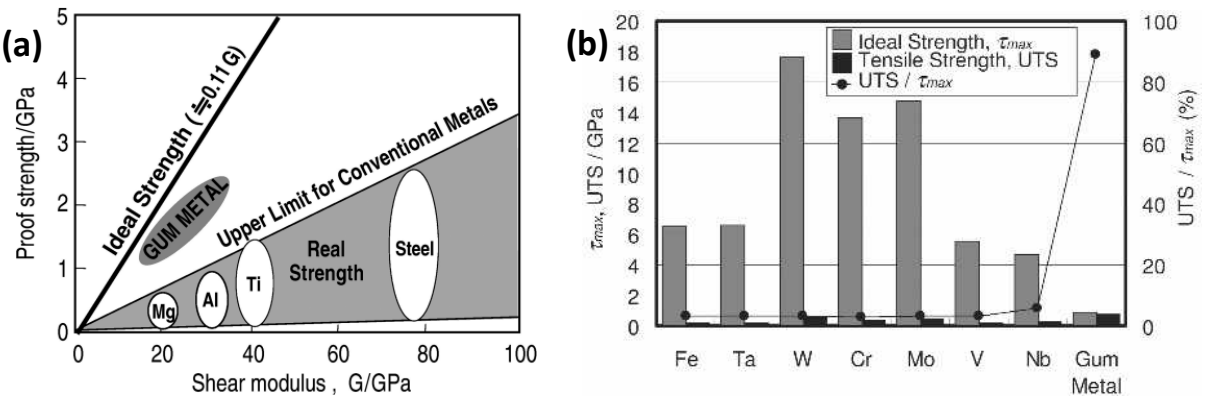

Fig. 1.26 (a) Comparison of proof strength vs. shear modulus for Gum Metal and conventional alloys with respect to its ideal strength [Hwang J. et al. 2005]; (b) Ideal strength, tensile strength and UTS of selected metals and Gum Metal [Kuramoto S. et al. 2006b].

The calculated ideal shear strength of Gum Metal was about 1 GPa, a calculated value that is almost equal to the actual tensile strength of Gum Metal of 0.9-1 GPa, as seen in Fig. 1.26(b). The ideal strength for pure metals is several dozen times the actual one. The strength can be increased to some extent, such as by alloying, cold working, or heat treatment, but conventional metallic materials are known to have lower strengths than their ideal ones. This gap between ideal and actual strength has been successfully explained by the dislocation theory; however, the ideal strength for Gum Metal is estimated to be so small as to be comparable to its actual strength. The low ideal strength of Gum Metal implies that plastic deformation can occur by ideal shear without any dislocation activity. Further work hardening hardly occurs at this alloy composition, which strongly suggests the possibility of a peculiar plastic deformation mechanism without the aid of any dislocation motion.

Gum Metal undergoes a significant plastic deformation with a dominant deformation mechanism that seems to involve microshears and well-developed shear bands rather than conventional dislocation plasticity [Saito T. et al. 2003, Kuramoto S. et al 2006b, Gutkin M.Y. et al. 2008]. The micro shear bands called giant faults were imaged by TEM and high resolution transmission electron microscopy (HRTEM) as shown in Fig. 1.27 (a, b) [Furuta T. et al. 2013].

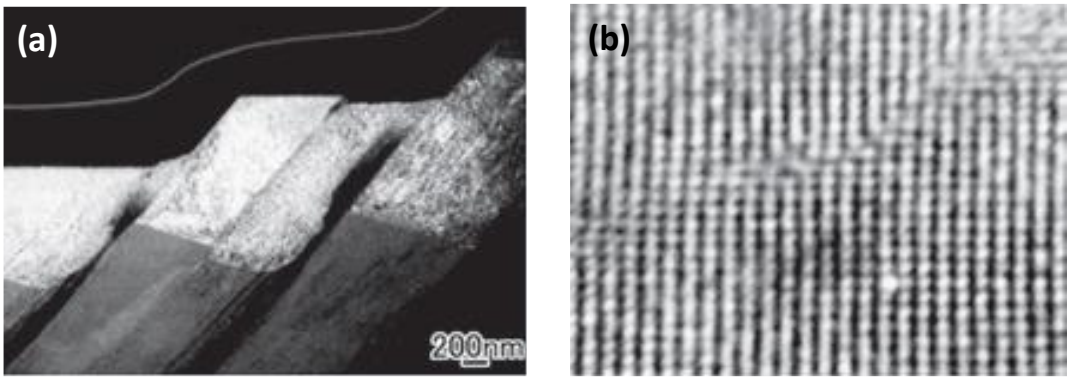

Fig. 1.27 TEM and HRTEM images of microshears and well-developed shear bands so-called giant faults in deformed Gum Metal [Furuta T. et al. 2013].

The unusual plastic deformability of Gum Metal led to an intensive characterization of the alloy on a nanometer scale. There is clear experimental evidence of a dense distribution of nanosized obstacles in Gum Metal that can serve as dislocation pinning sites. The mean separation of these obstacles is on the nanoscale, as required to achieve ideal strength. The nature of these obstacles is not yet clear. Candidates include Zr–O clusters and nanodomains of ω-phase or α-phase as reported in [Yano T. et al 2009]; in particular the presence of the nanometer-sized ω phase may affect the dislocation motion in Gum Metal [Yano T. et al 2009].

The microstructure of Gum Metal under plastic deformation was investigated in [Plancher E. et al. 2013, Lai M.J. et al. 2015, 2018]. A number of widely spaced deformation bands (DBs), which are actually channels that are significantly depleted of ω particles, was found. The channels were said to produce shear steps when intersecting the surface and large shear displacements when intersecting other channels, indicating a considerable amount of plastic flow concentrated within the channels. The plastic deformation within the channels devoid of ω particles is carried by dislocation motion on the {112} β slip planes. A model is proposed that the dissociation and motion of the perfect <111> β dislocations on {112} β slip planes can render the encountered ω phase transforming into the β phase. The passage of these dislocations, thus, leaves behind a channel almost completely consisted of β phase. 60% cold rolling can remove all the ω particles existed in the as homogenized alloys by creating enough dislocation channels that cover the entire material. Dark field image of Gum Metal including the DBs is presented in Fig. 1.28(a). A schematic representation of the formation of a DB within the initial β + ω microstructure is shown in Fig. 1.28(b).

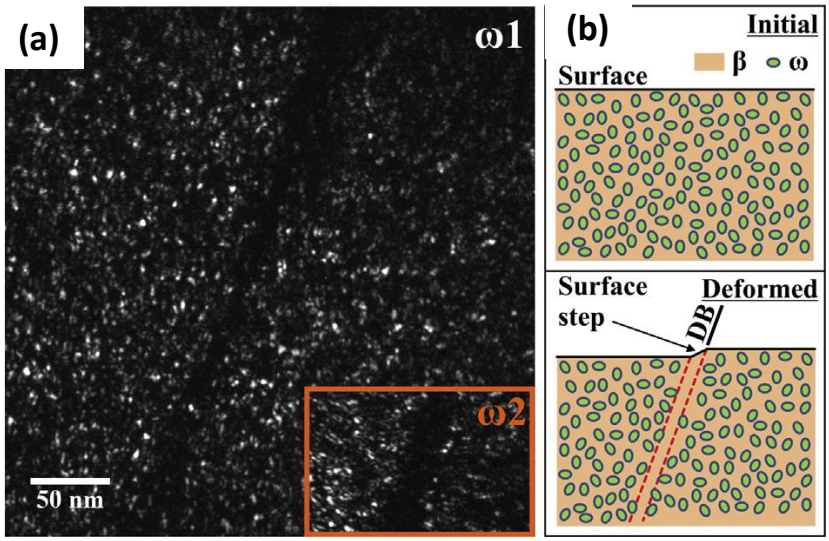

Fig. 1.28 (a) Dark field image of Gum Metal taken from (-1104) ω1 diffraction spot. The inset framed by an orange rectangle is a portion (including the DB-deformation band) taken from (-1100) ω2 diffraction spot. (b) Schematic representation of the formation of a DB within the initial β + ω microstructure [Lai M.J. et al. 2015].

The issue of dislocation pinning is further complicated by the possibility that dislocations in Gum Metal have anomalously diffuse core structures that may affect both their mobility and their interaction with pinning obstacles. In a theoretical work [Chrzan D.C. et al. 2010] found that the elastic anisotropy that develops near a composition-driven phase transition, such as that predicted for Gum Metal, can cause dislocation core radii to extend anisotropically to very large size. Under these circumstances, dislocation cores may actually overlap, producing structures reminiscent of the "nanodisturbances" observed in Gum Metals [Saito T. et al. 2003].

1.3.6. Applications of Gum Metal

Gum Metal definitely falls into a category of new generation of multifunctional materials thanks to a set of outstanding properties. Its super characteristics include low Young's modulus combined with high strength, large range of nonlinear reversible deformation and high plastic deformability without hardening. Gum Metal is also characterized by Elinvar- and Invar-like behaviors which guarantee its reliable use in a wide range of temperature, e.g. in rugged environments such as outer space. These superior properties enable meeting ever-

growing requirements for cutting-edge solutions applied in various technological areas e.g. automotive, precision, robotic, sport equipment industries. Examples of Gum Metal applications are shown in Fig. 1.29. Among them one can find optical frames, automobile springs, precision screws, various sporting goods as golf clubs and fishing line, medical devices like implants or guide wire for catheter and cases for wrist watches.

Fig. 1.29 Possible applications of Gum Metal in numerous fields [based on Saito T. et al. presentation].

Application of Gum Metal for springs results in lower rolling number (1/4), and reduction of weight (1/6) when compared to conventional steel spring.

The spring constant *K* can be calculated using the following formula (Eq. 1.2).

$$K = \frac{Gd^4}{8D^3N} \qquad \text{(Eq. 1.2)}$$

where

G is the shear modulus;

d is the wire diameter;

D is the coil diameter;

N is the rolling number.

Comparison of shear modulus and density of Gum Metal, piano wire and β-C Titanium alloy for spring applications is given in table 1.4.

Table 1.4 Comparison of Gum Metal, piano wire and β-C Titanium alloy for spring applications.

Material	G [GPa]	Density [g/cm^3]
Piano wire	78.4	7.9
β-C Titanium	39.2	5.0
Gum Metal	19.3	5.6

The use of Gum Metal as a key component has driven development of a big number of innovations which are reflected by various patents. Among them one can find fluid conduit for gas turbine engine (US 009970357B2), piston (US 20150252750A1), pressure and mechanical sensors (US 007437939B1), novel golf clubs (US OO8961332B2), etc.

Furthermore, the absence of toxic elements in the composition, high biocompatibility and value of Young's modulus similar to bone make it a promising candidate for biomedical applications, e.g.: bone fracture reconstruction device (US 201601 13697A1), device for performing surgical procedure (US 20140277209A1, US 20150223823A1), endodontic instrument (US 2006O18517OA1) or spinal implant system (US 2015O157362A1).

Gum Metal orthodontic wire is already a successful product being distributed by J. Morita Corporation in Japan and since 2018 in Europe and the US. Photographs of commercial products of J. Morita Corporation are shown in Fig. 1.30.

Fig. 1.30 Commercially available Gum Metal orthodontic wire (J. Morita Corporation).

Thanks to its characteristics, Gum Metal orthodontic wire has a high potential to cut down the treatment time and to relieve the pain of patients. The comparison of stress vs strain curves for conventional alloys used as orthodontic wires and Gum Metal are presented in Fig. 1.31.

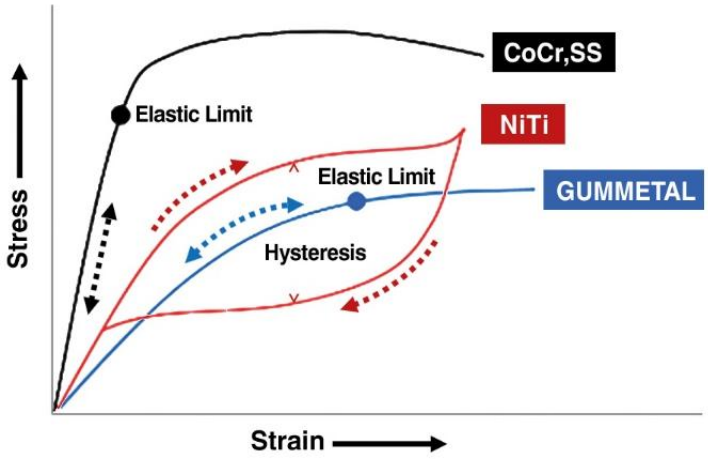

Fig. 1.31 Comparison of stress vs strain curves for conventional alloys used as orthodontic wires and Gum Metal [https://www.jmoritaeurope.de/en/products/auxiliaries/orthodontic-arch-wires/gummetal/?tab=features]

Key characteristics of biocompatible metallic alloys for dental use are listed in table 1.5.

Table 1.5 Comparison of biocompatible alloys and Gum Metal [https://www.jmoritaeurope.de/en/products/auxiliaries/orthodontic-arch-wires/gummetal/?tab=features].

Key characteristics of several conventional biocompatible metal alloys and GUMMETAL

Metal for dental use	Conventional metal	Main elements	Young's modulus GPa	Tensile strength MPa
Noble metal	12%Au-Ag-Pd alloy	Au-Ag-Pd	>250	900
Stainless steel	SUS316	Fe-Cr-Ni-Mo	200	860
Co-Cr alloy	ASTM F562	Co-Cr-Ni-Mo	170	1000
Titanium	Pure Titanium	Ti	102	270
Ni-Ti alloy	Nitinol	Ti-Ni	105	700
α+β Titanium alloy	ASTM F136	Ti-Ai-V	85	860
Ti-Nb alloy	**GUMMETAL**	**Ti-Nb-Ta-Zr**	**45**	**1100**
			(Cr,Ni,V are cytotoxic)	

According to the table 1.5 Gum Metal has the lowest Young's modulus and highest value of tensile strength with nontoxic chemical composition.

1.4. Goal, theses and scope of the dissertation

The superior recoverable strain of Gum Metal wire is compared to conventional stainless steel wire after bending in Fig. 1.32.

Fig. 1.32 The superior recoverable strain of Gum Metal wire compared to the one of conventional stainless steel wire after bending [https://www.jmoritaeurope.de/en/products/auxiliaries/orthodontic-arch-wires/gummetal/?tab=features].

The goal of the dissertation is to investigate unconventional deformation mechanisms of Gum Metal by analyzing the thermomechanical couplings in the alloy under selected loadings. The goal of the dissertation has been chosen in the light of the outstanding mechanical characteristics of Gum Metal in particular its relatively large, nonlinear, mechanically recoverable deformation caused by a stress-induced activity of unconventional deformation mechanisms described in subsection 1.3.4 and selected experimental results of thermomechanical couplings for various metals reviewed in the subsection 2.1.2. The results of this dissertation aim at better understanding of the nature of Gum Metal deformation, which is macroscopically reflected not only in mechanical characteristics but also in thermal responses of the alloy under loading.

Theses of the dissertation

1. The nonlinear, mechanically recoverable deformation of Gum Metal caused by a stress-induced activity of unconventional deformation mechanisms is macroscopically reflected in thermomechanical responses of the alloy.
2. Gum Metal is sensitive to the strain rate applied during its loading and deformation. It is manifested in mechanical and thermal responses of the alloy.

The scope of the dissertation covers the following research tasks:

1. Material characterization
   - 1.1. Examination of microstructure by optical microscopy
   - 1.2. Analysis of grain misorientation and texture
   - 1.3. Phase content characterization
   - 1.4. Study of chemical composition
   - 1.5. Determination of specific heat
2. Investigation of unique superelatic-like behavior of Gum Metal. Analysis of the relatively large recoverable strain in the context of thermomechanical couplings.
   - 2.1. Determination of the mechanically recoverable strain in the process of cyclic tension with an increasing strain.
   - 2.2. Determination of elastic deformation of Gum Metal under tension based on stress and temperature change vs. strain characteristics.
   - 2.3. Analysis of stress and temperature change vs. strain characteristics of Gum Metal under in subsequent loading-unloading tensile cycles.
   - 2.4. Investigation of strain rate effect on mechanical and thermal responses of Gum Metal under monotonic tension.
   - 2.5. Fractographic analysis of Gum Metal specimens after monotonic tensile rupture at selected strain rates and cyclic loading.
3. Determination of elastic constant matrix of Gum Metal rod using ultrasound measurement.
4. Investigation of mechanical anisotropy of Gum Metal using digital image correlation.
5. Analysis of stress and temperature change vs. strain characteristics of Gum Metal under cyclic compression in subsequent loading cycles.

1.5. Materials and specimens under investigation

This dissertation deals with investigation of three types of Gum Metal. Tension tests were conducted on two sets of flat specimens fabricated and machined at the Toyota Central Research and Development Laboratories and delivered to the IPPT PAN. Compression tests were performed using samples machined from a Gum Metal rod, which was delivered by Fukuoka University. Detailed descriptions of the material and specimens are presented in Chapers 3, 4 and 5.

A technical drawing of the flat Gum Metal flat specimen from set 1 is depicted in Fig. 1.33(a) while a photograph is shown in Fig. 1.33(b).

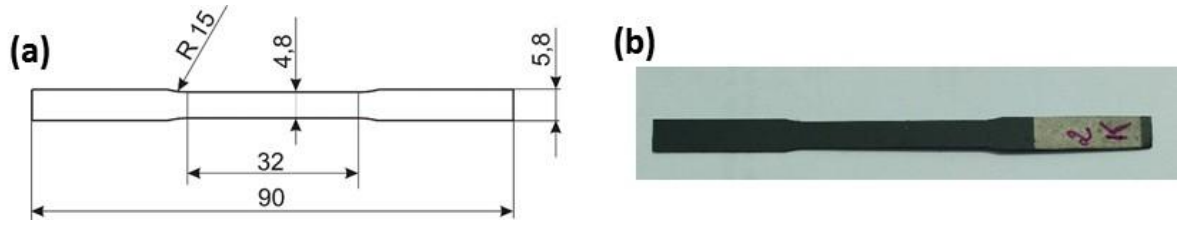

Fig. 1.33. Gum Metal flat specimen from set 1 (a) technical drawing; (b) photograph.

A technical drawing of the flat Gum Metal flat specimen from set 2 is depicted in Fig. 1.34(a) while a photograph is shown in Fig. 1.34(b).

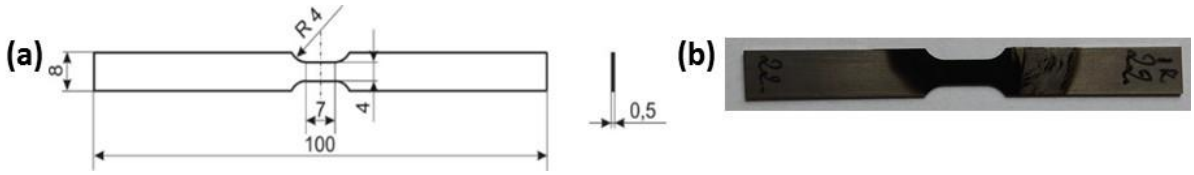

Fig. 1.34. Gum Metal flat specimen from set 2: (a) technical drawing; (b) a photograph.

Photographs of the Gum Metal rod and a sample machined for compression test are shown in Figs. 1.35(a) and (b), respectively.

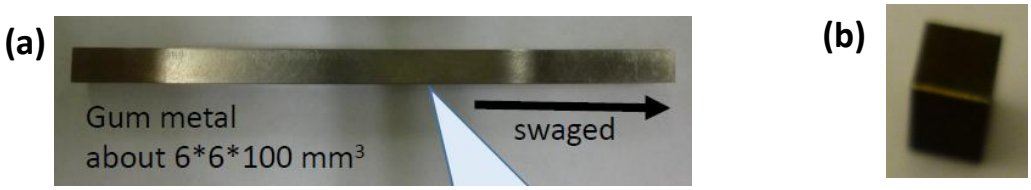

Fig. 1.35. Photographs of (a) a Gum Metal rod [courtesy of Takesue N.] and (b) a Gum Metal sample machined for compression test.

Chapter 2

2. Methodology applied for investigation of thermomechanical couplings in Gum Metal under loading

2.1. Fundamentals of thermomechanical couplings in metals

Deformation of a solid material can result in a change of its thermomechanical state, which subsequently causes temperature variation. It is a macroscopic manifestation of phenomena which occur in the microstructure of the material. Mutual interaction between mechanical and thermal effects is termed thermomechanical coupling. A scheme with general information about thermomechanical couplings and their origins as well as a commonly analyzed example of stress and temperature change vs. strain curves illustrating three regimes of deformation of a materials under tension in correlation to its temperature change is shown in Fig. 2.1. Origins of temperature increase of any materials under deformation can be associated with the dissipative nature of deformation mechanisms e.g. plasticity, phase change and damage. Irreversible thermodynamics for characterization and understanding of the mechanical behavior of metals under stress were described in [Beghi M.G. et al. 1986]. The temperature growth of a given material under deformation can be also related to the heat-coupling sources, indicating significant thermo-sensitivity of the material and strong interactions between thermal and mechanical states (thermodilatability, phase change of SMAs, etc.).

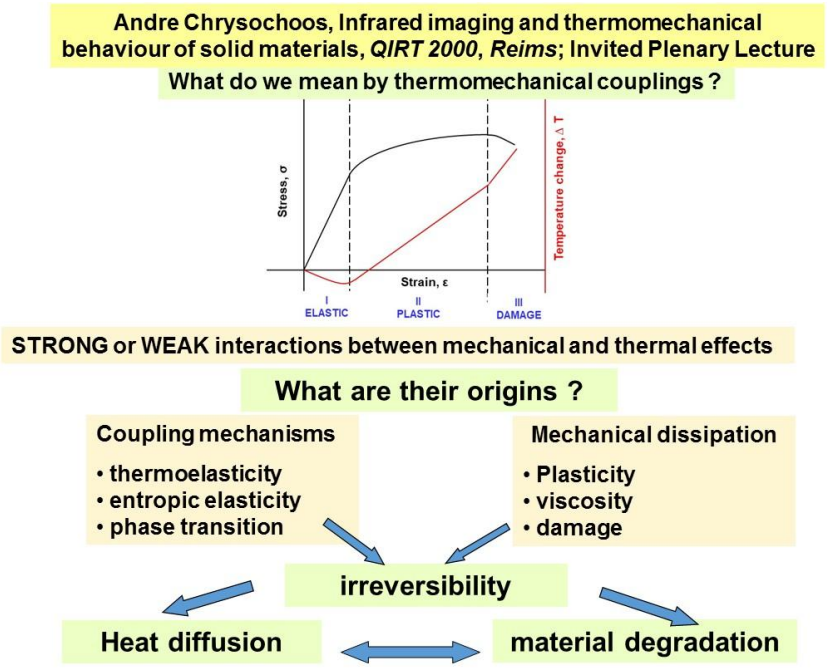

Fig. 2.1 A scheme with general information about thermomechanical coupling and its origins in a solid material under tension [based on Chrysochoos A. 2000, courtesy of Pieczyska E.].

2.1.1. Historical overview of the research of thermomechanical couplings in metals

Experimental and theoretical investigations of thermomechanical couplings in metals have been of interest for the last two centuries. In this section selected highlights and findings published in recent works are presented.

The first experimental investigation of thermoelasticity is attributed to W. Thomson [Thomson W. 1853]. According to the formula proposed by W. Thomson, during the adiabatic uniaxial elastic deformation under assumption of linear and isotropic elastic behavior of material, the temperature change, can be described by Eq. 2.1.

$$\Delta T = -\frac{\alpha T \Delta \sigma_{ik}}{c_p \rho} \qquad \text{(Eq. 2.1)}$$

where

α is the coefficient of linear thermal expansion,

T is the absolute temperature of the specimen,

$\Delta\sigma_{ik}$ is the stress tensor,

c_p is the specific heat at constant stress,

ρ is the density of the material.

The formula Eq. 2.1 can be explained within the framework of linear thermodynamics, because the change in the temperature of the specimen during elastic deformation is caused by mutual conversion of the energy of lattice atoms.

According to the formula Eq. 2.1, for materials with a positive thermal expansion coefficient, the temperature insignificantly decreases during tension, increases during compression and remains constant during shear or torsion in the elastic regime of deformation.

The formulation of the problem regarding estimation of the heat involved in irreversible mechanical transformations started a serious advancement in the field of thermoplasticity. Results of microcalorimetric tests were the pioneering work published [Farren W. et al. 1925, Taylor G. et al. 1934]. Analysis of the energy balance during strain hardening enabled to describe changes in microstructural features e.g. dislocation density, dislocation cell size, etc. as published in [Bever M.B. et al. 1973].

In the end of the 1970s infrared (IR) techniques started revolutionizing experimental investigations in the area of mechanics of materials and the related temperature changes. The early work focused on observations of localized plastic zones in low carbon steel subjected to torsion [Saix C. et al. 1980]. Further progress on design and application of the analogue–digital converter of video signals from infrared cameras was presented in [Nayroles B. et al. 1981]. Since then, the continuous advancement in the fields of electronics and computers led to the design of video signal digitization systems. Several publications were devoted to analysis of energy balance using microcalorimetry and/or infrared imaging. The process of energy storage in metals, particularly stainless, steel under tension was investigated in [Gadaj S.P. et al. 1981, 1983a, 1983b]. Tensile test conducted in microcalorimeter for investigation of thermomechanical behavior was presented in [Chrysochoos A. et al. 1989a]. Determination of plastic and dissipated work and stored energy was discussed in [Chrysochoos A. et al. 1989b]. The process of energy storage with its structural aspect in Armco iron and austenitic stainless steel under uniaxial tension was presented in [Oliferuk W. et al. 1985 and Oliferuk W. 1997]. Selected experimental cases of analysis of thermomechanical coupling by infrared thermography were presented in [Chrysochoos A. et al. 1991, 1992, 2000., Chrysochoos A. 2012]. Energy stored during plastic deformation of polycrystals determined based on experimentally measured stress–strain curve was discussed in [Oliferuk et al. 2009]. Determination of the energy storage rate distribution in the area of strain localization using infrared and visible imaging was analyzed in [Oliferuk W. and Maj M. 2015].

Additionally, over the last 20 years, optical techniques based on image processing were of an increasing interest in experimental mechanics. The use of a visible range digital camera allows recording a sequence of speckled images of a specimen under deformation. Further application of a digital image correlation (DIC) algorithm enables analysis of deformation fields for characterization and identification of material behavior during deformation.

In recent years, advanced visible and IR systems are simultaneously used for full-field measurements of deformation and thermal effects in materials under loading. Analysis of results obtained via DIC and infrared thermography (IRT) gives data useful to observe, understand and model the thermomechanical behavior of solids. Examples of recently obtained experimental results of thermomechanical characteristics of metals under loading

will be discussed in the next subsection. A detailed history of advancements in the research of thermomechanical couplings in various materials can be found in [Chrysochoos A. et al. 2010].

2.1.2. Selected experimental results of investigation of thermomechanical couplings in metals under loading

Thermomechanical couplings play an important role during loading and deformation of certain material. A solid material under loading can demonstrate endothermic, exothermic, or neutral behavior depending on the mode of the deformation process, its stage, and the material's microstructure. The temperature changes accompanying the initial deformation of the material enable investigators to determine its yield point [Pieczyska E.A. et al. 1998a, 1998b, 1999, 2002, Kumar J. et al. 2008, Oliferuk W. et al. 2012]. The thorough determination of the effects of thermomechanical couplings can contribute to the knowledge about the behavior of advanced materials, in particular stress-induced phase transformation [Pieczyska E.A. 2006, Pieczyska E. A. et al. 2010, 2013, Rodriguez-Martinez J.A. et al. 2011, Tobushi H. et al. 2013]. Moreover, full-field analyses of strain distribution provide interesting results about performance of SMAs under loading [Daly S. et al. 2007, Delpueyo D. et al. 2012]. IRT is a good tool to study the nucleation and development of the strain localization leading to damage [Venkataraman B. et al. 2001, Louche H. et al. 2001, Ranc N. et al. 2005, Badulescu C. et al. 2011]. Analyses of energy balance and estimation of stored energy are given in [Chrysochoos A. et al. 1989b, 1989b, 1991, 1992, 2000., Oliferuk W. et al. 1985, 2009, 2015, Oliferuk W. 1997, Chrysochoos A. 2012]. Selected case studies of thermomechanical coupling in different metals will be presented in the following paragraphs.

Analysis of thermomechanical couplings can serve to precisely determine yield point of materials under uniaxial loading [Pieczyska E.A. 1996, Pieczyska E.A. et al. 1997a, 1997b, 1998a, 1998b, 1999, 2002]. Thermoelastic effect in austenitic steel referred to its hardening using IRT was studied in [Pieczyska E.A. 1999]. Stress vs. strain curves in five consecutive loading and unloading cycles of stainless steel and the related temperature changes vs. stress curves are presented in Fig. 2.2(a) and 2.2(b), respectively. The discrepancy from the linear dependence of temperature change vs. stress related to maximal drop of temperature change in each cycle indicates the yield point of the steel specimen under cyclic tension. In addition, positive values of effects of thermomechanical unloading were demonstrated, as shown in Fig. 2.2(b) [Pieczyska E.A. 1999].

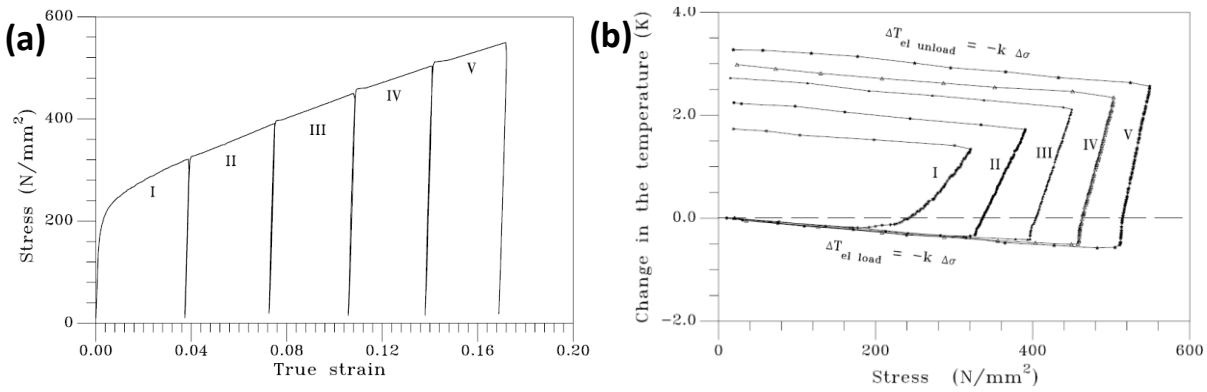

Fig. 2.2 (a) Stress vs. strain curves in consecutive loading and unloading cycles (I - V) and (b) Temperature changes vs. stress curves of stainless steel under cyclic tension [Pieczyska E.A. 1999].

The elastic-plastic transition under uniaxial tensile loading in austenitic steel, titanium and aluminum alloys was studied in [Oliferuk W. et al. 2012]. Maximal drop of temperature was related to the stress and strain values and yield point was determined. Thermographic studies on IMI-834 titanium alloy during tensile with respect to the specimen geometry was investigated in [Kumar J. et al. 2008]. The study of notched specimens of IMI-834 titanium alloy using IRT under tension indicated that the localized temperature rise was higher in case of the notched specimens compared to the smooth ones. It has been also shown that the stress in the thermoelastic region can be predicted from the temperature data using the W. Thomson's equation.

Furthermore, IRT was used to analyze the dissipative nature of deformation mechanisms (plasticity and damage) of metallic materials under loading. Lüders band propagation in S355MC steel specimens in tensile test was studied by IRT in [Louche H. et al. 2001]. It was observed that the low amplitude thermal wave propagation was attributed to the Lüders band propagation.

The deformation of an aluminum–copper alloy related to Portevin–Le Chatelier (PLC) bands was investigated using infrared technique in [Ranc N. et al. 2005]. The method was said to be a good tool for quantification of deformation increment related to temperature changes.

Thermal response of nuclear grade AISI type 316 stainless steel under tension was investigated in [Venkataraman B. et al. 2001]. A continuous temperature increase during plastic deformation was noticed. Furthermore, the onset of necking was identified by a clear temperature growth at the necking region. The study of plastic deformation in aluminum

multi-crystal specimens under tensile loading using IRT and grid method was published in [Badulescu C. et al. 2011]. It was observed that heat sources estimated from the acquired temperature data matches well with the strain distribution.

Several studies show that heat production due to phase transitions in selected materials can also induce measurable changes in temperature. IRT was used for studying martensitic transformation in AISI 304 stainless steel specimens under tensile loading at room temperature in [Rodriguez-Martinez J.A. et al. 2011]. It was observed that under low strain rate, martensitic transformation occurred for temperature difference greater than 140 ^{o}C. Fast and sensitive infrared camera was also applied for investigation of stress-induced phase transformation in TiNi shape memory alloys under selected loadings [Pieczyska E.A. et al. 2004, 2005, 2006a, 2006b, 2006c, 2010, 2013, Tobushi H. et al. 2013]. The stress-induced forward martensitic transformation was confirmed to be exothermal whereas, the reverse transformation endothermal as shown in stress and temperature variation vs. strain for TiNi SMA presented in Fig. 2.3(a). Subsequent stages of the transformation MT1, MT2 and MT3 were selected based on the determined temperature change. Two directions of stress-induced phase transformation bands were identified in a thermogram shown in Fig. 2.3(b). A significant thermo-sensitivity of the material and strong interactions between thermal and mechanical states (solid–solid phase transformation) of TiNi SMA was detected.

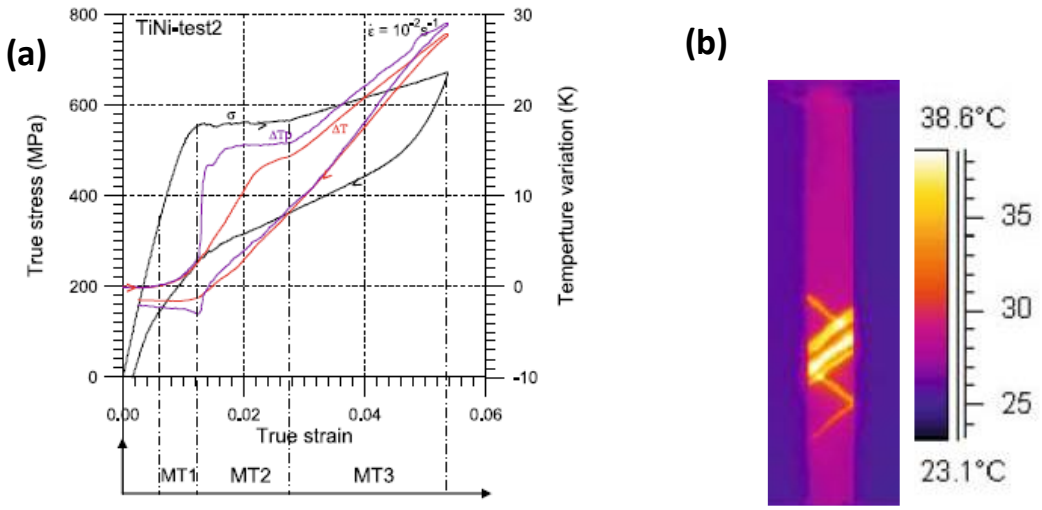

Fig. 2.3 (a) True stress σ, average temperature variation ΔT and temperature variation at point where martensitic transformation initiates ΔTp vs. true strain ε for shape memory alloy; (b) selected thermogram indicating martensitic transition in TiNi SMA under loading induced in bands [Pieczyska E.A. et al. 2006].

In [Daly S. et al. 2007] DIC was used to study the quantitative full-field strain maps of thin sheets of TiNi subjected to quasistatic uniaxial tension. The results of stress vs. strain and strain distributions determined by DIC at selected stages of TiNi loading with clear stress induced bands corresponding to phase transition are presented in Fig. 2.4.

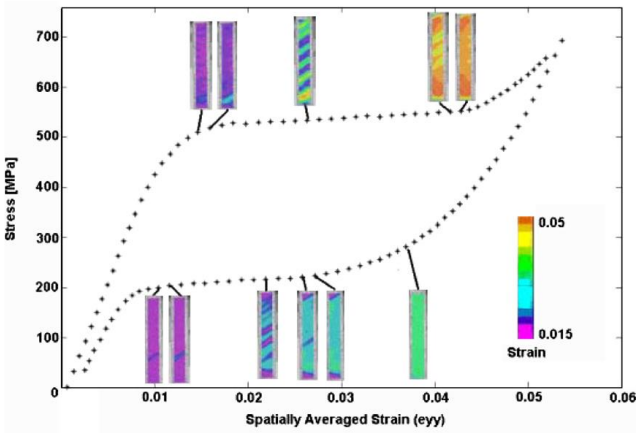

Fig. 2.4 Stress vs. strain with strain distributions determined by DIC at selected stages of TiNi tension loading [Daly S. et al. 2007].

The study of the martensitic microstructure evolution in a Cu–Al–Be shape-memory alloy during a stress-induced transformation with the grid method and infrared thermography was performed in [Delpueyo D. et al. 2012]. Exemplary strain maps and a temperature variation map indicating phase transformation bands are shown in Fig. 2.5.

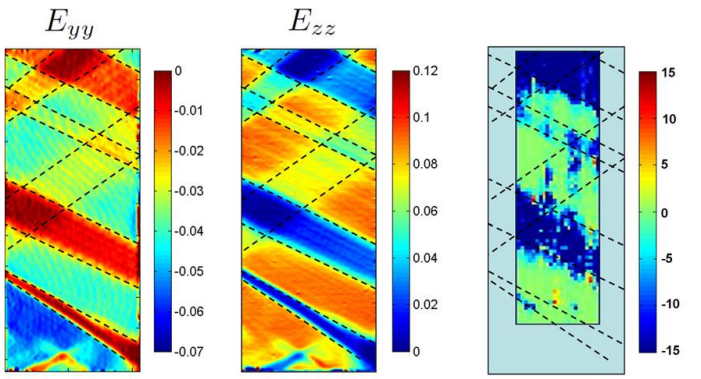

Fig. 2.5 Strain (a) and temperature (b) maps of monocrystalline Cu–Al–Be shape memory alloy under loading [Delpueyo D. et al. 2012].

2.2. Experimental methodology for determination of temperature change of Gum Metal under loading based on detection of infrared radiation

Experimental methodology for determination of temperature changes of Gum Metal under loading based on detection of infrared radiation was established thanks to long-term interest in research of various materials at IPPT [Gadaj S. et al. 1996, 1999, 2005, Oliferuk W. 1999]. In particular new, multifunctional materials e.g. TiNi SMA was successfully investigated using this experimental methodology [Pieczyska E.A. et al. 2004, 2006a, 2006b, 2006c, Pieczyska E.A. 2008].

The temperature field during the loading of Gum Metal specimen, was obtained based on infrared radiation emitted from the surface which was registered by a ThermaCam Phoenix IR camera operating in the infrared range 3–5μm and the maximum recording frequency 538 Hz.

The absolute temperature determination with high accuracy is possible only for the surface of known emissivity after the calibration procedure. Gum Metal specimens were covered with soot to increase and make uniform the surface emissivity, which was assumed to be 0.95. From the obtained temperature distribution, the mean temperature was determined with high thermal sensitivity, up to 0.02 °C from the gauge area of the specimen to neglect boundary effects as shown in Fig. 2.6.

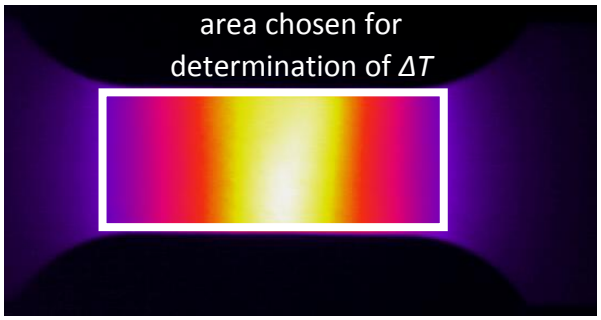

Fig. 2.6. Area of temperature field determination.

The temperature change ΔT denotes the difference between the mean value of the temperature calculated for the gauge part of the tested specimen at each instant of straining $T(t)$ and the mean temperature of the same area before the deformation $T(t_0)$:

$$\Delta T = T(t) - T(t_0). \qquad \text{(Eq. 2.2)}$$

The value of the mean temperature was calculated for the gauge part of the specimen defined in the reference configuration.

2.3. Experimental methodology for determination of mechanical characteristics of Gum Metal

Selected loadings of Gum Metal specimens, which are presented in further chapters of this work, were obtained using an MTS 858 testing machine. Crosshead displacement controlled tension and compression tests were realized. Crosshead displacement rates were selected in order to obtain desired strain rates values when taking into account the specimen geometry used in a certain test. During the test, the loading force as a function of time was recorded. Change in length of a tested specimen were measured either in a contact manner using a clip-on extensometer or in a noncontact manner using a virtual extensometer, which was a function of DIC software.

The mechanical characteristics of Gum Metal analyzed in this work are mainly showed in true stress vs. true strain curves. The true stress vs. true strain curves were calculated in reference to the current cross section of the sample assuming its constant volume, according to Eq. 2.3 and Eq. 2.4.

$$\sigma_{true} = \frac{(\Delta l + l_0) \cdot F}{l_0 \cdot S_0}, \qquad \text{(Eq. 2.3)}$$

$$\varepsilon_{true} = \ln\left(\frac{\Delta l + l_0}{l_0}\right). \qquad \text{(Eq. 2.4)}$$

where:

Δl is the change in specimen length determined on the basis of extensometer,

l_0 is the initial gauge length (GL),

F is the instantaneous force,

S_0 is the initial cross-section.

True stress denotes the stress determined by the instantaneous load acting on the current cross-sectional area, assuming material volume remains constant.

2.4. Experimental methodology for coupling mechanical and thermal characteristics of Gum Metal under loading

In this work, the plots of true stress and mean temperature change vs. true stress are most commonly analyzed. During a selected process of Gum Metal loading, two cameras IR camera and visible range camera were simultaneously monitoring the deformation of the alloy. There were several configurations of experimental setups. A specific setup modification, used in a certain experiment, is described in each chapter. An exemplary configuration is presented in Fig. 2.7, where the cameras capture the sequences of IR and visible range images from the opposite sides of the specimen under tension in order to determine temperature and deformation fields.

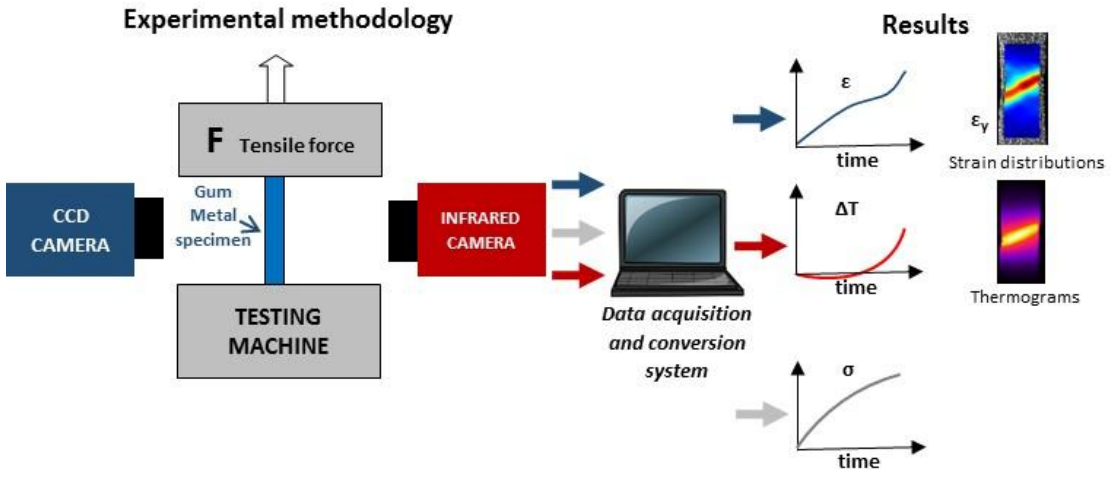

Fig. 2.7. Scheme of the experimental setup for coupling mechanical and thermal characteristics of Gum Metal under loading [Pieczyska E.A. et al. 2018a].

Since the desired parameters are presented as a function of time, it is possible to couple them and plot true stress and mean temperature change vs. true stress. The obtained temperature changes during deformation of Gum Metal specimens under straining served to analyze effects of thermomechanical couplings.

2.5. Description of Thermocorr sofware

ThermoCorr software was developed in IPPT PAN to use a numerical method for determining coupled thermomechanical fields based on experimental data obtained from two cameras working in the visible and infrared modes. A scheme of the experimental setup is shown in

Fig.2.8(a). It uses a digital image correlation (DIC) algorithm, which can capture the displacement fields from a sequence of visible range images. Subsequently, selected deformation fields such as strain as well as rate of tensor deformation fields can be calculated. The software has also a function of a virtual extensometer. The general idea behind DIC is to find a position of a material point in the deformed image, based on its initial position defined on the reference image using its local neighborhood and the correlation criterion $p=\varphi(P)$ as schematically illustrated in Fig. 2.8(b).

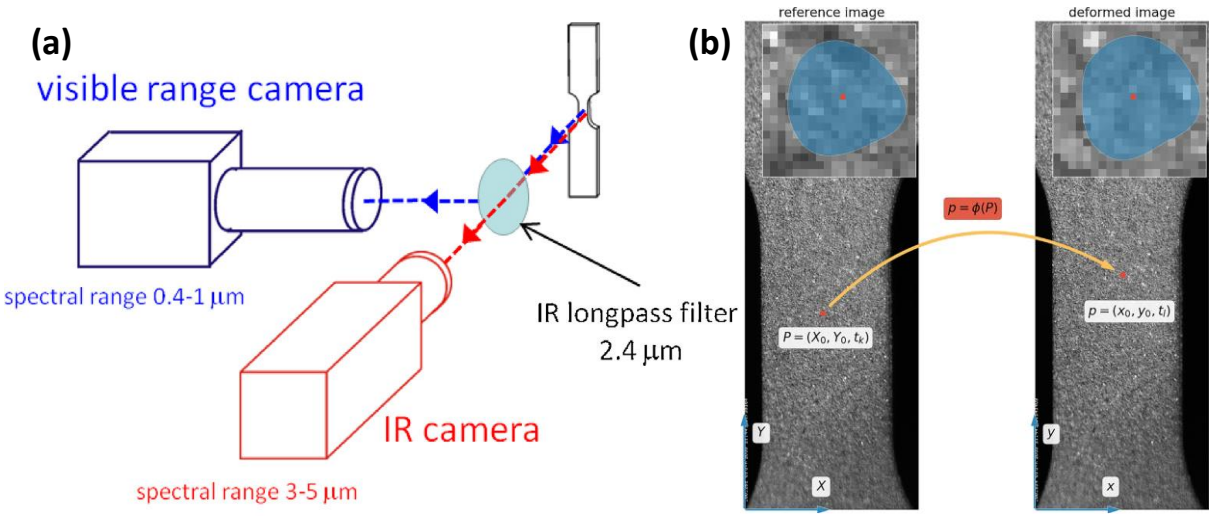

Fig. 2.8. (a) A scheme of the experimental setup; (b) the general idea of DIC used for tracking material points during deformation [Nowak M. et al. 2017].

Thermocorr enables to apply the coupling procedure of the experimental results when the DIC and IRT are simultaneously used. The mean temperature of all material points in the defined region can be calculated at each instant of straining. As a matter of fact, the experimentally obtained sequences of images from visible and IR cameras can differ and the time of acquisition start can be discordant in both cameras. Thermocorr software uses a space and time coupling procedure, which takes into account different coordinate systems, resolutions, frequency of acquisition as well as recording time of two cameras. Details of the numerical procedures are given in [Nowak M. et al. 2017].

Chapter 3

3. Preliminary investigation of thermomechanical couplings in Gum Metal under tension

The results presented in Chapter 3 were discussed during several conferences [Golasiński K. et al. 2016a, 2016b, 2017b, 2017c and Pieczyska E.A. et al. 2016b, 2016c, 2017a, 2017b, 2018b] and partially published in [Pieczyska E.A. et al. 2016a, 2018, Golasiński K. et al. 2017a].

3.1. Material and specimens

Gum Metal specimens used in this investigation were provided by the Toyota Central Research and Development Laboratories. The nominal composition of Gum Metal was Ti–23Nb–0.7Ta–2Zr–1.2O (at.%) and the fabrication included the several steps. A billet of Gum Metal was prepared by a powder technology. It was sintered at 1300 ^{o}C for 16 h in a vacuum of 10^{-4} Pa, hot forged to a 12.5 mm round bar, solution treated at 900 ^{o}C for 30 min, and subsequently quenched into water with ice. The heat-treated bar was removed with a surface oxidized layer and cold worked by a rotary swaging machine. The specimens were swaged to a diameter of 4 mm without annealing and then cold rolled to a thickness of 0.6 mm.

Several specimens were prepared from these sheets. A technical drawing of the specimen is depicted in Fig. 3.1(a) while a photograph is shown in Fig. 3.1(b).

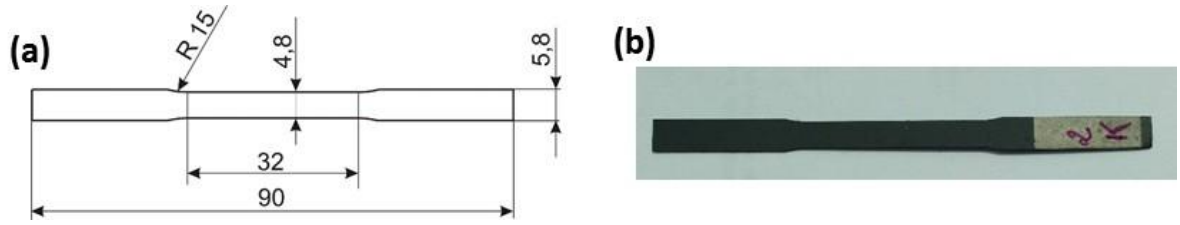

Fig. 3.1. Specimen of Gum Metal (a) technical drawing; (b) photograph.

Microstructural characterization of Gum Metal was conducted using optical microscopy. Polished specimens were prepared by a conventional mechanical technique and were etched with an aqueous 10% HF + 10% HNO_3 solution. Optical micrographs of Gum Metal are shown in Fig. 3.2 (a, b).

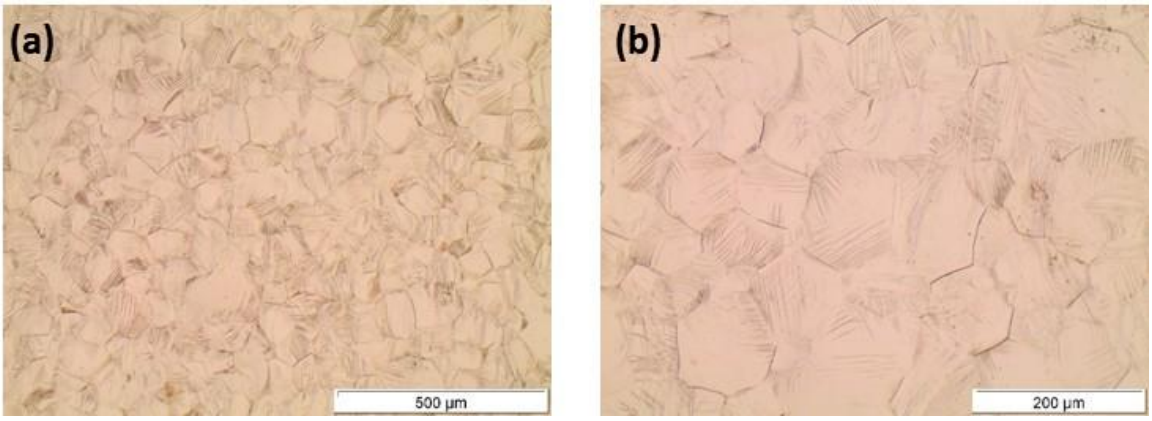

Fig. 3.2. Optical microstructure of Gum Metal with scale bars (a) 500 µm and (b) 200 µm.

The optical micrographs revealed nonhomogeneity of the Gum Metal microstructure, which comprises of α-Ti (needles) and β-Ti (hexagonal) phases. Most probably α-Ti phase was mechanically induced during the polishing procedure of Gum Metal but no clear evidence can be given.

3.2. Experimental details

The experimental set-up designed for the Gum Metal tension tests consisting of the MTS Testing Machine and Flir Co Phoenix Infrared System is depicted in a photograph shown in Fig. 3.3(a) and in a scheme presented in Fig. 3.3(b). Strain changes of Gum Metal specimen under loading were recorded by a contact extensometer. The fast and sensitive infrared camera captured the infrared radiation from the specimen surface (covered with soot) during the deformation process. An emissivity coefficient of the soot equal to 0.95 was assumed. The IRT allowed to calculate the specimen temperature changes in a contactless manner with a high thermal sensitivity up to 0.02 ^{o}C. Gum Metal specimens were subjected to displacement-controlled monotonic tension at crosshead displacement rates 0.32 mm/s and 0.032 mm/s as well as to cyclic tension at crosshead displacement rate 0.0128 mm/s. The obtained data were used to analyze effects of thermomechanical couplings accompanying the alloy loading. The IR camera parameters were as follows: a wavelength range 3 µm ÷ 5 µm, maximal frequency used in the experiment 538 Hz, window size 160 x 256 pixels.

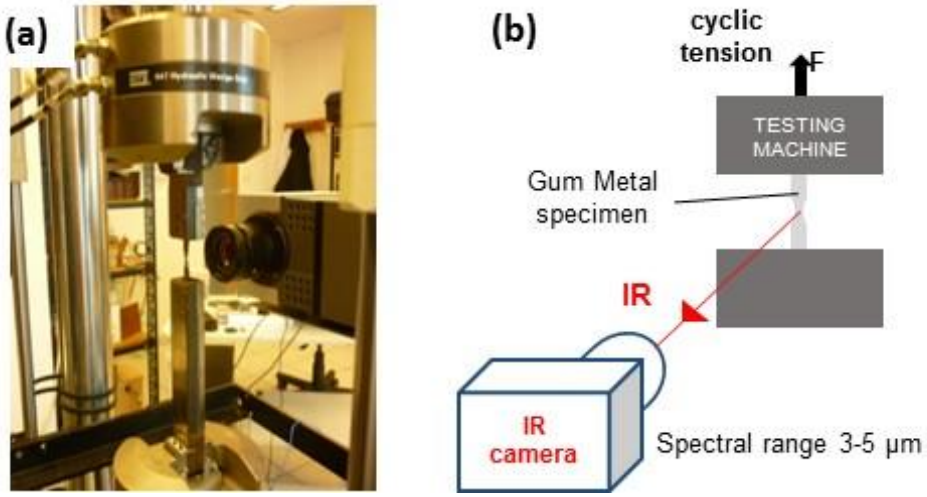

Fig. 3.3. Experimental set-up: (a) photograph and (b) scheme.

3.3. Analysis of elastic behavior of Gum Metal under monotonic and cyclic tension

A comparison of true stress vs. true strain curves plotted for Gum Metal subjected to monotonic tension on the testing machine up to rupture at the strain rates of 10^{-2} s^{-1} and 10^{-3} s^{-1} is presented in Fig. 3.4(a). The curves reveal unique mechanical characteristics of Gum Metal, namely low Young's modulus of around 68 GPa and high strength of over 1100 MPa. Figs. 3.4(b) and 3.4(c) show true stress vs. true strain curves plotted for Gum Metal subjected to monotonic tension up to 0.025 at the strain rates of 10^{-2} s^{-1} and 10^{-3} s^{-1}, respectively. The initial stress vs. strain curves for both strain rates are linear up to the stress level of around 400 MPa as marked in the curves. After reaching the stress of 400 MPa stress vs. strain curves get nonlinear.

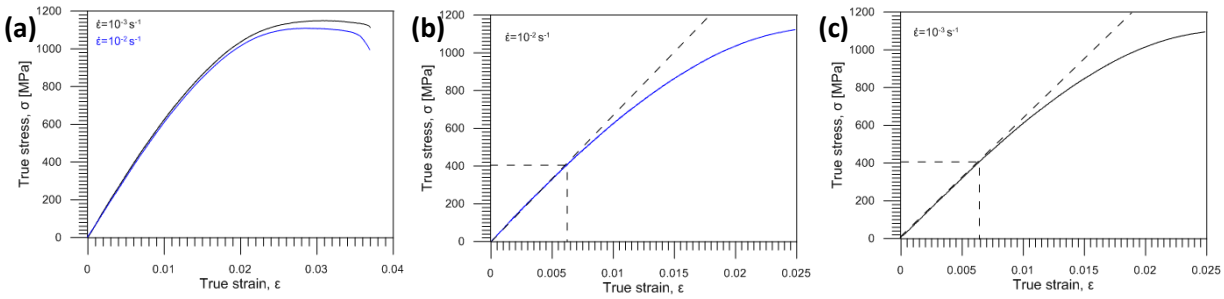

Fig. 3.4. True stress σ vs. true strain ε curves for Gum Metal under monotonic tension (a) comparison for two strain rates 10^{-2} s^{-1} and 10^{-3} s^{-1} up to specimen rupture; initial deformation range up to 0.025 for strain rate (b) 10^{-2} s^{-1}; (c) 10^{-3} s^{-1}.

True stress vs. true strain curves plotted for Gum Metal subjected to cyclic tension on the testing machine at the strain rate of $4x10^{-4}$ s^{-1} are presented in Fig. 3.5. The first cycle was realized within a strain of 0.002 and subsequent cycles were performed with a strain step of $\Delta\varepsilon$ = 0.002. The experiment consisted of 14 tension loading-unloading cycles. The rupture of the Gum Metal specimen occurred in cycle 14. High elastic characteristics of Gum Metal namely low Young's modulus (around 62 GPa) as well as the nonlinear superelasic-like deformation were confirmed. Maximal recoverable strain of the Gum Metal was observed in cycle 7 for strain value of 0.014, as shown in Fig. 3.5(b). High strength of Gum Metal (over 1000 GPa) was observed for cycles 10-14. During those cycles, the specimen was apparently deformed in plastic regime, which is also visible in the remaining strain after unloading in Fig. 3.5(a).

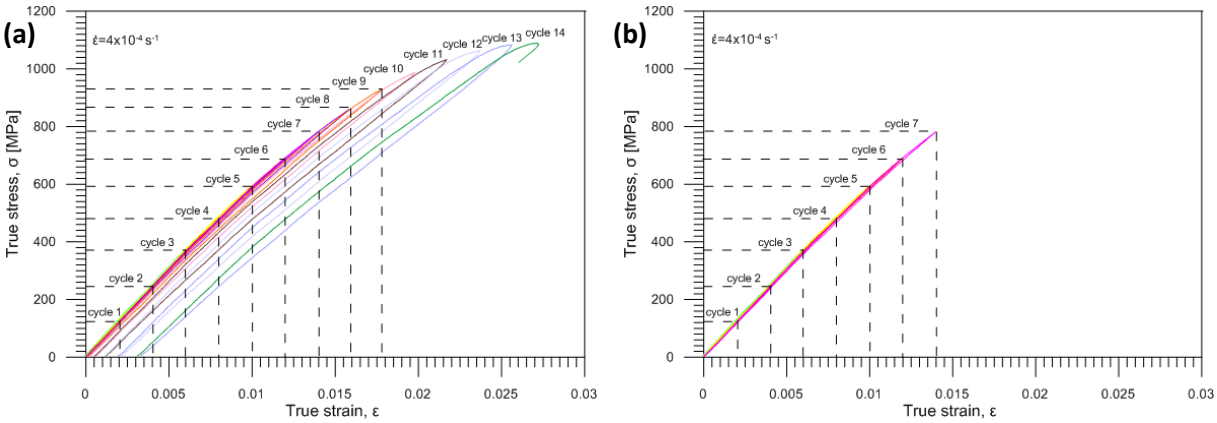

Fig. 3.5. Stress σ vs. strain ε curves of Gum Metal under subsequent loading-unloading cyclic tension at strain rate of $4x10^{-4}$ s^{-1} with a strain step $\Delta\varepsilon$=0.002: (a) cycles 1-14 up to specimen rupture; (b) cycles 1-7 characterized by recoverable strain.

3.4 Analysis of mechanical behavior and the related temperature change of Gum Metal under monotonic tension

The strain rates applied for Gum Metal loading had an effect on the mechanical behavior of the specimens. Higher maximal stress value of 1150 MPa has been obtained for the strain rate of 10^{-2} s^{-1} whereas for the strain rate of 10^{-3} s^{-1} the maximal stress value obtained equaled 1109 MPa as presented in Figs. 3.6(a) and 3.6(c), respectively. During initial loading, maximal average temperature drops of -0.11 ^{o}C and -0.08 ^{o}C related to stress values of 405 MPa and 422 MPa have been measured for the strain rates of 10^{-2} s^{-1} and 10^{-3} s^{-1}, respectively and presented in Figs. 3.6(b) and 3.6(d) . At higher loading stage, the temperature of the specimen

increases. The highest average temperature growth during tension until rupture at the strain rate of 10^{-2} s^{-1} has equaled 4.79 °C and has been greater in comparison to the value of 2.34 °C obtained at the strain rate of 10^{-3} s^{-1} as shown in Figs. 3.6(a) and 3.6(c). Critical values obtained from Gum Metal stress and temperature vs. strain plots presented in Figs. 3.6(a) and 3.6(c) are listed in table 3.1.

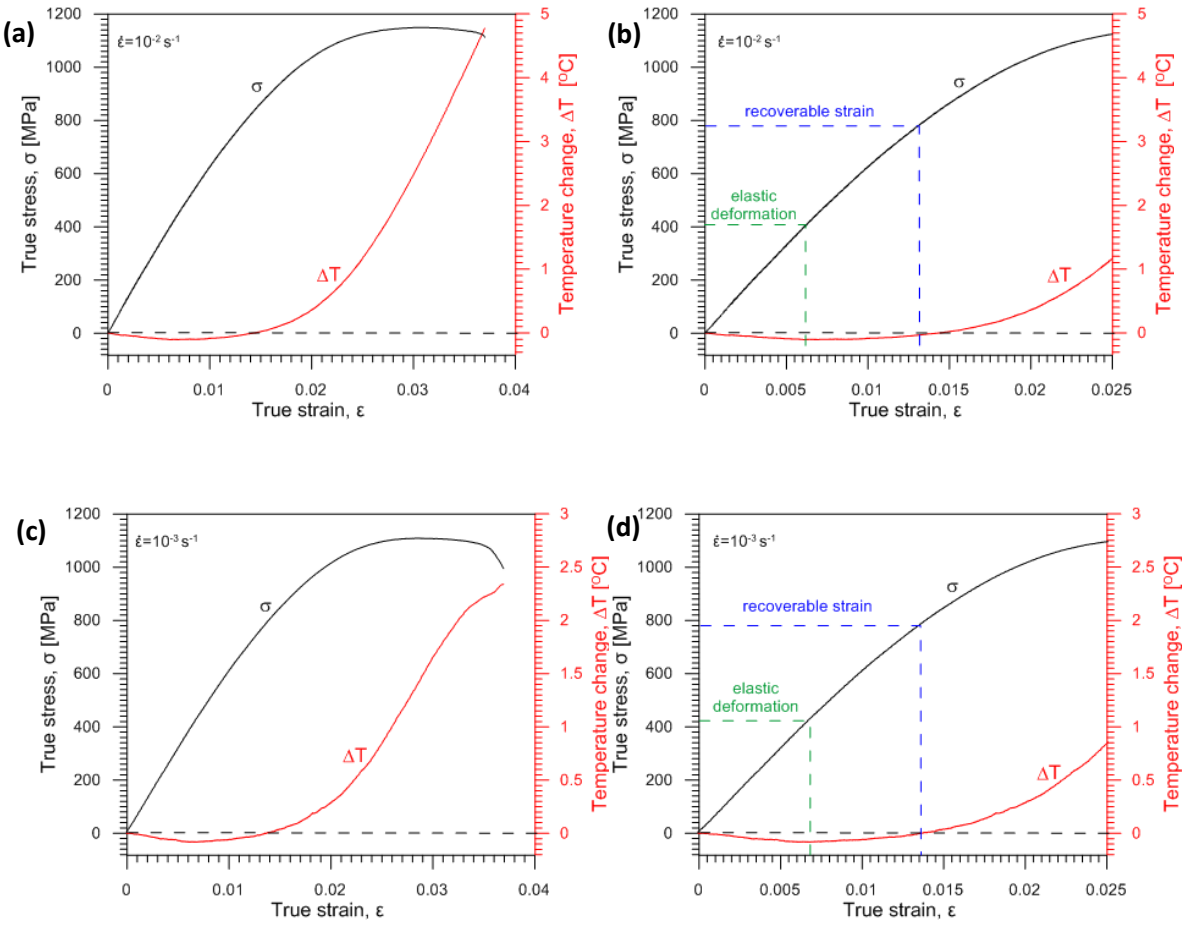

Fig. 3.6. Stress σ and average temperature change ΔT vs. strain ε curves of Gum Metal under tension at strain rate 10^{-2} s^{-1} (a) up to rupture and (b) up to strain 0.025 and at strain rate 10^{-3} s^{-1} (c) up to rupture and (d) up to strain 0.025.

Table 3.1. Critical values obtained from stress and temperature vs. strain plots of Gum Metal under tension at strain rates of 10^{-3} s^{-1} and 10^{-2} s^{-1}.

Strain rate [s^{-1}]	Max. stress [MPa]	Max. temperature drop [°C]	Stress at max. temperature drop [MPa]	Maximum temperature growth [°C]
10^{-2}	1150	-0.11	405	4.78
10^{-3}	1109	-0.08	422	2.34

The temperature distributions (thermograms) on the specimens surface of the Gum Metal at various deformation stages with stress-strains graphs for two strain rates of $10^{-3}s^{-1}$ and $10^{-2}s^{-1}$ are shown in Figs. 3.7 and 3.8, respectively. The following characteristic points of the graphs were selected to present the corresponding temperature distributions for the subsequent stages of the tensile test at the strain rate of 10^{-3} s^{-1} (Fig. 3.7):

(0) the beginning of elastic deformation (start of experiment);
(1) the end of linear elastic regime (decrease in temperature);
(2) the end of nonlinear recoverable deformation;
(3) the beginning of plastic regime;
(4) intermediate plastic deformation stage, reaching maximal stress;
(5) advanced plastic deformation stage;
(6) just before rupture;
(6a) just after rupture;
(7) fracture of the specimen (end of experiment).

The temperature variation plot and the thermograms (0) and (1) show that in the linear elastic regime the maximal temperature drop is observed. Subsequently, the temperature starts increasing slowly till the end of the nonlinear elastic stage (2) and it is distributed equally on the specimen surface. Following through the plastic regime via thermograms (3), (4) and (5); the temperature rises more significantly and its distribution starts being more concentrated. The thermograms (6) and (6a) show development of the strain localization, characterized by the highest local temperature increase, leading to the specimen rupture in thermogram (7).

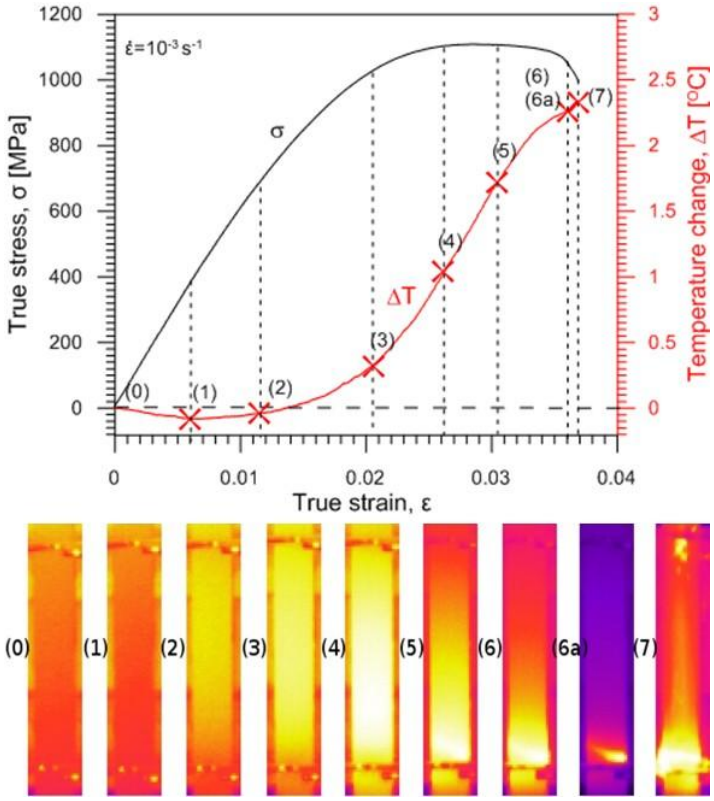

Fig. 3.7. Stress σ and average temperature change ΔT vs. strain ε curves with a set of thermograms correlated to selected deformation stages for Gum Metal under tension at strain rate of 10^{-3} s^{-1}.

The stress vs. strain plot for the tensile test of the Gum Metal specimen carried out at the strain rate of 10^{-2} s^{-1} is presented in Fig. 3.8. The characteristic points selected to show and analyze the corresponding thermograms are as follows:

(0) the beginning of elastic deformation (start of experiment);
(1) the end of linear elastic regime (increase in temperature);
(2) the end of nonlinear recoverable deformation;
(3) intermediate plastic deformation stage, reaching maximal stress;
(4) advanced plastic deformation stage;
(5) just before rupture;
(5a) just after rupture;
(6) fracture of the specimen (end of experiment).

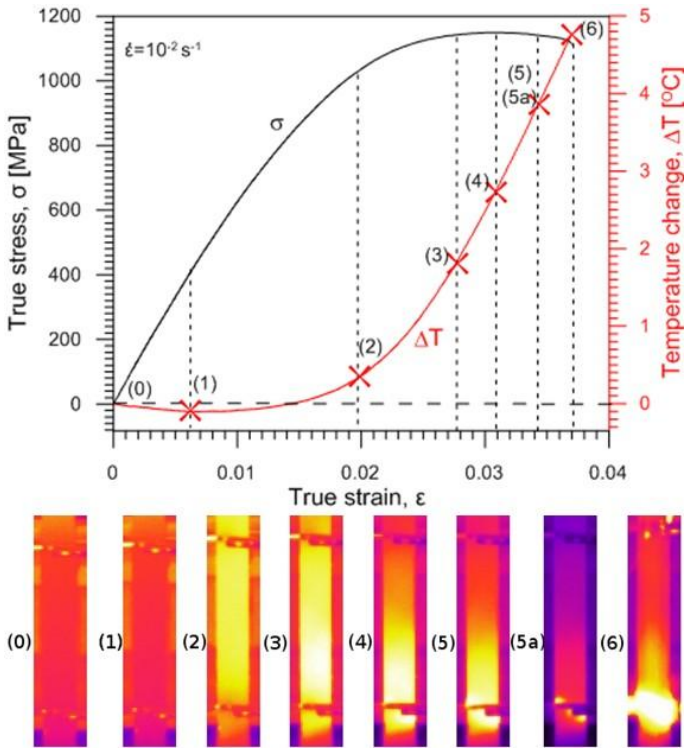

Fig. 3.8. Stress σ and average temperature change ΔT vs. strain ε curves with a set of thermograms correlated to selected deformation stages for Gum Metal under tension at strain rate of $10^{-2}\ s^{-1}$.

Similarly to the previous analysis for the test carried out at the strain rate of $10^{-3}\ s^{-1}$ shown in Fig. 3.7; Fig. 3.8 indicates that the average temperature drop occurs in the linear elastic regime which is observed between two characteristic points for thermograms (0) and (1). Subsequently, the temperature starts growing till the end of the nonlinear elastic stage (2) and it is distributed uniformly on the specimen surface. Then, via the plastic regime, the temperature increases more significantly and its distribution starts being more concentrated which is shown in thermograms (3) and (4). The thermograms (5) and (5a) demonstrate the localization development characterized by the highest local temperature growth leading to the specimen rupture in thermogram (6).

3.5. Investigation of thermomechanical couplings in Gum Metal subjected to subsequent cycles of tensile loading

A detailed analysis of thermomechanical behavior of subsequent stages of Gum Metal deformation, including purely elastic regime, recoverable stain and plastic region leading to necking and rupture for the test presented in Fig. 3.5 is discussed in this section. True stress σ and average temperature change ΔT vs. true strain ε curves of Gum Metal under cyclic tension at strain rate of $4x10^{-4}$ s^{-1} up to rupture are shown in Fig. 3.9. Subsequent loading-unloading cycles 1-14 of Gum Metal tension were analyzed using true stress σ and average temperature change ΔT vs. true strain ε and true stress σ, true strain ε and average temperature change ΔT vs. time curves are shown in in Figs. 3.10 – 3.17.

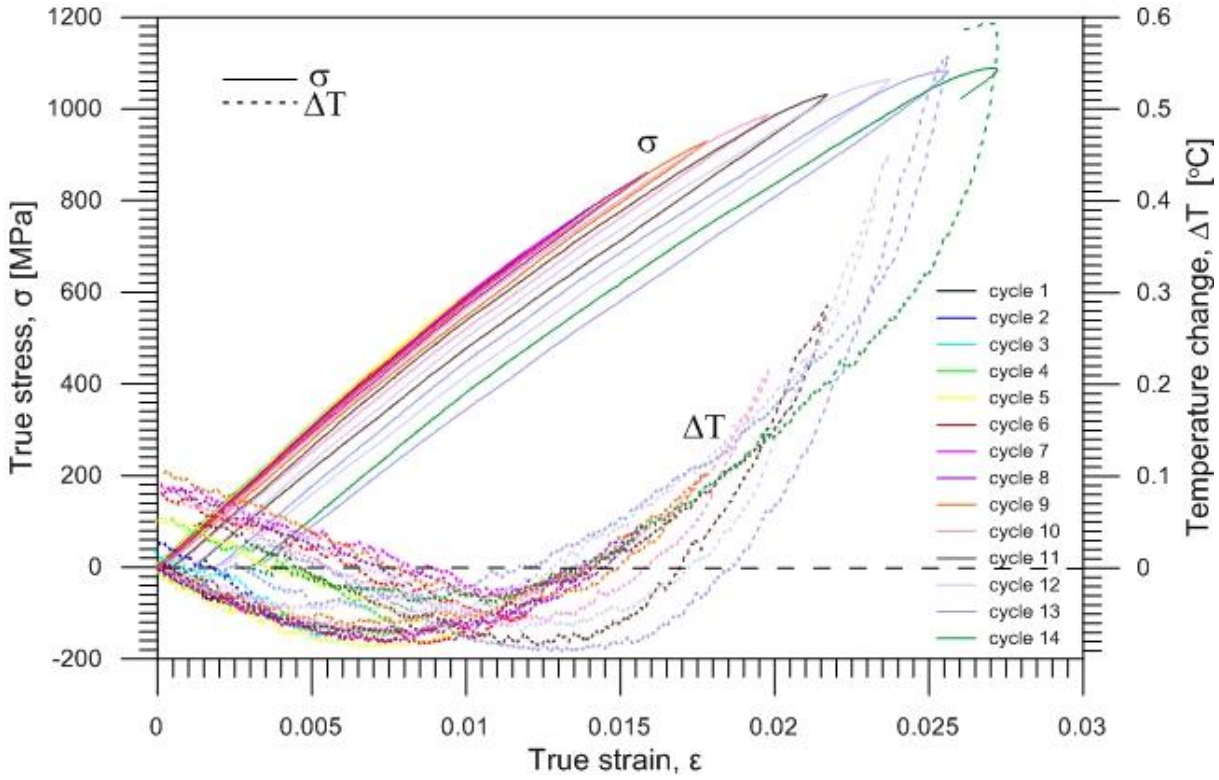

Fig. 3.9. Stress σ and average temperature change ΔT vs. strain ε curves of Gum Metal under cyclic tension at strain rate of $4x10^{-4}$ s^{-1} with a strain step $\Delta\varepsilon = 0.002$.

True stress and the related temperature change vs. true strain curves for tensile cycles 1 - 3 of Gum Metal are shown in Figs. 3.10 (a – c). On the one hand, the true stress vs. true strain plots in the loading-unloading process overlap for cycles 1, 2 and 3. It means that the strain is totally recoverable from the mechanical perspective for these cycles. Furthermore, the temperature change vs. true strain decreases during the loading stage and increases in a

recoverable way during unloading in cycles 1 - 3. Higher values of temperature change during unloading can be caused by heat exchange with surrounding and positive effects of thermoelastic unloading [Pieczyska E., 1999].

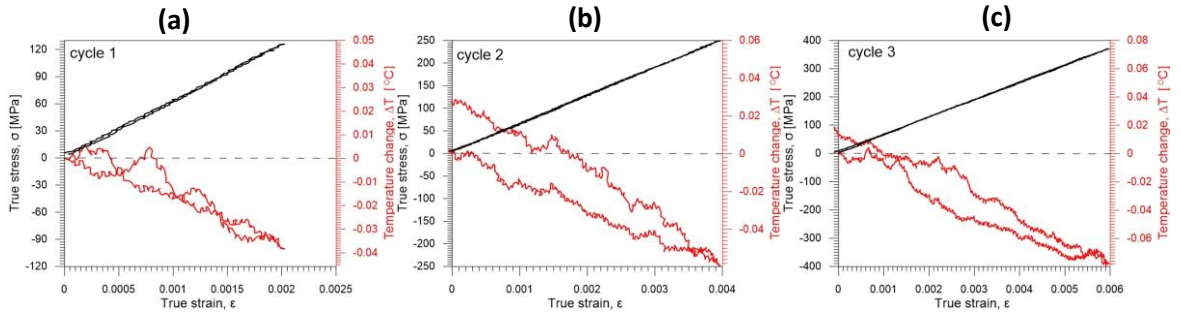

Fig. 3.10. Stress σ and average temperature change ΔT vs. strain ε curves for tensile cycles of Gum Metal: (a) cycle 1, (b) cycle 2 and (c) cycle 3.

Similar effects can be observed in Figs. 3.11 (a – c), which present true stress, true strain and temperature change vs. time for tensile cycles 1, 2 and 3 of Gum Metal. In cycles 1 – 3, during the elastic loading of Gum Metal the temperature drops, whereas during elastic unloading it rises in a recoverable way.

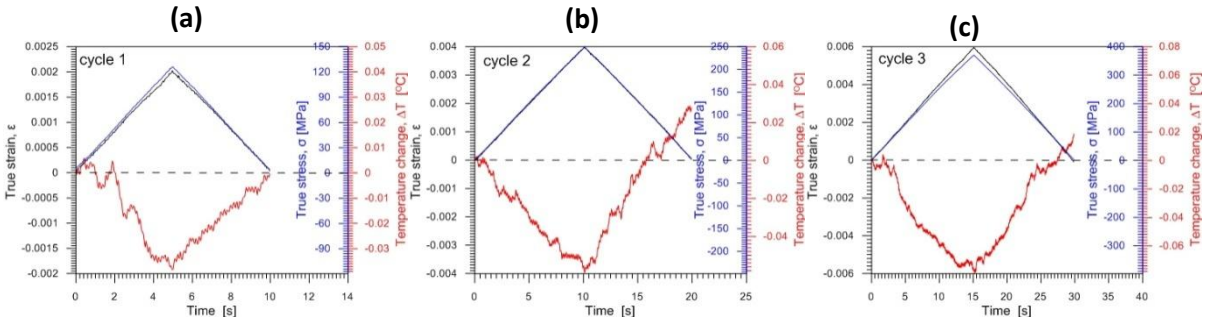

Fig. 3.11. Stress σ, strain ε and average temperature change ΔT vs. time curves for tensile cycles of Gum Metal: (a) cycle 1, (b) cycle 2 and (c) cycle 3.

In subsequent cycles 4, 5 and 6, the true stress vs. true strain plots in the loading-unloading process still overlap so the strain is recoverable, as shown in Figs. 3.12 (a-c). The temperature change vs. true strain during loading firstly decreases and then slightly increases in the final phase of Gum Metal loading, which is presented in a clearer way in Figs. 3.13 (a-c). The maximum value of temperature drop, which is equal to -0.08 ^{o}C, can indicate the range of purely elastic deformation of Gum Metal. It corresponds to the strain value of 0.007. During

unloading, the temperature increases what is caused by heat exchange with surroundings and positive value of thermoelastic effect [Pieczyska, 1999].

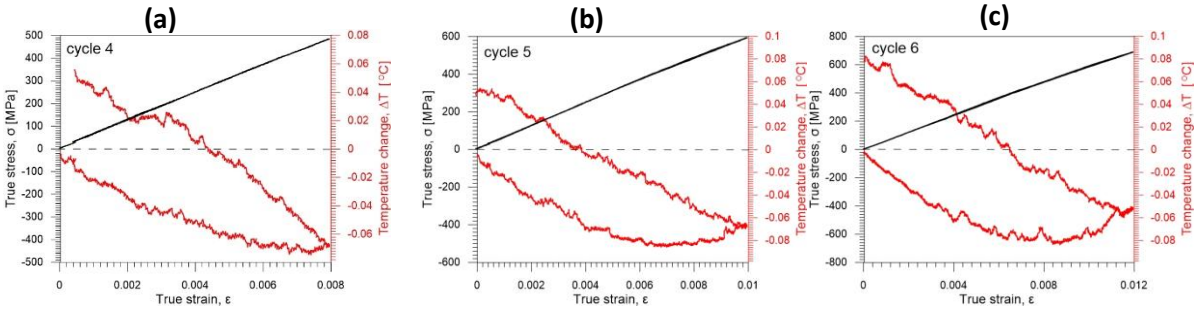

Fig. 3.12. Stress σ and average temperature change ΔT vs. strain ε curves for tensile cycles of Gum Metal: (a) cycle 4, (b) cycle 5 and (c) cycle 6.

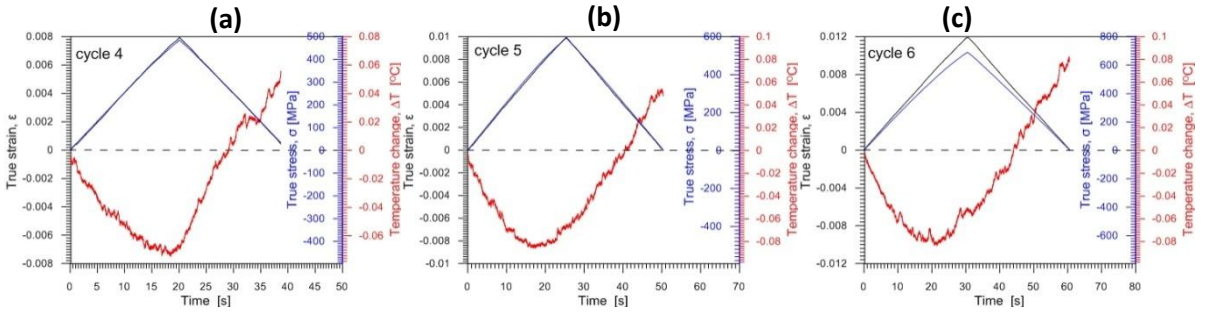

Fig. 3.13. Stress σ, strain ε and average temperature change ΔT vs. time curves for tensile cycles of Gum Metal: (a) cycle 4, (b) cycle 5 and (c) cycle 6.

True stress and temperature change vs. true strain as well as true stress, true strain and temperature change vs. time curves for tensile cycles 7 - 9 of Gum Metal are shown in Figs. 3.14 and 3.15 (a–c), respectively. Maximal recoverable strain of Gum Metal was observed in cycle 7 for strain of 0.014. In cycles 8 and 9, on one hand true stress vs. true strain curves do not overlap and an small value of permanent plastic deformation can be noticed. On the other hand, temperature change vs. true strain firstly decreases due to thermoelastic effect, secondly it increases still within the mechanically recoverable strain. Finally, there is a significant temperature growth which may accompany an exothermic phase transformation of α" nanodomains up to cycle 7 and overlapping of those and an plastic deformation in the subsequent loading cycles. During unloading, the temperature firstly decreases as a result of endothermic recoverable superelastic-like deformation and then increases due to positive thermoelastic effect accompanied by heat exchange with surroundings [Pieczyska, 1999].

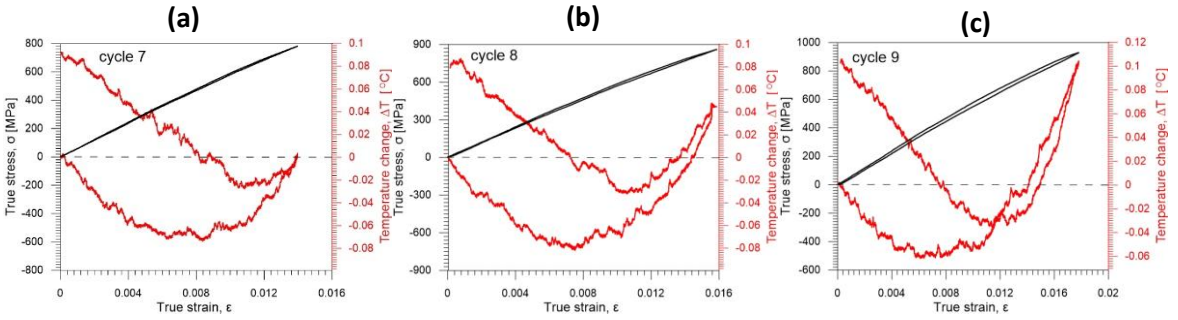

Fig. 3.14. Stress σ and average temperature change ΔT vs. strain ε curves for tensile cycles of Gum Metal: (a) cycle 7, (b) cycle 8 and (c) cycle 9.

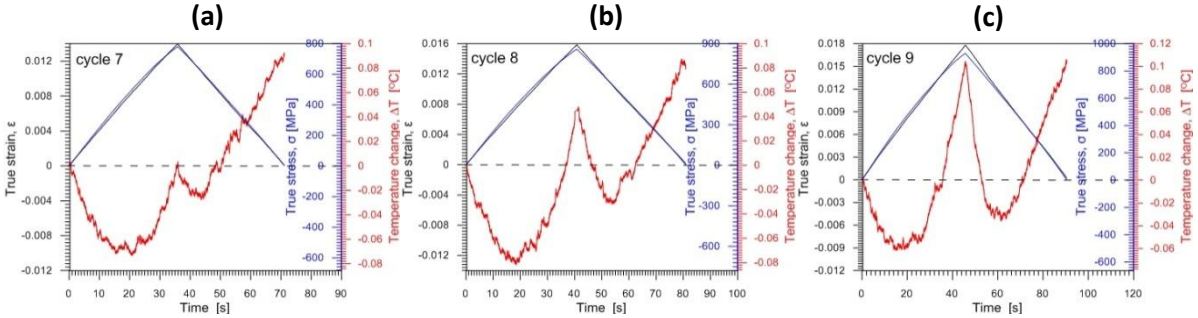

Fig. 3.15. Stress σ, strain ε and average temperature change ΔT vs. time curves for tensile cycles of Gum Metal: (a) cycle 7, (b) cycle 8 and (c) cycle 9.

It was estimated that the mechanically reversible deformation was present until performing cycle 7 within the strain range 0.014, as seen in Fig. 3.14(a). The maximal temperature drop ≈ -0.08 °C in the Gum Metal specimen under cyclic tension corresponds to the strain of around 0.007 (Fig. 3.12(a)). Thus, the thermodynamic nature of the mechanically estimated recoverable strain indicates a combination of two stages: linear elastic deformation and a nonlinear stage accompanied by a temperature growth. The latter demonstrates an exothermic nature within a relatively large reversible superelastic-like deformation. This phenomenon, published in this dissertation and selected communications [Golasiński K. et al. 2016a, 2016b, 2017a], is an original finding. It is believed to originate from other deformation mechanisms such as stress-induced exothermic phase transformations of martensite nanodomains [Miyazaki S. 2017], which cause an apparent dissipative behavior. True stress and temperature change vs. true strain as well as true stress, true strain and temperature change vs. time curves for tensile cycles 10 - 14 of Gum Metal are shown in Figs. 3.16 (a–e) and 3.17 (a–e).

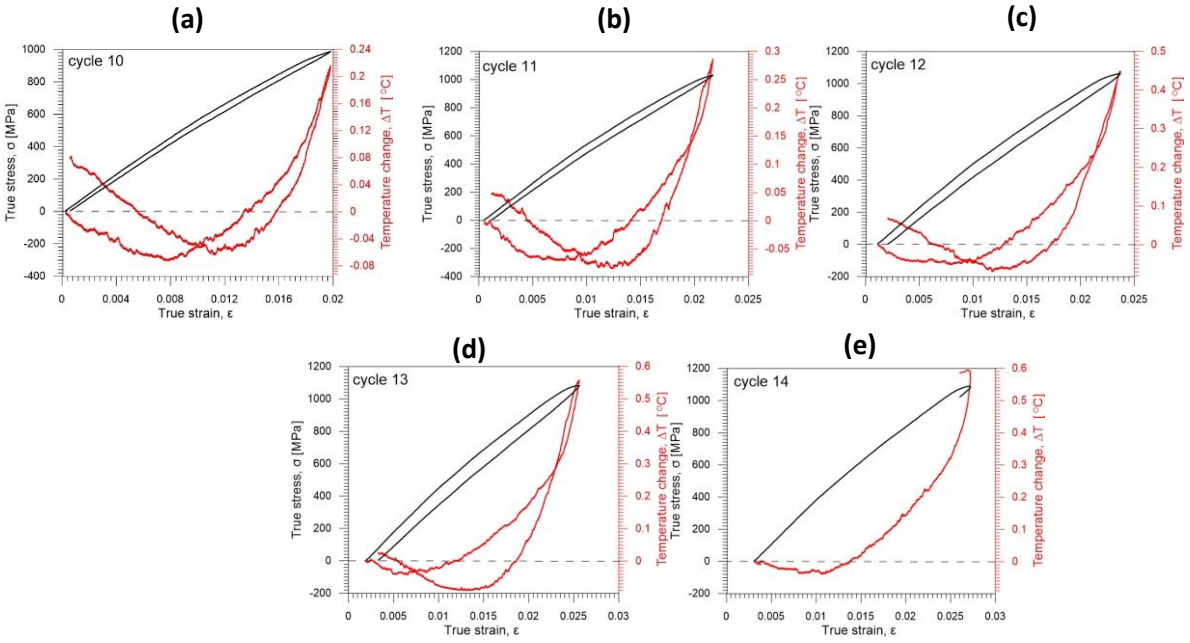

Fig. 3.16. Stress σ and average temperature change ΔT vs. strain ϵ curves for tensile cycles of Gum Metal: (a) cycle 10, (b) cycle 11, (c) cycle 12 , (d) cycle 13 and (e) cycle 14.

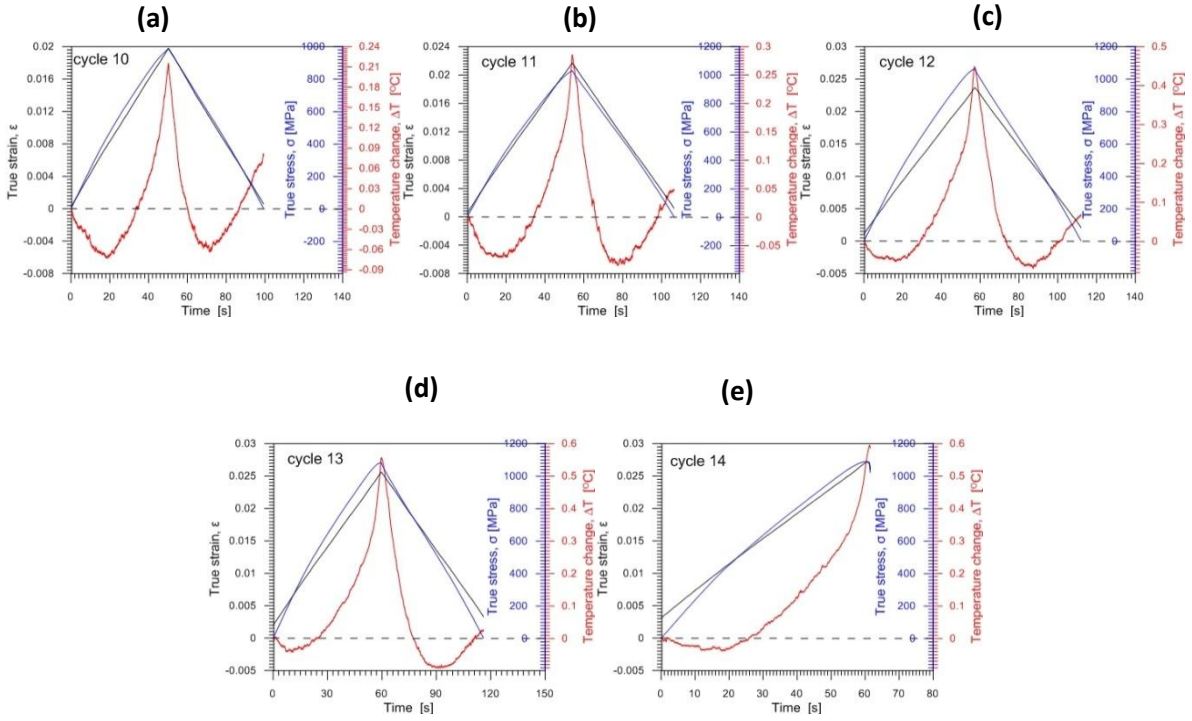

Fig. 3.17. Stress σ, strain ϵ and average temperature change ΔT vs. time curves for tensile cycles of Gum Metal: (a) cycle 10, (b) cycle 11, (c) cycle 12, (d) cycle 13 and (e) cycle 14.

In cycles 10 - 13, the presented plots reveal an evident plastic deformation which is accompanied by a significant temperature increase in the final stage of loading. Rupture of

Gum Metal specimen occurred in cycle 14, at the strain value of around 0.27 and was accompanied by a temperature increase of 0.6 ^{o}C.

In order to explain in more details evolution of effects of thermoelastic unloading, analysed in Figs 3.10-3.17, critical values of the temperature change (0) – (6) were presented in Fig. 3.18. The Gum Metal deformation stages marked exemplary in temperature change vs. time curve for cycle 13 are demonstrating:

(0) beginning of the loading process;

(A) maximum temperature drop during loading (thermoelastic effect) (ΔT_{Lmin});

(B) temperature change at superelastic-like deformation limit (temperature change corresponding to stress σ = 780 MPa determined in cycle 7) (ΔT_{trans});

(C) maximum temperature growth (ΔT_{max});

(D) temperature drop during unloading (ΔT_{Umin});

(E) slight increase of temperature (end of the unloading process) (ΔT_{fin}).

The temperature change values correspond to every of the following deformation stages of Gum Metal analyzed in each loading-unloading cycle indicated by arrows in Fig. 3.18:

(0)-(A) purely elastic loading;

(A)-(B) superelastic-like loading;

(B)-(C) plastic loading;

(C)-(D) superelastic-like unloading;

(D)-(E) elastic unloading.

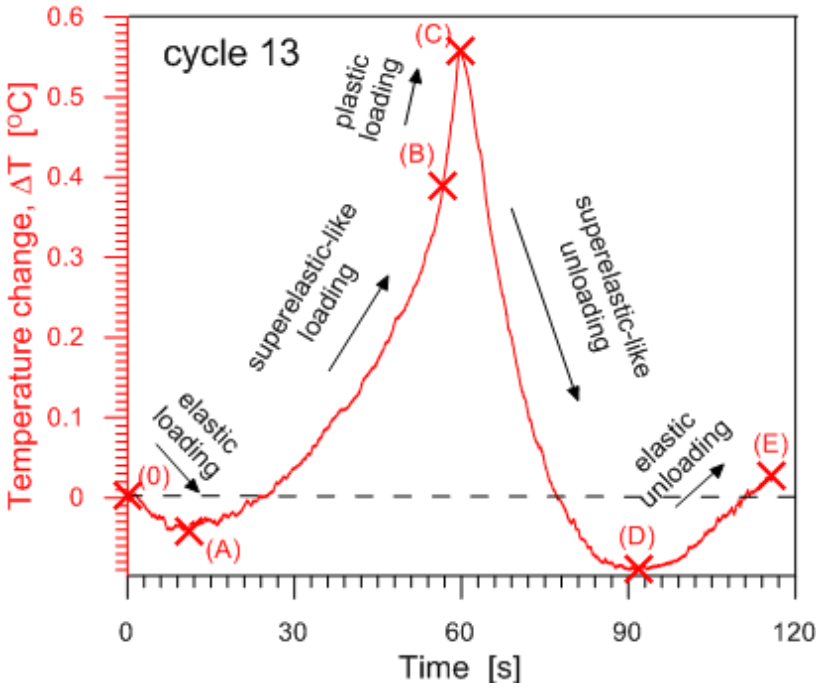

Fig. 3.18 Critical values of temperature change (0) – (E) corresponding to certain stages of Gum Metal deformation presented in *ΔT* temperature change vs. time curve for cycle 13 of Gum Metal cyclic tension.

Critical values of temperature change corresponding to certain stages of Gum Metal deformation in each of loading-unloading tensile cycles 1-14 are listed in Table 3.2. They include maximum temperature drop during the loading (ΔT_{Lmin}), temperature change at mechanically recoverable deformation limit (temperature change corresponding to stress σ = 780 MPa, ΔT_{trans}), maximal temperature change (ΔT_{max}), temperature change during plastic deformation (ΔT_{max} - ΔT_{trans}) and temperature drop accompanying the unloading process (ΔT_{Umin}) as well as final temperature change after unloading (ΔT_{fin}).

Table 3.2. Critical values obtained from stress and temperature vs. strain plots of Gum Metal under tension at strain rates of $4x10^{-4}$ s^{-1}.

Cycle number	Critical values of temperature change ΔT [°C]					
	LOADING				UNLOADING	
	ΔT_{Lmin}	ΔT_{trans} ($\Delta T_{\sigma = 780MPa}$)	ΔT_{max}	ΔT_{max}- ΔT_{trans}	ΔT_{Umin}	ΔT_{fin}
1	-0,038	-	0,006	-	-	-0,0004
2	-0,059	-	0,028	-	-	0,027
3	-0,079	-	0,018	-	-	0,019
4	-0,074	-	0,055	-	-0,068	0,056
5	-0,085	-	0,054	-	-0,067	0,048
6	-0,084	-	0,082	-	-0,052	0,078
7	-0,073	-	0,092	-	-0,027	0,092
8	-0,082	-0,012	0,087	0,099	-0,032	0,079
9	-0,062	0,004	0,106	0,102	-0,036	0,102
10	-0,073	0,015	0,215	0,200	-0,064	0,079
11	-0,085	0,017	0,286	0,268	-0,084	0,046
12	-0,069	0,069	0,449	0,379	-0,069	0,069
13	-0,091	0,105	0,557	0,451	-0,091	0,025
14	-0,038	0,108	0,595	0,487	-	-

True stress and temperature change vs. true strain curves of Gum Metal for a representative tensile cycle 13 of advanced deformation with selected points in the temperature change curve (0) – (E) and corresponding thermograms are presented in Fig. 3.19. The points were chosen for critical instants of the Gum Metal deformation:

(0) beginning of loading;

(A) minimal temperature change during loading;

(B) maximal recoverable strain (corresponding);

(C) maximal temperature change;

(D) minimal temperature change during unloading;

(E) end of unloading.

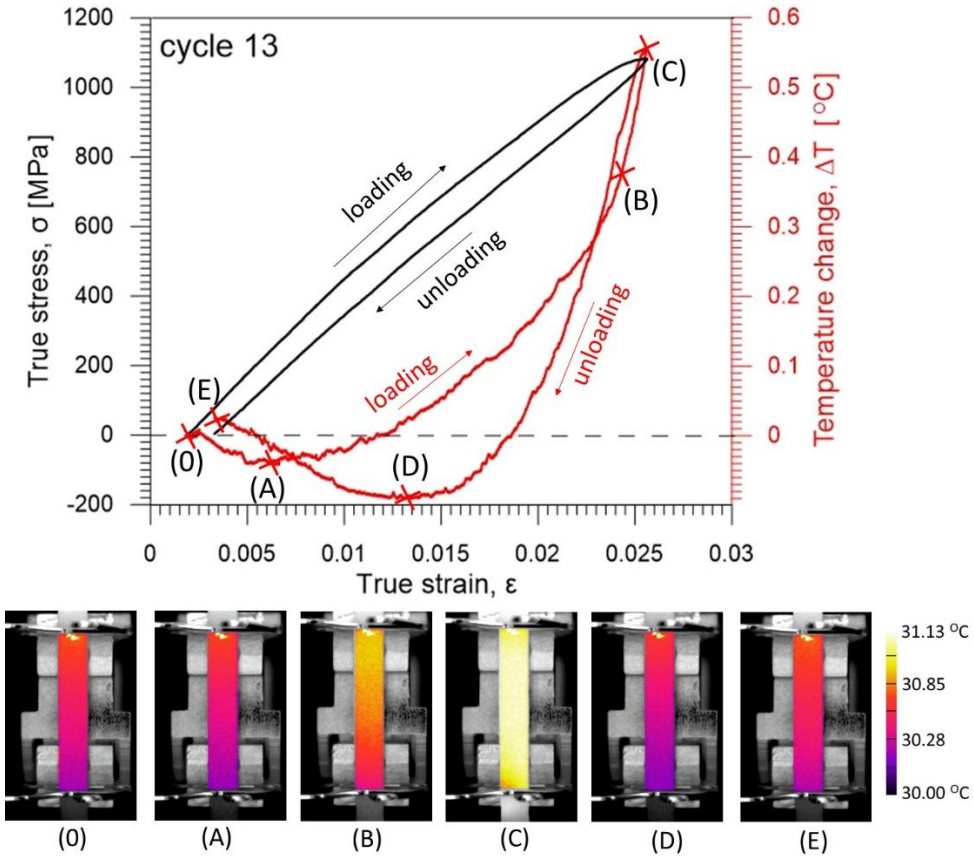

Fig. 3.19. Stress σ and average temperature change ΔT vs. strain ε curves of Gum Metal for an advanced tensile cycle 13 with selected points in the temperature change curve (0) – (6) and corresponding thermograms.

In the initial phase of Gum Metal loading, a drop in temperature is observed as shown between thermograms (0) and (A). Purely elastic deformation of Gum Metal is observed between points (0) and (A). Further loading is accompanied by a temperature growth caused by an activity of stress-induced growth of martensite nanodomains up to point (B), as shown in thermogram (B). Point (C) corresponds to plastic deformation of Gum Metal with significant increase in temperature change depicted in thermograms (C). Unloading of Gum Metal results in a drop of temperature change with minimal value in point (D), as presented in thermogram (D). The unloading process in cycle 13 ends in point (E) with a corresponding thermogram (E). In the stage of purely elastic unloading between thermograms (D) and (E) there is a temperature change increase due to positive value of thermoelastic effect and heat exchange with surroundings.

3.6 Analysis of thermoelastic effect in Gum Metal under selected loadings

In this section, thermoelastic effect in Gum Metal under selected loadings is analyzed by comparing values of maximal temperature drop obtained experimentally and theoretically. The calculations of theoretical values of the temperature change $\Delta T_{CALCmin}$ were performed using Eq. 2.1 $\Delta T = -\frac{\alpha T \Delta \sigma_{ik}}{c_p \rho}$ and taking the Gum Metal parameters listed in Table 3.3.

Table 3.3 Parameters of Gum Metal taken for estimation of energy balance.

Density, ρ	5.6 g/cm^3
Specific heat, c_p	0.455 J/gK
Thermal expansion coefficient, α	$8 \cdot 10^{-6}$ K^{-1}

The values of density ρ and thermal expansion coefficient α were taken from literature [Saito T. et al. 2003 and presentation]. The value of specific heat c_p of Gum Metal was taken the same as the value determined for the second set of flat specimens as shown in chapter 4. Analyzing the results of theoretical calculations of this dissertation one should remember that the Gum Metal parameters are rather tentative.

The values of stress $\Delta\sigma_{ik}$ corresponding to the temperature drop during loading ΔT_{Lmin} for Gum Metal were derived from Figs. 3.6 in the case of monotonic tension. Table 3.4 presents values of $\Delta\sigma_{ik}$, ΔT_{Lmin} and $\Delta T_{CALCmin}$ for Gum Metal under monotonic tension tests at two strain rates 10^{-3} s^{-3} and 10^{-2} s^{-1}.

Table 3.4 Values of stress $\Delta\sigma_{ik}$ corresponding to temperature drop during loading ΔT_{Lmin} for Gum Metal under monotonic tension tests at two strain rates 10^{-3} s^{-1} and 10^{-2} s^{-1} derived from the results presented in Figs. 3.6 and the calculated theoretical values of the temperature drop $\Delta T_{CALCmin}$.

Strain rate [s^{-1}]	$\Delta\sigma_{ik}$ [MPa]	ΔT_{Lmin} [°C]	$\Delta T_{CALCmin}$ [°C]
10^{-2}	405	-0.11	-0.376
10^{-3}	422	-0.08	-0.392

The values of ΔT_{Lmin} (experimental) and $\Delta T_{CALCmin}$ (theoretical) for Gum Metal under monotonic tension tests at two strain rates $10^{-3}\,s^{-3}$ and $10^{-2}\,s^{-1}$ are contrasted in Fig. 3.20.

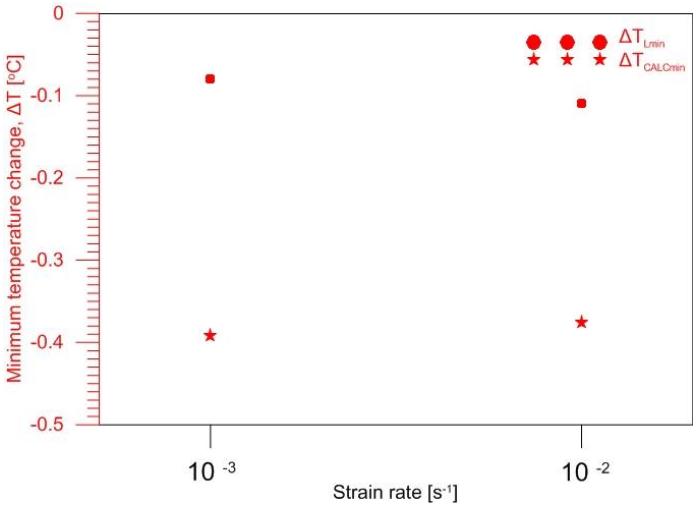

Fig. 3.20. Values of temperature change related to thermoelastic effect ΔT_{Lmin} (experimental) and $\Delta T_{CALCmin}$ (theoretical) for Gum Metal under monotonic tension tests at two strain rates $10^{-3}\,s^{-1}$ and $10^{-2}\,s^{-1}$.

In the case of cyclic tension, the values of stress $\Delta\sigma_{ik}$ corresponding to the minimum temperature change during loading ΔT_{Lmin} for Gum Metal were derived from Fig. 3.9. Table 3.5 presents values of $\Delta\sigma_{ik}$, ΔT_{Lmin} and $\Delta T_{CALCmin}$ for each cycle of Gum Metal loading-unloading tension test at strain rate $4x10^{-4}\,s^{-1}$.

Table 3.5 Values of stress $\Delta\sigma_{ik}$, minimum temperature change during loading ΔT_{Lmin} derived from the results presented in Fig. 3.9 and the calculated theoretical values of the temperature change $\Delta T_{CALCmin}$ for Gum Metal under cyclic tension.

Cycle number	$\Delta\sigma_{ik}$ [MPa]	ΔT_{Lmin} [°C]	$\Delta T_{CALCmin}$ [°C]
1	125,97	-0,038	-0,117
2	249,03	-0,059	-0,231
3	367,6	-0,079	-0,341
4	452,9	-0,074	-0,421
5	431,71	-0,085	-0,401
6	520,26	-0,084	-0,483
7	499,62	-0,074	-0,464
8	447,64	-0,082	-0,415
9	365,62	-0,062	-0,339
10	447,47	-0,073	-0,415
11	588,28	-0,085	-0,546

12	501,91	-0,069	-0,466
13	476,09	-0,091	-0,442
14	411,254	-0,038	-0,382

The values of ΔT_{Lmin} (experimental) and $\Delta T_{CALCmin}$ (theoretical) for each cycle of Gum Metal loading-unloading tension test at strain rate $4x10^{-4}$ $s^{-1}$are contrasted in Fig. 3.21.

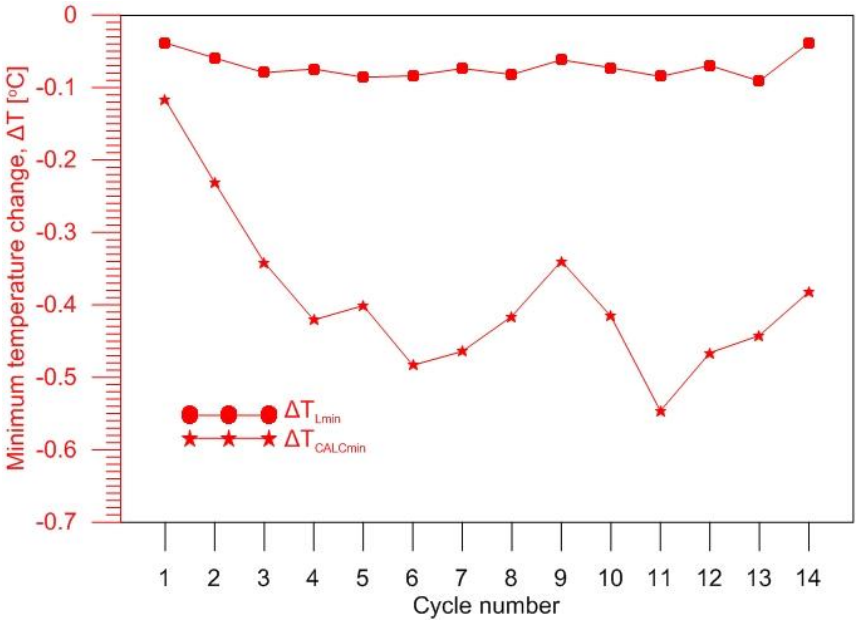

Fig. 3.21. Values of temperature change related to thermoelastic effect ΔT_{Lmin} and $\Delta T_{CALCmin}$ for each cycle of Gum Metal loading-unloading cyclic tension test at strain rate $4x10^{-4}$ s^{-1}.

In the case of both monotonic and cyclic tension tests, the values of $\Delta T_{CALCmin}$ obtained theoretically are lower than the values of ΔT_{Lmin} derived experimentally, as presented in Figs. 3.20 and 3.21. This discrepancy is not very significant and can be connected with the lack of precise parameters of Gum Metal since the values of density ρ and thermal expansion coefficient α used in the calculations were taken from literature.

3.7 Summary

Preliminary results of the effects of thermomechanical coupling in Gum Metal specimens under tension were analyzed. The unique mechanical characteristics of Gum Metal i.e., low elastic modulus and nonlinear recoverable deformation as well as high strength of the alloy were confirmed by performing monotonic tension tests. It has been also shown that mechanical performance of Gum Metal depends on the applied strain rate. The limit of the

nonlinear recoverable deformation of Gum Metal was determined by performing subsequent tensile cycles with a small strain step.

Subsequent stages of Gum Metal deformation were investigated based on the obtained stress and temperature change vs. strain characteristics. A purely elastic deformation range of Gum Metal was determined basing on the temperature drop (according to thermoelastic effect analysis). The temperature plots with their maximal drop occurring before the end of the recoverable deformation recorded under tension suggest the exothermal activity of unconventional deformation mechanisms with dissipative character activated in the alloy during loading. Most probably, it is a stress-induced exothermic transformation of martensite nanodomains, confirmed by other researchers including Prof. Shuichi Miyazaki and Prof. Hee Young Kim from the University of Tsukuba, via microscopic observations. The thermograms captured by a sensitive infrared camera showed effects of strain localization characterized by high temperature concentration leading to necking and rupture. The temperature change plots for loading-unloading cycles of Gum Metal under tension showed an endothermic character of superelastic-like deformation of Gum Metal during unloading. The plastic stage of Gum Metal under cyclic tension was seen to be accompanied with a significant temperature change increase ending with rupture in cycle 14. Finally, the analysis of thermoelastic effect in Gum Metal under monotonic and cyclic loadings was performed. The values of minimum temperature change of Gum Metal during loading derived from the results were compared to the theoretical values basing on thermodynamic theory`. Quite good agreement between experimental and theoretical values was obtained.

Chapter 4

4. Comprehensive investigation of thermomechanical couplings in Gum Metal under tension

Interesting results of the preliminary investigation of the effects of thermomechanical couplings in Gum Metal under monotonic and cyclic tension presented in Chapter 3 were a motivation to conduct a more detailed study on a different set of Gum Metal specimens. The comprehensive results are shown in Chapter 4 and they were partially presented during several conferences [Golasiński et. al 2016a, 2016b, 2017b, 2017c, 2019c and Pieczyska E.A. et al 2016b, 2016c, 2017a, 2017b, 2018b] and published in [Pieczyska E.A. et al 2016a, 2018, Golasiński et. al 2017a, Kowalczyk-Gajewska K. et al. 2019].

4.1. Material and specimens

Gum Metal specimens used in this investigation were provided by the Toyota Central Research and Development Laboratories. The nominal composition of Gum Metal was Ti–23Nb–0.7Ta–2Zr–1.2O (at.%) and the fabrication included the several steps. A billet of Gum Metal was prepared by a powder technology. It was sintered at 1300 ^{o}C for 16 h in a vacuum of 10^{-4} Pa, hot forged to a 12.5 mm round bar, solution treated at 900 ^{o}C for 30 min, and subsequently quenched into water with ice. The heat-treated bar was removed with a surface oxidized layer and cold worked by a rotary swaging machine. The specimens were swaged to a diameter of 4 mm, then cold rolled to a thickness of 0.5 mm and annealed at 900 ^{o}C for 30 min.
Several specimens were prepared from these sheets. A technical drawing of the specimen is shown in Fig. 4.1(a), while a photograph is depicted in Fig. 4.1(b).

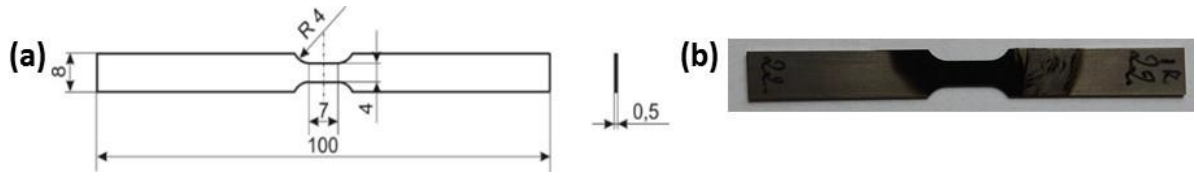

Fig. 4.1. Gum Metal specimen: (a) geometry and dimensions; (b) a photograph.

4.2. Microstructural analysis of Gum Metal

Microstructural characterization was conducted using a combination of optical microscopy and electron backscatter diffraction (EBSD). All specimens were prepared in the section vertical to the rolling direction. Polished specimens were prepared by a conventional mechanical technique and were etched with an aqueous 10% HF + 10% HNO_3 solution.

4.2.1 Optical microstructure of Gum Metal

Optical microscope image revealed homogeneity of the microstructure. The entire area of the sample presents equiaxed grains of β-Ti phase (Fig. 4.2).

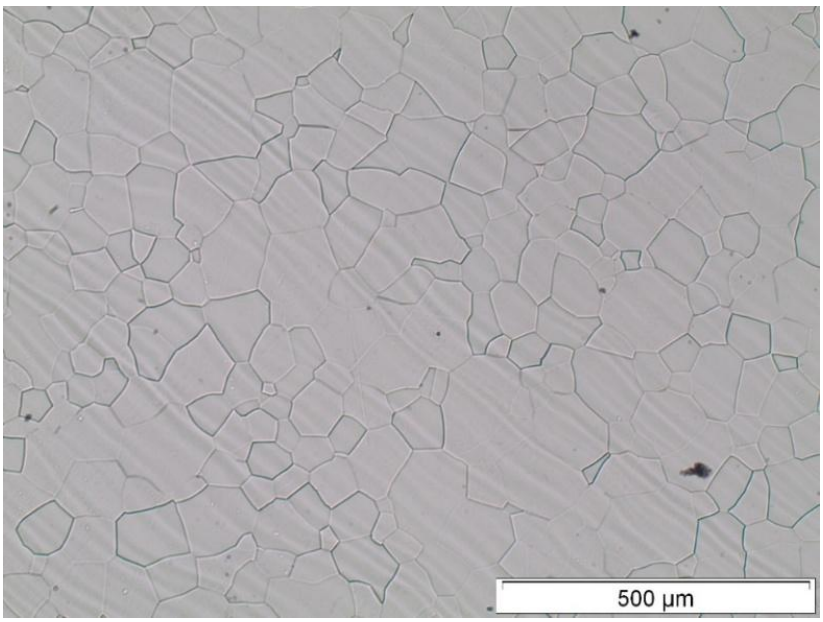

Fig. 4.2. Optical microscope image of Gum Metal sample.

4.2.2. Determination of crystallographic texture

Texture analysis of the Gum Metal was carried out on a JEOL JSM-6480 scanning electron microscope (SEM) equipped with Nordlys II electron diffraction diffuse detector and Channel 5. The EBSD results were analyzed using the Tango HKL software. The test was conducted at an accelerating voltage of 20 kV.

The crystallographic orientation maps made by the EBSD method were performed for area where only β-Ti was observed in order to determine the shape and size of grains as well as potential preferred crystallographic orientation. This studies revealed that the sample had equiaxed grains with a β-Ti phase structure as shown in Fig. 4.3.

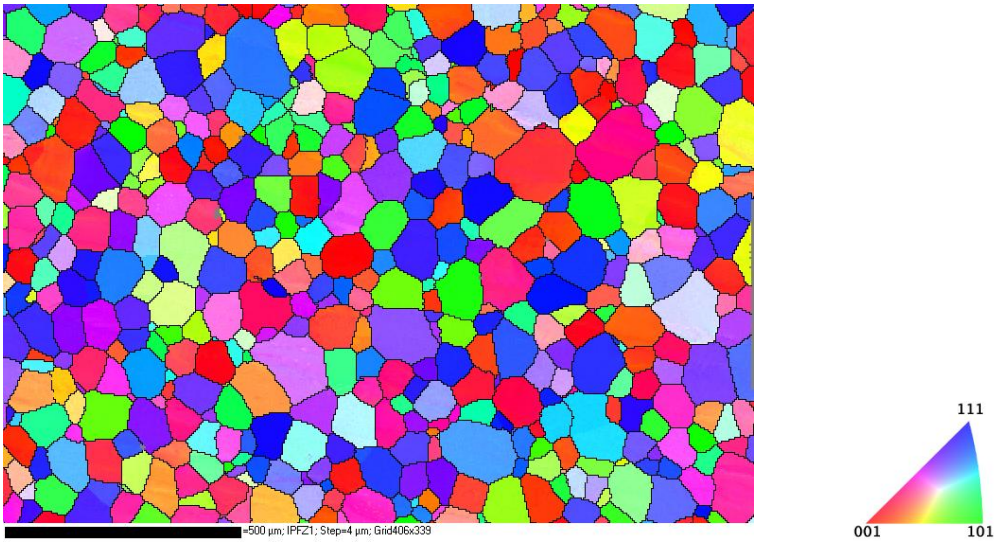

Fig. 4.3. Map of the crystallographic orientation distribution of Gum Metal sample.

A histogram of the grain size distribution is shown in Fig. 4.4(a). The average grain size is equal to 84.8 µm. The histogram of aspect ratios confirms that the grains are mostly equiaxial, i.e. its aspect ratio is close to 1. The shape of grain boundaries suggests large grains grow at the expense of small grains as shown in Fig. 4.4(b).

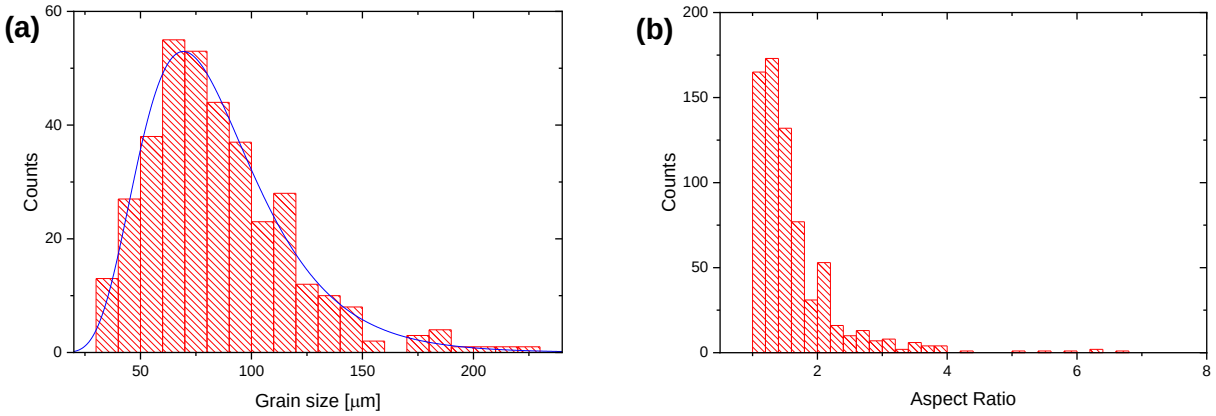

Fig. 4.4. (a) Histogram of grain size distribution and (b) and corresponding histogram of grains aspect ratio.

Pole figures showing a preferred crystallographic orientation in the sample of Gum Metal are shown in Fig. 4.5.

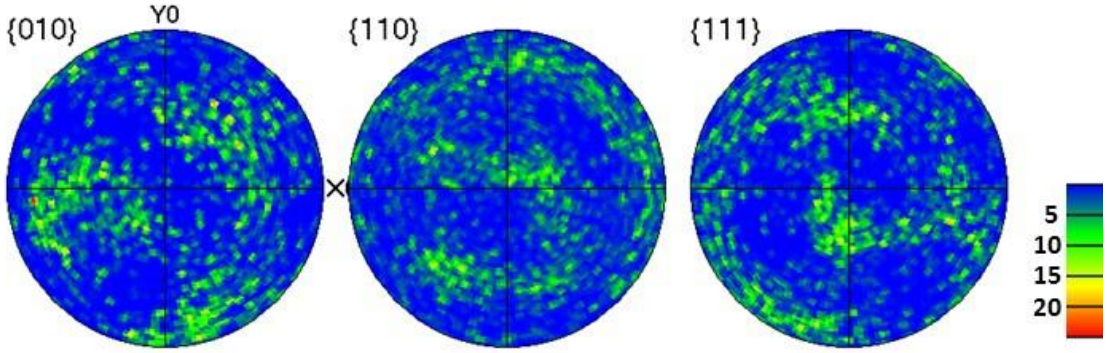

Fig. 4.5. Pole figures calculated on the basis of the crystallographic orientation map of Gum Metal.

No dominant texture component in Gum Metal can be observed.

4.2.3. Analysis of chemical composition

Analysis of the chemical composition of Gum Metal was carried out using energy-dispersive X-ray spectroscopy on a JEOL JSM-6480 SEM. The study was carried out at an accelerating voltage of 20 kV on selected material areas. An infrared Fourier-transform spectrometer (IRFS) was used for the analysis. An example of an electron dispersive spectroscopy (EDS) spectrum obtained for Gum Metal is shown in Fig. 4.6.

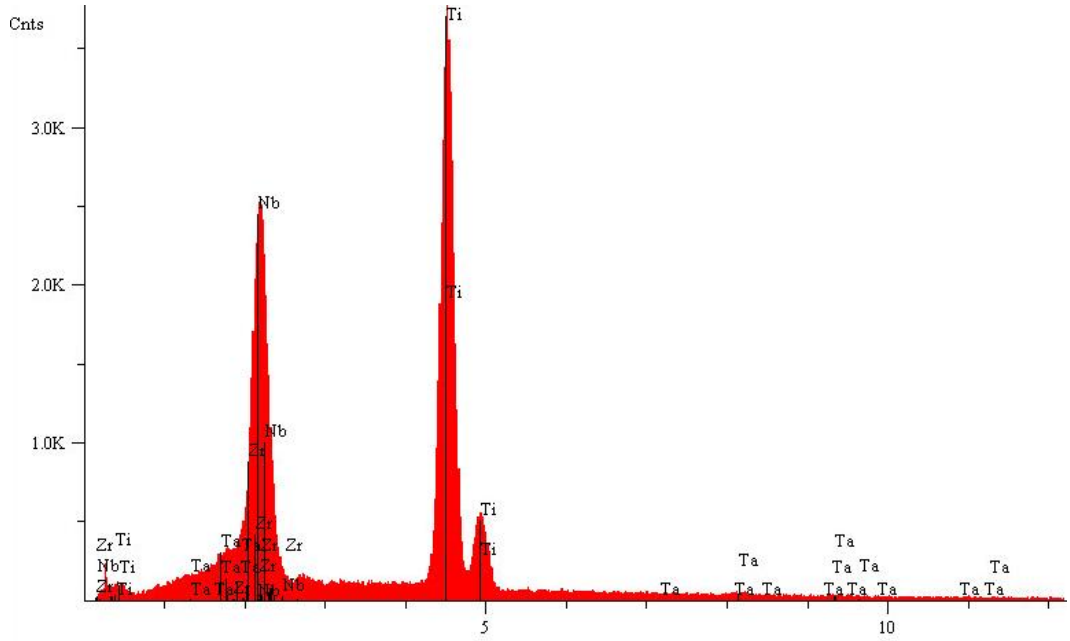

Fig. 4.6. Energy-dispersive X-ray spectroscopy spectrum of Gum Metal.

The chemical composition analysis performed by the EDS method was carried out in 10 areas of the sample. The results are presented in Table 4.1.

Table 4.1. Energy-dispersive X-ray spectroscopy analysis of the Gum Metal chemical composition.

Spectra number	CHEMICAL COMPOSITION [wt. %]			
	Ti	Nb	Zr	Ta
1	63.2(3)	30.2(4)	5.5(2)	1.0(2)
2	63.4(3)	30.1(4)	5.5(2)	1.0(2)
3	63.4(3)	30.0(4)	5.5(2)	1.1(3)
4	63.7(3)	30.4(4)	5.0(2)	0.9(2)
5	63.2(3)	30.6(4)	5.2(2)	1.0(2)
6	63.4(3)	30.4(4)	5.3(2)	0.9(2)
7	63.4(3)	30.5(4)	5.2(2)	0.9(2)
8	63.0(3)	30.7(4)	5.2(2)	1.1(2)
9	63.6(3)	30.3(4)	5.2(2)	0.9(2)
10	63.5(3)	30.1(4)	5.2(2)	1.2(2)

The oxygen content could not be measured using this characterization technique. The chemical composition analyzed by EDS Ti–30Nb–1Ta–5Zr (wt.-%) is slightly different than the nominal composition of Gum Metal Ti–36Nb–2Ta–3Zr–0.3O (wt.-%). However, the EDS technique has a limited accuracy.

4.2.4. Investigation of Gum Metal specific heat

The investigation was carried out using power-compensation differential scanning calorimeter, Pyris 1 DSC (Perkin-Elmer), equipped with cooling device Intracooler 2P. Temperature calibration was carried out using the melting points of indium and zinc of the heat flux using the melting heat of indium and of the specific heat using sapphire. The

measurements were carried out on samples in the form of a disk with a thickness of c.a. 1 mm and weighing c.a. 55-56 mg, in the temperature range from -65 ^{o}C to 450 ^{o}C, under high purity nitrogen (99.999%.) flow at 20 ml/h The measurements were performed at stepwise heating mode with temperature increase 2 ^{o}C at a rate of 75 ^{o}C /min followed by isothermal step to achieve an equilibrium state of the heat flow, c.a. 2 min. This method is called as StepScan. As a result, the sample is subjected to the action of non-periodic heat pulses. Analysis of the measured heat flow as a function of time, using the Laplace transform, leads to determination of the heat capacity spectrum, allowing, in effect, determination of precise heat capacity. To take into account the dynamic effects of the instrument and perform a calibration of specific heat, additional measurement at the same parameters, shall be carried out by means of two samples of Sapphire with different masses. A detailed description of the method and theoretical basics are presented in [Merzlyakov M. et al. 1999, 2001 and Kwon Y.K. et al. 2001].

Specific heat vs. temperature curves for three samples of Gum Metal denoted by GM1, GM2 and GM3 are presented in Figs. 4.7: (a) - plain results with an averaged curve; (b) an averaged curve with standard deviation and (c) standard deviation approximated by the 9th degree polynomial, respectively.

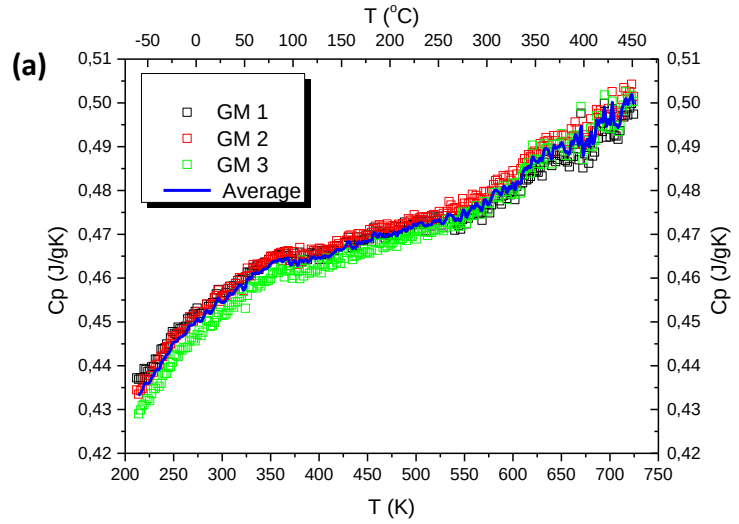

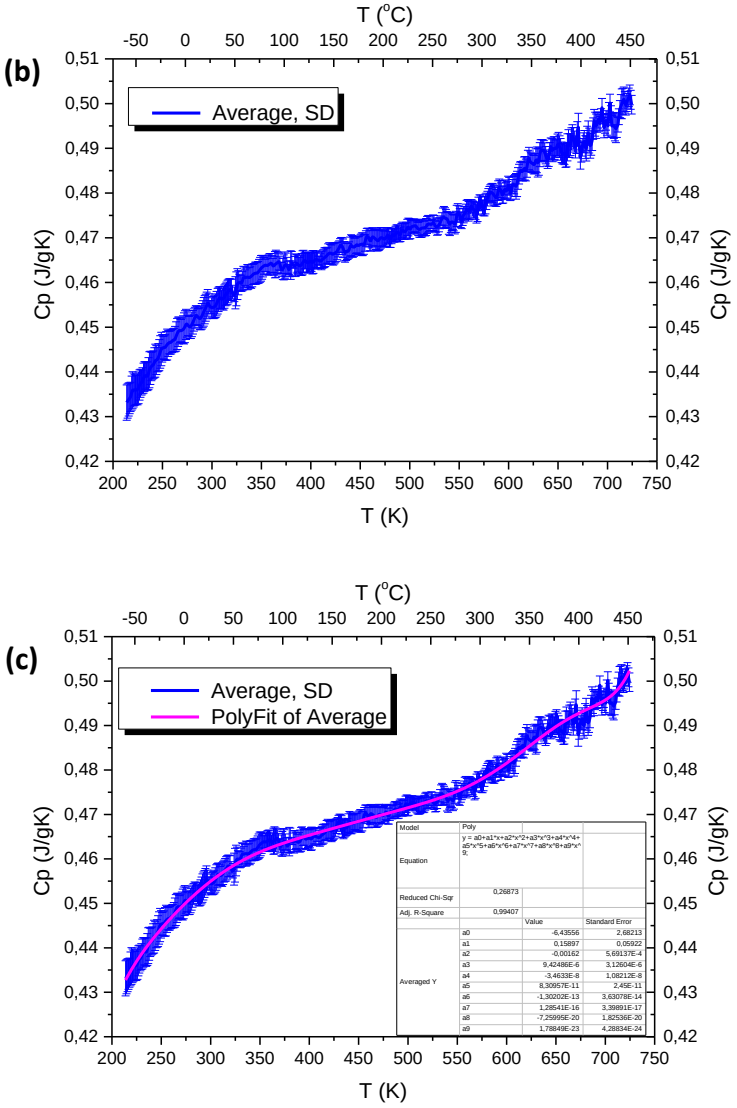

Fig. 4.7. Specific heat vs. temperature curves for three samples of Gum Metal denoted by GM1, GM2 and GM3: (a) plain results with an averaged curve; (b) an averaged curve with standard deviation and (c) standard deviation approximated by the 9th degree polynomial.

The values of Gum Metal specific heat determined based on measurements by DSC are in the range between 0.43 J/gK and 0.50 J/gK. They grow with the increase of temperature. At the room temperature the specific heat of Gum Metal is around 0.455 J/gK. This value is lower in comparison to the specific heat of pure titanium 0.544 J/gK mainly because of a significant content of niobium in Gum Metal. The specific heat of niobium equals 0.267 J/gK.

4.3. Analysis of mechanical behavior of Gum Metal under monotonic and cyclic tension

4.3.1. Experimental details

Experimental set-up used for investigation of the mechanical response of Gum Metal under tension included a high-performance testing machine and a DIC system. A diagram of the experimental set-up is shown in Fig. 4.8(a). A photograph of the specimen placed in the grips of the testing machine is shown in Fig. 4.8(b). During the tension process, the specimens of Gum Metal were monitored continuously by a visible range Manta G-125B camera. The camera resolution was 1100 x 410 pixels. A pixel size of 9.5 µm and the maximal recording frequency of 58 Hz were used. Based on the acquired sequence of digital images, the evolution of the displacement distributions were determined. On the basis of the obtained displacement distributions, the Hencky strain and rate of deformation tensor components were calculated. ThermoCorr software with built-in implementation of 2D DIC algorithm developed in IPPT PAN was used. A detailed description of the applied DIC methodology is presented in [Nowak et al. 2017].

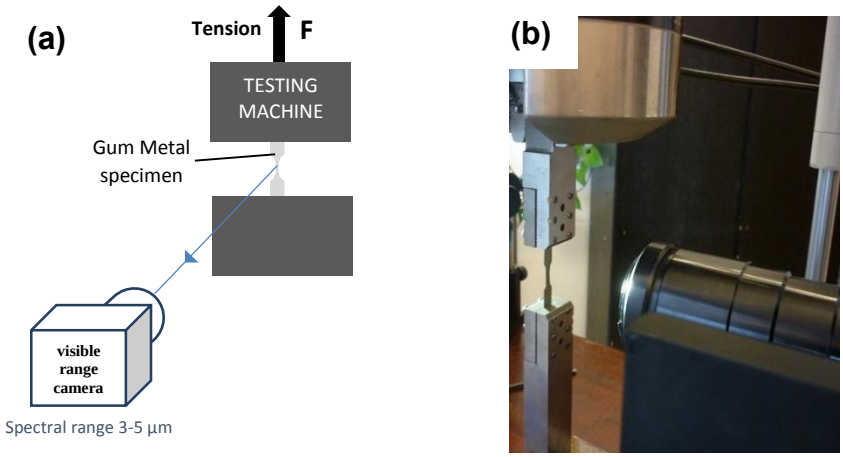

Fig. 4.8. Experimental set-up used for investigation of Gum Metal under tension at various strain rates: (a) scheme and (b) photograph.

After performing tensile loadings of Gum Metal specimens up to rupture, fracture surfaces of selected specimens were observed through JEOL JSM-6480 scanning electron microscope.

4.3.2. Investigation of strain rate effect on mechanical behavior of Gum Metal under monotonic tension

To analyze the influence of strain rate on the mechanical behavior of the Gum Metal tension tests up to the rupture were conducted at various strain rates. The Gum Metal samples were subjected to crosshead displacement controlled tension until rupture at five displacement rates: 0.00007 mm/s, 0.0007 mm/s, 0.007 mm/s, 0.07 mm/s and 0.7 mm/s. These values correspond to the average strain rates of $10^{-5}s^{-1}$, $10^{-4}s^{-1}$, $10^{-3}s^{-1}$, $10^{-2}s^{-1}$ and $10^{-1}s^{-1}$ when specimen geometry is taken into account. The obtained force vs. crosshead displacement curves are shown in Fig. 4.9(a). Average strains were calculated on the basis of displacement fields obtained by DIC using virtual extensometers (VE) of two different lengths, i.e. 7 mm and 1 mm. The results for the VE with initial length of 7 mm and for the initial length of 1 mm placed in the localization area of the specimen are presented in Figs. 4.9(b) and 4.9(c), respectively.

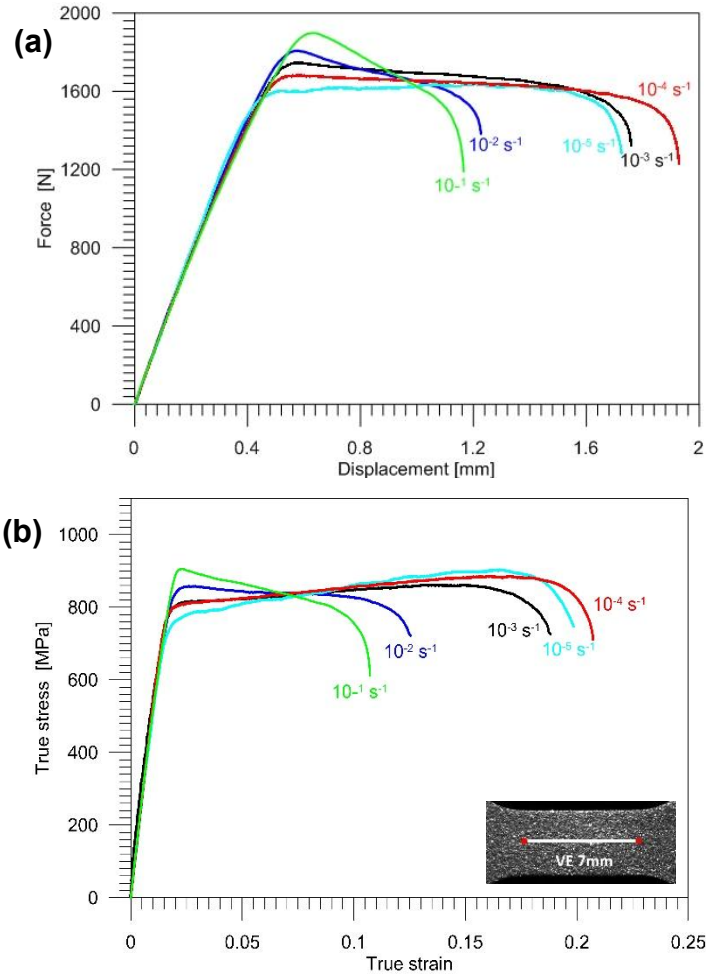

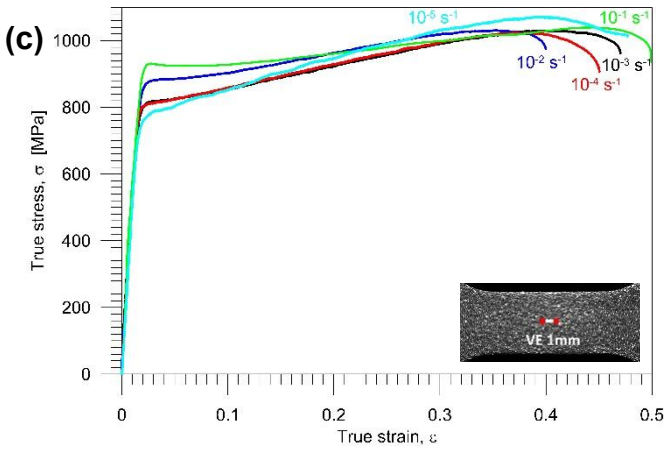

Fig. 4.9. Comparison of mechanical characteristics of Gum Metal subjected to tension until rupture at strain rates: $10^{-5}s^{-1}$, $10^{-4}s^{-1}$, $10^{-3}s^{-1}$, $10^{-2}s^{-1}$ and $10^{-1}s^{-1}$: (a) force vs. displacement curves; true stress vs. true strain curves for initial VEs lengths of (b) 7 mm and (c) 1 mm.

Analyzing Fig. 4.9 it can be seen that Gum Metal is very sensitive to the strain rate. It is worth noting that the mechanical characteristics presented in Figs. 4.9(a) and 4.9(b) show a similar tendency. The stress vs. strain curves reflect the macroscopic demonstration of the dependence, averaged by the VE length 7 mm as shown in diagram Fig. 4.9(b) and 1 mm as shown in the diagram in Fig. 4.9(c). It can be noticed that, the stress vs. strain curves for the length of VE equal to 7 mm obtained at strain rates $10^{-5}s^{-1}$, $10^{-4}s^{-1}$ and $10^{-3}s^{-1}$ show a macroscopically observed hardening effect, whereas that obtained at strain rates $10^{-2}s^{-1}$ and $10^{-1}s^{-1}$ demonstrate a macroscopically observed softening effect (see Fig. 4.9(b)). Drops in the loading force observed in Fig. 4.9(a) and drops of stress observed for the VE length 7 mm (equal to the gauge length of the specimen) shown in Fig. 4.9(b), demonstrate a sudden nucleation and development of strain localization. Thermal softening does not seem to occur, because Gum Metals are considered to be thermally stable. The softening effects are not observed in the case of VE equal to 1 mm, as shown in Fig. 4.9(c). It means, that there is no softening of the material itself, but the effect caused by the understating the strain, and consequently the stress values by assigning it to whole gauge part of the specimen, even if the deformation is localized in the narrow zone.

Determination of yield point in Gum Metal from the stress vs. strain curve is not trivial because of its nonlinear superelastic-like deformation. In the case of conventional materials, when a yield point is not easily defined based on the shape of the stress vs. strain curve an offset yield point is arbitrarily defined. The value for this is commonly set at 0.001 or 0.002 plastic strain.

In the case of Gum Metal, we propose to draw a straight line through point A (ε=0.004) at the same slope as the initial portion of the stress vs. strain curve, as presented in Fig. 4.10. The resulting red point of intersection of the drawn line and the stress vs. strain curve is projected to the stress axis and gives the yield strength value.

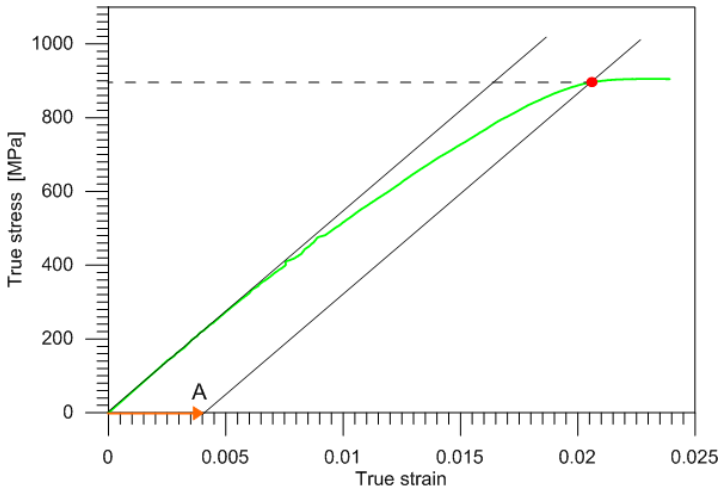

Fig. 4.10 Determination of yield point of Gum Metal using stress vs. strain curve.

Critical mechanical values of yield strength determined using the methodology presented in Fig. 4.10 and elongation of Gum Metal derived from the stress-strain curves for various strain rates calculated for the 7 mm VE length are listed in Table 4.2.

Table 4.2 Comparison of yield strength and elongation to rupture of Gum Metal derived from the stress vs. strain curves obtained at five strain rates

Strain rate	**10^{-5} s^{-1}**	**10^{-4} s^{-1}**	**10^{-3} s^{-1}**	**10^{-2} s^{-1}**	**10^{-1} s^{-1}**
Yield strength [MPa]	741.32	797.36	796.50	829.63	896.27
Elongation to rupture	0.197	0.226	0.188	0.125	0.107

Values of yield strength increased with higher strain rates, and varied from 741.32 MPa obtained for the lowest strain rate 10^{-5} s^{-1} to 896.27 MPa for the highest strain rate 10^{-1} s^{-1}. Elongation, at which point rupture of the Gum Metal sample occurred, decreased with

increasing strain rate. This rate ranged from 0.226 for the strain rate 10^{-4} s^{-1} to 0.107 for the strain rate $10^{-1}s^{-1}$. Therefore, the higher the strain rate, the lower the elongation to rupture. However, it can be seen in Fig. 4.9(b). that at the lowest strain rate, 10^{-5} s^{-1} , the strain range is lower than that obtained for the strain rate 10^{-4} s^{-1}. At a low strain rate of 10^{-5} s^{-1}, a creep-like deformation mechanism occurs, and this plays an important role in the loading and deformation process. Comparison of the critical mechanical properties of Gum Metal were determined for various strain rates as listed in Table 4.2. The yield strength and relative elongation to rupture vs. strain rate are shown in logarithmic scale in Figs. 4.11(a) and 4.11(b).

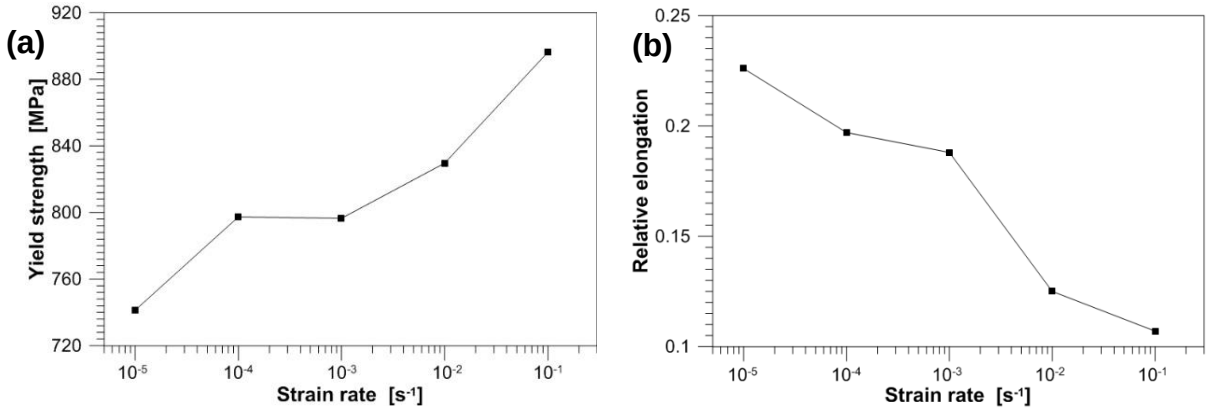

Fig. 4.11 Comparison of critical mechanical properties of Gum Metal: (a) yield strength and (b) elongation to rupture presented vs. strain rate.

It can be seen that the yield strength of the Gum Metal increases at increasing strain rate, while total elongation decreases.

Results obtained for different extensometer lengths show that at higher strain rates the strain localization process starts immediately after irreversible deformation occurs. It means that the true stress vs. true strain characteristics are not good measures of Gum Metal deformation and a full-field measurement approach using DIC technique would be better to understand the mechanical behavior of the alloy under tension.

4.3.4. Effect of strain rate on evolution deformation fields of Gum Metal under tension determined by digital image correlation

Based on the analysis of the stress-strain curves, the distributions of the Hencky strain **ε** and rate of deformation **D** tensor components were related to four critical stages of tension:

(1) ε=0.015 - end of recoverable strain

(2) ε=0.030 - around yielding

(3) ε=0.075 - advanced plastic deformation

(4) ε_{max} - just before rupture.

The components of the Hencky strain tensor ε were determined on the basis of the displacement gradient tensor **H** obtained from displacement field measured using 2D DIC method. In this case the **H** tensor has the form expressed by Eq. 4.1.

$$\mathbf{H} = \frac{\partial \mathbf{u}}{\partial \mathbf{X}} = \begin{bmatrix} \frac{\partial u_x}{\partial X} & \frac{\partial u_x}{\partial Y} & 0 \\ \frac{\partial u_y}{\partial X} & \frac{\partial u_y}{\partial Y} & 0 \\ 0 & 0 & [\cdot] \end{bmatrix}, \qquad \text{(Eq. 4.1)}$$

where **u = (**u_x, u_y**)** is the displacement vector and **X** = (*X,Y*) is a position of a material point in the Lagrangian coordinate system. The $\frac{\partial u_z}{\partial Z}$ component, which is not measured in 2D DIC analysis, was calculated under assumption of a constant volume. The detailed procedure of Hencky strain tensor **ε** determination is presented in [Nowak et al. 2018].

The rate of deformation tensor **D**, expressed by Eq. 4.2, were determined on the basis of the velocity field **v** as a symmetric part of the velocity gradient **L**:

$$\mathbf{D} = \frac{1}{2}(\mathbf{L} + \mathbf{L^T}), \qquad \text{(Eq. 4.2)}$$

where $\mathbf{L} = \frac{\partial \mathbf{v}}{\partial \mathbf{x}}$ and **x**=(*x*,*y*) is a position of a material point in the Eulerian coordinate system.

Selected distributions of the ε_{yy} and D_{yy} components (where y is tension direction) under tension at strain rate of 10^{-1} s^{-1} at four selected stages specified above are presented in Fig. 4.12.

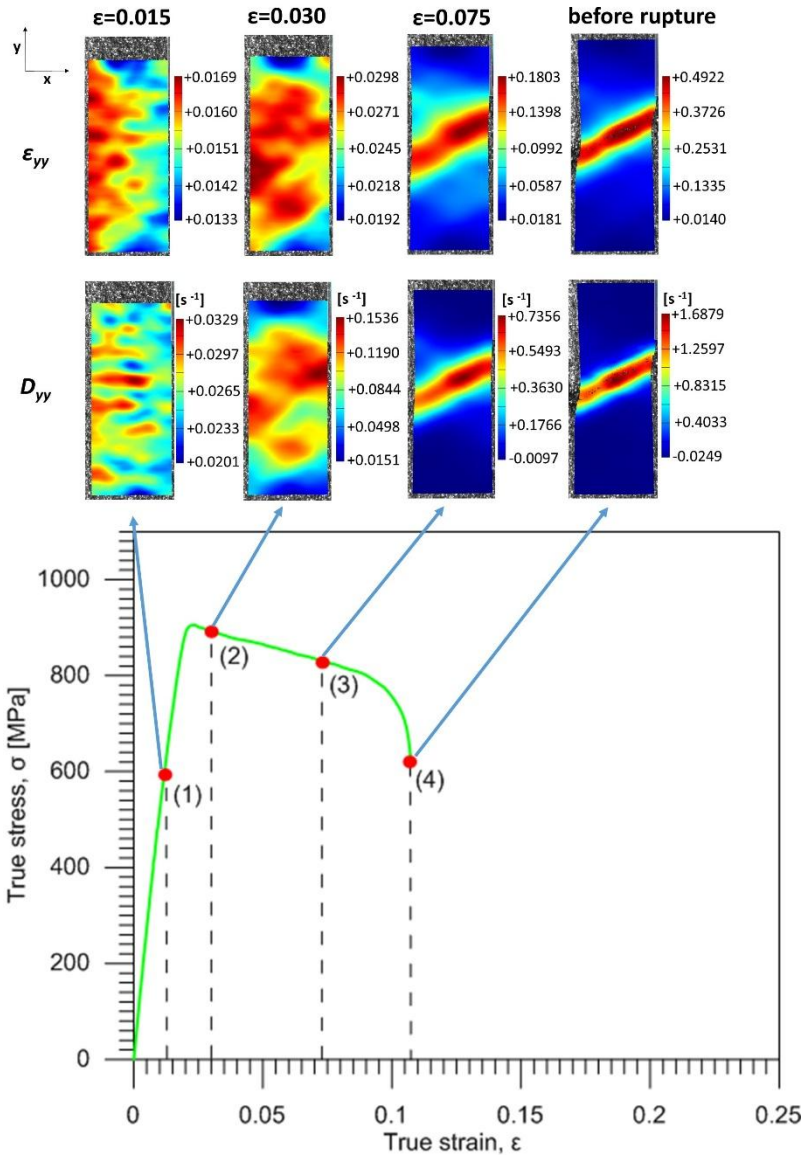

Fig. 4.12. Hencky strain ε_{yy} and rate of deformation tensor D_{yy} components distributions of Gum Metal under tension at strain rate of 10^{-1} s^{-1} at four stages of loading.

Development of ε_{yy} distributions obtained using the DIC algorithm for Gum Metal tension at five strain rates are shown in Fig. 4.13. In addition, profiles passing through a point with maximal value of ε_{yy} and parralel to the loading direction *y* are shown on the right of distributions captured at ε=0.075 and before rupture of the Gum Metal specimens.

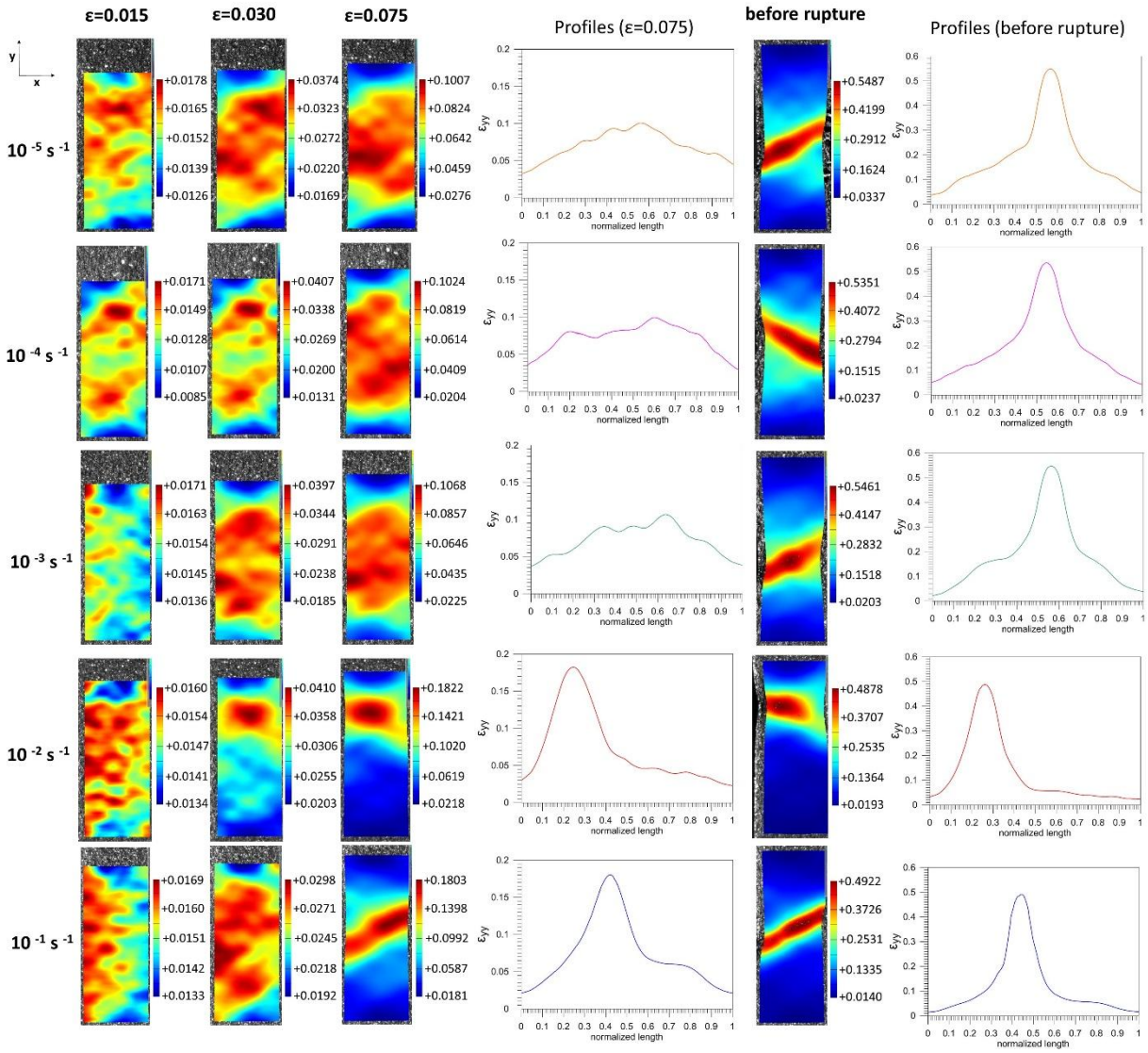

Fig. 4.13 Development of Hencky strain ε_{yy} distributions of Gum Metal subjected to tension until rupture at strain rates $10^{-5}s^{-1}$, $10^{-4}s^{-1}$, $10^{-3}s^{-1}$, $10^{-2}s^{-1}$ and $10^{-1}s^{-1}$ and strain profiles along the sample obtained at ε=0.075 and immediately before rupture.

Hencky strain ε_{yy} distributions were approximately the same at strains ε=0.015 and ε=0.030 for all of the applied strain rates (as presented in Fig. 4.13 the scale bar has a short range). At strain ε=0.075 the strain localization was already visible for the higher strain rates $10^{-1}s^{-1}$ and $10^{-2}s^{-1}$ in contrast to that obtained for the lower strain rates of $10^{-3}s^{-1}$, $10^{-4}s^{-1}$ and $10^{-5}s^{-1}$. Immediately before the rupture of the Gum Metal specimen the strain localization was clearly defined for all strain rates, and was accompanied by maximum local strains of approximately 0.5 as shown in the strain distributions and corresponding profiles for all strain rates.

In order to analyze strain distributions more comprehensively, points from the localization zones with maximal values of ε_{yy} (just before rupture) were selected and their time evolutions at various strain rates were analyzed. In Figs.: 4.14 (a-e), the time dependencies of the points with maximal strain value before the rupture for strain rates: $10^{-5}s^{-1}$, $10^{-4}s^{-1}$, $10^{-3}s^{-1}$, $10^{-2}s^{-1}$ and $10^{-1}s^{-1}$ are presented. The profiles shown appear to become smoother with a decreasing strain rate.

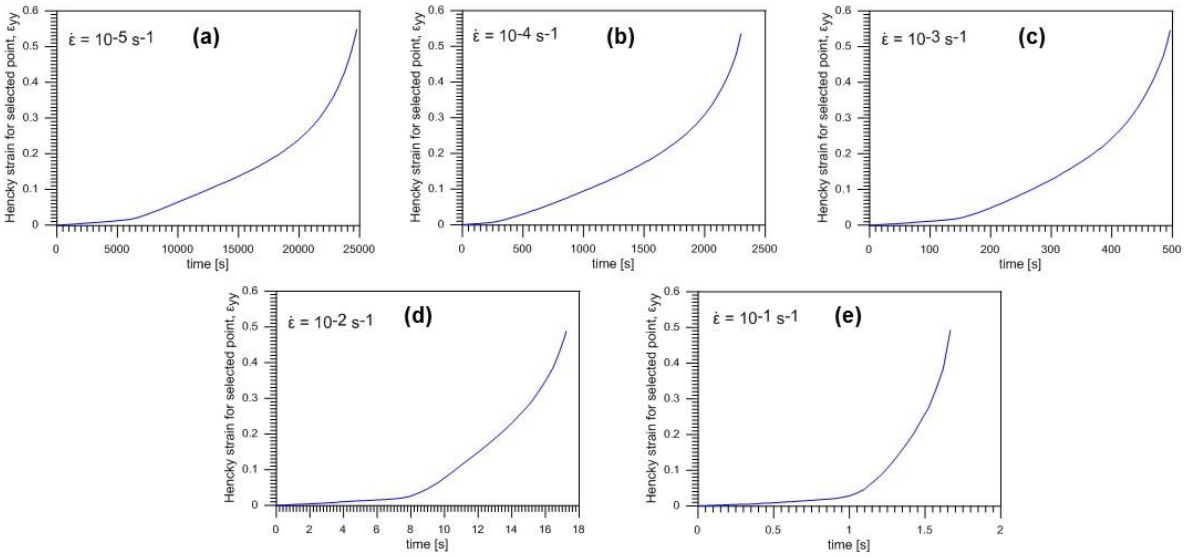

Fig. 4.14 Hencky strain ε_{yy} vs. time curves for selected points of Gum Metal under tension at strain rates of (a) $10^{-5}\,s^{-1}$; (b) $10^{-4}\,s^{-1}$, (c) $10^{-3}\,s^{-1}$, (d) $10^{-2}\,s^{-1}$ and (e) $10^{-1}\,s^{-1}$.

Because of an obvious fact that the processes of Gum Metal tension at different strain rates have various durations, it is difficult to contrast results from Figs. 4.14 (a-e). Thus, it is relevant to plot histories of Hencky strain ε_{yy} vs. displacement curves of selected points with maximal value of Hencky strain ε_{yy} just before rupture for Gum Metal for five strain rates, which are compared in Fig. 4.15.

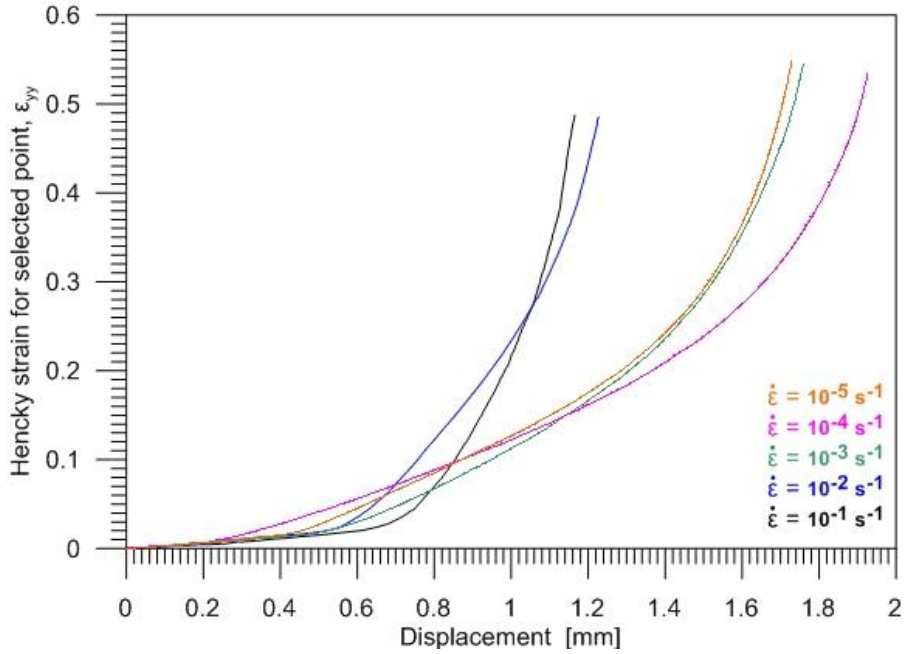

Fig. 4.15 Hencky strain ε_{yy} vs. crosshead displacement curves for selected points of Gum Metal under tension at five strain rates: $10^{-5}s^{-1}$, $10^{-4}s^{-1}$, $10^{-3}s^{-1}$, $10^{-2}s^{-1}$ and $10^{-1}s^{-1}$.

The records of Hencky strain ε_{yy} vs. displacement show a tendency to grow faster with an increasing strain rate.

Deformation rate tensor distributions in y direction D_{yy} obtained using the DIC algorithm for Gum Metal tension at five strain rates are presented in Fig. 4.16. In addition, profiles passing through a point with maximum value of strain and parralel to the loading direction y are shown on the right of distributions captured at ε=0.075 and before rupture of the Gum Metal specimen.

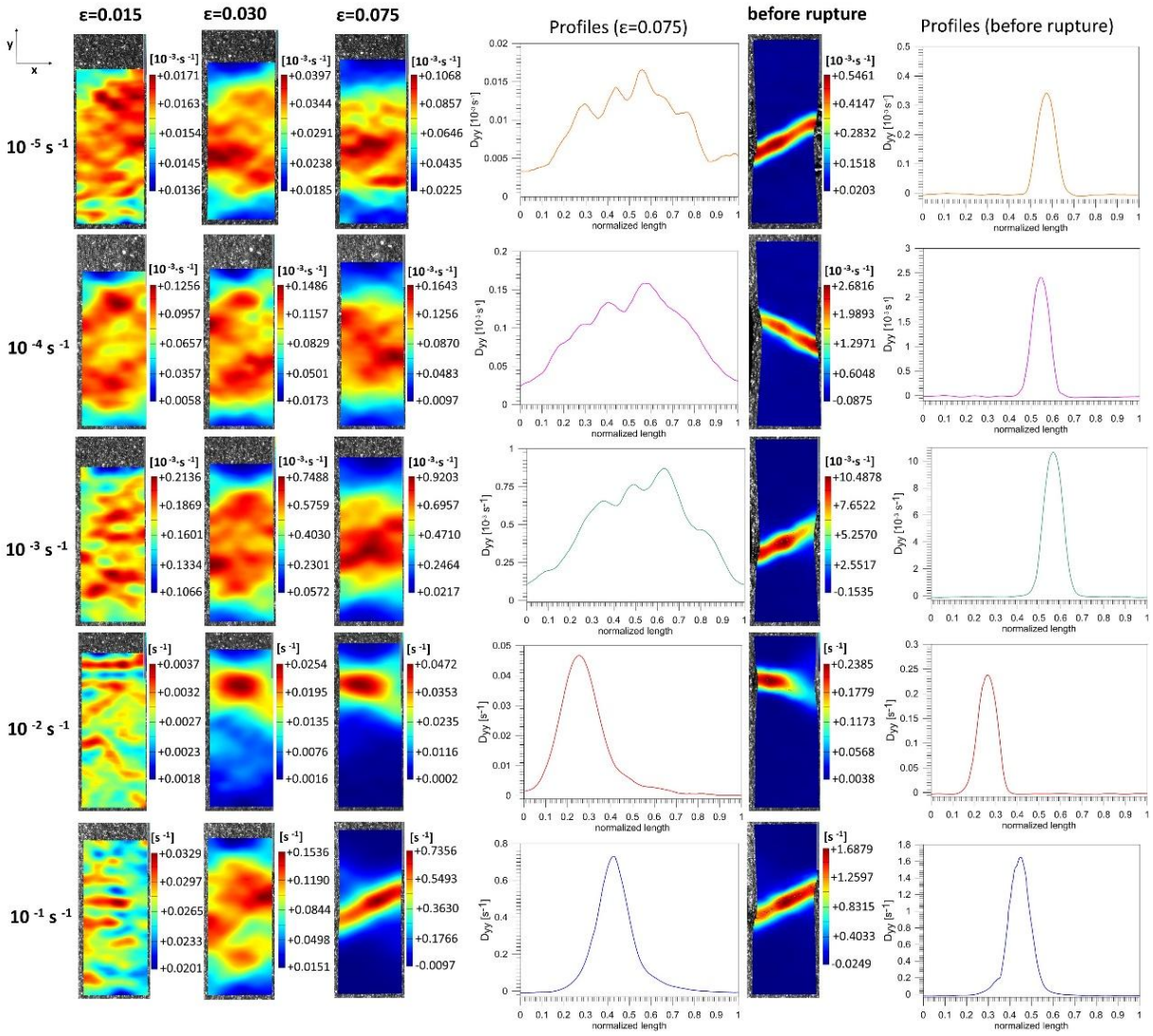

Fig. 4.16 Development of deformation rate tensor D_{yy} distributions of Gum Metal subjected to tension until rupture at strain rates $10^{-5}s^{-1}$, $10^{-4}s^{-1}$, $10^{-3}s^{-1}$, $10^{-2}s^{-1}$ and $10^{-1}s^{-1}$ and deformation rate tensor profiles along the specimen (at ε=0.075 and immediately before rupture).

Similarly to the Hencky strain H_{yy} distributions, the deformation rate tensor D_{yy} distributions were approximately the same at strains ε=0.015 and ε=0.030 for all strain rates (as presented in Fig. 4.16 the scale bar has a short range). At strain ε=0.075 the deformation rate tensor D_{yy} was localized for higher strain rates $10^{-1}s^{-1}$ and $10^{-2}s^{-1}$ in contrast to the deformation rate tensor D_{yy} distributions for lower strain rates $10^{-3}s^{-1}$, $10^{-4}s^{-1}$ and $10^{-5}s^{-1}$. Immediatley before rupture of the Gum Metal sample, the deformation rate tensor D_{yy} distributions were clearly localized in a shear band at all strain rates. Maximum values of local deformation rate tensor D_{yy} values were two orders higher when compared to average strain rate values, as shown in the profiles for all strain rates.

Full-field analysis of Gum Metal tension at various strain rates confirmed its inhomogeneity. Thus, deformation rate tensor D_{yy} vs. time curves presenting histories of selected points with maximal value of deformation rate tensor D_{yy} just before rupture for Gum Metal under tension at five strain rates, shown in Figs. 4.17 (a-e), are worth analyzing. The presented profiles tend to become smoother with a decreasing strain rate.

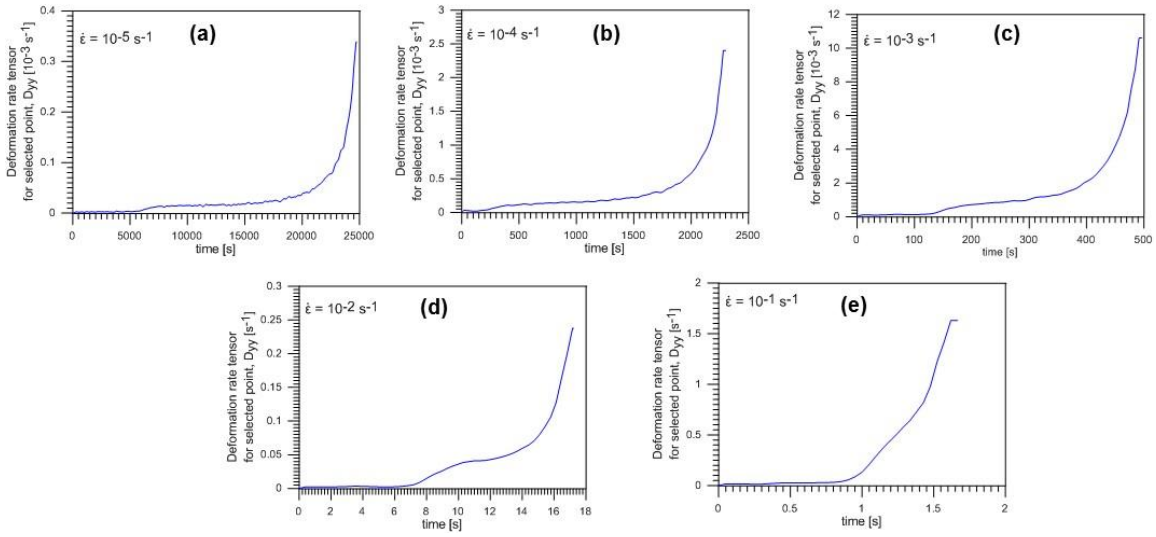

Fig. 4.17 Deformation rate tensor D_{yy} vs. time curves for selected points of Gum Metal under tension at strain rates of (a) 10^{-5} s^{-1}; (b) 10^{-4} s^{-1}, (c) 10^{-3} s^{-1}, (d) 10^{-2} s^{-1} and (e) 10^{-1} s^{-1}.

Because of an obvious fact that the processes of Gum Metal tension at different strain rate have various durations, it is difficult to contrast results from Figs. 4.17 (a-e). Thus, it is relevant to plot histories of deformation rate tensor D_{yy} vs. displacement of selected points with maximal value of deformation rate tensor D_{yy} just before rupture for Gum Metal for five strain rates, which are compared in Fig. 4.18.

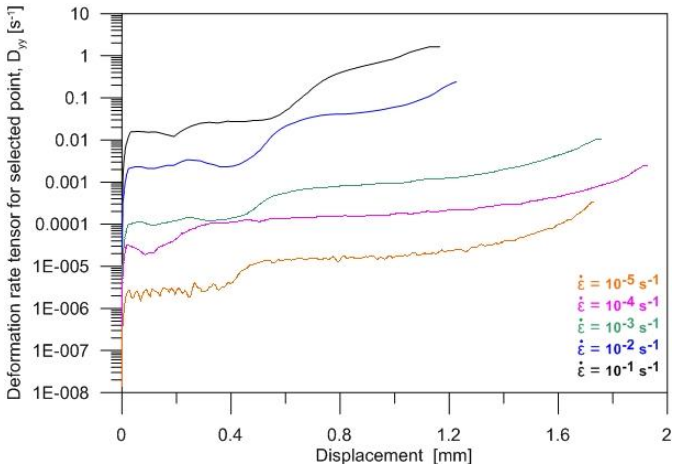

Fig. 4.18 Deformation rate tensor D_{yy} vs. displacement curves for selected points of Gum Metal under tension at five strain rates: 10^{-5} s^{-1}; 10^{-4} s^{-1}, 10^{-3} s^{-1}, 10^{-2} s^{-1} and 10^{-1} s^{-1}.

Deformation rate tensor D_{yy} values grow fast in the initial stage of deformation at low displacements for five strain rates. The maximal values of deformation rate tensor D_{yy} are two orders higher in comparison to average strain rate applied during tension. Maximal Hencky strain ε_{yy} and deformation rate D_{yy} values for each strain rate are shown in Table 4.3.

Table 4.3 Maximum Hencky strain and deformation rate values for each strain rate.

Strain rate [s^{-1}]	**Maximum Hencky strain** ε_{yy}	**Maximum deformation rate tensor D_{yy} [s^{-1}]**
10^{-5}	0.5487	0.5461×10^{-3}
10^{-4}	0.5351	2.6816×10^{-3}
10^{-3}	0.5461	10.4878×10^{-3}
10^{-2}	0.4878	0.2385
10^{-1}	0.4922	1.6879

4.3.4. Analysis of Gum Metal fracture features

Imaging of the fracture surfaces of Gum Metal after the mechanical tests, was performed on JEOL's JSM-6480 scanning electron microscope. The study was conducted at an accelerating voltage of 20 kV in selected material areas. SEM images of the fracture surfaces (fractographs) obtained after tensile tests of Gum Metal at five strain rates $10^{-5}\ s^{-1}$; $10^{-4}\ s^{-1}$, $10^{-3}\ s^{-1}$, $10^{-2}\ s^{-1}$ and $10^{-1}\ s^{-1}$ are shown in Fig. 4.19 (a-e), respectively.

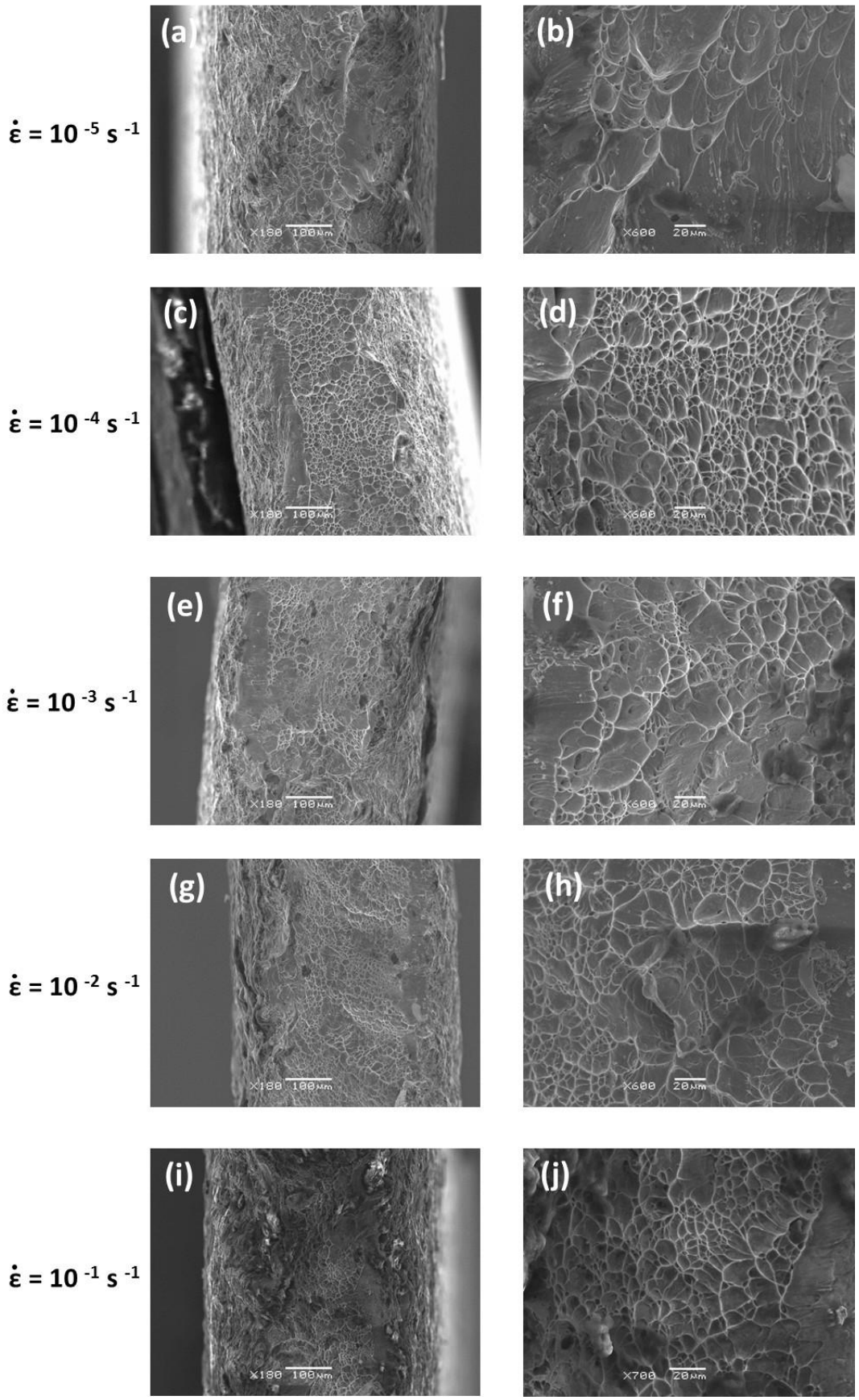

Fig. 4.19. Low and high magnifications of SEM fractographs of Gum Metal subjected to tension at strain rates of (a, b) $10^{-5}\ s^{-1}$; (c, d) $10^{-4}\ s^{-1}$, (e, f) $10^{-3}\ s^{-1}$, (g, h) $10^{-2}\ s^{-1}$ and (i, j) $10^{-1}\ s^{-1}$.

The fractographs exhibited mainly ductile features. As shown in stress vs. strain curves obtained experimentally, the specimens underwent a significant amount of elongation before rupture occurred. Many equiaxed dimples distributed equably are seen for the fracture surface of Gum Metal after monotonic tension at strain rates 10^{-3} s^{-1}, 10^{-2} s^{-1} and 10^{-1} s^{-1} in Fig. 4.19(e-j). The features for fractographs after tension at strain rates 10^{-5} s^{-1} and 10^{-4} s^{-1} seem to appear a little larger and deeper (Fig. 4.19(a-d)).

4.4. Analysis of mechanical and thermal characteristics of Gum Metal under monotonic and cyclic tension

4.4.1. Experimental details

A photograph of the experimental setup applied for investigation of thermomechanical couplings in Gum Metal during tension are presented in Fig. 4.20. The setup consists of an MTS 858 testing machine and two cameras working in two different spectral ranges, i.e., in the visible range (0.3–1 µm) a Manta G-125B camera and in the infrared range (3–5 µm) a ThermaCam Phoenix IR camera.

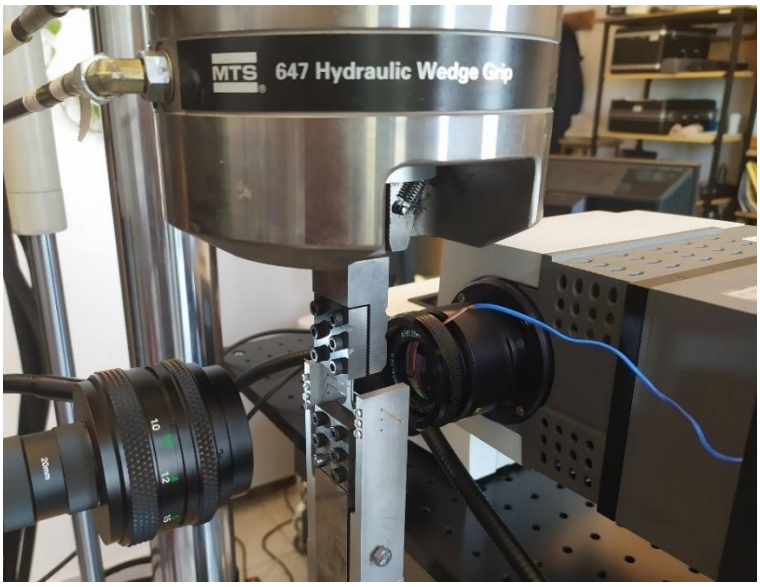

Fig. 4.20. A photograph of the experimental setup applied for investigation of thermomechanical couplings in Gum Metal using DIC and IRT.

A comparison of the main settings of both cameras used in the experiment is presented in Table 4.4. The cameras were placed on the opposite sides of the Gum Metal specimen. One side, observed using the visible range camera, was covered with a speckle pattern of paint

with micrometer-size metal particles in order to perform DIC analysis. The other side, observed by the IR camera, was covered by soot to increase and make uniform emissivity of the specimen surface.

Table 4.4. Settings of visible and infrared cameras used in the experiment.

Specifications	Manta G-125B	ThermaCam Phoenix
Resolution (pixel)	1100 × 410	320 × 150
Recording frequency (Hz) used for:		
10^{-2} s^{-1}	14.57	116.6
10^{-1} s^{-1}	58	583
Exposure/integration time (ms)	0.2	0.5
Pixel size (µm)	9.5	30

The tests were conducted with two different displacement rates 0.07 mm/s, and 0.7 mm/s for monotonic tension tests, which for the given geometry of the specimen corresponded to the mean strain rates 10^{-2} s^{-1} and 10^{-1} s^{-1}, respectively. The cyclic tension was realized with a displacement rate 0.07 mm/s corresponding to the strain rate of 10^{-2} s^{-1}. In each subsequent cycle, the total displacement range was increased by the displacement step 0.05 mm. During the deformation process, the loading force as a function of time and two image sequences in the visible and infrared ranges were recorded. The displacement and strain distributions were obtained from the visible range image sequence using a digital image correlation algorithm implemented in ThermoCorr software. The average strain values for the gauge length l_0 = 7 mm of the specimens were determined on the basis of DIC results using a virtual extensometer in the loading direction.

4.4.2. Analysis of the mechanically recoverable deformation of Gum Metal under cyclic tension

True stress vs. true strain curves plotted for Gum Metal subjected to cyclic tension up to rupture at the strain rate of 10^{-2} s^{-1} on the testing machine are presented in Fig. 4.21(a). The experiment consisted of 24 tension loading-unloading cycles. Stress vs. strain curves obtained for the cycles 1-7 are presented in Fig. 4.21(b). It was found that the mechanically reversible deformation was present up to cycle 5. The recoverable strain was equal to 0.014. Low Young's modulus (under 60 GPa) as well as the nonlinear superelasic-like deformation were confirmed.

High strength of Gum Metal (over 900 GPa) was observed for cycles 7-24, in which the specimen was apparently deformed in plastic regime. Maximal recoverable strain of Gum Metal was observed in cycle 5 for strain of 0.014.

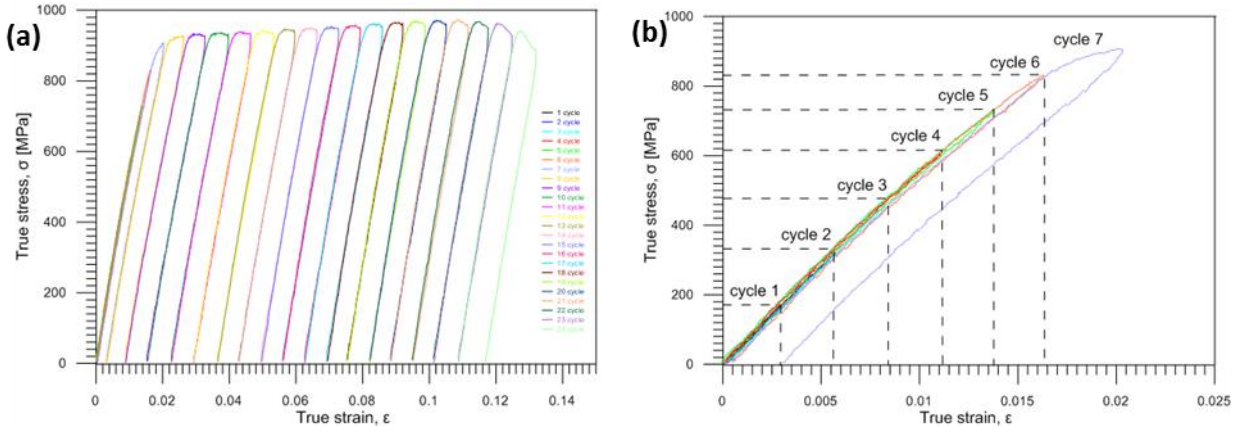

Fig. 4.21. Stress σ vs. strain ε curves for Gum Metal under cyclic tension at strain rate of 10^{-2} s^{-1} with a displacement step 0.05 mm: (a) cycles 1-24; (b) cycles 1-7 [Pieczyska E.A. et al. 2018a].

Since the Gum Metal is characterized by the nonlinear superelasic-like deformation it reveals an interesting feature of showing so-called tuneable Young's modulus. The moduli for reversible parts of loading and unloading stages dividing them into three stress ranges: 0–300MPa, 300–600MPa and >600MPa were calculated for cycles 1-9, according to a procedure schematically shown in Fig. 4.22.

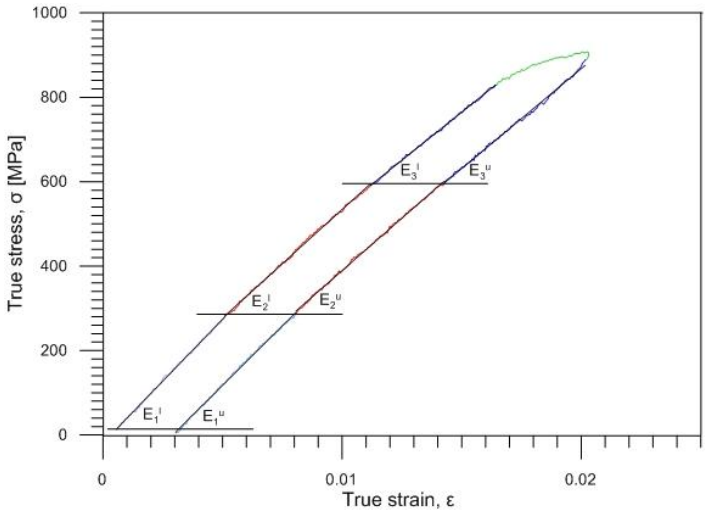

Fig. 4.22. Scheme illustrating the calculation procedure applied to find incremental moduli [Kowalczyk-Gajewska K. et al. 2019].

The obtained results of incremental moduli are listed in Table 4.5.

Table 4.5. Incremental moduli of Gum Metal in three stress ranges for loading-unloading cycles 1-9.

Cycle	E_1^l [GPa]	E_1^u[GPa]	E_2^l[GPa]	E_2^u[GPa]	E_3^l[GPa]	E_3^u[GPa]
1	57.92	57.97	-	-	-	-
2	57.73	57.77	-	-	-	-
3	58.83	57.94	54.07	54.50	-	-
4	58.67	58.17	50.80	52.06	-	-
5	58.02	57.86	51.56	51.16	44.18	47.51
6	58.86	57.85	51.85	51.19	43.27	46.96
7	58.60	56.41	51.36	49.91	45.54	47.22
8	57.30	55.47	51.07	48.52	45.32	48.19
9	56.84	55.12	49.48	48.90	45.82	48.95

The highest incremental modulus between 55-58 GPa is at the first stress range (0–300 MPa). In the second stress range (300–600 MPa), the incremental modulus is between 48-52 GPa. The lowest incremental modulus between 45-48 GPa is in the third stress range (> 600 MPa).

4.4.3. Investigation of thermomechanical couplings in Gum Metal under monotonic tension at two strain rates

This section concerns analysis of the effects of thermomechanical couplings monitored in the initial stage of Gum Metal loading. A thermomechanical investigation of the elastic-plastic transition and recoverable strain is presented. The results were determined and discussed for strain rates 10^{-2} s^{-1} and 10^{-1} s^{-1}, since these tests were conducted close to adiabatic conditions (corresponding to the test durations 17.45 s and 1.67 s, respectively). The stress σ and average temperature changes ΔT vs. strain ε for the initial stage of tension at strain rates of 10^{-2} s^{-1} and 10^{-1} s^{-1} are shown in Figs. 4.23(a) and 4.23(b), respectively. In the same figures, strain distributions in the direction of tension ε_{yy} obtained by the DIC algorithm and temperature distributions obtained by IRT are presented. The thermogram marked by 0 denotes the temperature distribution before the specimen loading. The marked points A*-A, B*-B, and C*-C denote the stress and temperature values corresponding to the Gum Metal's elastic limit

(maximal drop in temperature), the limit of the mechanically reversible deformation, and the start of almost linear, significantly higher increase in temperature, respectively (Fig. 4.23).

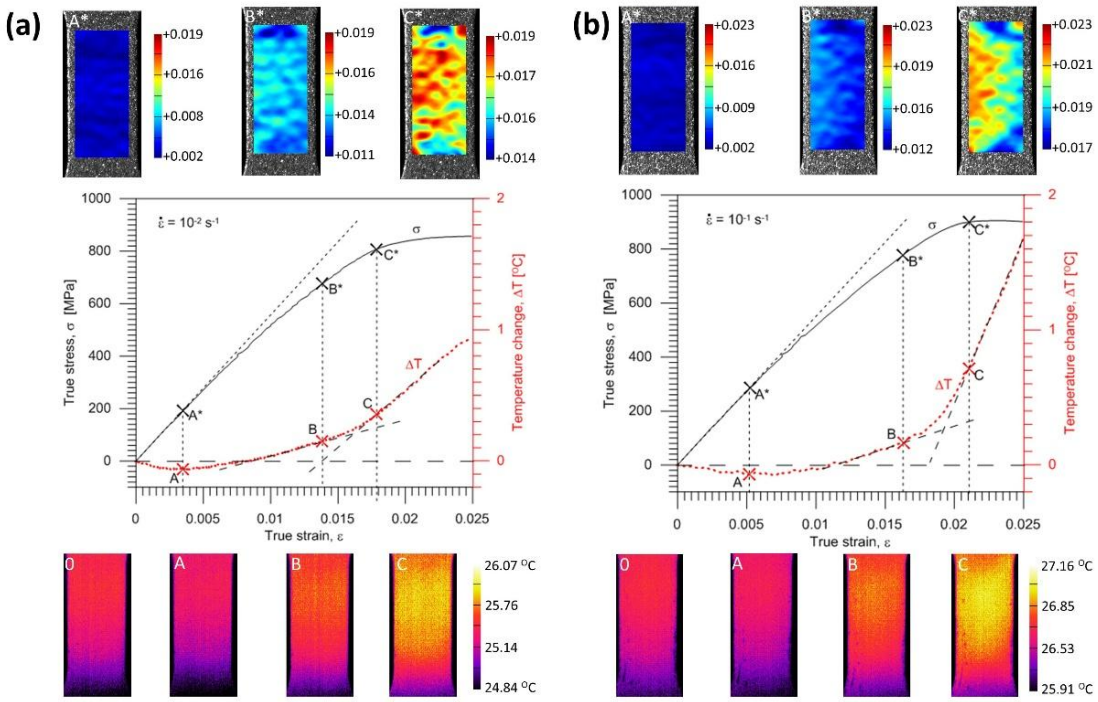

Fig. 4.23. Stress σ and average temperature change ΔT vs. strain ε curves for Gum Metal under tension in the initial deformation range at strain rates of (a) 10^{-2} s^{-1} and (b) 10^{-1} s^{-1} with Hencky strain ε_{yy} distributions (above; A*-C*) and thermograms (below; 0, A-C).

The thermal response in the initial loading range reaches its minimal value (points A-A*) significantly before the end of the nonlinear reversible deformation of Gum Metal (points B-B*) as shown in Fig. 4.23(a). Recoverable strain was determined in the incremental cyclic tension at 10^{-2} s^{-1} and is presented in Fig. 4.21(b). Similar results were found at the higher strain rate of 10^{-1} s^{-1} as depicted in Fig. 4.23(b). A comparison of the estimated values of characteristic deformation stages 0-A-B-C depicted in Fig. 4.23(a, b) is presented in Table 4.6.

Table 4.6. Comparison of estimated values of characteristic deformation stages.

Strain Rate [s^{-1}]	Maximal Drop in Temperature [°C]	Strain at Minimal Temperature	Stress at Minimal Temperature [MPa]	Temperature at Reversible Deformation [°C]	Strain at Reversible Deformation	Stress at Reversible Deformation [MPa]
10^{-2}	−0.062	0.0035	192	+0.15	0.0138	674
10^{-1}	−0.071	0.0052	285	+0.22	0.0163	780

For the strain rate 10^{-2} s^{-1}, the strain value related to the maximal drop in temperature equals 0.0035 (the related stress is 192 MPa), whereas the limit of reversible strain is equal to 0.0138. For the higher strain rate 10^{-1} s^{-1}, the strain value related to the maximal drop in temperature is 0.0052 (the related stress is 285 MPa), whereas the limit of reversible strain is equal to 0.0163.

A significant variation in the mean temperature change ΔT vs. strain ε characteristics observed in the range of the mechanically reversible deformation includes an important message about the Gum Metal deformation process from a thermodynamic point of view. At the strain rates of 10^{-2} s^{-1} and 10^{-1} s^{-1}, the maximal drops in temperature (points A) occur at true strain values of approximately 0.0035 and 0.0052, whereas the mechanically reversible strain limits (points B) at the strain values of approximately 0.0138 and 0.0163, respectively. The following increase in the specimen's temperature, which starts from point A, reveals the initiation of the dissipative character of the deformation process. **The dissipation observed between points A and B is caused by the exothermal-stress-induced phase transition of α'' nanodomains phase reported in the literature [Miyazaki S. 2017].** Furthermore, such a small increase in the temperature obtained in this range can be a sign that the phase transition takes place in a very small volume of the alloy, which is consistent with microstructural analyses [Miyazaki S. 2017]. At larger strains, a significant increase in temperature starts from point C. It means that plastic deformation becomes a dominant process at this stage, whereas the stage B-C is the transient period where both the phase transitions and plastic deformation in some areas of the specimen can take place simultaneously. From point B, the deformation process is irreversible from both the thermodynamic and mechanical points of view. According to the field data, the temperature distributions obtained for loading points 0, A, B, and C are quite uniform for both considered strain rates whereas the strain fields demonstrate some non-uniformities, especially at the stage related to point C*, where plastic deformation is evident. The strain and temperature distributions shown in Figs. 4.24 and 4.25, respectively, represent more advanced stages of the deformation process in comparison to those depicted in Figs. 4.23 (a, b). A comparison of the results of the coupled thermomechanical fields obtained using DIC and IRT for investigation of nucleation and development of the strain localization, leading to the Gum Metal specimen's necking and damage was analyzed. The stress and temperature change vs. strain curves obtained for the strain rates of 10^{-2} s^{-1} and

10^{-1} s^{-1} are depicted in Figs. 4.24 and 4.25, respectively. In the same figures, the strain and temperature distributions are shown at the values of the average strain equal to 0.04 (D*-D), 0.06 (E*-E), 0.08 (F*-F), 0.10 (G*-G), and just before the specimen's rupture (H*-H); 0.13 for the strain rate of 10^{-2} s^{-1} and 0.108 for the strain rate of 10^{-1} s^{-1}.

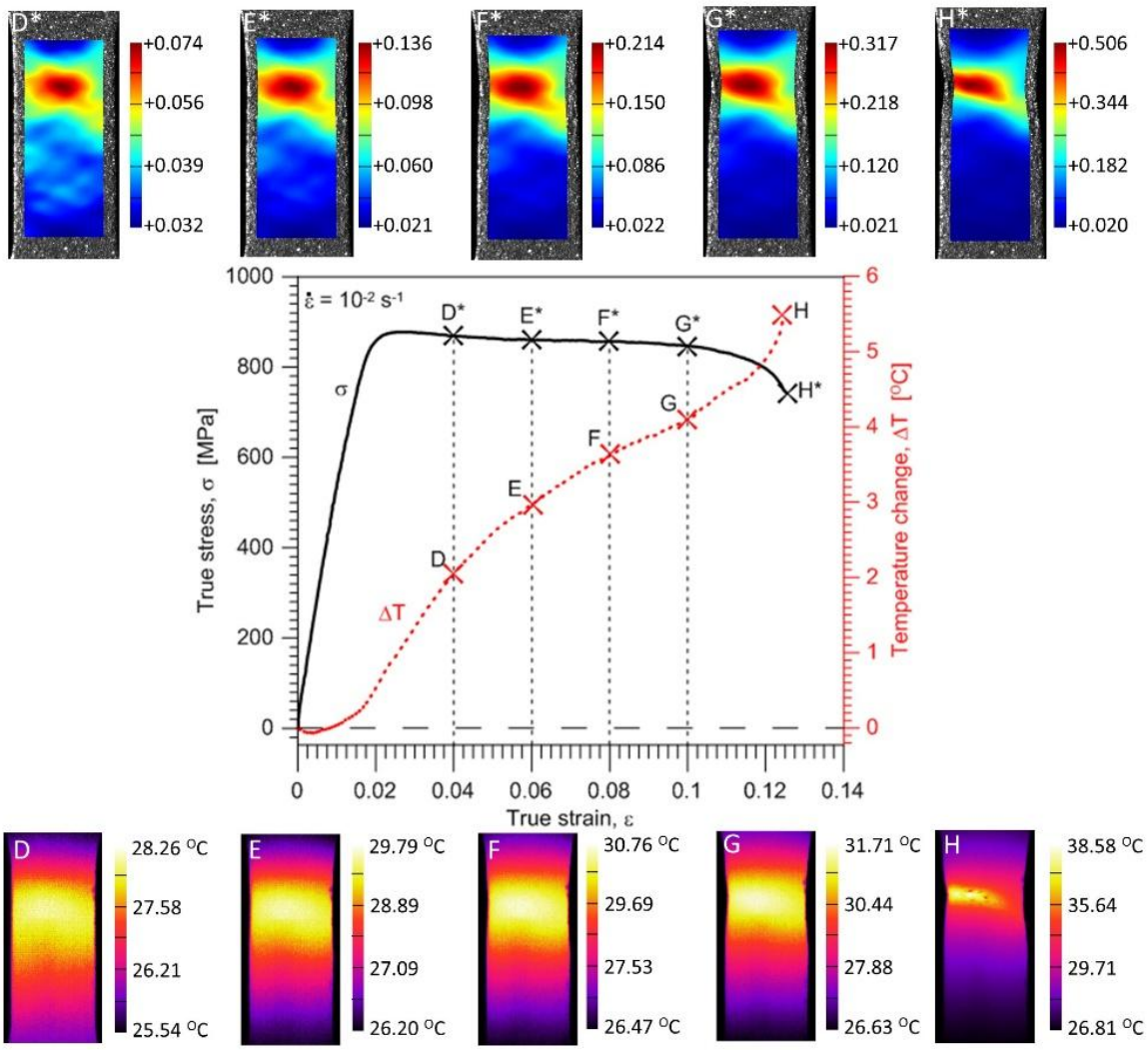

Fig. 4.24. Stress σ and average temperature change ΔT vs. strain ε curves completed by related Hencky strain ε_{yy} (above) and IR temperature (below) distributions for Gum Metal under tension at the strain rate of 10^{-2} s^{-1}.

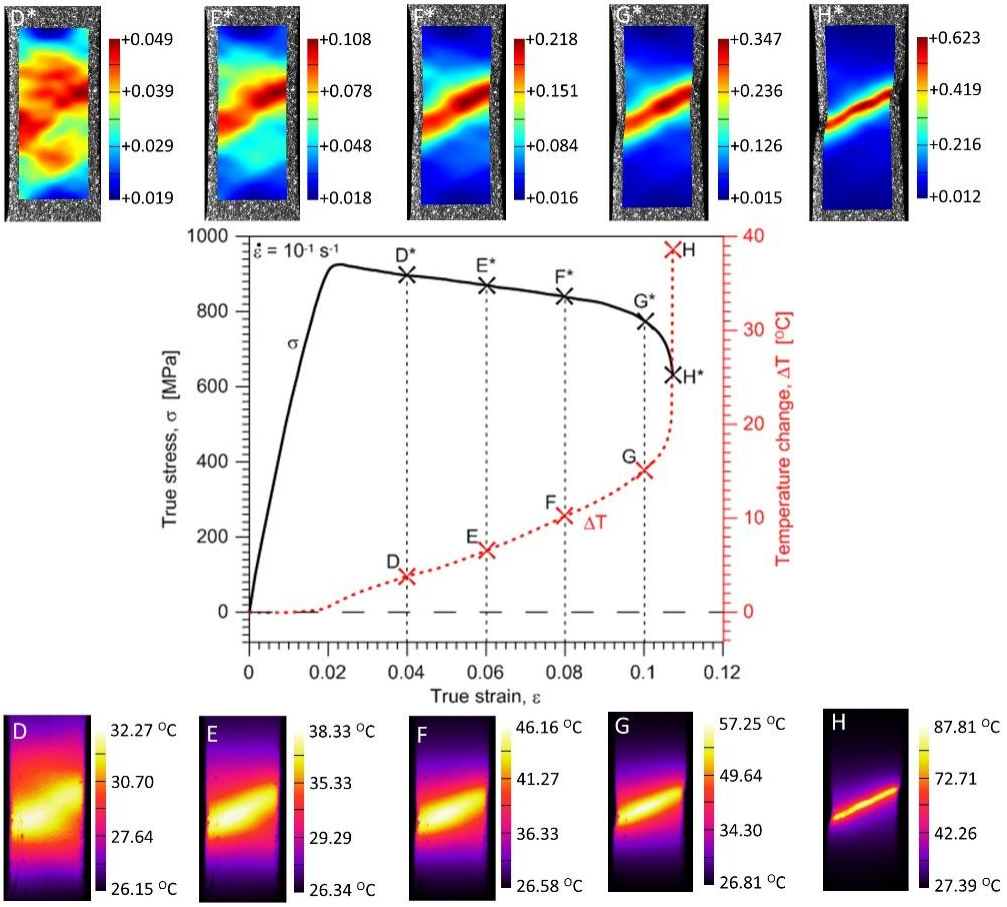

Fig. 4.25. Stress σ and average temperature change ΔT vs. strain ε curves completed by related Hencky strain ε_{yy} determined by DIC (above) and IR temperature (below) distributions for Gum Metal under tension at the strain rate of 10^{-1} s^{-1}.

The maximal average temperature change related to the specimen's rupture at the strain rate of 10^{-2} s^{-1} equals 5 °C, whereas that obtained at the strain rate of 10^{-1} s^{-1} equals 38 °C.

As shown in Figs. 4.24 and 4.25, the strain localization starts at point C* and proceeds from point D* up to the specimen's rupture. In the case of the strain rate 10^{-2} s^{-1}, the deformation is localized in the bigger area in comparison to the strain rate 10^{-1} s^{-1} (F*, G*, H*). As could be expected, the temperature distributions obtained for the strain rate of 10^{-1} s^{-1} presented in Fig. 4.25 are much more distinct, since the test was conducted closer to adiabatic conditions. The changes of stress and related temperature are larger and the mean strain range to rupture is shorter at the higher strain rates. Nevertheless, the maximal strain value calculated by the DIC algorithm in the strain localization area for the strain rate of 10^{-1} s^{-1} (0.623) is higher than that observed for the strain rate of 10^{-2} s^{-1} (0.506).

4.4.4. Analysis of thermomechanical couplings in Gum Metal under cyclic tension

Stress σ and average temperature change ΔT vs. strain ε curves for tensile cycles 1-24 of Gum Metal with strain rate 10^{-2} s^{-1} are shown in Fig. 4.26. Stress σ vs. strain ε curves for these cycles, presented in Fig. 4.23(a), were already used for analysis of mechanically recoverable deformation of Gum Metal.

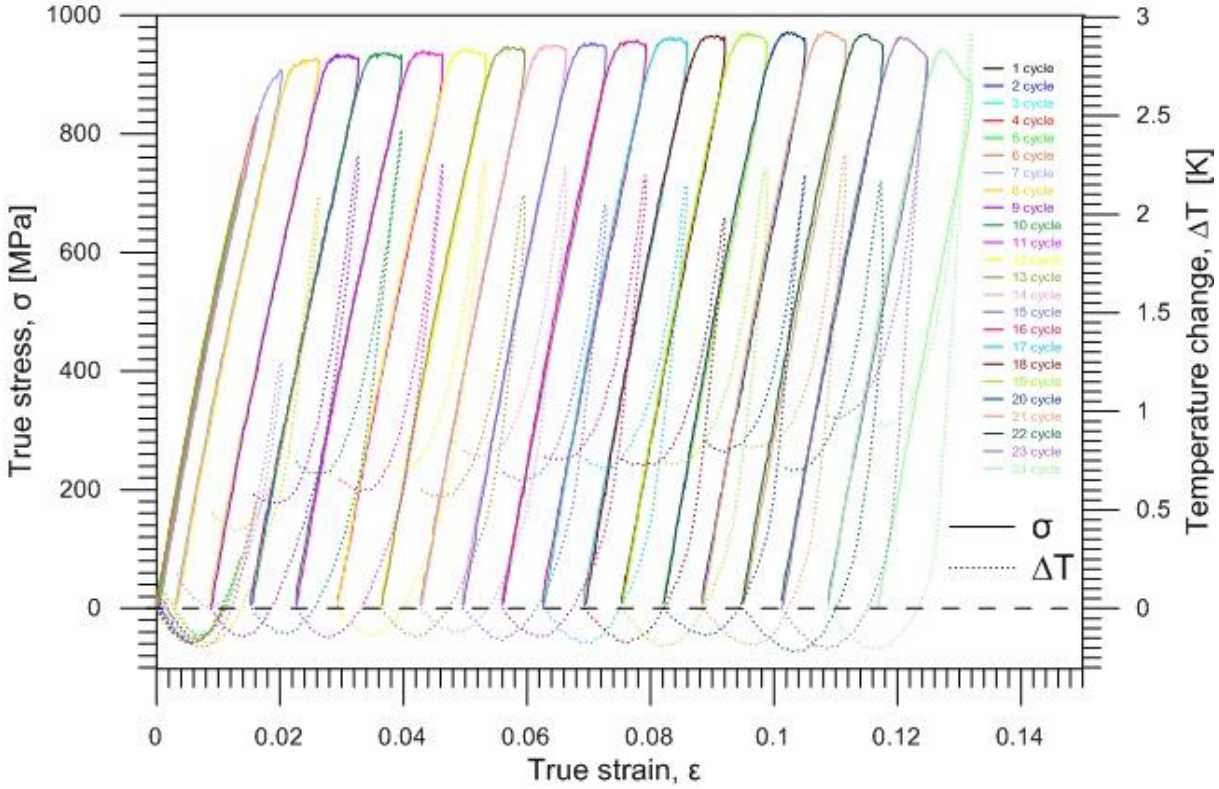

Fig. 4.26. Stress σ and average temperature change ΔT vs. strain ε curves for tensile cycles 1-24 of Gum Metal with strain rate 10^{-2} s^{-1}.

From this point on, the results will be analyzed in each of the subsequent loading-unloading cycles of Gum Metal tension in order to better understanding of the temperature change related to the deformation of Gum Metal. Stress σ and average temperature change ΔT vs. strain ε curves for cycles 1 - 3 of Gum Metal under tension at the strain rate 10^{-2} s^{-1} are shown in Figs. 4.27 (a – c). On the one hand, the true stress vs. true strain plots in the loading-unloading process overlap for cycles 1 – 3. It means that the strain is totally recoverable from the mechanical perspective for these cycles. On the other hand, the temperature change vs. true strain decreases during the loading stage in cycles 1 - 2. However, during loading in cycle 3 at strain of around 0.006 one can observe a slight increase of temperature which signalizes

dissipation. Similar observations can be made in true strain, true stress and temperature change vs. time curves shown in Fig. 4.28 (a-c).

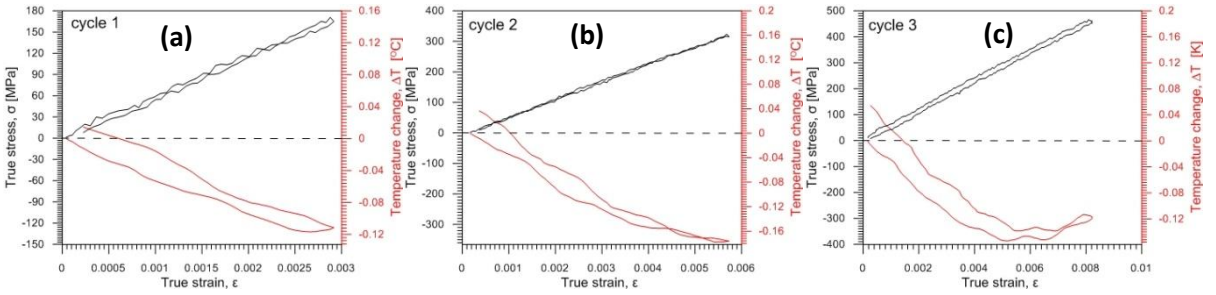

Fig. 4.27. Stress σ and average temperature change ΔT vs. strain ε curves for tensile cycles of Gum Metal: (a) cycle 1, (b) cycle 2 and (c) cycle 3.

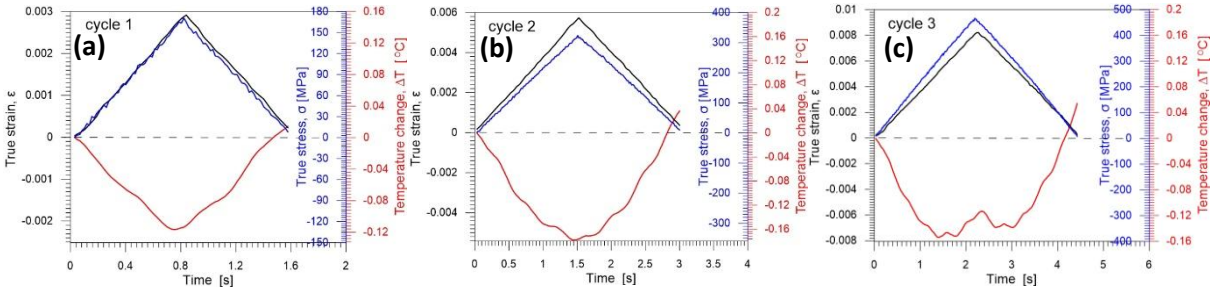

Fig. 4.28. Stress σ, strain ε and average temperature change ΔT vs. time curves for tensile cycles of Gum Metal: (a) cycle 1, (b) cycle 2 and (c) cycle 3.

In subsequent cycles 4 and 5, the true stress vs. true strain plots in the loading-unloading process still overlap so the strain is recoverable, as shown in Fig. 4.29 (a – b). It means that, the maximal recoverable strain of Gum Metal was observed in cycle 5 for strain of 0.014. True stress vs. true strain plot of cycle 6 has a residual plastic deformation after unloading (Fig. 4.29(c)). In cycles 4-6, the temperature change vs. true strain during loading firstly decreases and then slightly increases in the final phase of Gum Metal loading. Similar observations can be made in true strain, true stress and temperature change vs. time curves shown in Fig. 4.30 (a-c). The minimum value of temperature change, which is equal to -0.16 ^{o}C, can indicate the range of purely elastic deformation of Gum Metal. It corresponds to the strain value of 0.006.

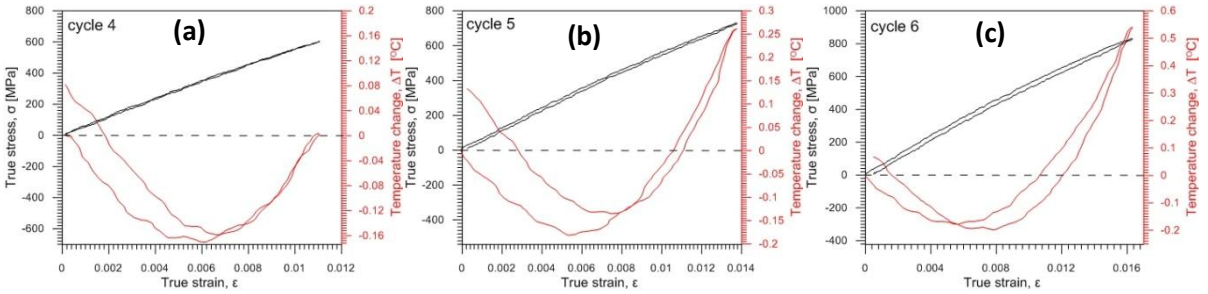

Fig. 4.29. Stress σ and average temperature change ΔT vs. strain ε curves for tensile cycles of Gum Metal: (a) cycle 4, (b) cycle 5 and (b) cycle 6.

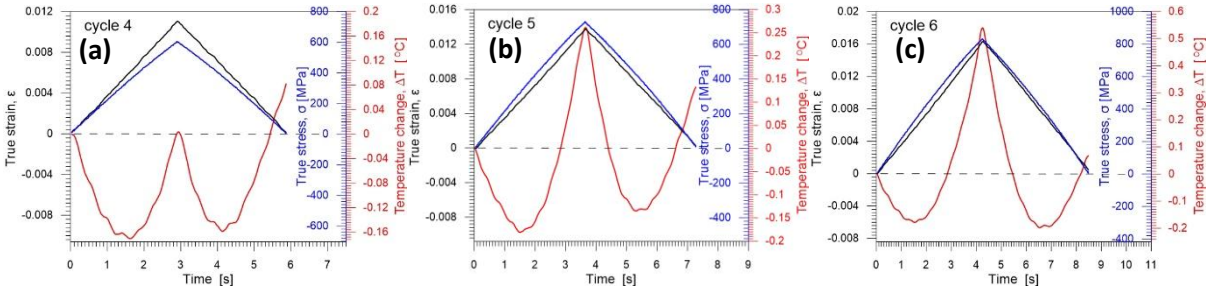

Fig. 4.30. Stress σ, strain ε and average temperature change ΔT vs. time curves for tensile cycles of Gum Metal: (a) cycle 4, (b) cycle 5 and (c) cycle 6.

True stress and temperature change vs. true strain curves for tensile cycles 7 - 9 of Gum Metal are shown in Figs. 4.31 (a – c). In cycles 8 and 9, on one hand true stress vs. true strain curves do not overlap and permanent plastic deformation can be observed. There is also a significant temperature growth in the final stage of loading which accompanies the plastic deformation of Gum Metal. Similar observations can be made analyzing true strain, true stress and temperature change vs. time curves shown in Fig. 4.32 (a – c).

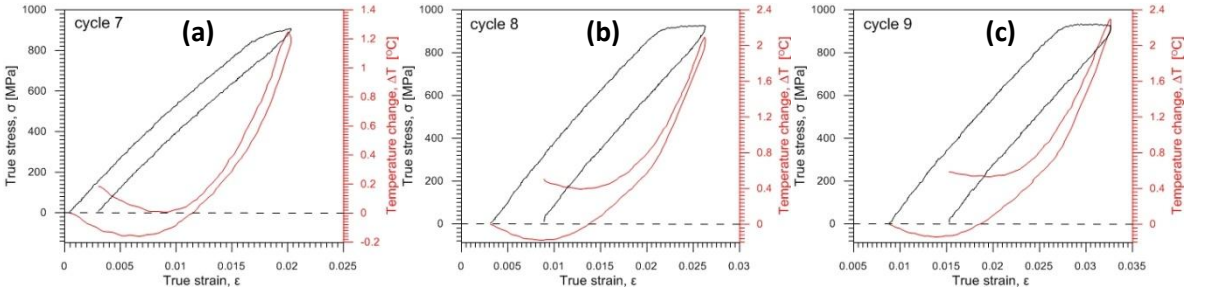

Fig. 4.31. Stress σ and average temperature change ΔT vs. strain ε curves for tensile cycles of Gum Metal: (a) cycle 7, (b) cycle 8 and (b) cycle 9.

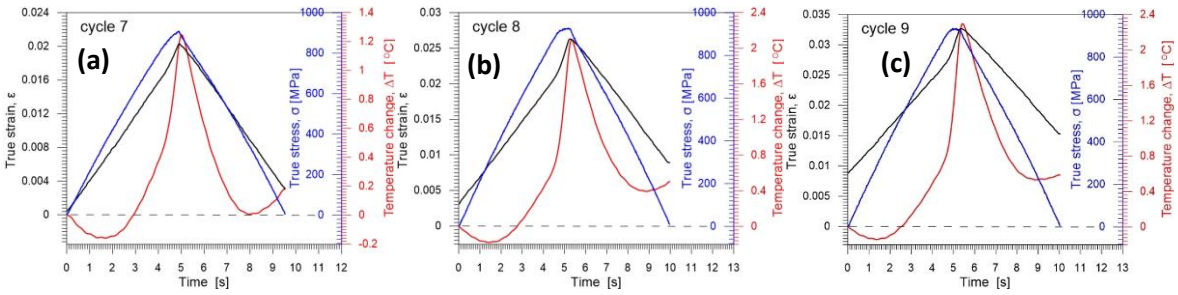

Fig. 4.32. Stress σ, strain ε and average temperature change ΔT vs. time curves for tensile cycles of Gum Metal: (a) cycle 7, (b) cycle 8 and (c) cycle 9.

True stress and temperature change vs. true strain curves for tensile cycles 10 - 24 of Gum Metal are shown in Figs. 4.33 (a – o), whereas true stress, true strain and temperature change vs. time for tensile cycles 10 - 24 of Gum Metal are presented in Figs. 4.34 (a-o).

In each cycle, the thermomechanical characteristics can be associated to following stages:

1) the initial linear, purely elastic deformation accompanied by the temperature drop;

2) nonlinear super-elastic deformation related to the temperature growth;

3) plastic regime with a significant growth of temperature;

4) unloading phase, consisting of superelastic-like and elastic regimes, accompanied by a drop of temperature with a slight increase of temperature in the final stage of unloading affected by heat exchange with surroundings.

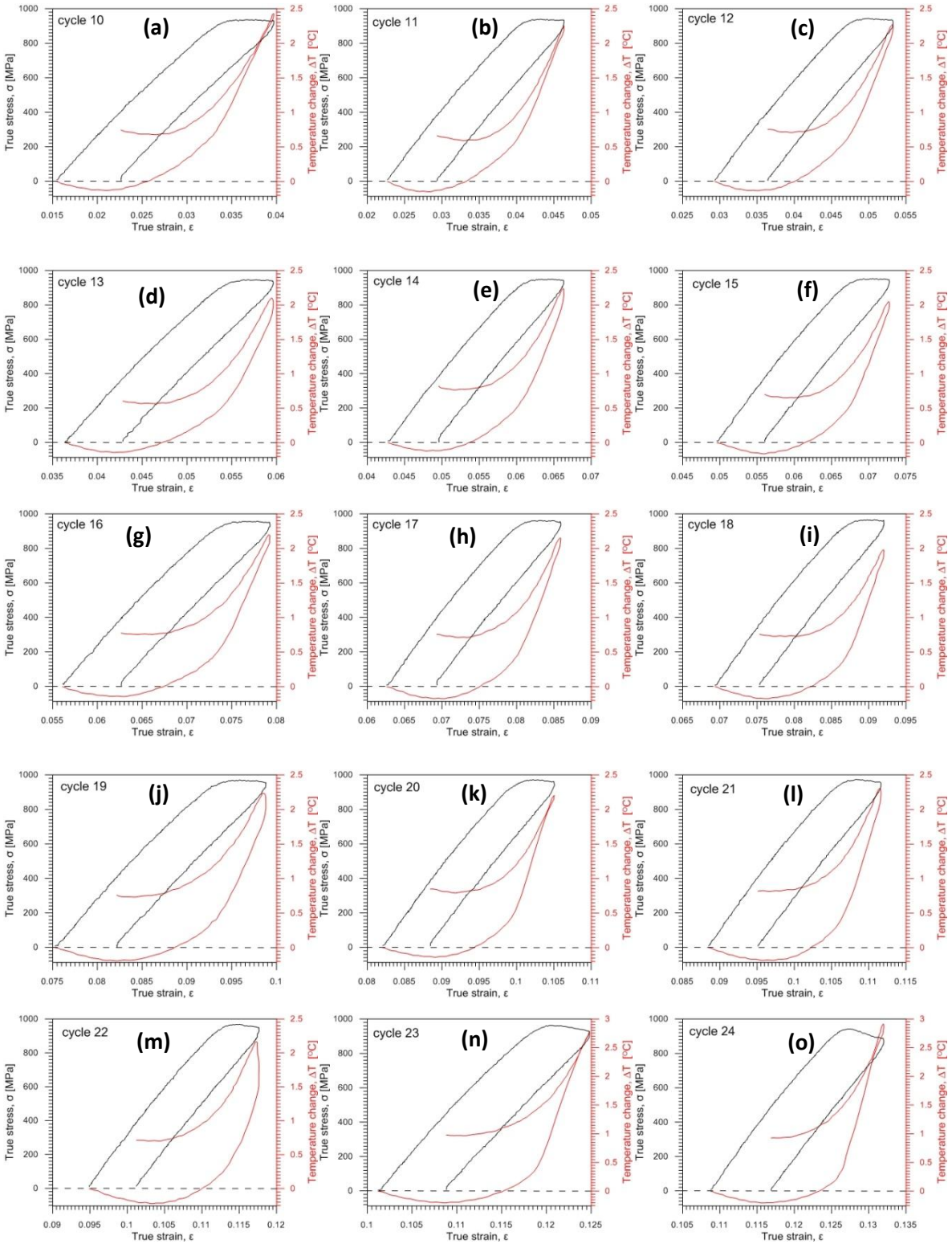

Fig. 4.33. Stress σ and average temperature change ΔT vs. strain ε curves for tensile cycles of Gum Metal with strain rate 10^{-2} s^{-1}: (a-o) cycles 10-24.

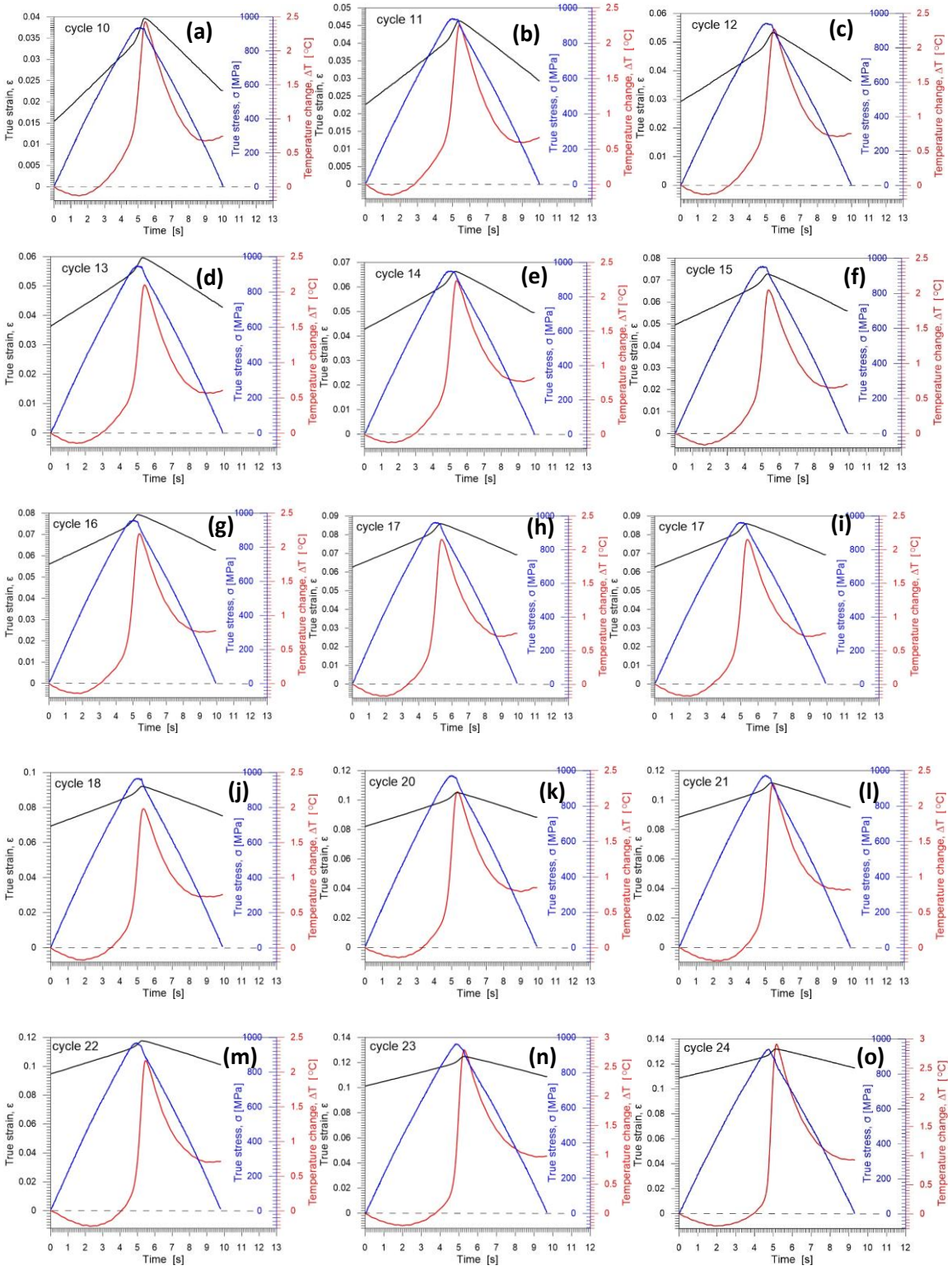

Fig. 4.34. Stress σ, strain ε and average temperature change ΔT vs. time curves for tensile cycles of Gum Metal with strain rate 10^{-2} s^{-1}: (a-o) cycles 10-24.

Based on the analysis of 24 cycles of Gum Metal tension, selected stages of the alloy deformation can be distinguished:

(0)-(A) elastic loading

(A)-(B) superelastic-like loading

(B)-(C) plastic loading

(C)-(D) superelastic-like unloading

(D)-(E) elastic unloading

The deformation stages of Gum Metal are indicated by arrows exemplary for cycle 12 in true stress σ vs. true strain ε curves separately during loading and unloading as presented in Figs. 4.35(a) and (b), respectively. The deformation stages of Gum Metal are corresponding to different thermal responses of the alloy, which are marked with red crosses in average temperature change ΔT vs. true strain ε curves.

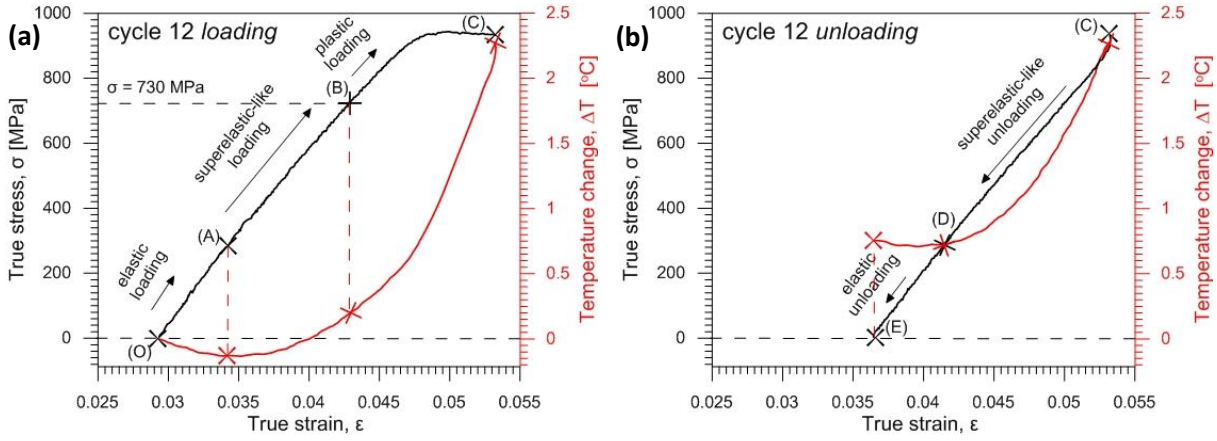

Fig. 4.35. The deformation stages of Gum Metal indicated in true stress σ and average temperature change ΔT vs. true strain ε curves for cycle 12 separately during (a) loading and (b) unloading.

Temperature change ΔT vs. time curve for cycle 12 presented in Fig. 4.36 shows critical values of temperature, which are as follows:

(0) beginning of the loading process;

(A) maximum temperature drop during loading (thermoelastic effect) (ΔT_{Lmin});

(B) temperature change at superelastic-like deformation limit (temperature change corresponding to stress σ = 730 MPa determined in cycle 5) (ΔT_{trans});

(C) maximum temperature growth (ΔT_{max});

(D) temperature drop during unloading (ΔT_{Umin});

(E) slight increase of temperature (end of the unloading process) (ΔT_{fin}).

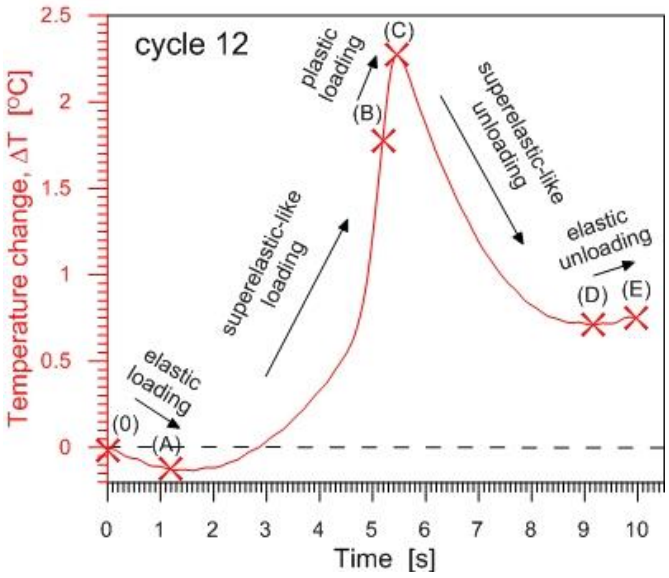

Fig. 4.36. Critical values of temperature change (0) – (E), marked exemplary in temperature change ΔT vs. time curve for cycle 12.

Critical values of temperature change corresponding to certain stages of Gum Metal deformation in each of loading-unloading tensile cycles 1 - 24 are listed in Table 4.7. They include maximum temperature drop during the loading (ΔT_{Lmin}), temperature change at mechanically recoverable deformation limit (temperature change corresponding to stress σ = 730 MPa, ΔT_{trans}), maximal temperature change (ΔT_{max}), temperature change during plastic

deformation (ΔT_{max} - ΔT_{trans}) and temperature drop accompanying the unloading process (ΔT_{Umin}) as well as final temperature change after unloading (ΔT_{fin}).

Table 4.7. Critical values of temperature obtained from stress and average temperature change vs. strain plots of Gum Metal under cyclic tension at strain rate 10^{-2} s^{-1}.

Cycle number	Critical values of temperature change ΔT [°C]					
	LOADING				UNLOADING	
	ΔT_{Lmin}	ΔT_{trans} ($\Delta T_{\sigma = 730MPa}$)	ΔT_{max}	ΔT_{max}- ΔT_{trans}	ΔT_{Umin}	ΔT_{fin}
1	-0,116	-	0,014	-	-	0,014
2	-0,178	-	0,033	-	-	0,036
3	-0,154	-	0,049	-	-0,146	0,054
4	-0,170	-	0,078	-	-0,039	0,082
5	-0,181	0,206	0,261	0,055	-0,134	0,133
6	-0,178	0,239	0,539	0,300	-0,197	0,068
7	-0,158	0,232	1,245	1,012	0,006	0,186
8	-0,179	0,303	2,093	1,789	0,394	0,505
9	-0,143	0,368	2,296	1,927	0,531	0,587
10	-0,129	0,269	2,427	2,158	0,676	0,745
11	-0,149	0,225	2,257	2,032	0,593	0,665
12	-0,132	0,203	2,272	2,069	0,709	0,754
13	-0,141	0,151	2,098	1,947	0,567	0,606
14	-0,119	0,166	2,234	2,067	0,767	0,822
15	-0,162	0,082	2,047	1,966	0,652	0,696
16	-0,142	0,108	2,196	2,087	0,756	0,775
17	-0,173	0,048	2,149	2,101	0,712	0,754
18	-0,174	0,006	1,981	1,974	0,728	0,760
19	-0,190	-0,018	2,232	2,250	0,732	0,761
20	-0,137	0,038	2,200	2,162	0,792	0,848
21	-0,184	-0,064	2,304	2,368	0,813	0,815
22	-0,220	-0,138	2,165	2,304	0,701	0,712
23	-0,203	-0,050	2,786	2,837	0,967	0,977
24	-0,205	-0,088	2,912	3,002	0,925	0,924

4.4.5 Analysis of thermoelastic effect in Gum Metal under selected loadings

In this section, thermoelastic effect in Gum Metal under selected loadings is analyzed by comparing values of maximal temperature drop obtained experimentally and theoretically.

The calculations of theoretical values of the temperature change $\Delta T_{CALCmin}$ were performed using Eq. 2.1 $\Delta T = -\frac{\alpha T \Delta \sigma_{ik}}{c_p \rho}$ and taking the Gum Metal parameters listed in Table 3.3.

The values of stress $\Delta\sigma_{ik}$ corresponding to the temperature drop during loading ΔT_{Lmin} for Gum Metal were derived from Figs. 4.23 in the case of monotonic tension. Table 4.8 presents values of $\Delta\sigma_{ik}$, ΔT_{Lmin} and $\Delta T_{CALCmin}$ for Gum Metal under monotonic tension tests at two strain rates 10^{-2} s^{-1} and 10^{-1} s^{-1}.

Table 4.8 Values of stress $\Delta\sigma_{ik}$ corresponding to temperature drop during loading ΔT_{Lmin} for Gum Metal under monotonic tension tests at two strain rates 10^{-2} s^{-1} and 10^{-1} s^{-1} derived from the results presented in Figs. 4.23 and the calculated theoretical values of the temperature drop $\Delta T_{CALCmin}$.

Strain rate [s^{-1}]	$\Delta\sigma_{ik}$ [MPa]	ΔT_{Lmin} [°C]	$\Delta T_{CALCmin}$ [°C]
10^{-2}	192	-0,062	-0,178
10^{-1}	285	-0,071	-0,265

The values of ΔT_{Lmin} (experimental) and $\Delta T_{CALCmin}$ (theoretical) for Gum Metal under monotonic tension tests at two strain rates 10^{-2} s^{-1} and 10^{-1} s^{-1} are contrasted in Fig. 4.37.

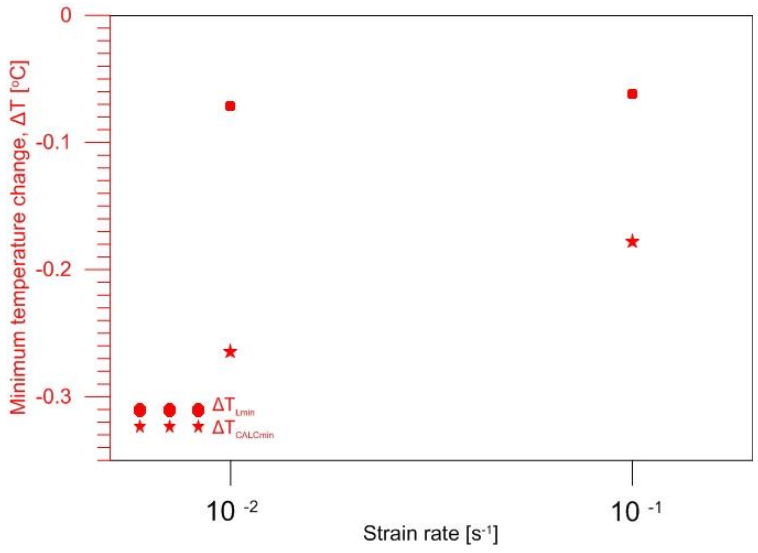

Fig. 4.37. Values of temperature change related to thermoelastic effect ΔT_{Lmin} (experimental) and $\Delta T_{CALCmin}$ (theoretical) for Gum Metal under monotonic tension tests at two strain rates 10^{-2} s^{-1} and 10^{-1} s^{-1}.

In the case of cyclic tension, the values of stress $\Delta\sigma_{ik}$ corresponding to the minimum temperature change during loading ΔT_{Lmin} for Gum Metal were derived from Fig. 4.24. Table 4.9 presents values of $\Delta\sigma_{ik}$, ΔT_{Lmin} and $\Delta T_{CALCmin}$ for each cycle of Gum Metal loading-unloading tension test at strain rate 10^{-2} s^{-1}.

Table 4.9 Values of stress $\Delta\sigma_{ik}$, minimum temperature change during loading ΔT_{Lmin} derived from the results presented in Fig. 4.26 and the calculated theoretical values of the temperature change $\Delta T_{CALCmin}$ for Gum Metal under cyclic tension.

Cycle number	$\Delta\sigma_{ik}$ [MPa]	ΔT_{Lmin} [°C]	$\Delta T_{CALCmin}$ [°C]
1	156	-0,117	-0,145
2	306	-0,178	-0,285
3	306	-0,154	-0,285
4	352	-0,170	-0,328
5	318	-0,181	-0,296
6	331	-0,178	-0,308
7	360	-0,159	-0,335
8	304	-0,179	-0,282
9	286	-0,144	-0,266
10	315	-0,129	-0,293
11	325	-0,149	-0,302
12	340	-0,132	-0,316
13	323	-0,141	-0,300
14	298	-0,119	-0,277
15	366	-0,162	-0,340
16	410	-0,143	-0,381
17	446	-0,173	-0,415
18	417	-0,174	-0,387
19	413	-0,191	-0,383
20	421	-0,137	-0,391
21	443	-0,185	-0,411
22	506	-0,221	-0,470
23	439	-0,204	-0,408
24	420	-0,205	-0,390

Values of temperature change related to thermoelastic effect ΔT_{Lmin} and $\Delta T_{CALCmin}$ for each cycle of Gum Metal loading-unloading cyclic tension test at strain rate 10^{-2} s^{-1} are compared in Fig. 4.38.

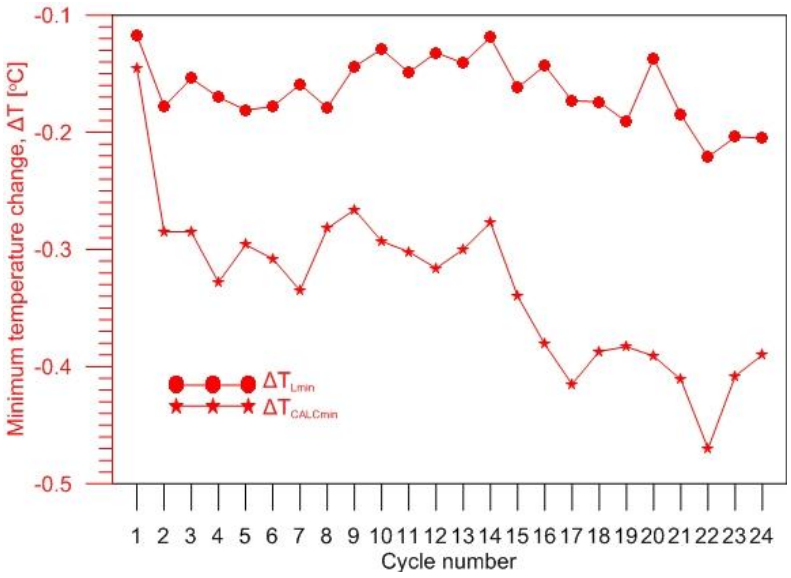

Fig. 4.38. Values of temperature change related to thermoelastic effect ΔT_{Lmin} (experimental) and $\Delta T_{CALCmin}$ (theoretical) for each cycle of Gum Metal loading-unloading cyclic tension test at strain rate 10^{-2} s^{-1}.

In the case of both monotonic and cyclic tension tests, the values of $\Delta T_{CALCmin}$ obtained theoretically are lower than the values of ΔT_{Lmin} derived experimentally, as presented in Figs. 4.37 and 4.38. However, this discrepancy is not big and can be connected with the lack of precise parameters of Gum Metal. The parameters used in the calculations which were taken from literature [Saito T. et al. 2003, presentation].

4.4.5. Estimation of energy balance in subsequent loading-unloading cycles of Gum Metal

Analysis of the energy behavior of solid materials by identification of different heat sources and forms of the energy balance associated with load–unload cycles is an important issue, as it was raised in Chapter 3. Certain behavior effects can be distinguished: irreversibility and rate dependence associated with thermoelasticity, strain localization and hardening/softening, solid–solid phase change in SMAs, and necking leading to damage and failure. Estimation of energy balance in materials with such effects based on load–unload stress and temperature change vs. strain curves can contribute to the understanding of deformation mechanisms in the material.

In the case of elastic-plastic solids, irrecoverable mechanical energy W_{ir} expended on plastic deformation can be determined based on load–unload stress vs. strain curve taking into account density of the deformed material, as shown in Fig. 4.39.

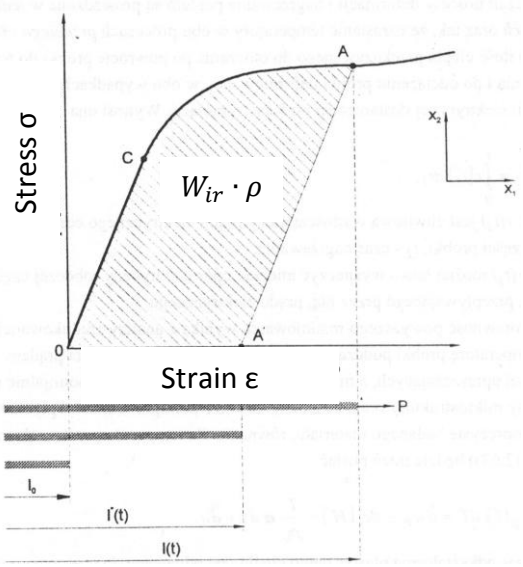

Fig. 4.39. Method for determination of irrecoverable mechanical energy W_{ir} expended on plastic deformation based on tensile load–unload stress vs. strain curve [Oliferuk W. 1997].

A part of W_{ir} which is converted into heat W_{dir} can be estimated by multiplying specific heat of the material c_p and change of temperature accompanying the deformation.

The stored energy $E_s = W_{ir} - W_{dir}$ is the remaining part, which is a part of energy related to defects of crystal lattice, mainly dislocation structures.

The stored energy E_s represents a change in internal energy of the deformed material and it is an essential measure of its cold-worked state. In the initial studies on this topic, a part of plastic work stored in metal was believed to be about 10 % of the entire plastic work [Taylor et al. 1934].

However, further experimental studies found that the ratio of the stored energy to the plastic work is not constant and depends on deformation level of the tested material.

Therefore, a concept of the energy storage rate as a measure of energy conversion at each instant of plastic deformation process was introduced. The energy storage rate Z is defined as the plastic work derivative of the stored energy and expressed by Eq. 4.3.

$$Z = \frac{dE_s}{dW_{ir}} \qquad \text{(Eq. 4.3)}$$

Analysis of the energy balance allows to get an insight into the nature of deformation mechanisms involved in the deformation process of a given material. Thus, this aspect is of particular interest in the case of Gum Metal.

Estimation of energy balance in Gum Metal during 24 subsequent loading-unloading cycles has been carried out based on analysis of true stress and temperature change vs. true strain curves. The parts of certain energies were calculated by determining particular areas in the true stress vs. true strain curves and subsequently dividing the obtained values by the density of Gum Metal (ρ=5.6 g/cm^3). As a result, values of energies per mass unit measured in J/g were obtained. An exemplary analysis of cycle 12 for estimation of energy balance is presented in Fig. 4.40.

The entire work needed to deform the alloy W_{ext} since the beginning of loading in point O until unloading in point A is equal to the area OAB. W_{ext} can be divided into two parts used for recoverable W_{rec} and irrecoverable W_{ir} deformation, as expressed by Eq. 4.4.

$$W_{ext} = W_{rec} + W_{ir} \qquad \text{(Eq. 4.4)}$$

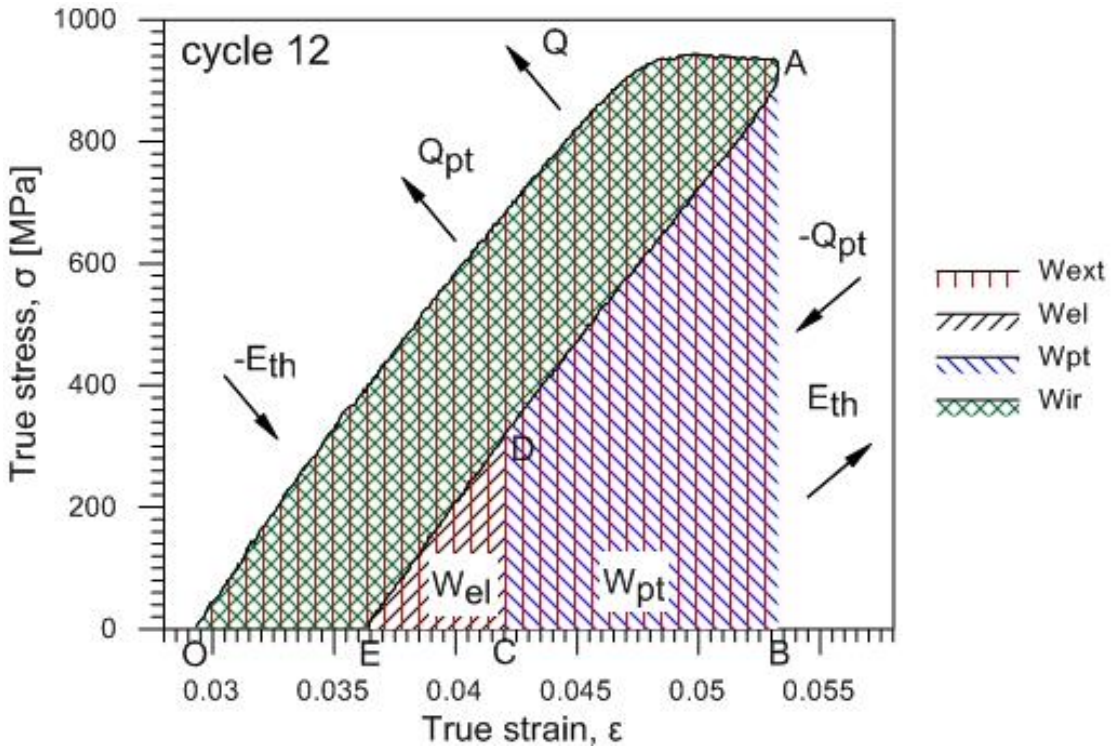

Fig. 4.40. Methodology for estimation of energy balance in Gum Metal during loading-unloading cycle based on true stress *σ* vs. true strain *ε* for cycle 12.

In the case of Gum Metal, the work used for recoverable deformation W_{rec} can be divided into the first part of work used for elastic deformation W_{el} and the second part of work used for superelastic-like and mechanically recoverable deformation caused by phase transformation of nanodomains W_{pt}, as expressed by Eq. 4.5.

$$W_{rec} = W_{el} + W_{pt} \quad \text{(Eq. 4.5)}$$

The purely elastic deformation of Gum Metal is accompanied by a temperature drop during loading and temperature increase during unloading due to thermoelastic effect. The mechanically recoverable deformation caused by phase transformation of nanodomains is exothermic during loading and recoverably endothermic during unloading. Thus, we can assume that the energy associated with thermoelastic effect E_{th} and the energy of the stress-induced activity of nanodomains Q_{pt} are balanced during each of the loading-unloading cycles.

The energy associated with thermoelastic effect E_{th} can be calculated using Eq. 4.6.

$$E_{th} = -\frac{\alpha T_0 \Delta\sigma_{ik}}{\rho} \quad \text{(Eq. 4.6)}$$

where

α is the coefficient of linear thermal expansion,

T_0 is the absolute temperature of the specimen,

$\Delta\sigma_{ik}$ is the stress tensor,

ρ is the density of the material.

The fraction of work used for irrecoverable deformation W_{ir} means the work used for plastic deformation. W_{ir} is equal to the heat dissipated W_{dir} and the energy stored in the alloy E_s in the process of deformation, as expressed by Eq. 4.7.

$$W_{ir} = W_{dir} + E_s \quad \text{(Eq. 4.7)}$$

The entire heat dissipated W_d in the process of deformation should include heat losses related to heat conductivity W_{ind} , convection W_{conv} and radiation W_{rad}, as given in Eq. 4.8.

$$W_d = Q + W_{ind} + W_{conv} + W_{rad} \quad \text{(Eq. 4.8)}$$

The strain rate 10^{-2} s^{-1} used during the cyclic tension of Gum Metal was quite high. So for simplicity we can assume that the conditions were close to adiabatic and the losses were negligible.

Therefore we obtain Eq. 4.9,

$$W_d = W_{dir} = Q = c_v \Delta T \quad \text{(Eq. 4.9)}$$

where

c_v is the specific heat of Gum Metal at constant volume;

ΔT is the temperature change determined in the process of plastic deformation.

For simplicity, there is an assumption that the recoverable deformation of Gum Metal under cyclic tension occurs up to the same level of stress (730 MPa) for each loading-unloading cycle. However, one should remember that certain microstructural changes induced to the alloy in the process of cyclic tension may affect this critical stress value.

Following the assumption we obtain (Eq. 4.10),

$$\Delta T = \Delta T max - \Delta T(730MPa), \quad \text{(Eq. 4.10)}$$

where

$\Delta T(730MPa)$ is the temperature change corresponding to the stress level at which the fully recoverable deformation of Gum Metal ends, as found in cycle 5.

It means that the entire work needed to deform the alloy W_{ext} is given by Eq. 4.11.

$$W_{ext} = E_s + Q + W_{el} + W_{pt} \quad \text{(Eq. 4.11)}$$

As a consequence, the stored energy is expressed by Eq. 4.12.

$$E_s = W_{ext} - Q - W_{el} - W_{pt} \quad \text{(Eq. 4.12)}$$

The parameters taken for estimation of energy balance in each loading-unloading cycle are given in table 3.3 (Chapter 3).

The values of energies estimated via the energy balance and the ratio $Z = \frac{E_s}{W_{ir}}$ for each loading-unloading cycle are listed in table 4.10.

Table 4.10 Estimation of certain energies of Gum Metal in subsequent loading-unloading cycles.

Values of certain energies of Gum Metal [J/g]								
Cycle number	W_{ext}	W_{el}	W_{pt}	W_{ir}	E_{th}	Q	E_s	Z [%]
1	0.045	0.045	0	0	-0.509	0	0	-
2	0.164	0.164	0	0	-0.997	0	0	-
3	0.359	0.146	0.213	0	-0.997	0	0	-
4	0.628	0.2	0.428	0	-1.147	0	0	-
5	0.964	0.161	0.803	0	-1.036	0	0	-
6	1.314	0.187	1.046	0.080	-1.076	0.232	0	-
7	1.858	0.217	1.217	0.423	-1.172	0.455	0	-
8	2.364	0.158	1.282	0.923	-0.988	0.801	0.121	13.1
9	2.476	0.158	1.282	1.035	-0.931	0.867	0.168	16.2
10	2.591	0.171	1.269	1.150	-1.026	0.971	0.178	15.5
11	2.516	0.175	1.217	1.123	-1.058	0.911	0.211	18.8
12	2.560	0.167	1.216	1.176	-1.105	0.931	0.245	20.8
13	2.464	0.169	1.226	1.067	-1.050	0.873	0.193	18.1
14	2.514	0.169	1.226	1.117	-0.969	0.930	0.187	16.7
15	2.485	0.219	1.248	1.017	-1.192	0.884	0.133	13.1
16	2.510	0.271	1.139	1.100	-1.334	0.939	0.161	14.6
17	2.539	0.205	1.208	1.125	-1.451	0.945	0.179	15.9
18	2.442	0.221	1.189	1.032	-1.355	0.888	0.143	13.9
19	2.582	0.233	1.178	1.169	-1.343	1.012	0.156	13.4
20	2.512	0.280	1.141	1.091	-1.368	0.972	0.118	10.8
21	2.553	0.316	1.076	1.160	-1.441	1.065	0.094	8.1
22	2.485	0.400	0.980	1.105	-1.645	1.036	0.068	6.2
23	2.583	0.325	0.983	1.275	-1.428	1.276	0	-
24	2.519	0.296	0.875	1.348	-1.366	1.351	0	-

The values of entire work needed to deform the Gum Metal W_{ext} calculated by determining particular areas in the true stress vs. true strain curves for each cycles of tensile loading are shown in Fig. 4.41.

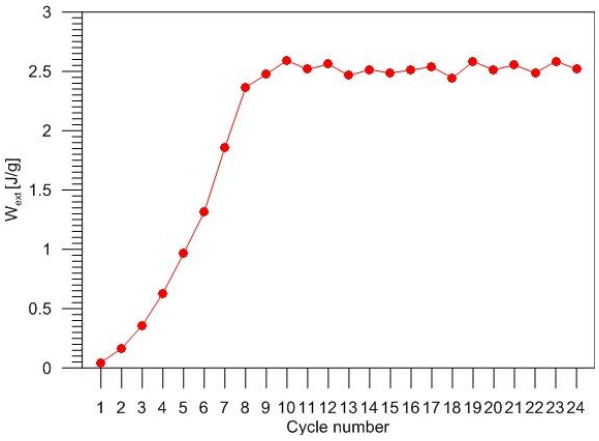

Fig. 4.41. The values of entire work needed to deform the Gum Metal W_{ext} calculated for each cycle of tensile loading calculated by determining particular areas in the true stress vs. true strain curves.

As presented in Fig. 4.41, in the early tensile cycles 1-8 of Gum Metal loading-unloading process W_{ext} rises until reaching a value around 2.5 J/g and is pretty constant for the advanced cycles 9-24. It confirms similar mechanical behavior of the alloy in subsequent cycles.

The values of part of work used for elastic deformation of Gum Metal W_{el} calculated by determining particular areas in the true stress vs. true strain curves for each cycle of tensile loading are shown in Fig. 4.42.

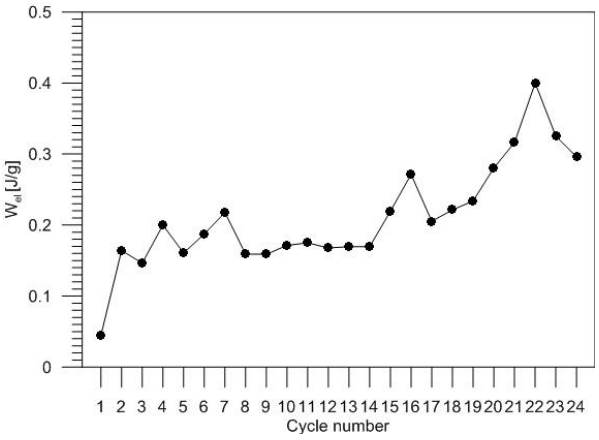

Fig. 4.42 The values of part of work used for elastic deformation of Gum Metal W_{el} calculated by determining particular areas in the true stress vs. true strain curves for each cycle of tensile loading.

W_{el} is low in the cycle 1 which does not reach the total pure elastic strain and oscillates in the range 0.14 – 0.4 in subsequent cycles 2-24. The discrepancy is affected by inertia of the testing

machine. The values of energy related to thermoelastic effect E_{th} of Gum Metal calculated for each cycle of tensile loading are shown in Fig. 4.43 using Eq. 4.6.

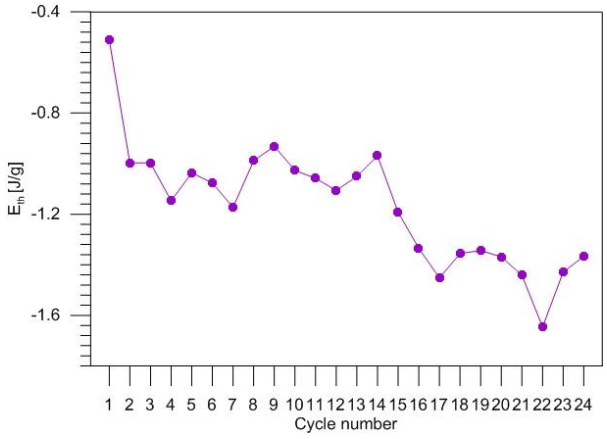

Fig. 4.43. A curve presenting the values of energy related to thermoelastic effect E_{th} of Gum Metal calculated for each cycle of tensile loading using Eq. 4.6.

E_{th} equals -0.5 J/g in cycle 1 and further on in cycles 2-24 it reaches the values which are in the range between -1 J/g and -1.6 J/g. The data reflect a slight hardening effect of the alloy in previous cycles. The values of part of work used for superelastic-like and mechanically recoverable deformation of Gum Metal caused by phase transformation of nanodomains W_{pt} calculated by determining particular areas in the true stress vs. true strain curves for each cycle of tensile loading are shown are Fig. 4.44.

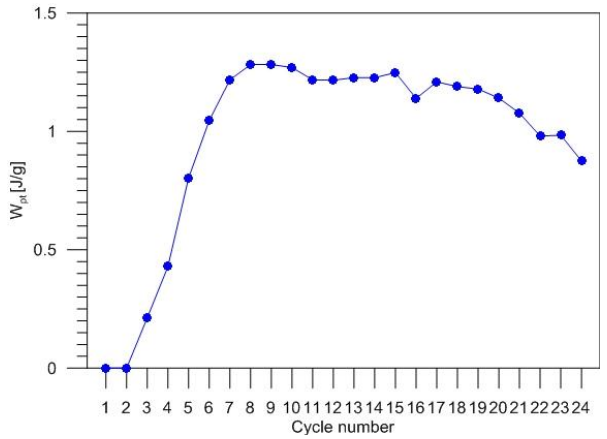

Fig. 4.44. The values of part of work used for superelastic-like and mechanically recoverable deformation of Gum Metal caused by phase transformation of nanodomains W_{pt} calculated for each cycle of tensile loading.

Superelastic-like deformation of Gum Metal starts in cycle 3. The energy W_{pt} rises in cycles 3-5 and in the next cycles 6-24 W_{pt} falls in the range between 0.9 J/g and 1.2 J/g. The plastic deformation of Gum Metal initiates in cycle 6. The values of part of work used for irrecoverable plastic deformation of Gum Metal W_{ir} calculated by determining particular areas in the true stress vs. true strain curves for each cycle of tensile loading are shown in Fig. 4.45, which confirm saturation stage of the exothermic transision.

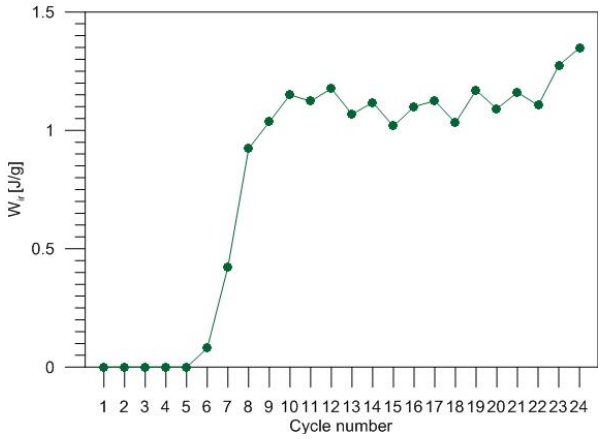

Fig. 4.45. The values of part of work used for irrecoverable plastic deformation W_{ir} of Gum Metal calculated for each cycle of tensile loading.

The values of energy used for irrecoverable plastic deformation W_{ir} of Gum Metal are low in cycles 6 and 7 where the range of plastic deformation is short. They grow in subsequent cycles 8-24 and are in the a range between 0.9 J/g and 1.2 J/g. The highest values of W_{ir} are in cycles 23-24 in which the temperatures of the specimen are significant (damage). The values of heat Q generated with plastic deformation of Gum Metal calculated for each cycle of tensile loading using Eq. 4.9 are shown in Fig. 4.46.

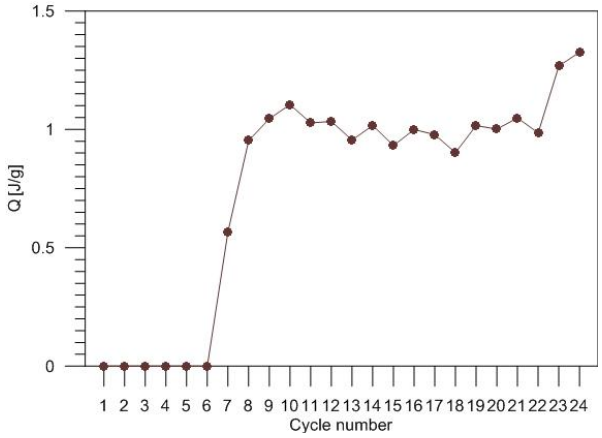

Fig. 4.46. The values of heat Q generated with plastic deformation of Gum Metal calculated for each cycle of tensile loading using Eq. 4.9.

The heat Q generated with plastic deformation of Gum Metal is low in cycles 6 and 7 and in subsequent cycles 8-24 oscillates in the a range between 0.8 J/g and 1.35 J/g reaching the highest values in cycles 23-24. The values of stored energy E_s of Gum Metal estimated for each cycle of tensile loading using Eq. 4.12 are shown in Fig. 4.47.

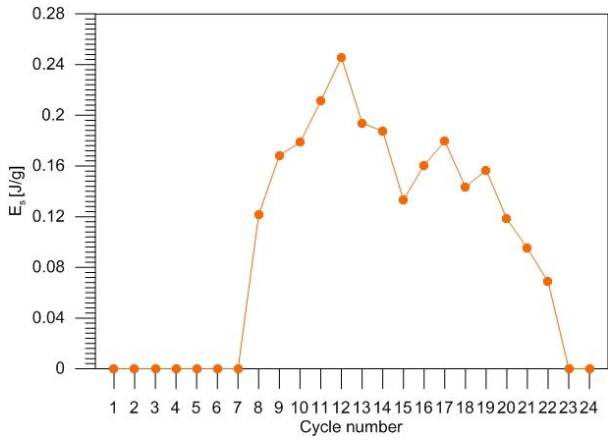

Fig. 4.47. The values of stored energy E_s of Gum Metal estimated for each cycle of tensile loading using Eq. 4.12.

The stored energy E_s is equal to 0 in the early cycles 1-7 where there is no or little plastic deformation involved in the process of tension. In cycles 8-20, E_s is in the range between 0.12 J/g and 0.25 J/g. Finally in cycles 21-24, E_s drops because the value of the heat Q generated with plastic deformation grows significantly due to developing damage mechanisms. The values of the ratio of the stored energy to the plastic work $Z = \frac{E_s}{W_{ir}}$ calculated for each cycle of tensile loading of Gum Metal are shown in Fig. 4.48.

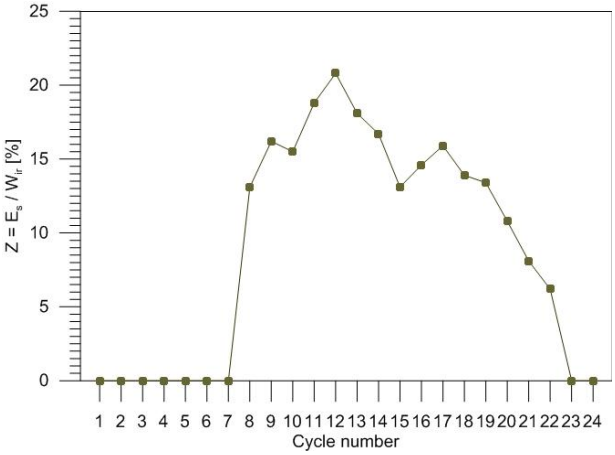

Fig. 4.48 The values of the ratio of the stored energy to the plastic work $Z = \frac{E_s}{W_{ir}}$ calculated for each cycle of tensile loading of Gum Metal.

The values of the ratio $\boldsymbol{Z = \frac{E_s}{W_{ir}}}$ are in the range between 13% and 20% for cycles 8-18. In the last cycles the values of *Z* gradually decrease down to zero in the stage close to failure.

4.5. Summary

A comprehensive analysis of the effects of thermomechanical couplings in the second set of Gum Metal specimens under selected loading has been presented. Monotonic tensile tests were performed at strain rates of $10^{-5}s^{-1}$, $10^{-4}s^{-1}$, $10^{-3}s^{-1}$, $10^{-2}s^{-1}$ and $10^{-1}s^{-1}$ with application of DIC for analysis of subsequent loading stages of the alloy. Stress vs. strain curves revealed that values of yield stress had tendency to grow, whereas values of elongation to the specimen rupture tended to fall with increasing strain rates. Phenomena of macroscopically observed work hardening were observed for strain rates of $10^{-5}s^{-1}$, $10^{-4}s^{-1}$ and $10^{-3}s^{-1}$, while phenomena of macroscopically observed softening effect were noticed at strain rates of $10^{-2}s^{-1}$ and $10^{-1}s^{-1}$. In spite of the fact that character of the stress-strain curve depend on the length of the virtual extensometer, it was confirmed that in the case when the extensometer length is closer to the gage length, the stress-strain curve is similar to the force-displacement mechanical characteristics.

Measurements of the strain distributions determined by DIC and analyzed at selected stages of Gum Metal tensile loading demonstrated a tendency of developing of a strain localization at various strain rates. The analysis of strain and deformation rate tensor fields demonstrated that in case of strain rate below $10^{-3}s^{-1}$ the deformation is macroscopically uniform up to the mean strain value equal to 0.075 whereas for $10^{-2}s^{-1}$ and $10^{-1}s^{-1}$ the strain localization occur at the earlier stage of the process and is localized in smaller area. No peculiarities related to secondary phase activity were observed at strain maps. Fractographic analysis performed for post-mortem specimens exhibited mainly ductile features.

It was demonstrated that a large limit of the Gum Metal's mechanically reversible nonlinear deformation, underlined as the new titanium alloy's "super property", is caused by stress-induced activity of *α*" phases of exothermic character.

It was found that, irrespective of the applied strain rate, the maximal drop in the Gum Metal's temperature (thermoelastic effect) occurs significantly earlier than the limit of its mechanically reversible deformation. The increase in the temperature between the maximal drop and mechanically reversible stage reveals a dissipative character of the deformation in

this range. Due to the dissipative nature of the process, the large recoverable deformation of Gum Metal should be called “superelastic-like behavior” rather than “nonlinear elasticity”, which have been used interchangeably in the literature. This finding can be concluded as follows. A scheme of general dependence of the stress and temperature vs. strain for solid material in tension is shown in Fig. 4.49(a), and that observed for Gum Metal in presented in Fig. 4.49(b).

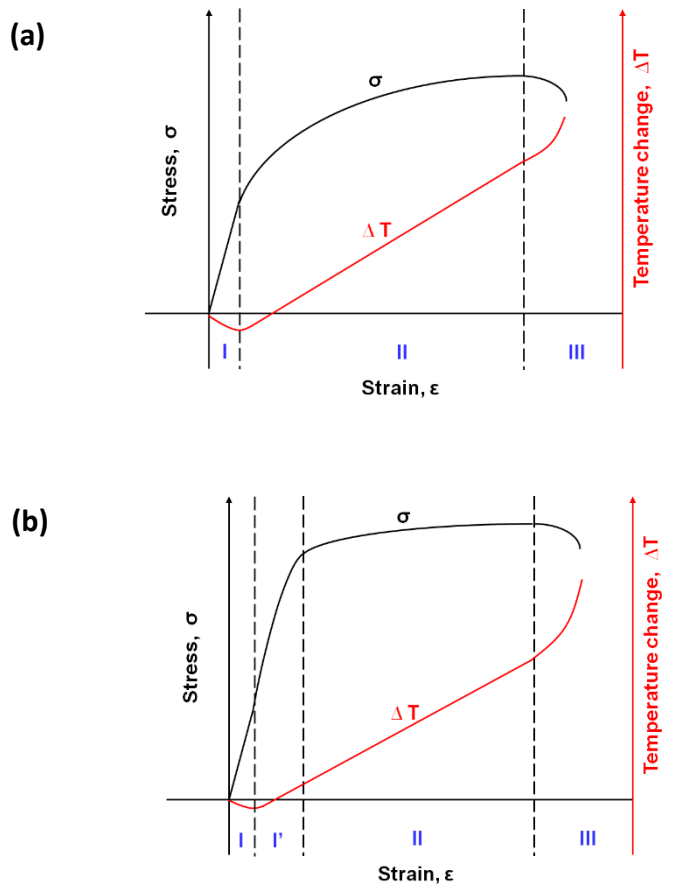

Fig. 4.49. General scheme of stress σ and average temperature change ΔT vs. strain ε in tension up to rupture representing behavior of (a) any solid material, where subsequent deformation stages are distinguished: I = linear elastic, II = plastic, III = damage; (b) Gum Metal, where subsequent deformation stages can be distinguished: I = linear elastic, I’ = nonlinear mechanically reversible, II = plastic, III = damage [Pieczyska E.A. et al. 2018a].

The typical solid material subjected to tension in the elastic range gives a decreasing thermal response (a thermoelastic effect) (stage I), followed by its growth when plastic deformation begins (stage II), and finally its intense growth during localization and damage (stage III) (Fig.

4.49(a)). Thus, as was studied by [Farren W. et al. 1925, Taylor G. et al. 1934, Bever M.B. et al. 1973], assuming adiabatic conditions, the stress corresponding to the lowest temperature can be associated to the yield limit, because the increase in temperature reveals the dissipative character of the deformation process, which is related to the permanent change in the material's structure. The stress and temperature results formerly obtained for stainless steel, titanium alloy, polymers, etc. are in line with the scheme shown in Fig. 4.49(a) and allowed us to indicate the material yield limit with a high accuracy.

In the case of Gum Metal, the results showed that the maximal drop in temperature occurred significantly earlier (stage I) than the limit of its recoverable deformation (stages I and I′) as demonstrated in Fig. 4.49(b).

It may be noted that this aspect of experimental analysis of the large nonlinear reversible deformation of the Gum Metal explained on the grounds of effects of thermomechanical couplings is a unique result obtained in IPPT PAN. This is appreciated by coauthors of the first paper devoted to Gum Metal published in Science in 2003 (Tadehiku Furuta and Shigeru Kuramoto] [Saito T. et al 2003, Golasiński K. et al. 2017a, Pieczyska et al. 2018a] as well as expert in investigation of Ni-free Ti alloys - Shuichi Miyazaki [Miyazaki S., private communications].

Subsequent stages of tensile loading of multifunctional Ti alloy—Gum Metal—were studied by analysis of coupled mechanical and thermal field data obtained by DIC and IRT techniques. The mechanical characteristics confirmed the Gum Metal's large nonlinear superelastic-like behavior, low elastic modulus, and high strength, while the related temperature changes provided new thermodynamic data for analysis of the alloy's elastic-plastic transition and development of the strain localization leading to the necking and rupture. The analysis of the strain and temperature fields showed that the increase in the strain rate affects both the onset and development of the strain localization. The increase in the strain rate accelerates the strain localization process and causes the area where the strain is localized to be much smaller. Thermoelastic effect in Gum Metal under selected loadings was analyzed by comparing values of maximal temperature drop obtained experimentally and theoretically. In the case of both monotonic and cyclic tension tests, there was not big discrepancy between the values of temperature calculated and those derived experimentally.

Finally, the estimation of energy balance was performed for 24 subsequent loading-unloading cycles of Gum Metal. Importantly, the stored energy, which is usually a part of energy related to defects of crystal lattice, mainly dislocation structures, was calculated. The results allowed to better understand the nature of deformation mechanisms involved in the deformation process of the alloy.

Chapter 5

5. Investigation of Gum Metal subjected to compression

The results presented in Chapter 5 were partially disseminated during conferences [Golasiński K. et. al 2016c, 2017d, 2018a, 2018b, 2019a, 2019b and Pieczyska E.A. et al 2018c, 2018d] and published in [Golasiński K. et. al 2019d].

5.1 Gum Metal material and samples

A polycrystalline rod of Gum Metal with the composition near Ti–36Nb–2Ta–3Zr–0.3O (wt.%) and dimensions around 6 mm x 6 mm x 100 mm was supplied by Fukuoka University, Japan. The fabrication route included several steps consisting of preparatory processes such as billet forming from mixed powders of the constituents, sintering and hot forging. Finally, the Gum Metal rod was cold-swaged. A picture of the Gum Metal rod including cold-swaging direction is shown in Fig. 5.1.

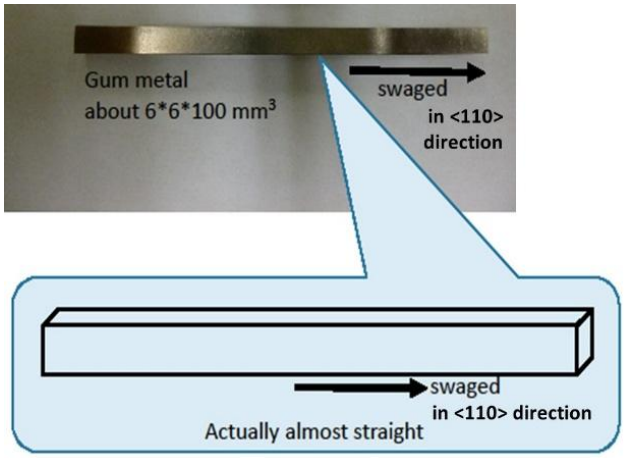

Fig. 5.1. Dimensional and technical specifications of Gum Metal rod [courtesy of Takesue N.].

5.1.1 Analysis of phase content

Gum Metal phase composition was characterized using PHILIPS X`Pert-Pro XRD system at parameters of 40 kV and 30 mA. The samples were scanned through 2θ ranging from 20° to 145° with a scan rate of 0.08 °/min. The XRD pattern with Rietveld refinement obtained for the Gum Metal sample is presented in Fig. 5.2(a). The lattice parameters for the studied material were determined as 3.2985(1) Å. The zoomed XRD pattern for 2θ ranging from 51° to 87°, shown in Fig. 5.2(b), presents strong diffraction peaks corresponding to β phase. In this region marked with a triangle at approximately 66°, one can notice a very faint increase of background. Such a feature can indicate a presence of low amount of hexagonal ω phase.

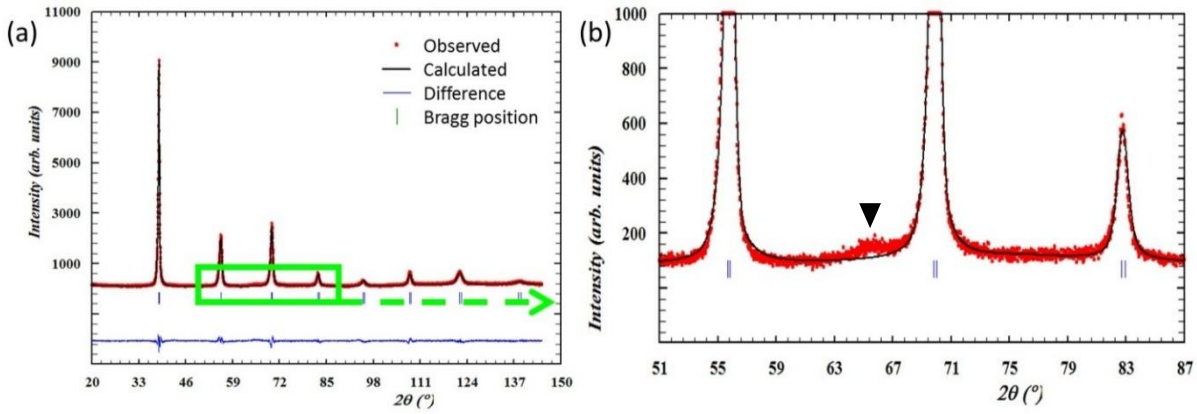

Fig. 5.2. XRD patterns of Gum Metal for 2θ ranging from: (a) 20° to 145° and (b) 51° to 87°.

5.1.2 Analysis of grain misorientation and texture

The EBSD analysis was conducted on a JEOL JSM-6480 scanning electron microscope (SEM) with HKL EBSD Channel 5 system equipped with the Nordlys II camera at the acceleration voltage of 20 kV. The analysis of the EBSD results was carried out using HKL Tango software. EBSD orientation maps of a transverse cross-section of Gum Metal are shown in Figs. 5.3(a) and 5.3(b). Elongated grains with fiber-like structures and near random orientations can be noticed.

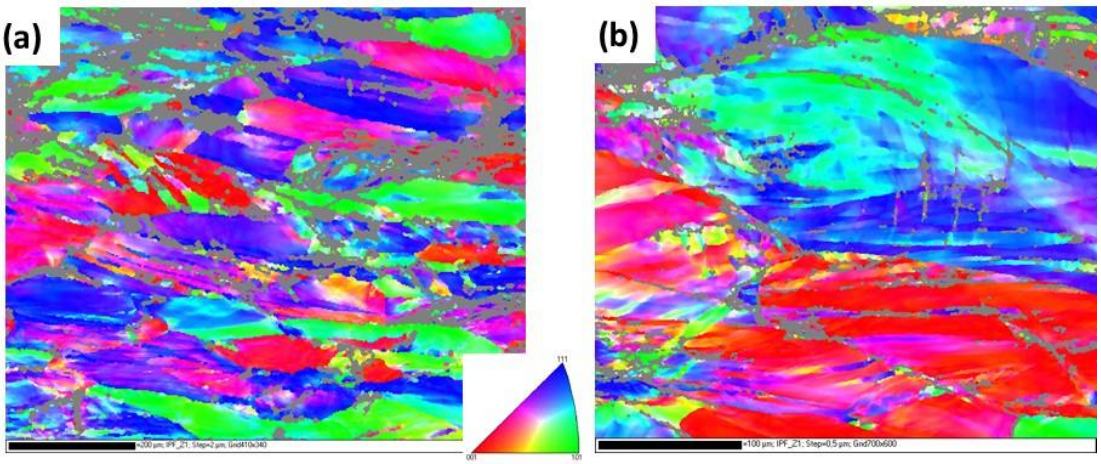

Fig. 5.3. EBSD orientation maps of grain orientations of Gum Metal transverse cross-section with scale bars (a) 200 µm and (b) 100 µm.

EBSD orientation maps of grain orientations of two zones in Gum Metal transverse cross-section are shown in Figs. 5.4(a) and 5.4(b). The corresponding misorientation profiles A-A and B-B lines are presented in Figs. 5.4(c) and 5.4(d). The misorientation profile analyzed across

line A–A (Fig. 5.4(c)) passes along two relatively large grains. There is a gradual change in orientation up to ~14° and up to ~9° within the elongated area of the first and the second grains, respectively. The misorientation profile analyzed across line B–B (Fig. 5.4(d)) passes along one selected grain. Even in one grain there is an orientation change up to ~17°. A significant difference in misorientation of Gum Metal grains can be attributed to the severe cold-swaging applied to the alloy during its fabrication route.

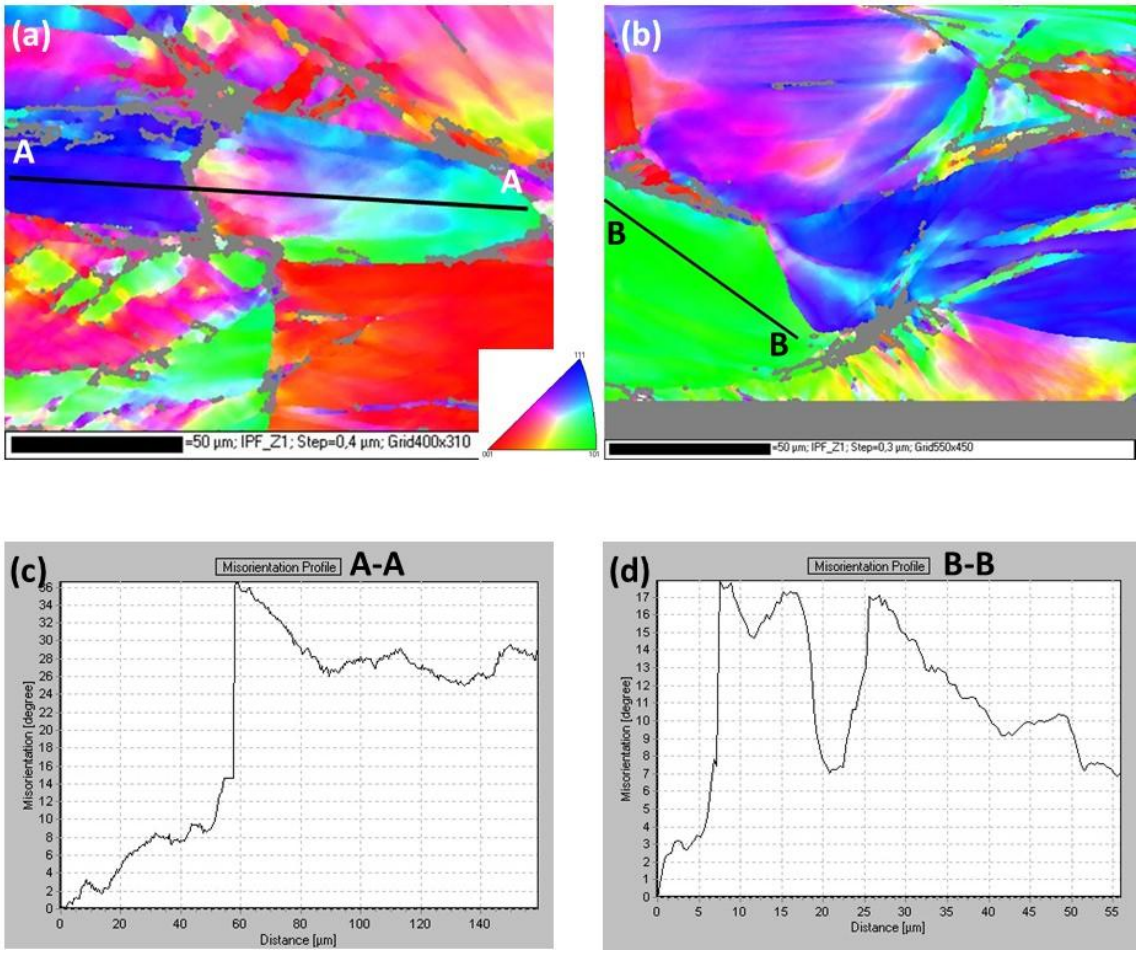

Fig. 5.4. (a, b) EBSD orientation maps of grain orientations of two zones in Gum Metal transverse cross-section with scale bar 50µm with corresponding misorientation profiles (c, d) along A-A and B-B lines.

Moreover, texture of the Gum Metal was investigated in order to clarify the orientation after the applied cold swaging process. The obtained pole figures are presented in Fig. 5.5.

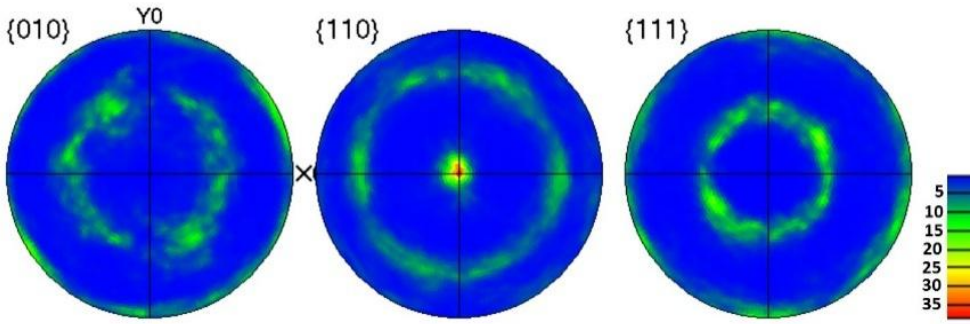

Fig. 5.5. Texture analysis of the Gum Metal sample; {0 1 0}, {1 1 0} and {1 1 1} pole figures.

The pole figures clearly indicate a pronounced fiber <110> texture along the cold swaging axis, which is consistent with results for cold worked Gum Metal obtained in [Morris Jr. J.W et al. 2010]. The texture in metals is the main source of mechanical anisotropy.

5.2 Determination of elastic constants using ultrasonic test

Elastic constants and Young's moduli in Gum Metal were determined by measurements of ultrasonic wave propagation. Ultrasonic waves were generated and detected in the material by a piezoelectric transducer oscillating at the desired frequency. Ultrasonic velocities have been determined by time-of-flight measurements using a pulse-echo method [Auld B.A., 1990]. The polycrystalline Gum Metal rod submitted for ultrasonic testing exhibited a transversal isotropy around its longitudinal axis (3); see Fig. 5.5. It was proved by the EBSD analysis and confirmed by measurements of ultrasonic velocities in all 3 directions of the Gum Metal rod. The difference between velocities of longitudinal waves in directions (1) and (2) was lower than 0.2%, that was comparable to the measurement error of the applied ultrasonic technique. For comparison, the difference between ultrasonic velocities in directions (1) and (3) was over 3%. In the case of a material characterized by a transversal isotropy, the matrix (c_{ij}) of elastic constants has five independent elements and takes the form expressed by Eq. 5.1.

$$[c_{ij}]=\begin{bmatrix} c_{11} & c_{12} & c_{13} & 0 & 0 & 0 \\ c_{12} & c_{11} & c_{13} & 0 & 0 & 0 \\ c_{13} & c_{13} & c_{33} & 0 & 0 & 0 \\ 0 & 0 & 0 & c_{44} & 0 & 0 \\ 0 & 0 & 0 & 0 & c_{44} & 0 \\ 0 & 0 & 0 & 0 & 0 & c_{66}=\frac{(c_{11}-c_{12})}{2} \end{bmatrix} \quad \text{(Eq. 5.1)}$$

In order to determine all five independent elements of the elastic constants matrix at least five different values of velocities of ultrasonic waves propagating in different directions and/or with different polarizations must be measured in the material. For this purpose, two samples, denoted as U1 and U2, were cut out from the Gum Metal rod in the way shown in Fig. 5.6. Sample U2 was cut out from the rod at an angle of 45° to the axis 3.

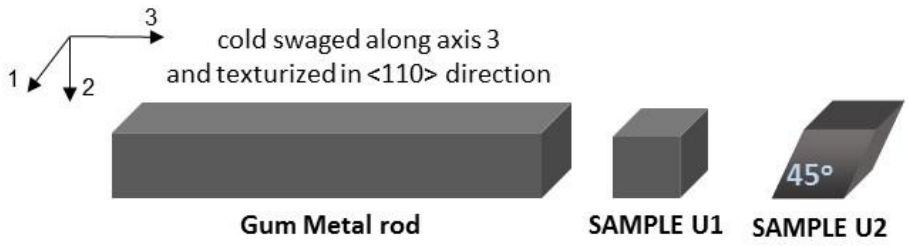

Fig. 5.6. Configuration and orientation of the samples U1 and U2 cut out from Gum Metal rod for ultrasonic measurements.

Four ultrasonic velocities were measured in sample U1 and one in sample U2. Table 5.1 shows values of the measured velocities in sample U1: longitudinal waves propagating in direction (1) and (3), shear waves propagating in direction (1) and polarized in direction (2) and direction (3) respectively, as well as in sample U2: quasi longitudinal wave propagating in direction deviated 45° from the axis (3).

Table 5.1 Ultrasonic velocities measured in Gum Metal

Sample	Propagation direction	Wave type	Wave velocities [m/s]
U1	1 and 3	longitudinal	V_{11} = 5184
			V_{33} = 5018
	1	shear polarized in 2 and 3	V_{12} = 2116
			V_{13} = 2100
U2	45° to 3	quasi longitudinal	V_{L45} = 5175

Taking the measured ultrasonic velocities and assuming that the mass density of Gum Metal is equal to 5.6 g/cm^3, the elastic constants of the alloy were determined using Christoffel equations [Auld B.A. 1990] shown above (Eq. 5.2-5.7).

$$c_{11} = \rho v_{11}^{\ 2} \quad \text{(Eq. 5.2)}$$

$$c_{33} = \rho v_{33}^{\ 2} \quad \text{(Eq. 5.3)}$$

$$c_{44} = \rho v_{13}^{\ 2} \quad \text{(Eq. 5.4)}$$

$$c_{66} = \rho v_{12}^{\ 2} \quad \text{(Eq. 5.5)}$$

$$c_{12} = c_{11} - 2c_{66} \quad \text{(Eq. 5.6)}$$

$$c_{13} = 2\sqrt{[\frac{1}{2}(c_{11} + c_{66}) - \rho v_{L45}^{\ 2}][\frac{1}{2}(c_{33} + c_{66}) - \rho v_{L45}^{\ 2}]} - c_{66} \quad \text{(Eq. 5.7)}$$

The elastic constants were accurately and explicitly determined without the aid of any estimation technique. The obtained results are listed in Table 5.2.

Table 5.2 Elastic constants of polycrystalline Gum Metal

Elastic constant	**c_{11}**	**c_{12}**	**c_{13}**	**c_{33}**	**c_{44}**	**c_{66}**
Value [GPa]	150.5	100.3	104.0	141.0	24.7	25.1

Based on the established elastic constants, the Young's moduli of the tested Gum Metal were calculated. The elastic moduli were worked out for directions 1/2 parallel to the cold-swaging axis 3 and for direction 3 perpendicular to the cold-swaging axis using Eq. 5.8 and 5.9.

$$E_{1/2} = \frac{2}{\frac{c_{33}}{c'} + \frac{1}{c_{11} - c_{12}}} \quad \text{(Eq. 5.8)}$$

$$E_3 = \frac{c'}{c_{11} + c_{12}} \quad \text{(Eq. 5.9)}$$

where $c' = c_{33}(c_{11} + c_{12}) - 2c_{13}^{\ 2}$ (Eq. 5.10).

The obtained results were E_3 = 54.8 GPa and $E_{1/2}$ = 66.2 GPa and they are listed in Table 5.3.

Table 5.3 Young's moduli of polycrystalline Gum Metal in relation to cold swaging axis

Relation to cold swaging axis	Parallel	Perpendicular
Young's modulus [GPa]	54.8	66.2

Different values of the Young moduli in two perpendicular directions indicate considerable elastic anisotropy of Gum Metal.

5.3 Mechanical anisotropy of Gum Metal under compression

5.3.1 Experimental details

The Gum Metal cube samples with sizes of 2.85 mm x 2.85 mm x 3.55 mm were cut out from the Gum Metal cold swaged rod using electro-erosion machining, as presented in Fig. 5.7(a). Samples with two orientations, shown in Fig. 5.7(b) and 5.7(c), were prepared mechanical compressive loading perpendicular (sample A) and parallel (sample B) to <110> texture induced by cold swaging. A picture of a sample machined from the Gum Metal rod is presented in Fig. 5.7(d). Subsequently, surfaces of two perpendicular walls of each sample were uniformly coated by soot and then tiny drops of white paint were sprayed onto the surface for DIC analysis.

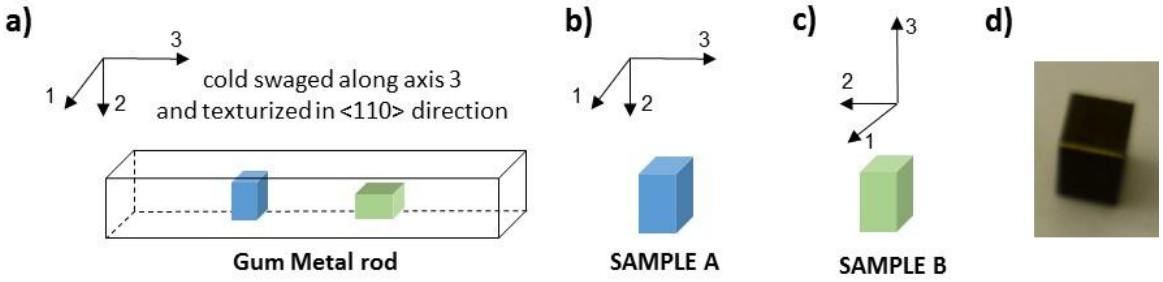

Fig. 5.7. Orientations of Gum Metal samples for compression; (a) position in the Gum Metal rod; (b) sample A; (c) sample B; and (d) a picture of the machined sample.

A scheme of the experimental setup used for investigation of deformation behavior of Gum Metal under compression is shown in Fig. 5.8. The samples were deformed using an MTS 858 testing machine by displacement controlled load-unload compressive loading at the strain rate of 10^{-2} s^{-1}. During the test, the loading force as a function of time was recorded.

Simultaneously, surfaces of two perpendicular walls of a sample were monitored by two visible range cameras Manta G-125B, denoted by CAM 1 and CAM 2 in Fig. 5.8. In this manner, sequences of visible range images were recorded for two different perpendicular surfaces. On the basis of the obtained image sequences, displacement field component u_y, deformation rate tensor component D_{yy} and Hencky strain field component ε_{yy} (where y is the loading direction) were determined using DIC procedure implemented in ThermoCorr software [Nowak M. et al. 2017].

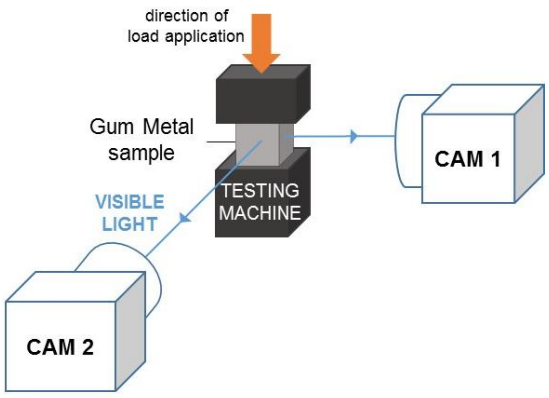

Fig. 5.8. Scheme of the experimental setup used for investigation of deformation behavior of Gum Metal under compression.

5.3.2 Mechanical anisotropy of Gum Metal under compression analyzed by digital image correlation

Force vs. crosshead displacement curves for Gum Metal samples with two orientations under load-unload compression perpendicular (sample A) and parallel (sample B) to cold swaging axis are plotted in Fig. 5.9(a). Additionally, displacement fields with respect to the loading axis y (u_y) measured by DIC for two compression stages, denoted by points P and Q of the advanced plastic deformation of Gum Metal loading are presented in Fig. 5.9(a).

(a)

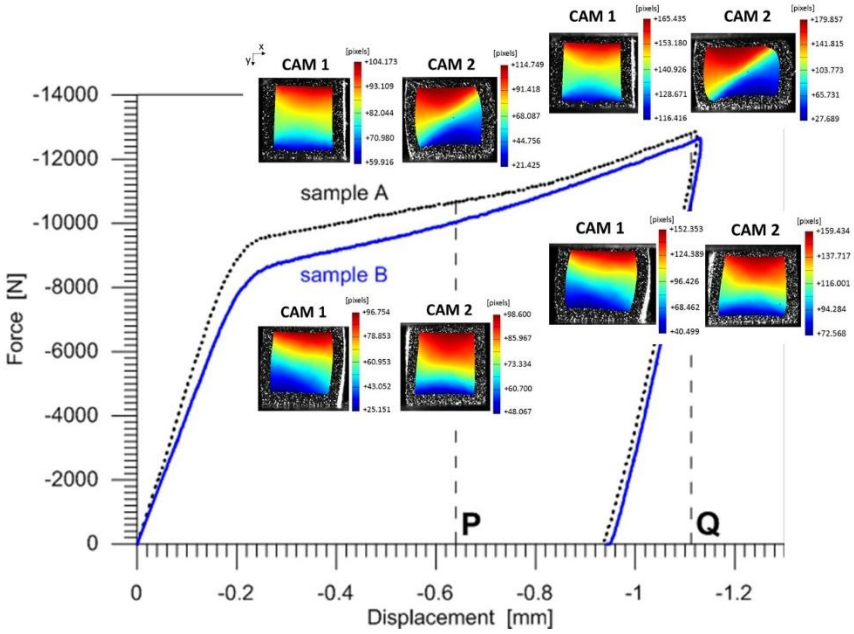

(b)

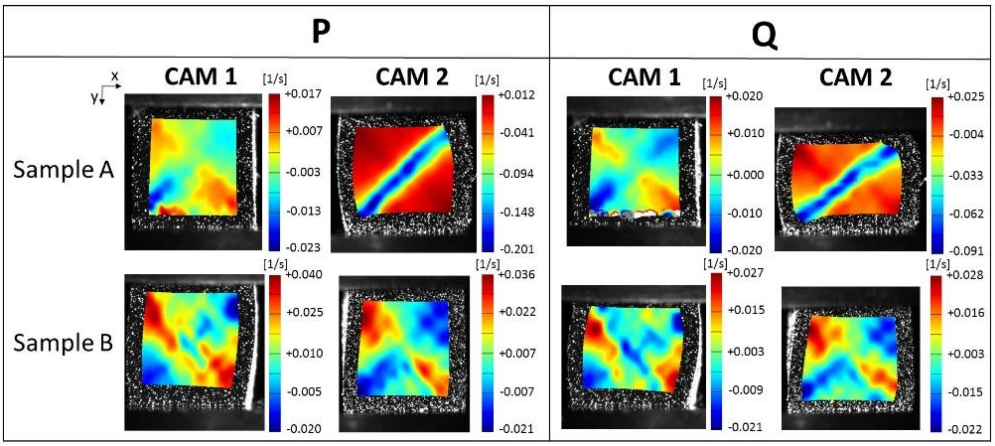

(c)

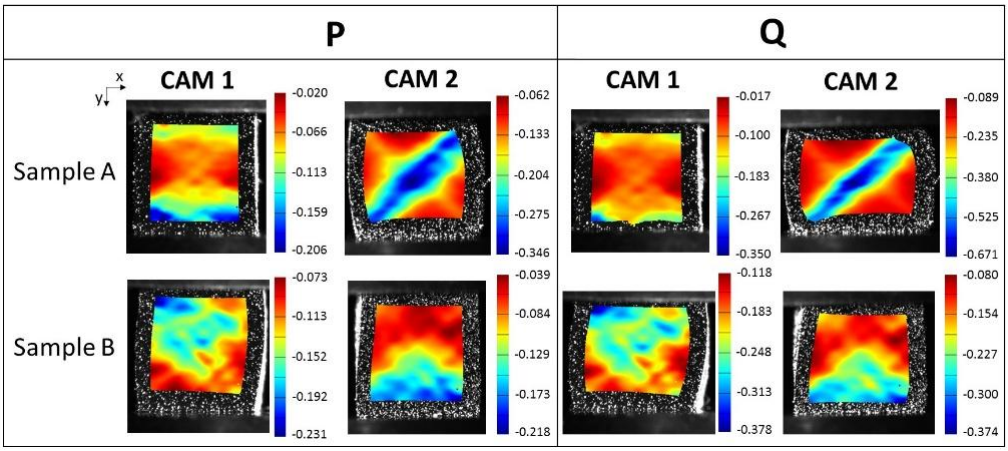

Fig. 5.9. Force vs. crosshead displacement curves for Gum Metal under compression perpendicular (dashed black line, sample A) and parallel (solid blue line, sample B) to cold swaging axis with (a) displacement fields (u_y), (b) deformation rate tensor component (D_{yy}) and (c) Hencky strain component (ε_{yy}) determined by DIC in points P and Q.

It is seen that in the case of Sample A compressed perpendicular to the swaging axis, the yielding occurs at higher force value in comparison to Sample B compressed parallel to the swaging axis. The fields of displacement component u_y shown in Fig. 5.9(a) are not homogenous for both Samples A and B. However, in the case of sample A there is a significant difference in u_y fields obtained by CAM 1 and CAM 2 whereas in case of sample B the fields are very similar. The displacement field determined on the basis of image sequence from CAM 1 for sample A is similar to that obtained for sample B, whereas that measured by CAM 2 shows strong localization at the angle of about 45^o to the loading direction. The localization zone in form of macroscopic shear band is very well seen at the field of deformation rate tensor component (D_{yy}) presented in Fig. 5.9(b). As it is seen, the deformation rate within the band is about 10 times higher in comparison to the areas outside the band and about 10 times higher than that observed for sample B (see Fig. 5.9(b) point P). The plastic anisotropy is also seen at the fields of Hencky strain component (ε_{yy}), shown in Fig. 5.9(c). In the case of sample A almost homogenous distribution of ε_{yy} is observed for CAM1 and shear band formation for CAM 2. In the case of B sample the distribution of Hencky strain component ε_{yy} for CAM1 is similar to that obtained for CAM 2 with the difference that the obtained distributions are reflected with respect to the horizontal axis of the sample. For the CAM1 the deformed zone is concentrated in the upper part of the sample, whereas for CAM 2 it is concentrated in its lower part.

5.4. Analysis of thermomechanical couplings in Gum Metal under cyclic compression

5.4.1. Experimental details

The Gum Metal cube samples with sizes of 2.85 mm x 2.85 mm x 3.55 mm were cut out from the Gum Metal cold swaged rod in the cold working direction using electro-erosion machining, as presented in Fig. 5.10(a, b). A picture of a sample machined from the Gum Metal rod is presented in 5.10(c). Subsequently, surface of one sample wall was uniformly coated by soot and later by tiny drops of white paint.

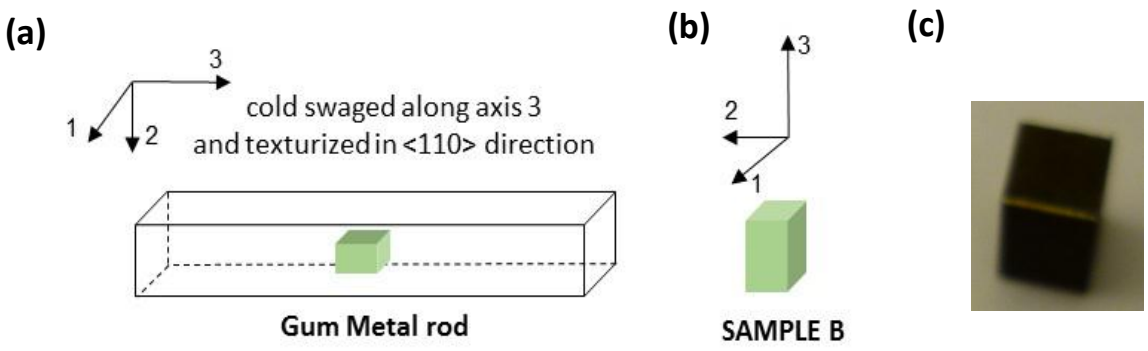

Fig. 5.10. Gum Metal sample: (a, b) orientation of machining and (c) photo.

A scheme of an experimental setup used for investigation of thermomechanical coupling in Gum Metal under cyclic compression are shown in Fig. 5.11. Displacement controlled compressive tests were performed using an MTS 858 testing machine. During the loading, the deformation of Gum Metal was being monitored by an infrared and a CCD cameras. An infrared longpass filter was applied to divide an infrared (3-5 µm) and a visible (0.4-1 µm) spectra emitted from a surface of a sample. The infrared radiation captured during the compression served to determine a thermal response of Gum Metal during loading. Continuous images of the sample during test recorded by the visible range camera were used as a video extensometer. Changes in the dimension of the sample were determined using a DIC algorithm.

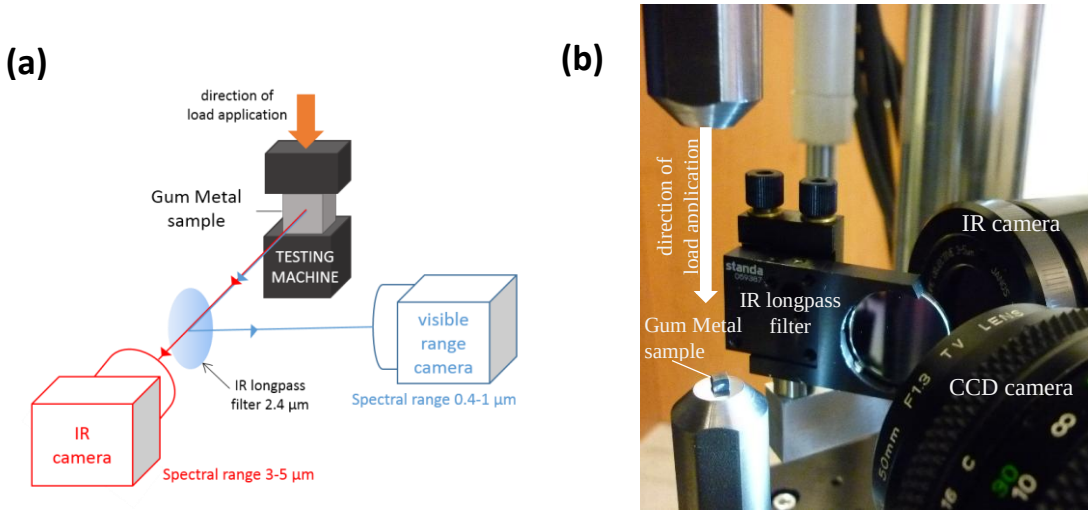

Fig. 5.11. Experimental setup used for investigation of thermomechanical coupling in Gum Metal under cyclic compression: (a) scheme and (b) photo.

5.4.2. Mechanical behavior of Gum Metal under cyclic compression

Stress vs. strain curves for 10 cycles of Gum Metal under cyclic compression at the strain rate $5x10^{-2}$ s^{-1} are shown in Fig. 5.12. The changes in strain during the process of cyclic compression of Gum Metal were measured using VE 3 mm in length placed in the center of the sample as shown in Fig. 5.12.

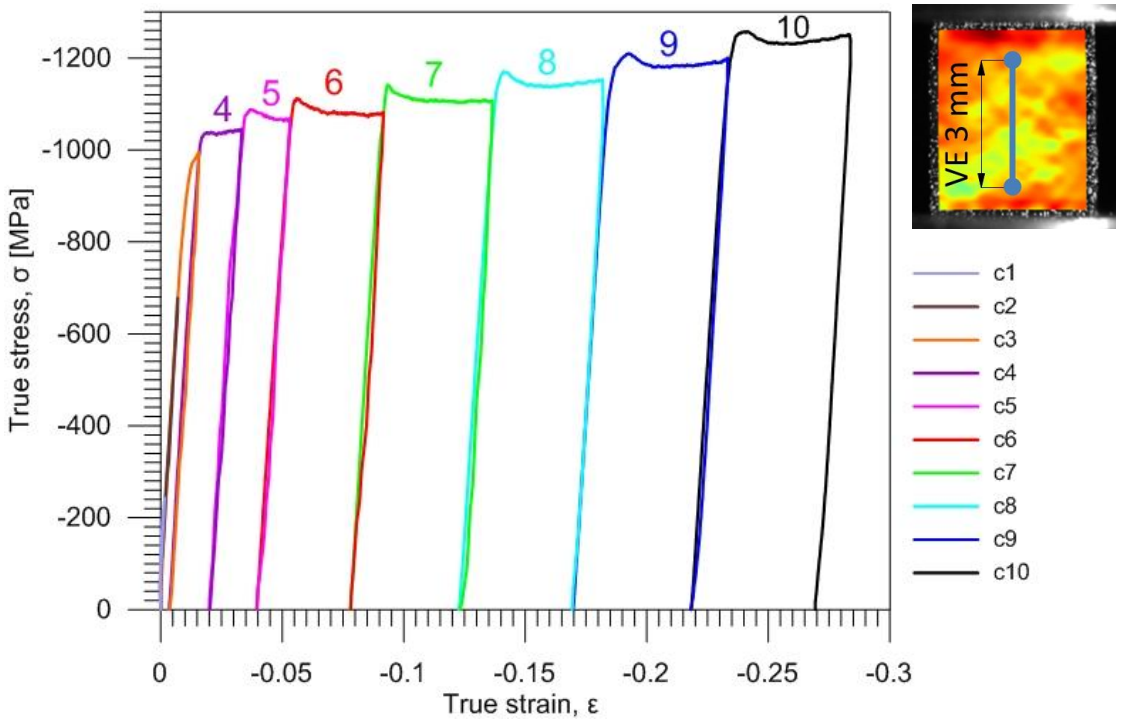

Fig. 5.12. True stress σ vs. true strain ε curves for Gum Metal under cyclic compression at the strain rate $5x10^{-2}$ s^{-1}; 10 loading-unloading cycles 1-5 for strain step ~0.025 and 6-10 for strain step ~0.05 and initial position of VE 3mm on the sample.

The curves profiles change significantly with each cycle and reveal clearly pronounced yield points starting in cycle 4 and developing in further cycles. Moreover, in comparison to commonly reported nonlinearity of mechanical response of Gum Metal, in subsequent cycles almost a linear elastic behavior is observed.

A comparison of experimentally obtained values of maximal stress and the remaining strain after unloading derived from Fig. 5.12 for cycles 4-10 during cyclic compression of Gum Metal are shown in Fig. 5.13.

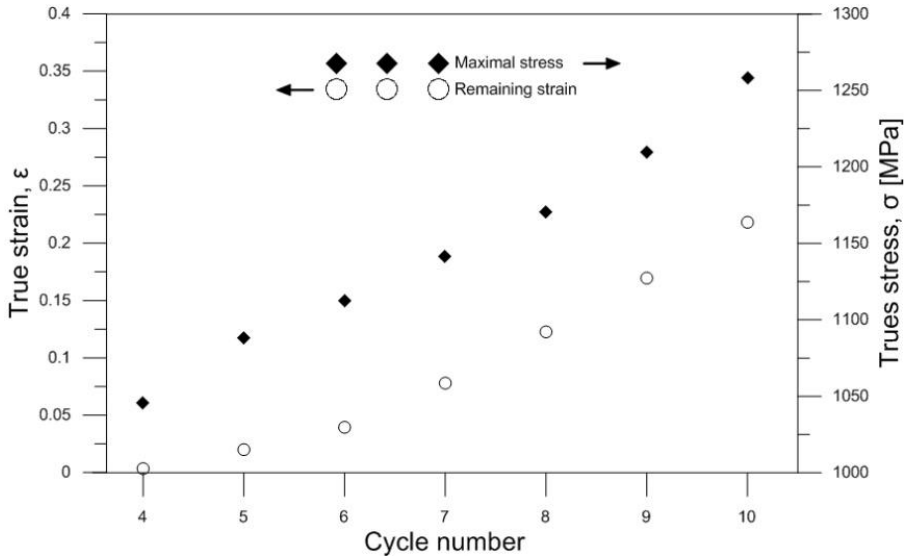

Fig. 5.13. Comparison of experimental values of maximal stress and remaining strain after unloading obtained for cycles 4-10.

A clearly increasing value of maximal stress indicated for each cycle demonstrates a smooth and almost linear hardening in the subsequent compression cycles. The evolutions of displacement fields (u_x, u_y) measured by DIC and the calculated strain fields (ε_{xx}, ε_{yy}) are presented in Fig. 5.14. Selected distributions correspond to the end of certain loading cycles 4-10.

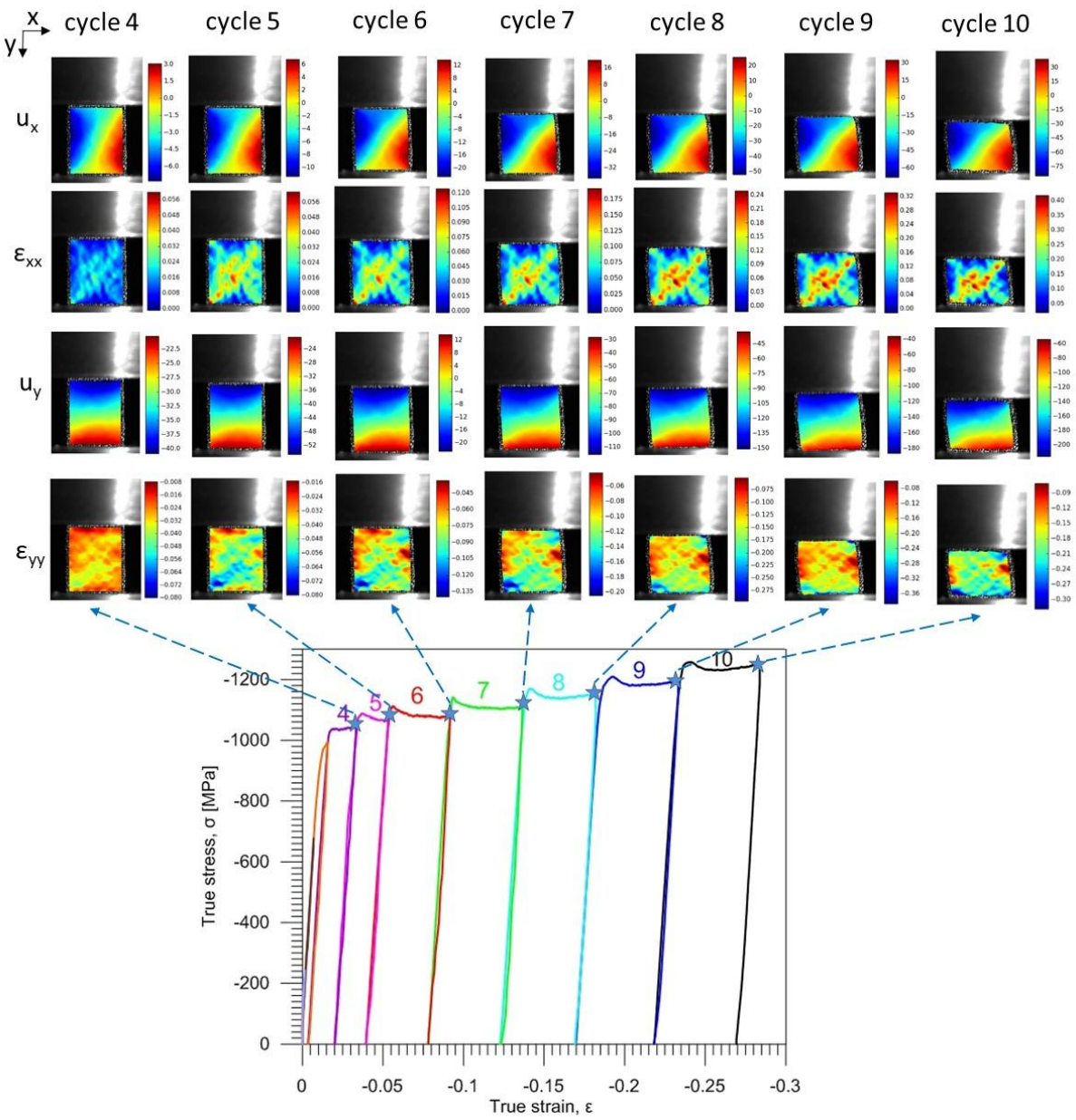

Fig. 5.14. Evolutions of displacement fields (u_x, u_y) and strain distributions(ε_{xx}, ε_{yy}) derived at the end of cycles 4-10.

It is seen that deformation proceeds in a macroscopically non-uniform manner from the very beginning of the compression process (cycle 4) and develops in subsequent compression cycles. As a consequence, the shear zones become more and more distinct in the upcoming cycles, that is illustrated by the strain distributions.

5.4.3. Investigation of temperature changes of Gum Metal under cyclic compression

Thermal responses of Gum Metal under cyclic compression were determined for all 10 loading-unloading cycles. True stress and temperature change vs. strain characteristics for 10 subsequent loading-unloading cycles are shown in Fig. 5.15.

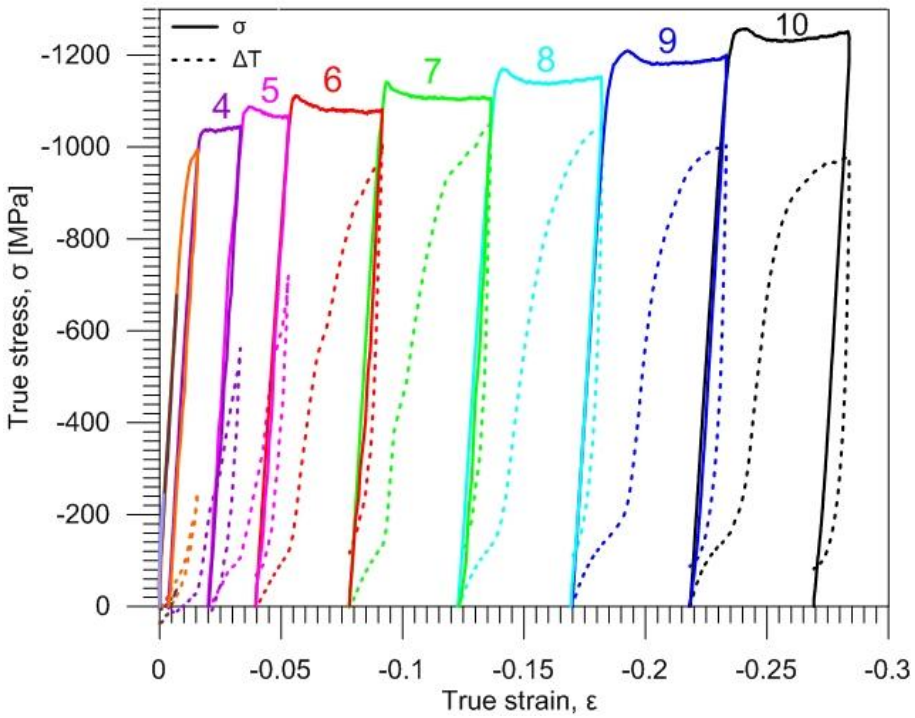

Fig. 5.15. True stress σ and temperature change ΔT vs. strain ε characteristics for 10 subsequent loading-unloading cycles of Gum Metal sample at the strain rate $5x10^{-2}$ s^{-1}.

Results of true stress (solid line) vs. true strain and related temperature (dashed line) change vs. true strain obtained for cycles 5, 7 and 9 are shown in Fig. 5.16. The cycles were selected to contrast various loading conditions; cycle 5 was realized with a strain step ~0.025, cycle 7 was realized with a strain step ~0.05 as well as cycle 9 which represents an advanced stage of the cyclic compression.

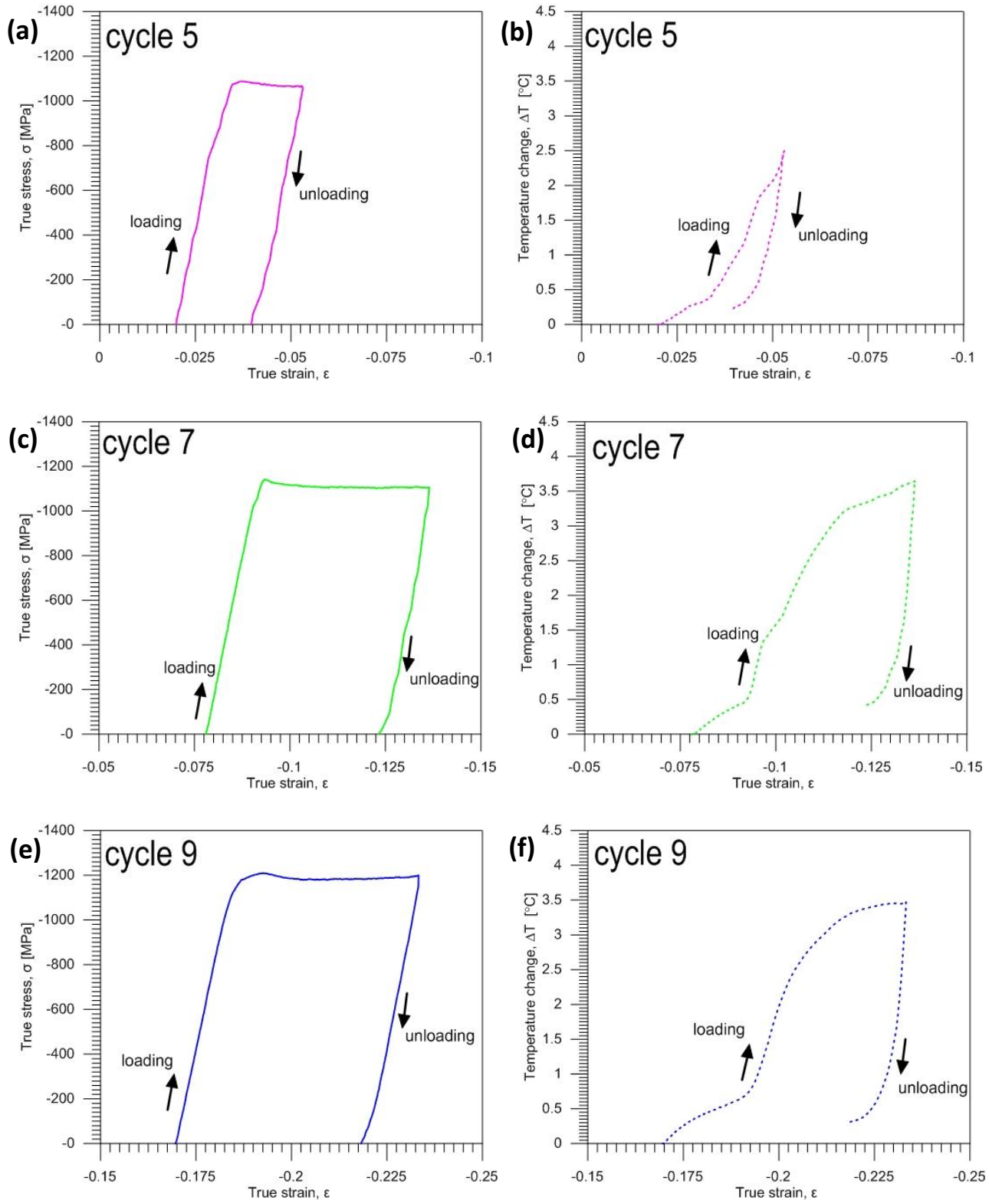

Fig. 5.16. Mechanical and thermal responses of Gum Metal under compression at the strain rate 5×10^{-2} s^{-1} for cycles 5, 7 and 9; (a, c, e) true stress σ vs. true strain ε and (b, d, f) temperature change ΔT vs. true strain ε.

It is worth noting that, the thermal responses of Gum Metal, recorded in cycles 5, 7, 9, show similar profiles, which can be related to various stages of compression. Subsequent profiles seem to have rounder slopes, probably as a result of accumulated plastic deformation induced during previous loading cycles.

Cycles 5, 7 and 9 with different strain steps were selected for deeper analysis of Gum Metal thermomechanical behavior. True stress and temperature change vs. true strain and true strain, true stress and temperature change vs. time curves for cycles 5, 7 and 9 are shown in Fig. 5.17 (a-f).

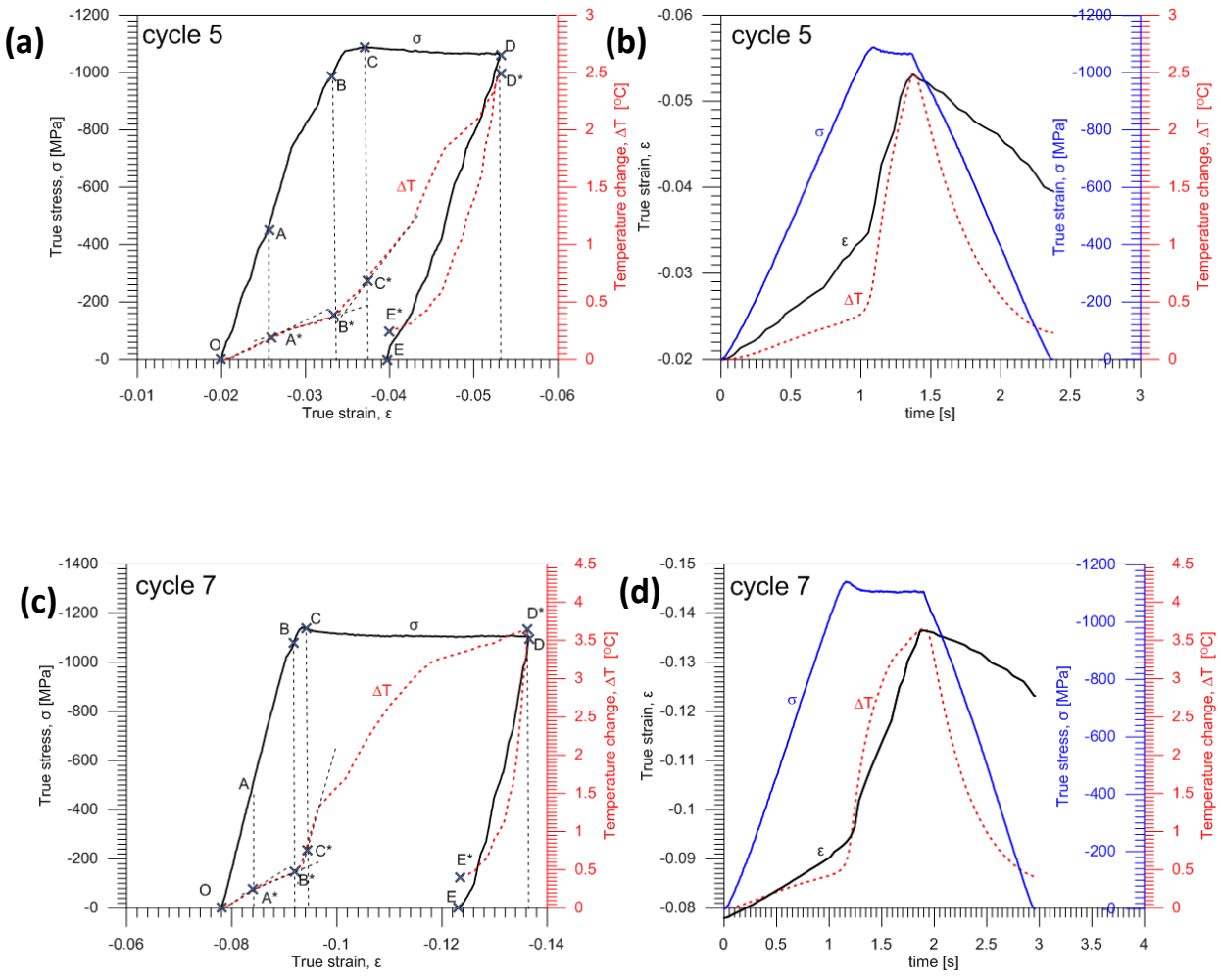

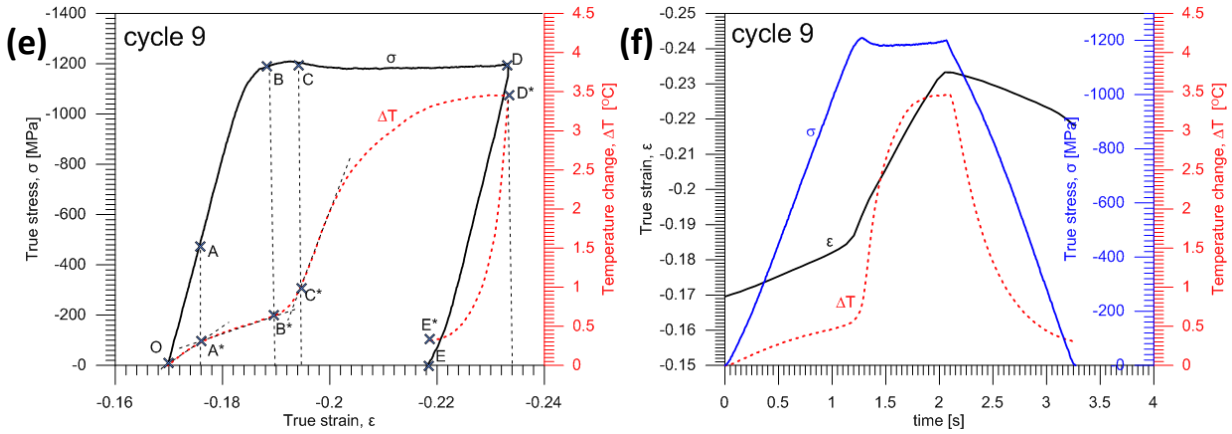

Fig. 5.17. True stress σ and temperature change ΔT vs. true strain ε and true strain ε, true stress σ and temperature change ΔT vs. time for (a, b) cycle 5 (c, d) cycle 7 and (e, f) cycle 9.

Thermal responses of Gum Metal, recorded in cycles 5, 7 and 9, show similar temperature change slopes in the initial stage of loading. However the thermal profile determined for cycle 9 seem to have rounder slopes, probably as a result of accumulated plastic deformation induced during previous loading cycles.

In general, during compression a thermal response of a given material is growing when loaded and decreasing when unloaded. Gum Metal is characterized with a large recoverable strain, which is a sum of elastic and superelastic-like deformation as described in the previous chapter. Thermoelastic effect, in the very initial stage of loading, is expressed by Kelvin's formula. Looking at the temperature change curves for cycles 5, 7 and 9 in the initial stage of loading one can notice slope changes marked with A*, B* and C* and related stress values marked with A, B and C. Point A* can be associated with the thermoelastic effect and can determine the purely elastic limit of Gum Metal deformation. Further change of slope between A*-B* can be related to dissipative character of stress-induced activity of martensite-like α'' nanodomains. The next change of the thermal slope B*-C* is related to yielding. Further fast increase of the temperature change is a result of plastic deformation of Gum Metal. The temperature change during unloading of the alloy is difficult to be assessed due to an intensive thermal exchange with surroundings. Nevertheless, the temperature slope in the final phase of unloading might be associated to the thermoelastic effect. Selected loading stages can be correlated with specific thermal responses as marked by capital letters in Fig. 5.17 (a, c and e) and summarized in Table 5.4.

Table 5.4 Selected loading stages correlated with specific thermal responses as marked by capital letters in Fig. 5.17.

Loading stage		**Temperature change**	
O-A	Elastic deformation	**O*-A***	Growth due to thermoelastic effect
A-B	Superelastic-like deformation	**A*-B***	Growth with a decreased rate of temperature change
B-C	Yielding	**B*-C***	Moderate growth
C-D	Plastic deformation	**C*-D***	Fast growth
D-E	Recoverable unloading	**D*-E***	Decrease of temperature change affected by heat exchange with surroundings

Strain and temperature change vs. time of an advanced cyclic deformation of Gum Metal selected for analysis of strain ε_{yy} (O-7) and temperature ΔT (O-7*) fields for cycle 8 at selected stages of loading is presented in Fig. 5.18.

As presented in Fig. 5.18. during the elastic deformation of Gum Metal (O) – (1), there is a growth of temperature (O) – (1*) due to thermoelastic effect. The subsequent superelastic-like deformation is related to the decrease in the rate of the temperature growth (1*) – (2*). During yielding of Gum Metal (2) – (3), a moderate temperature growth (2*) – (3*) is observed. Next stage of plastic deformation of the alloy (3) – (4) – (5) is accompanied by a fast growth of temperature (3*) – (4*) – (5*). The recoverable compressive unloading of Gum Metal (5) – (6) – (7) is connected to the decrease of temperature change affected by heat exchange with surroundings (5*) – (6*) – (7*) and probably a reflection of endothermic reverse phase transition.

Selected stages of compression marked in Fig. 5.18 are listed in table 5.5.

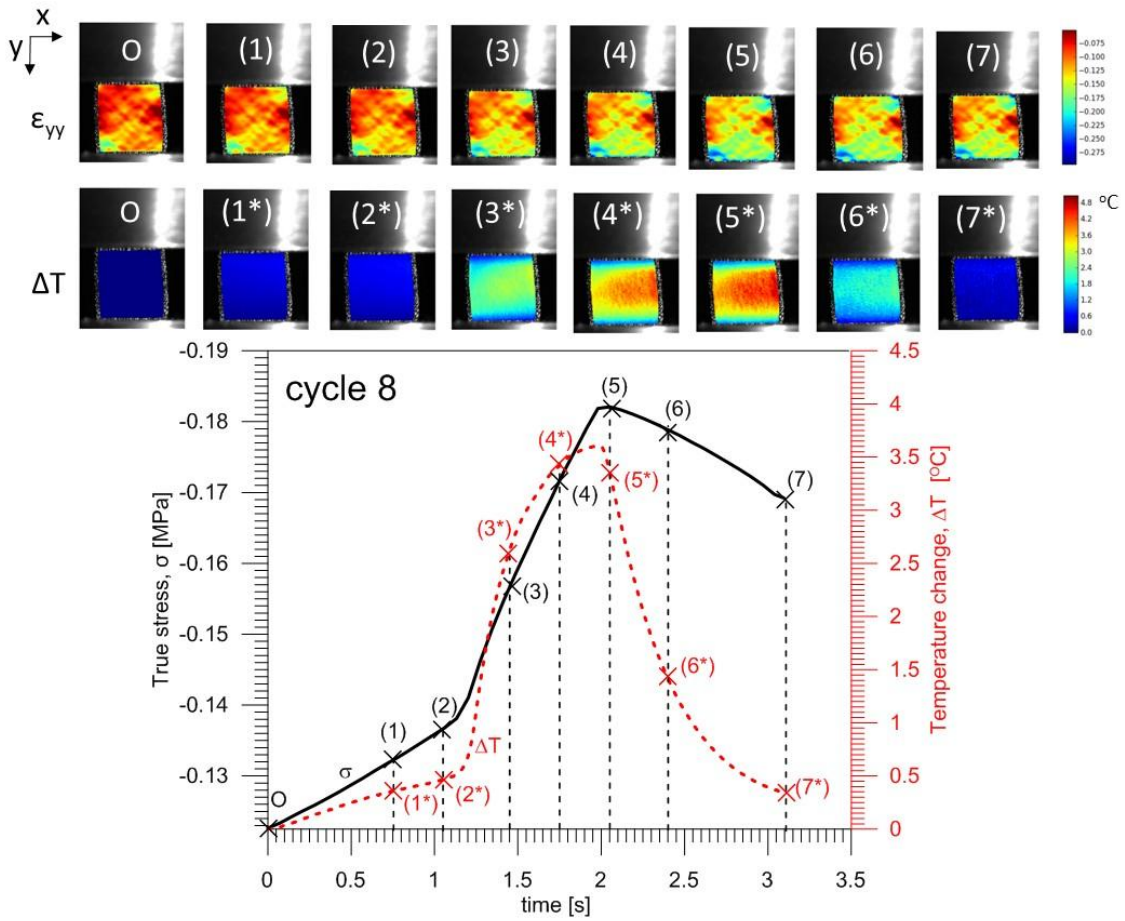

Fig. 5.18. True strain ε and temperature change ΔT vs. time for cycle 8 of Gum Metal compressive loading with strain distributions (O-7) and thermograms (O-7*) corresponding to selected stages of compression.

Table 5.5 Selected loading stages correlated with specific thermal responses as marked by numbers in Fig. 5.18.

Loading stage		**Temperature change**	
(O) – (1)	Elastic deformation	**(O) – (1*)**	Growth due to thermoelastic effect
(1) – (2)	Superelastic-like deformation	**(1*) – (2*)**	Growth with a decreased rate of temperature change
(2) – (3)	Yielding	**(2*) – (3*)**	Moderate growth
(3) – (4) – (5)	Plastic deformation	**(3*) – (4*) – (5*)**	Fast growth
(5) – (6) – (7)	Recoverable unloading	**(5*) – (6*) – (7*)**	Decrease of temperature change affected by heat exchange with surroundings

5.5 Summary

Results of experimental investigation of Gum Metal mechanical anisotropy were reported. Structural analysis performed on Gum Metal samples revealed almost pure β phase with a potential trace composition of hexagonal ω phase (XRD patterns). The microscopic observations showed elongated grains with fiber-like structures and significant misorientation (EBSD boundary maps). Texture analysis indicated a pronounced <110> texture induced during the process of cold swaging. The elastic anisotropy of Gum Metal was evaluated by a nondestructive ultrasonic technique. The results demonstrated a significant difference between the Young's moduli determined in the cold-swaging and perpendicular directions. The mechanical anisotropy of Gum Metal under compression was analyzed with a special focus on its plastic behavior. Significant difference between mechanical characteristics obtained for Gum Metal samples with two orientations during the compression was observed. The strain fields determined by DIC with the aid of two cameras observing perpendicular surfaces (walls) of the sample indicated clearly dissimilar characters of deformation. In the case of Gum Metal compressed in perpendicular direction shear formation was seen, while in the case of Gum Metal compressed in parallel direction distinct character. This is caused by a transversal isotropy of the polycrystalline Gum Metal rod texturized in <110> direction via the cold swaging process. The transversal isotropy of the alloy was confirmed by analysis of both the EBSD and ultrasonic test results. Additional cyclic compressive loading of Gum Metal conducted along its swaging direction confirmed the unique mechanical performance of Gum Metal, i.e. low Young's modulus and high strength. The curves profiles change significantly with each cycle and reveal clearly pronounced yield points starting in cycle 4 and developing in further cycles. Hardening phenomena of the alloy were observed at subsequent loading cycles increasing maximal stress values. Analysis of strain distributions during the cyclic compression of Gum Metal showed that, from the very beginning, the deformation process proceeds in a non-uniform way. It was seen, that the deformation was localized in the two zones of intersecting, macroscopic shear bands. Analysis of thermomechanical coupling during the cyclic loading of Gum Metal was presented. A thermal response of the alloy under loading served to determine critical stages and transition points of its unique mechanical behavior. Infrared thermography was successfully applied to study the thermal nature of unconventional deformation mechanisms occurring in Gum Metal subjected to compressive

loading. The technique of infrared thermography was successfully applied to determine temperature change of Gum Metal under compression and identify selected stages of loading. In particular, the thermomechanical nature of the unconventional deformation mechanisms namely *α"* martensite-like nanodomains activated in Gum Metal under loading was analyzed. The changes of the temperature slope were discussed in terms of being indicators of subsequent stages of Gum Metal deformation.

Chapter 6

6 Conclusions

6.1 Summary

A brief history of advancements in the development of Ti-based materials with special focused on shape memory and superelastic alloys and a detailed background of an innovative alloy Gum Metal with an up-to-date literature review was given in Chapter 1. Outstanding mechanical characteristics of Gum Metal, including its low Young's modulus, relatively large, nonlinear, mechanically recoverable deformation and high strength, were described. A role and an origin of unconventional deformation mechanisms, namely stress-induced activity of martensitic-like nanodomains and omega nanoprecipitates, were discussed. Applications and potential use of Gum Metal as a multifunctional alloy, applied in a variety of engineering solutions, was presented.

A methodology applied for determination of thermomechanical couplings in Gum Metal under loading was given in Chapter 2. Fundamentals of thermomechanical couplings in metals were described in the view of exemplary experimental results including use of novel full-field techniques. Experimental methodology applied for determination of mechanical characteristics and temperature change of Gum Metal under loading with their further coupling was presented.

Results of preliminary investigation of Gum Metal specimens realized using an IRT technique during the deformation of the alloy was presented in Chapter 3. Mechanical behavior of the alloy was analyzed based on the obtained stress vs. strain characteristics. The activity of unconventional deformation mechanisms during monotonic and cyclic deformation of Gum Metal was investigated based on the obtained stress and temperature change vs. strain characteristics. Thermomechanical behavior of Gum Metal under monotonic tension up to rupture at two strain rates was compared. Thermograms captured at selected stages of the loading process for monotonic and cyclic tension served to analyze homogeneity of the deformation of Gum Metal.

Interesting results of the preliminary investigation of the effects of thermomechanical couplings in Gum Metal under monotonic and cyclic tension presented in Chapter 3 were a motivation to conduct a more comprehensive study on a different set of Gum Metal specimens. In Chapter 4, an analysis of Gum Metal specimens subjected to selected tensile

loading programs using DIC and IRT was provided. Strain rate sensitivity of Gum Metal under tension up to rupture was analyzed based on stress vs. strain curves and Hencky strain as well as deformation rate tensor distributions determined for selected stages of the loading process. The activity of unconventional deformation mechanisms during monotonic and cyclic deformation of Gum Metal was analyzed based on the obtained stress and temperature change vs. strain characteristics. Thermomechanical behavior of Gum Metal under monotonic tension up to rupture at two strain rates was compared. Thermograms captured at selected stages of the loading process for monotonic and cyclic tension served to analyze homogeneity of the deformation of Gum Metal. Finally, the estimation of energy balance, including a rough determination of stored energy, was performed for 24 subsequent loading-unloading cycles of Gum Metal. The results allowed to better understand the nature of deformation mechanisms involved in the deformation process of the alloy.

Results of experimental investigation of Gum Metal mechanical anisotropy caused by cold swaging process were reported in Chapter 5. Texture analysis of Gum Metal rod was conducted using EBSD. The elastic anisotropy of Gum Metal was evaluated by a nondestructive ultrasonic technique. Elastic constants of the alloy were explicitly determined. The mechanical anisotropy of Gum Metal under compression was analyzed with a special focus on its plastic behavior. A comparison of mechanical characteristics obtained for Gum Metal samples with two orientations during the compression tests was discussed. The deformation fields determined by DIC with the aid of two cameras observing perpendicular surfaces (walls) of samples at selected stages of Gum Metal loading were analyzed.

Furthermore, the investigation of Gum Metal samples under compressive cyclic loading was performed using DIC and IRT simultaneously. The activity of unconventional deformation mechanisms during the deformation of Gum Metal was analyzed based on the obtained stress and temperature change vs. strain characteristics. The changes of the temperature slope were discussed in terms of being indicators of subsequent stages of Gum Metal deformation. Thermograms as well strain distributions determined for selected stages of the loading process served to analyze homogeneity of the deformation of Gum Metal.

6.2 Original elements of the dissertation

1. Investigation of thermoelastic effect in Gum Metal under monotonic tension at different strain rates and cyclic tension with further determination of purely elastic regime of Gum Metal deformation.

2. Thermomechanical analysis of unconventional deformation mechanisms of Gum Metal manifested during its superelastic-like deformation based on stress and temperature change vs. strain characteristics obtained for selected loadings.

3. Investigation of strain rate sensitivity of Gum Metal under monotonic tension at selected strain rates using full-field techniques of infrared thermography and digital image correlation. Analysis of development of strain, deformation rate tensor and temperature fields during loading of the alloy resulting in damage and rupture.

4. Estimation and analysis of energy balance in Gum Metal under cyclic tension.

5. Experimental investigation of mechanical anisotropy of Gum Metal using ultrasonic measurements and in-situ compression tests.

6.3 Main results of the dissertation

1. The analysis of the thermal responses of Gum Metal in subsequent tensile cycles show that the specimen temperature during loading reaches minimum at significantly lower strain than the recoverable strain limit.

2. It was demonstrated that the mechanically recoverable deformation of Gum Metal is recoverable from the thermodynamic viewpoint.

3. The activity of stress-induced unconventional deformation mechanisms of Gum Metal was found to be exothermic during the loading and endothermic during unloading of the alloy.

4. It was presented that Gum Metal is highly sensitive to the strain rate applied during its loading and deformation. The effect was manifested by both mechanical and thermal responses of the alloy subjected to monotonic tension at various strain rates. In particular, the analysis of the evolutions of deformation and temperature fields

captured at selected stages of Gum Metal tension was important for understanding the strain rate sensitivity of the alloy exhibited particularly in the plastic regime of deformation.

5. Mechanical anisotropy of Gum Metal was experimentally proved. The elastic anisotropy of Gum Metal was evaluated by ultrasonic testing. The results demonstrated a significant difference between the Young's moduli determined in the cold-swaging and perpendicular directions. The mechanical anisotropy of Gum Metal under compressive loading was analyzed with a special focus on its plastic behavior. Significant difference between mechanical characteristics and dissimilar characters of the deformation fields obtained for Gum Metal samples with two orientations during the compression was demonstrated.

6. The effect of cyclic compressive loading of Gum Metal conducted along its swaging direction was discussed by analyzing effects of thermomechanical couplings obtained with a high sensitivity. Hardening phenomena of the alloy in subsequent loading cycles was revealed. Clearly pronounced yield point were presented. A thermal response of Gum metal under compressive loading served to determine critical stages and transition points of the Gum Metal unique mechanical behavior.

6.4 Plans for future studies

During the studies realized in the scope of this dissertation additional research questions and directions have been formulated.

1. The superelastic-like behavior of Gum Metal appears in the alloy after applying the process of cold-working (usually up to 90% in area reduction) during its fabrication. It would be interesting to conduct experimental investigation of thermomechanical couplings in non-cold-worked Gum Metal specimens under selected loadings and compare the results with those obtained in this dissertation for cold-worked Gum Metal specimens.

2. Another important factor shaping the mechanical properties of Gum Metal is its chemical composition. In particular the oxygen content over 1% in at. % hinders the stress-induced long-range phase transformation in the alloy subjected to loading.

Thus, it would be interesting to conduct research on Gum Metal specimens with various oxygen content. In this dissertation Gum Metal with composition Ti-23Nb-0.7Ta-2Zr-1.2O (at. %) was investigated. Future studies could be realized using specimens of selected alloys with compositions Ti-23Nb-0.7Ta-2Zr- x O (where x = 0, 0.3, 0.5, 0.8, 1; at. %). Analysis of thermomechanical couplings in this set of alloys using full-field techniques of IRT and DIC would contribute to understanding of nucleation and development of phase transformations induced in the alloys during loading.

3. Very recent developments of Ti-based alloys resulted in design and fabrication of materials with extremely low Young's modulus (around 30 GPa) and high strength (around 800 MPa). It was achieved by tuning the chemical composition of the alloys and substituting oxygen content present in Gum Metal by nitrogen. The general mechanical performance of the new alloys is similar to Gum Metal. However, it would be intriguing to investigate the activity of deformation mechanisms in particular, the stress-induced phase transitions, on the grounds of thermomechanical couplings.

4. Results presented in this dissertation deal with investigation of strain-rate sensitivity of Gum Metal under tension at selected strain rates in the quasi-static range (10^{-5} s^{-1}, 10^{-4} s^{-1}, 10^{-3} s^{-1}, 10^{-2} s^{-1} and 10^{-1} s^{-1}). It is worth conducting mechanical testing of Gum Metal under dynamic (10^{1} s^{-1}, 10^{2} s^{-1}, 10^{3} s^{-1} and 10^{4} s^{-1}) loading in order to comprehensively understand the mechanical performance of the alloy. These tasks are being realized in the scope of a project funded by National Science Centre, Poland, no. 2017/27/B/ST8/03074, coordinated by Elżbieta A. Pieczyska, Ph.D., Dr. Habil., Eng.

References

[1] Arrazola P.-J., Garay A., Iriarte L.-M., Armendia M., Marya S., Le Maître F., Machinability of titanium alloys (Ti6Al4V and Ti555.3), *Journal of Materials Processing Technology* 209, 5, 2223-2230, 2009.

[2] Ashby M., *Materials Selection in Mechanical Design 5th Edition*, Butterworth-Heinemann, 2016.

[3] Auld B.A., Acoustic Fields and Waves in Solids, Malabar, FL: Krieger Publishing Company, 1990.

[4] Badulescu C., Grediac M., Haddadi H., Mathias J.-D., Balandraud X., Tran H.-S., Applying the grid method and infrared thermography to investigate plastic deformation in aluminium multicrystal, *Mechanics of Materials* 43, 36–53, 2011.

[5] Banerjee S., Mukhopadhyay P., *Phase Transformations, Volume 12 1st Edition Examples from Titanium and Zirconium Alloys,* Oxford: Elsevier Science, 2007

[6] Banerjee S., Williams J.C., Perspectives on Titanium Science and Technology, *Acta Materialia* 61, 3, 844-879, 2013.

[7] Beghi M.G., Bottani C.E., Caglioti G., Irreversible thermodynamics of metals under stress, *Res Mechanica* 19, 365-379, 1986.

[8] Bever M. B., Holt, D. L., Titchener, A. L., The Stored Energy of Cold Work. *Progress in Materials Science, 1st edn*. Pergamon Press Ltd, Oxford, 1973.

[9] Buehler W. J., Gilfrich J. V., Wiley R. C., Effect of Low-Temperature Phase Changes on the Mechanical Properties of Alloys near Composition TiNi, *Journal of Applied Physics* 34, 1475, 1963.

[10] Chrysochoos A., Martin G., Tensile test microcalorimetry for thermomechanical behaviour law analysis, Materials Science and Engineering: A 108, 25-32, 1989a.

[11] Chrysochoos A., Maisonneuve O., Martin G., Caumon H., Chezeaux J.C., Plastic and dissipated work and stored energy, Nuclear Engineering and Design 114, 3, 323-333, 1989b.

[12] Chrysochoos A., Dupre J.C., Experimental Analysis of Thermomechanical Coupling by Infra-Red Thermography. In: Boehler JP., Khan A.S. (eds) Anisotropy and Localization of Plastic Deformation. Springer, Dordrecht, 1991.

[13] Chrysochoos A., Belmahjoub F., Thermographic analysis of thermomechanical couplings, Archives of Mechanics 44, 1, 55-68, 1992.

[14] Chrysochoos A., Louche H., An infrared image processing to analyse the calorific effects accompanying strain localisation, International Journal of Engineering Science 38, 16, 1759-1788, 2000.

[15] Chrysochoos A., Infrared imaging and thermomechanical behaviour of solid materials, Quantitative InfraRed Thermography (QIRT) conference 2000 proceedings, Reims, http://dx.doi.org/10.21611/qirt.2000.050.

[16] Chrysochoos A., Thermomechanical analysis of the cyclic behavior of materials, Procedia IUTAM, 4, 15-26, 2012.

[17] Chrysochoos A., Huon V., Jourdan F., Muracciole J.-M., Peyroux R., Wattrisse B., Use of Full-Field Digital Image Correlation and Infrared Thermography Measurements for the Thermomechanical Analysis of Material Behaviour, *Strain* 46, 1, 117-130, 2010.

[18] Chrysochoos A., Infrared thermography applied to the analysis of material behaviour: a brief overview, *Quantitative InfraRed Thermography Journal*, 2012, 9, 2, 193-208, 2012.

[19] Chrzan D.C., Sherburne M.P., Hanlumyuang Y., Li T., Morris, Jr. J.W., Spreading of dislocation cores in elastically anisotropic body-centered-cubic materials: The case of gum metal, *Physical Review B* 82, 184202, 2010.

[20] Daly S., Ravichandran G., Bhattacharya K., Stress-induced martensitic phase transformation in thin sheets of Nitinol, *Acta Materialia* 55, 10, 3593-3600, 2007.

[21] Delpueyo D., Grédiac M., Balandraud X., Badulescu C., Investigation of martensitic microstructures in a monocrystalline Cu–Al–Be shape memory alloy with the grid method and infrared thermography, *Mechanics of Materials* 45, 34-51, 2012.

[22] Denkhaus E., Salnikow K., Nickel essentiality, toxicity, and carcinogenicity, *Critical reviews in oncology/hematology* 42, 1, 35–56, 2002.

[23] Farren, W., Taylor, G. I. The heat developed during plastic extension of metals, *Proceedings of the Royal Society A: Mathematical, Physical and Engieneering Sciences* 107, 422–451, 1925

[24] Furuta T., Kuramoto S., Hwang J., Nishino K., Saito T., Elastic Deformation Behavior of Multi-Functional Ti–Nb–Ta–Zr–O Alloys, *Materials Transactions* 46, 12, 3001-3007, 2005

[25] Furuta T., Kuramoto S., Morris J.W., Nagasako N., Withey E., Chrzan D.C., The mechanism of strength and deformation in Gum Metal, *Scripta Materialia* 68, 767–772, 2013

[26] Gadaj S.P., Gałkowska E., Kaczmarek J., Oliferuk W., Wyznaczanie energii zmagazynowanej w metalu podczas procesu rozciągania, *Prace IPPT - IFTR Reports* 36, 1-24, 1981

[27] Gadaj S.P., Kaczmarek J., Oliferuk W., Proces magazynowania energii podczas rozciągania metalu, *Prace IPPT - IFTR Reports* 28, 1-13, 1983a

[28] Gadaj S.P., Kaczmarek J., Oliferuk W., Pieczyska E., Wpływ obróbki powierzchniowej na proces magazynowania energii podczas rozciągania stali 1H18N9T, *Prace IPPT - IFTR Reports* 28, 1-9, 1983b

[29] Golasiński K., Pieczyska E., Maj M., Staszczak M., Takesue N., Investigation of Gum Metal under compressive cyclic loading, Plastmet 2016, Jubileuszowe X Seminarium Naukowe ZINTEGROWANE STUDIA PODSTAW DEFORMACJI PLASTYCZNEJ METALI, 2016-11-22/11-25, Łańcut (PL), 41-42, 2016c

[30] Golasiński K., Pieczyska E., Maj M., Staszczak M., Takesue N., Superelastic-like behavior of Gum Metal under compression inspected by infrared thermography, 11th European Symposium on Martensitic Transformations, 2018-08-27/08-31, Metz (FR), 84, 2018b

[31] Golasiński K., Pieczyska E., Staszczak M., Cristea M., Experimental investigation of thermomechanical properties of multifunctional materials at IPPT PAN, MACRO Iasi, The XXVI-th Symposium PROGRESS IN ORGANIC AND POLYMER CHEMISTRY, 2017-10-05/10-06, Jassy (RO), 1, 2017b

[32] Golasiński K., Pieczyska E., Staszczak M., Furuta T., Kuramoto S., Thermomechanical Investigation of Gum Metal – a New Innovative Titanium Alloy for Biomedical Applications, The 10th International Congress of Societas Humboldtiana Polonorum “Longevity - a blessing or a curse”, 2016-06-30/07-02, Łódź (PL), 43, 2016a

[33] Golasiński K., Pieczyska E., Staszczak M., Maj M., Furuta T., Kuramoto S., Thermomechanical behavior of gum metal under cyclic loading, SolMech 2016, 40th Solid Mechanics Conference, 2016-08-29/09-02, Warszawa (PL), P208, 1-2, 2016b

[34] Golasiński K., Pieczyska E.A., Mackiewicz S., Staszczak M., Zubko M., Takesue N., Analysis Gum Metal crystallographic texture and misorientation in correlation to its

mechanical behavior, XXIV CONFERENCE ON APPLIED CRYSTALLOGRAPHY, 2018-09-02/09-06, Arłamów (PL), OY1-5, 37-38, 2018a

[35] Golasiński K.M., Pieczyska E., Detsch R., Boccaccini A.R., Takesue N., Evaluation of mechanical properties and biocompatibility of Gum Metal for implant applications, 7th KMM-VIN Industrial Workshop: Biomaterials: Key Technologies for Better Healthcare, 2017-09-27/09-28, Erlangen (DE), 46, 2017c

[36] Golasiński K.M., Pieczyska E.A., Maj M., Staszczak M., Takesue N., Unique mechanical performance of an innovative Ti-based superalloy Gum Metal under compression, International Scientific Conference Humboldt-Kolleg Limits of Knowledge, 2017-06-22/06-25, Cracow (PL), P35-NS, 218-219, 2017d

[37] Golasiński K.M., Pieczyska E.A.., Staszczak M., Maj M., Furuta T., Kuramoto S., Infrared thermography applied for experimental investigation of thermomechanical couplings in Gum Metal, Quantitative InfraRed Thermography Journal, 14, 2, 226-233, 2017a

[38] Golasiński K., Pieczyska E., Maj M., Staszczak M., Takesue N., Thermomechanical behavior of gum metal under cyclic compression, PCM-CMM, 4th Polish Congress of Mechanics 23rd International Conference on Computer Methods in Mechanics, 2019-09-08/09-12, Kraków (PL), 2019a.

[39] Golasiński K., Pieczyska E., Maj M., Mackiewicz S., Staszczak M., Zubko M., Takesue N., Elastic and plastic anisotropy of gum metal investigated by ultrasound measurements and digital image correlation, ISMMS, 10th International Symposium on Mechanics of Materials and Structures, 2019-06-02/06-06, Augustów (PL), pp.43-44, 2019b

[40] Golasiński K., Pieczyska E., Polish-Japanese Joint Research on a Multifunctional Titanium Alloy Gum Metal, 11. Kongres Societas Humboldtiana Polonorum Nauka w dobie globalizacji, Szczecin (PL), 2019-09-12/09-15, 2019c

[41] Golasiński K., Pieczyska E., Maj M., Mackiewicz S., Staszczak M., Kowalewski Z., Urbański L., Zubko M., Takesue N., Anisotropy of Gum Metal analysed by ultrasonic measurement and digital image correlation, MATERIALS SCIENCE AND TECHNOLOGY, pp.1-7, 2019d

[42] Gordin D.M., Ion R., Vasilescu C., Drob S.I., Cimpean A., Gloriant T., Potentiality of the “Gum Metal” titanium-based alloy for biomedical applications, *Materials Science and Engineering: C* 44, 362-370, 2014.

[43] Gutkin M.Y., Ishizaki T., Kuramoto S., Ovidko I.A., Skiba N.V., Giant faults in deformed Gum Metal, *International Journal of Plasticity* 24, 8, 1333-1359, 2008.

[44] Hwang J., Kuramoto S., Furuta T., Nishino K., Saito T., Phase-Stability Dependence of Plastic Deformation Behavior in Ti-Nb-Ta-Zr-O Alloys, *Journal of Materials Engineering and Performance* 14, 6, 747-754, 2005

[45] Ikehata H., Nagasako N., Furuta T., Fukumoto A., Miwa K., Saito T., First-principles calculations for development of low elastic modulus Ti alloys, *Physical Review B* 70, 174113, 2004.

[46] Kim H.Y., Hashimoto S., Kim J.I., Hosoda H., Miyazaki S., Mechanical properties and shape memory behavior of Ti-Nb alloys, Materials transactions 45 (7), 2443-2448 (2004).

[47] Kim H.Y., Ikehara Y., Kim J.I., Hosoda H., Miyazaki S., Martensitic transformation, shape memory effect and superelasticity of Ti–Nb binary alloys, *Acta Materialia* 54, 9, 2419-2429, 2006.

[48] Kim H.Y., Miyazaki S., Shape Memory and Superelasticity, 2, 4, 380–390, 2016.

[49] Kim H.Y., Wei L., Kobayashi S., Tahara M., Miyazaki S., Nanodomain structure and its effect on abnormal thermal expansion behavior of a Ti–23Nb–2Zr–0.7 Ta–1.2 O alloy, *Acta Materialia* 61, 13, 4874-4886, 2013.

[50] Klepaczko J.R., Sprzężenia termomechaniczne w metalach, Instytut Podstawowych Problemów Techniki PAN, 1978.

[51] Kowalczyk-Gajewska K., Pieczyska E.A., Golasiński K., Maj M., Kuramoto S., Furuta T., A finite strain elastic-viscoplastic model of Gum Metal, *International Journal of Plasticity*, 2019 (In press)

[52] Kudoh Y., Tokonami M., Miyazaki S., Otsuka K., Crystal structure of the martensite in Ti-49.2 at.% Ni alloy analyzed by the single crystal X-ray diffraction method, *Acta Metallurgica* 33, 11, 2049-2056, 1985.

[53] Kumar J., Baby S., Kumar V., Thermographic studies on IMI-834 titanium alloy during tensile loading, *Material Science and Engineering A* 496 303–307, 2008.

[54] Kuramoto S., Furuta T., Hwang J., Nishino K., Saito T., Elastic properties of Gum Metal, *Materials Science and Engineering A* 442, 454 – 457, 2006a.

[55] Kuramoto S., Furuta T., Hwang J., Nishino K., Saito T., Plastic deformation in a multifunctional Ti-Nb-Ta-Zr-O alloy, *Metallurgical and Materials Transactions A* 37, 3, 657–662, 2006b.

[56] Kuroda D., Niinomi M., Morinagac M., Katod Y., Yashirod T., Design and mechanical properties of new β type titanium alloys for implant materials, *Materials Science and Engineering: A* 243, 1–2, 244-249, 1998.

[57] Kwon Y.K., Pyda M., Wunderlich B., Multi-frequency sawtooth modulation of a power-compensation differential scanning calorimeter, *Thermochimica Acta* 367, 203-215, 2001.

[58] Lai M.J., Li T., Raabe D., ω phase acts as a switch between dislocation channeling and joint twinning- and transformation-induced plasticity in a metastable β titanium alloy, *Acta Materialia* 151, 67-77, 2018.

[59] Lai M.J., Tasan C.C., Raabe D., Deformation mechanism of ω-enriched Ti–Nb-based gum metal: Dislocation channeling and deformation induced ω–β transformation, *Acta Materialia* 100, 290-300, 2015.

[60] Leyens C., Peters M., *Titanium and titanium alloys*, Weinheim: Wiley-VCH, 2003.

[61] Leyens C., Peters M., *Titanium and Titanium Alloys: Fundamentals and Applications,* Wiley-VCH Verlag GmbH & Co. KGaA, 2003.

[62] Leclercq S., Lexcellent C., A general macroscopic description of the thermomechanical behavior of shape memory alloys, *Journal of the Mechanics and Physics of Solids* 44, 6, 953-980, 1996.

[63] Litwinko R., Oliferuk W., Yield point determination based on thermomechanical behaviour of polycrystalline material under uniaxial loading, *Acta mechanica et automatica,* 3, 4, 1-3, 2009

[64] Louche H., Chrysochoos A., Thermal and dissipative effects accompanying Lüders band propagation, Materials Science and Engineering: A 307, 1–2, 15-22, 2001.

[65] Lutjering G., Williams J.C., *Titanium. 2nd ed.*, Berlin: Springer, 2007.

[66] Tane M., Nakano T., Kuramoto S., Hara M., Niinomi M., Takesue N., Yano T., Nakajima H., Low Young's modulus in Ti–Nb–Ta–Zr–O alloys: Cold working and oxygen effects, *Acta Materialia* 59, 18, 6975-6988, 2011.

[67] Tane M., Nakano T., Kuramoto S., Hara M., Niinomi M., Takesue N., Yano T., Nakajima H., ω Transformation in cold-worked Ti–Nb–Ta–Zr–O alloys with low body-centered cubic phase stability and its correlation with their elastic properties, *Acta Materialia* 61, 1, 139-150, 2013.

[68] Majumdar P., Singh S.B., Chakraborty M., Elastic modulus of biomedical titanium alloys by nano-indentation and ultrasonic techniques—A comparative study*, Materials Science and Engineering: A*, 489 1–2, 419-425*,* 2008.

[69] Merzlyakov M., Schick C., Step response analysis in DSC — a fast way to generate heat capacity spectra, *Thermochimica Acta* 380, 1, 5-12, 2001

[70] Merzlyakov M., Schick C., Thermochim. Complex heat capacity measurements by TMDSC. Part 2. Algorithm for amplitude and phase angle correction, *Acta* 330 65-73, 1999

[71] Miyazaki S., Kim H.Y., Hosoda H., Development and characterization of Ni-free Ti-base shape memory and superelastic alloys, *Materials Science and Engineering: A*, 438, 18-24, 2006.

[72] Miyazaki S., My Experience with Ti–Ni-Based and Ti-Based Shape Memory Alloys, *Shape Memory and Superelasticity* 3, 279–314, 2017.

[73] Miyazaki S., Otsuka K., Development of shape memory alloys, *Isij International* 29, 5, 353-377, 1989a.

[74] Miyazaki S., Otsuka K., Suzuki Y., Transformation pseudoelasticity and deformation behavior in a Ti-50.6 at% Ni alloy, *Scripta Metallurgica* 15, 3, 287-292, 1981a.

[75] Kim J.I., Miyazaki S., Effect of nano-scaled precipitates on shape memory behavior of Ti–50.9at%Ni alloy, Acta Materialia 53, 4545–4554, 2005a.

[76] Kim J.I., Miyazaki S., Comparison of shape memory characteristics of a Ti–50.9 At. Pct Ni alloy aged at 473 and 673 K, Metallurgical and Materials Transactions A 36, 3301–3310, 2005b.

[77] Kim J.I., Liu Y., Miyazaki S., Ageing-inducede two-stage R-phase transformation in Ti–50.9at%Ni, Acta Materialia 52, 487–499, 2004.

[78] Miyazaki S., Imai T., Otsuka K., Suzuki Y., Luders-like deformation in the transformation pseudoelasticity of a Ti–Ni alloy, Scripta Metallurgica 15, 853–856, 1981b.

[79] Miyazaki S., Ohmi Y., Otsuka K., Suzuki Y., Characteristics of deformation and transformation pseudoelasticity in Ti–Ni alloys, *Journal de Physique Colloques* 43 (Suppl. 12) C4-255–C4-260, 1982.

[80] Miyazaki S., Imai T, Igo Y., Otsuka K., Effect of cyclic deformation on the pseudoelasticity characteristics of Ti-Ni alloys, *Metallurgical Transactions A* 17, 1, 115–120, 1986.

[81] Miyazaki S., Kimura S., Otsuka K., Suzuki Y., The habit plane and transformation strains associated with the martensitic transformation in Ti–Ni single crystals, *Scripta Metallurgica* 18, 883–888, 1984.

[82] Miyazaki S., Otsuka K., Deformation and transformation behavior associated with the R-phase in Ti–Ni alloys, *Metallurgical Transactions A* 17, 53–63, 1986

[83] Miyazaki S., Kimura S., Takei F., Miura T., Otsuka K., Suzuki Y., Shape memory effect and pseudoelasticity in a Ti–Ni single crystal, Scripta Metallurgica 17, 1057–1062, 1983

[84] Miyazaki S., Otsuka K., Wayman C.M., The shape memory mechanism associated with the martensitic transformation in Ti– Ni alloys: part I: self-accommodation. Acta Metallurgica 37, 1873–1884, 1989b

[85] Miyazaki S., Otsuka K., Wayman C.M., The shape memory mechanism associated with the martensitic transformation in Ti– Ni alloys: part II: variants coalescence and shape recovery. Acta Metallurgica 37, 1885–1890, 1989c

[86] Takei F., Miura T., Miyazaki S., Kimura S., Otsuka K., Suzuki Y., Stress-induced martensitic transformation in a Ti–Ni single crystal, Scripta Metallurgica 17, 987–992, 1983

[87] Kudoh Y., Tokonami M., Miyazaki S., Otsuka K., Crystal structure of Ti–Ni martensite analyzed by the single crystal X-ray diffraction method, *Acta Metallurgica* 33, 2049–2056, 1985

[88] Moreau S., Chrysochoos A., Muracciole J.M., Wattrisse B., Analysis of thermoelastic effects accompanying the deformation of PMMA and PC polymers, *Comptes Rendus Mécanique*, 333, 8, 648-653, 2005.

[89] Morris Jr. J.W., Hanlumyuang Y., Sherburne M., Withey E., Chrzan D.C., Kuramoto S., Hayashi Y., Hara M., Anomalous transformation-induced deformation in 〈1 1 0〉 textured Gum Metal, *Acta Materialia* 58, 9, 3271-3280, 2010.

[90] Morris Jr. J.W., Hanlumyuang Y., Sherburne M., Withey E., Chrzan D.C., Kuramoto S., Hayashi Y., Hara M., Anomalous transformation-induced deformation in 〈1 1 0〉 textured Gum Metal, *Acta Materialia* 58, 9, 3271-3280, 2010.

[91] Nayroles B., Bouc R., Caumon H., Chezeaux J.-C., Giacometti E. Telethermographie infrarouge et mecanique des structures, *International Journal of Engineering Science* 19, 929–947, 1981.

[92] Niinomi M., Mechanical properties of biomedical titanium alloys, *Materials Science and Engineering: A* 243, 1–2, 231-236, 1998.

[93] Niinomi M., Nakai M., Hieda J., Development of new metallic alloys for biomedical applications, *Acta Biomaterialia* 8, 11, 3888-3903, 2012.

[94] Niinomi M., Boehlert C.J. Titanium Alloys for Biomedical Applications. In: Niinomi M., Narushima T., Nakai M. (eds) Advances in Metallic Biomaterials. Springer Series in Biomaterials Science and Engineering, vol 3. Springer, Berlin, Heidelberg, 2015.

[95] Nishino K., *R&D Review of Toyota CRDL* 38, 3, 50, 2003.

[96] Nowak M., Maj M., Determination of coupled mechanical and thermal fields using 2D digital image correlation and infrared thermography: Numerical procedures and results, *Archives of Civil and Mechanical Engineering* 18, 2 630–644, 2018.

[97] Oliferuk W., Experimental investigations of thermomechanical couplings in TiNi shape-memory alloy during a torsion - tension (compression) test, *Archives of Mechanics* 51, 6, 717-726, 1999.

[98] Oliferuk W., Maj M., Litwinko R., Urbański L., Thermomechanical coupling in the elastic regime and elasto-plastic transition during tension of austenitic steel, titanium and aluminium alloy at strain rates from 10^{-4} to 10^{-1} s^{-1}, *European Journal of Mechanics A-Solids* 35, 111-118 , 2012.

[99] Oliferuk W., Maj M., Zembrzycki K., Determination of the Energy Storage Rate Distribution in the Area of Strain Localization Using Infrared and Visible Imaging, *Experimental Mechanics* 55, 753-760, 2015.

[100] Oliferuk W., Proces magazynowania energii i jego strukturalny aspekt podczas jednoosiowego rozciągania stali austenitycznej, Rozprawa habilitacyjna, IFTR Reports, 1997.

[101] Oliferuk, W., Gadaj, S.P., Grabski, M.W., Energy storage during the tensile deformation of Armco iron and austenitic steel, *Materials Science and Engineering A* 70, 131–141, 1985.

[102] Oliferuk, W., Maj, M., Stress–strain curve and stored energy during uniaxial deformation of polycrystals, *European Journal of Mechanics A/Solids* 28, 2, 266–272, 2009.

[103] Peyroux R., Chrysochoos A., Licht C., Löbel M., THERMOMECHANICAL COUPLINGS AND PSEUDOELASTICITY OF SHAPE MEMORY ALLOYS, *International Journal of Engineering Science* 36, 4, 489-509, 1998.

[104] Pieczyska E.A., Critical Point of the Elastoplastic Transition in terms of Thermomechanical Coupling, *J. Theor. Appl. Mech.,* 2, 34, 281-306, 1996.

[105] Pieczyska E.A. and Gadaj S.P., Thermoelastic effect during tensile cyclic deformation, *Eng. Trans.,* 45, 2, 295-303, 1997a.

[106] Pieczyska E.A. and Gadaj S.P., *Thermoelastic effect behaviour during cyclic deformation*, 3rd EUROMECH Solid Mechanics Conference, Stockholm, 1997b.

[107] Pieczyska E.A., Gadaj S.P., Nowacki W., Investigation of thermomechanical coupling in an austenitic steel subjected to subsequent tensile deformation, *Proceedings of 11th International Conference of Experimental Mechanics*, Oxford, 681-685, 1998a

[108] Pieczyska E., Wpływ umocnienia cyklicznego materiału na efekt termosprężysty stali austenitycznej, Doctoral dissertation, Instytut Podstawowych Problemów Techniki Polskiej Akademii Nauk, 1998b.

[109] Pieczyska E.A., Thermoelastic effect in austenitic steel referred to its hardening, *Journal of Theoretical and Applied Mechanics* 2, 37, 349 – 368, 1999.

[110] Pieczyska E.A., Gadaj S.P., Nowacki W.K., Thermoelastic and thermoplastic effects investigated in steel, polyamide and shape memory alloys, *Proceedings of SPIE, Thermosense XXIV*, USA, 4710, 479-497, 2002.

[111] Pieczyska E.A., Gadaj S.P., Nowacki W.K., Tobushi H., Thermomechanical investigations of martensitic and reverse transformations in TiNi shape memory alloy, *Bulletin of the Polish Academy of Sciences: Technical Sciences* 52, 3, 165-171, 2004.

[112] Pieczyska E.A., Gadaj S.P., Nowacki W.K. and Tobushi H., Stress relaxation during superelastic behavior of TiNi SMA, *International Journal of Applied Electromagnetic & Mechanics*, 23, 3-8, 2006a.

[113] Pieczyska E.A., Tobushi H., Gadaj S.P. and Nowacki W.K., Superelastic deformation behaviors based on phase transformation bands in TiNi shape memory alloy, *Materials Transactions,* Special Issue on Shape Memory Alloys and Applications, 47, 3, 670-676, 2006b.

[114] Pieczyska E. A., Gadaj S. P., Nowacki W. K., Tobushi H., Phase-Transformation Fronts Evolution for Stress- and Strain-Controlled Tension Tests in TiNi Shape Memory Alloy, *Experimental Mechanics* 46, 4, 531–542, 2006c.

[115] Pieczyska E.A., Activity of stress-induced martensite transformation in TiNi shape memory alloy studied by infrared technique, *Journal of modern optics* 57, 18, 1700-1707, 2010.

[116] Pieczyska E.A., Tobushi H.., Kulasiński K., Development of transformation bands in TiNi SMA for various stress and strain rates studied by a fast and sensitive infrared camera, Smart materials and structures, 22, 3, 035007-1-8, 2013.

[117] Pieczyska E.A., Maj M., Furuta T., Kuramoto S., Gum Metal– unique properties and results of initialinvestigation of a new titanium alloy—extended paper. Advances in Mechanics: Theoretical, Computationaland Interdisciplinary; Kleiber, M., Burczyński, T., Wilde, K., Górski, J., Winkelmann, K., Smakosz, Ł., Eds.;CRC Press/Balkema, Taylor & Francis: London, UK, 469–47, 2016a.

[118] Pieczyska E., Golasiński K., Staszczak M., Maj M., Furuta T., Kuramoto S., High elasto-plastic properties of new titanium alloy gum metal in wide spectra of the strain rates, 17th International Conference on Experimental Mechanics, 2016-07-03/07-07, Rhodes (GR), 388, 1-2, 2016b.

[119] Pieczyska E.A., Golasiński K., Staszczak M., Maj M., Furuta T., Kuramoto S., Gum metal subjected to cyclic tension loading analysed by fast and sensitive infrared camera, ICMFM18, XVIII International Colloquium MECHANICAL FATIGUE OF METALS, 2016-09-05/09-07, Gijón (ES), 1, 2016c.

[120] Pieczyska E.A., Staszczak M., Golasiński K., Maj M., Tobushi H., Kuramoto S., Furuta T., Investigation of Shape Memory Alloys, Polymers and Gum Metals for Biomedical Applications, Materials Science and Nanoscience 2-d Global Congress and Expo, 2017-09-25/09-27, Valencia (ES), 1, 2017a.

[121] Pieczyska E.A., Golasiński K., Staszczak M., Maj M., Furuta T., Kuramoto S., A thermomechanical analysis of high elasto-plastic properties of gum metal at various strain rates, M2D, 7th International Conference on Mechanics and Materials in Design, 2017-06-11/06-15, Albufeira (PT), 393-394, 2017b.

[122] Pieczyska E.A., Maj M., Golasiński K., Staszczak M., Furuta T., Kuramoto S., Thermomechanical studies of yielding and strain localization phenomena of Gum Metal under tension, *Materials* 11, 567, 1-13, 2018a.

[123] Pieczyska E.A., Golasiński K., Maj M., Staszczak M., Kowalewski Z.L., Furuta T., Kuramoto S., Yielding and strain localization effects in gum metal - a unique ti alloy - investigated by digital image correlation and infrared thermography, 35th Danubia-Adria Symposium on Advances in Experimental Mechanics, 2018-09-25/09-28, Sinaia (RO), 57-58, 2018b.

[124] Pieczyska E., Golasiński K., Maj M., Staszczak M., Mackiewicz S., Zubko M., Takesue N., Gum metal in compression – investigation of mechanical anisotropy caused by texture, ICEM 2018, 18TH INTERNATIONAL CONFERENCE ON EXPERIMENTAL MECHANICS, 2018-07-01/07-05, BRUKSELA (BE), 454, 1-2, 2018c.

[125] Pieczyska E., Golasiński K., Maj M., Mackiewicz S., Staszczak M., Zubko M., Takesue N., Mechanical anisotropy of Gum Metal analyzed by ultrasonic measurements and digital image correlation, 41st SOLID MECHANICS CONFERENCE, 2018-08-27/08-31, Warszawa (PL), 352-353, 2018d.

[126] Plancher E., Tasan C.C., Sandloebes S., Raabe D., On dislocation involvement in Ti–Nb gum metal plasticity, *Scripta Materialia* 68, 10, 805-808, 2013.

[127] Ranc N., Wagner D., Some aspects of Portevin–Le Chatelier plastic instabilities investigated by infrared pyrometry, *Materials Science and Engineering: A* 394, 1–2, 2005, 87-95.

[128] Raniecki B., Lexcellent C., Tanaka K., Thermodynamic models of pseudoelastic behaviour of shape memory alloys, *Archives of Mechanics* 44, 3, 261-284, 1992.

[129] Rodriguez-Martinez J.A., Pesci R., Rusinek A., Experimental study on the martensitic transformation in AISI 304 steel sheets subjected to tension under wide ranges of strain rate at room temperature, *Materials Science and Engineering A* 528 5974–5982, 2011.

[130] Saito T., Furuta T., Hwang J.H., Kuramoto S., Nishino K., Suzuki N., Chen R., Yamada A., Ito K., Seno Y., Nonaka T., Ikehata H., Nagasako N., Iwamoto C., Ikuhara Y., Sakuma T., Multifunctional Alloys obtained via a dislocation free plastic deformation mechanism, *Science,* 300, 464-467, 2003.

[131] Saito T., Nishino K., Furuta T., Introduction of Gum Metal. Soft Modulus & Flexible Titanium Alloy. https://www.nissey-sabae.co.jp/past/pdf/eng_gummetal01.pdf, presentation.

[132] Saix C., Jouanna P., Analyse de la dissipation plastique par thermographie de surface, resultats experimentaux et modelisation, *Revue Roumaine des Sciences Techniques - Serie de Mecanique Appliquee* 25, 203,719. 1980

[133] Furuta T., Kuramoto S., Morris Jr J.W., Nagasako N., Withey E., Chrzan D.C., The mechanism of strength and deformation in Gum Metal, *Scripta Materialia* 68, 10, 767-772 (2013).

[134] Tahara M., Kim H.Y., Inamura T., Hosoda H., Miyazaki S., Role of interstitial atoms in the microstructure and non-linear elastic deformation behavior of Ti–Nb alloy, *Journal of Alloys and Compounds*, 577, Supplement 1, S404-S407, 2013.

[135] Takesue N., Shimizu Y., Yano T., Hara M., Kuramoto S., Single-crystal growth of Ti–Nb–Ta–Zr–O alloys and measurement of elastic properties, *Journal of Crystal Growth* 311, 12, 3319, 2009.

[136] Tanaka K., Kobayashi S., Sato Y., Thermomechanics of transformation pseudoelasticity and shape memory effect in alloys, *International Journal of Plasticity* 2, 1, 59-72, 1986.

[137] Taylor, G., Quinney, H. The latent energy remaining in a crystal after cold working. *Proceedings of the Royal Society A: Mathematical, Physical and Engieneering Sciences* 143, 307–325, 1934.

[138] Thomson W. (Lord Kelvin), On the thermoelastic and thermomagnetic properties of matter, *Transactions of the Royal Society of Edinburgh*, 20, 161, 57-77, 1853.

[139] Tobushi H., Matsui R., Takeda K., Pieczyska E.A., Mechanical Properties of Shape Memory Materials, Nova Science Publishers, New York, 2013.

[140] Venkataraman B., Raj B., Mukhopadhyay C.K., Jayakumar T., Correlation of infrared thermographic patterns and acoustic emission signals with tensile deformation and fracture processes, in: D.O. Thompson, D.E. Chiment (Eds.), *Review of Progress in Quantitative Nondestructive, Evaluation,* 1443–1450, 2001.

[141] Vorontsov V.A., Jones N.G., Rahman K.M., Dye D., Superelastic load cycling of Gum Metal *Acta Materialia* 88, 323, 2015.

[142] Wei L.S., Kim H.Y., Koyano T., Miyazaki S., Effects of oxygen concentration and temperature on deformation behavior of Ti-Nb-Zr-Ta-O alloys, *Scripta Materialia* 123, 55, 2016.

[143] Wei L.S., Kim H.Y., Miyazaki S., Effects of oxygen concentration and phase stability on nano-domain structure and thermal expansion behavior of Ti–Nb–Zr–Ta–O alloys, *Acta Materialia* 100, 313–322, 2015.

[144] Wei Q., Wang L., Fu Y., Qin J., Lu W., Zhang D., Influence of oxygen content on microstructure and mechanical properties of Ti–Nb–Ta–Zr alloy, *Materials & Design* 32, 5, 2934-2939, 2011.

[145] Withey E.A., Minor A.M., Chrzan D.C., Morris Jr. J.W., Kuramoto S., The deformation of Gum Metal through in situ compression of nanopillars, *Acta Materialia* 58, 7, 2652-2665, 2010.

[146] Yamauchi K., Ohkata I., Tsuchiya K., Miyazaki S., *Shape Memory and Superelastic Alloys 1st Edition Applications and Technologies,* Woodhead Publishing Published, 2011.

[147] Yano T., Murakami Y., Shindo D., Kuramoto S. Study of the nanostructure of Gum Metal using energy-filtered transmission electron microscopy, *Acta Materialia* 57, 628–633, 2009.

[148] Zhang J., Tasan C. C., Lai M. J., Dippel A.-C., Raabe D., Complexion-mediated martensitic phase transformation in Titanium, *Nature Communications* 8, 14210, 2017.